7. SITE 949[1]

Shipboard Scientific Party[2]

HOLE 949A

Date occupied: 29 June 1994

Date departed: 30 June 1994

Time on hole: 11 hr, 30 min

Position: 15°32.215′N, 58°42.862′W

Bottom felt (drill-pipe measurement from rig floor, m): 5020.5

Distance between rig floor and sea level (m): 11.3

Water depth (drill-pipe measurement from sea level, m): 5009.2

Total depth (from rig floor, m): 5076.7

Penetration (m): 56.2

Number of cores (including cores having no recovery): 1

Total length of cored section (m): 3.0

Total core recovered (m): 2.95

Core recovery (%): 98.3

Oldest sediment cored:
Depth (mbsf): 2.95
Nature: clay with nannofossils
Age: Quaternary

Comments: Jetting test and core to establish mud line.

HOLE 949B

Date occupied: 30 June 1994

Date departed: 3 July 1994

Time on hole: 3 days, 5 hr, 15 min

Position: 15°32.161′N, 58°42.848′W

Bottom felt (drill-pipe measurement from rig floor, m): 5024.0

Distance between rig floor and sea level (m): 11.3

Water depth (drill-pipe measurement from sea level, m): 5012.7

Total depth (from rig floor, m): 5488.2

Penetration (m): 464.2

Number of cores (including cores having no recovery): 25

Total length of cored section (m): 218.1

Total core recovered (m): 86.80

Core recovery (%): 39.8

Oldest sediment cored:
Depth (mbsf): 464.20
Nature: at 156-949B-25H-2, 115 cm, silty claystone to clayey siltstone; flow-in from -25H-2, 115 cm, to -25H-4, 103 cm
Age: late Oligocene
Measured velocity (km/s): 1.707 at 460.59 mbsf

Comments: Drilled 0–244.1 mbsf and 456.4–458.4 mbsf

HOLE 949C

Date occupied: 3 July 1994

Date departed: 23 July 1994

Time on hole: 20 days, 6 hr

Position: 15°32.214′N, 58°42.855′W

Bottom felt (drill-pipe measurement from rig floor, m): 5016.0

Distance between rig floor and sea level (m): 11.3

Water depth (drill-pipe measurement from sea level, m): 5004.7

Total depth (from rig floor, m): 5484.3

Penetration (m): 468.3

Drilled (mbsf): 0–401.0 and 463.8–468.3

Cored (mbsf): 401.0–463.8

Number of cores (including cores having no recovery): 7

Total length of cored section (m): 62.80

Total core recovered (m): 2.18

Core recovery (%): 3.5

Oldest sediment cored:
Depth (mbsf): 463.8
Nature: claystone
Age: early Miocene
Measured velocity (km/s): 1.727 at Section 156-949C-7R-CC

Casing:
16-in.: 0–46 mbsf
13⅜-in.: 0–398.2 mbsf
10¾-in.: 0–465.5 mbsf
Perforated and screened section: 398.0–450.0 mbsf

Comments: Hole was cased and dedicated for VSP, packer, and CORK experiments.

Principal results: Site 949 sedimentology deduced from the limited recovery is similar to that of Site 948. The poor recovery precluded any detailed comparison with other sites cored in this area during Legs 78A or 110. Even so, the basic stratigraphy can be reconstructed using Site 948 for reference.

A stratigraphic inversion indicates that a thrust fault displaces the upper part of the cored section by a significant amount. Early Miocene radiolarians in a pale yellowish brown claystone occur at about 400 m, in the same core as some scaly fabric, and similar to the décollement association at other sites. Examples of the underthrust brownish gray to greenish gray claystone, with interbeds of siltstone turbidites and remobilized nannofossil chalks, occur in the lower part of the cored interval.

Only two cores yielded sediment material in the presumed décollement zone, with the lower one containing the lithologic boundary that occurs within the décollement at Site 948. Deformation structures are similar to those from Site 948, including inclined bedding, core-scale faults, mineralized veins, sediment-filled veins, brecciated zones and fracture networks,

[1] Shipley, T.H., Ogawa, Y., Blum, P., et al., 1995. *Proc. ODP, Init. Repts.*, 156: College Station, TX (Ocean Drilling Program).
[2] Shipboard Scientific Party is as given in list of participants preceding the contents.

stratal disruptions, and scaly fabric. Scaly zones are narrower, and the overall intensity of deformation is weaker, more diffuse, and more widely spaced than that at Site 948. Anisotropic magnetic susceptibility mineral fabrics show a distinct difference in orientation of principal strains between the prism and décollement zone.

Headspace gas analysis indicates that methane concentrations were below 20 ppm by volume, but did not show any trend with depth. Trace quantities of ethane and occasionally propane were found, with the methane-to-ethane ratio being between 20 and 200. Organic carbon content was low, mostly below 0.2%, although slightly higher in the siltstone turbidites.

Chloride concentration-vs.-depth profiles indicate that the cored section has been diluted by freshwater. Three distinct zones of low chloride concentration are located at about 290, 360, and 425 mbsf. Two are within the prism and the other is within the décollement zone. Reversals in most concentration profiles from about 270 to 350 mbsf suggest vertical displacement of about 80 m. Because little diffusion was observed across the inferred thrust within this interval, we hypothesize that it has a maximum age of about 35,000 yr.

Four WSTP measurements were performed at 265, 313, 351, and 458 mbsf that yielded a fairly linear thermal gradient of about 80°C/km with a bottom-hole temperature of 39°C at 458 m, suggesting that heat flow is not constant with depth. Paleomagnetic data, primarily bulk susceptibility variations downhole, follow the Site 948 trends and help define the transition into the décollement. Physical properties data for Holes 949B and 949C are sparse, and thus downhole profiles are incomplete. Specific relationships between observed reflections and their possible physical cause remain uncertain. The increase in velocity and density across the lithologic boundary, for example, does not explain the negative-polarity reflection observed here and correlated seaward into the basin. The physical property data will serve as a background for evaluating thermal and chemical information gained from the long-term measurements in the CORK hole. These data will also add to the general data sets collected during Legs 156, 78A, and 110.

A shear-wave vertical seismic profiling experiment used explosive charges on the seafloor around Hole 949C. Eighteen shots were recorded at two intervals to observe shear-wave velocities and polarizations, which relate to deformation fabric alignment. A conventional air-gun VSP followed, and the resulting velocity estimates and images confirmed our depth estimates within the borehole relative to the seismic reflection data. As at Site 948, velocities are about 2% higher than values used in the original three-dimensional seismic migration and depth conversion, and these velocities decrease just above the décollement.

The packer was used to perform a series of formation shut-in and flow tests to measure hydrologic characteristics at the décollement. Preliminary analyses suggest modest overpressures, less than the pressures recorded at Site 948. This result is consistent with the more subdued evidence for flow and casing filling at this site.

The CORK installation included a string of 10 thermistors and two pressure transducers, plus the associated data logger. A mechanical continuous fluid sampler, driven by an osmotic pump, was deployed by attaching it to the thermistor string. Pressure and temperature will be monitored and fluid samples collected for 2 yr.

BACKGROUND AND SCIENTIFIC OBJECTIVES

A prime objective at Site 949 was to compare the décollement with that at other Leg 156 sites, where the seismic signatures are in sharp contrast. At Site 949, we explored the negative-polarity waveform. This waveform is modeled as a low-velocity and high-porosity zone, so that fault properties may be significantly different from those at Site 948. While we originally had planned to conduct a comparison between Sites 948 and 947, time and difficulties at Site 948 led us to Site 949, which has a thinner overlying section and where the seismic signature of the fault is not so high in amplitude. The seismic data indicate a fault zone splay from about 150 to 225 mbsf, another fault at about 275 mbsf and deeper that cuts off subhorizontal reflections, and the main décollement at about 375 mbsf. A second reversed polarity reflection at about 425 mbsf, possibly a proto-décollement or a stratigraphic unit, has been traced seaward into the incoming sedimentary section (see "Structural Setting" chapter, this volume).

Site 949 is 1.8 km west of the trench thrust front and about 0.8 km north-northeast of Site 675 (Figs. 1–3), which was drilled during Leg 110 (Mascle, Moore, et al., 1988). Site 675 was an exploratory hole for packer work during Leg 110, but hole conditions were unstable and so the hole was abandoned after coring from 321 to 388 mbsf. Barren mudstone and claystone overlying 25 m of siliceous lower Miocene mudstone were recovered at Site 675, similar to the upper part of the décollement zone drilled at Sites 671 and 948. Leg 110 scientists found scaly fabric in two intervals, at 335 mbsf and 360 to 378 mbsf, with the latter being interpreted as the décollement.

Site 949 was planned for coring, wireline-logging, VSP, packer, and CORK experiments. The specific objectives follow those of Site 948, with the addition of a shear-wave VSP experiment to evaluate anisotropy associated with deformation fabric.

OPERATIONS

Because of the amount of time necessary to complete Site 948 and because of the remaining amounts of heavy mud, the originally planned program at Site 947 (NBR-3) was abandoned. A new site, NBR-7, was proposed and approved to provide an opportunity to penetrate the décollement in a similar geological setting, but at a shallower depth.

The new site is located about 2.4 km northeast of Site 948 and 3.9 km east-northeast of Site 947. A positioning beacon was launched on dithered global positioning system (GPS) coordinates at 1615 EST (local time), 29 June 1994, to begin operations at Site 949.

Hole 949A

When the APC/XCB bottom-hole assembly (BHA) had been run to the seafloor, a "mud-line" APC core was taken to determine seafloor depth (Table 1). The corer was actuated at 5014 mbrf, 2 m above the PDR depth. Core recovery from the 9.5-m stroke was 2.95 m and fixed seafloor depth at 5020.5 mbrf.

A jet-in test for conductor casing setting depth then was performed. The sediment was somewhat less firm than at Site 948, and the drillers determined that a minimum of 56 m of conductor casing could be jetted into the seafloor. Maximum parameters used for jetting were 17.7 L/s (275 gpm) and 9000 kg (20,000 lb) weight-on-bit. When the test had been completed, the bit was pulled clear of the seafloor, and the jetting core barrel was retrieved.

Hole 949B

During the wireline trip, the vessel was offset 125 m south and 30 m east, and a core barrel equipped with a center bit was pumped into place at the bit. When stable positioning had been achieved, the bit was lowered until a weight indication was seen on the driller's gauge that established the seafloor depth at 5024 mbrf. Spudding-in time was 0545 EST on 30 June 1994.

An $11\frac{7}{16}$-in. hole was drilled ahead without coring to 244 mbsf in a little more than 7 hr, after which the wash barrel was recovered and an XCB core barrel was pumped into place. Continuous coring then began.

Core recovery was variable, ranging from 0% to 102% and averaging 86.8% (Table 1). Some cores appeared to have been lost as a result of some core catchers having been stuck open, but in most cases, the liners showed no traces of mud inside, probably indicating that core had never entered the chamber. Various combinations of drilling parameters and core-catcher samples were tried, with no consistent results.

Coring was interrupted at 263, 312, and 350 mbsf for water sampler temperature probe (WSTP) runs, in temperature-only mode,

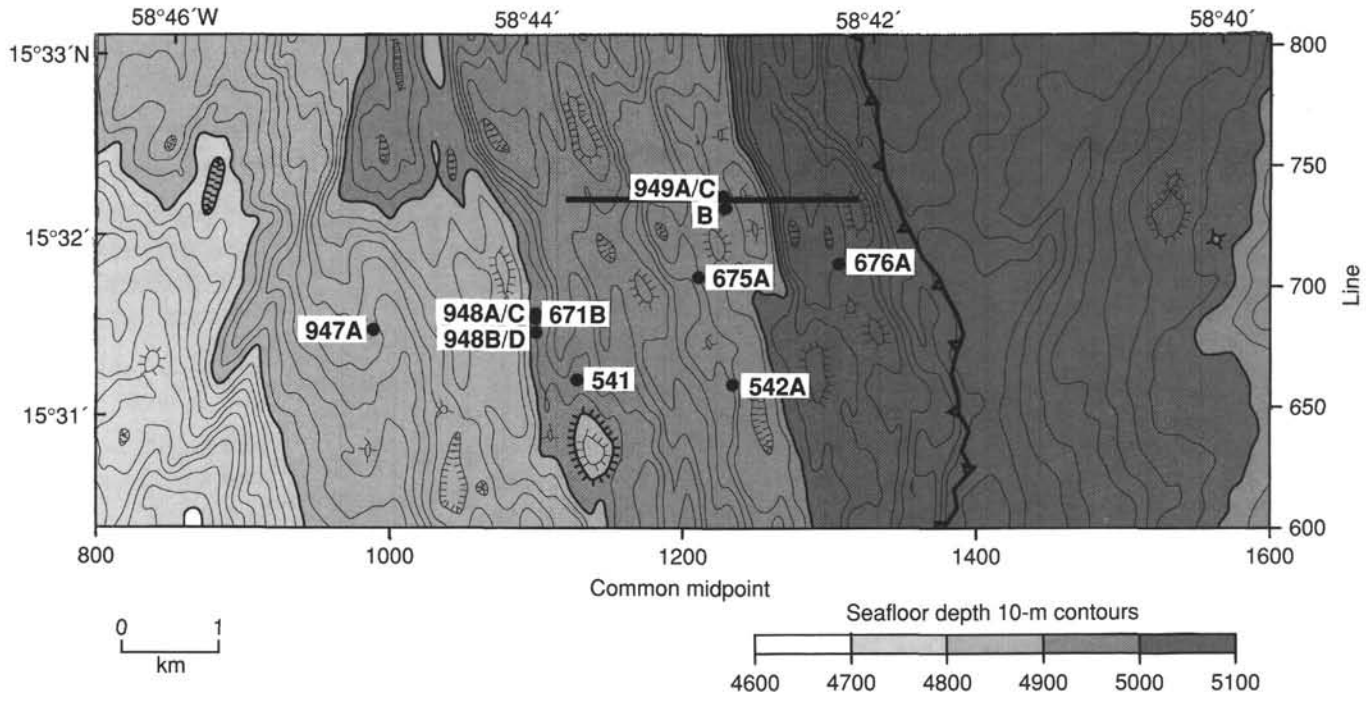

Figure 1. Location map showing the area around Site 949. Bathymetry based on digitizing the three-dimensional seismic data and assuming a water velocity of 1500 m/s. The frontal thrust (barbed line) and DSDP and other ODP drill sites are shown. Black line locates the seismic section in Figure 2.

which returned good results. In anticipation of potential problems when closing the hole, such as had occurred in other holes drilled in the region, a "precautionary" wiper trip was made back to 311 mbsf after the hole had been advanced to 399 mbsf.

When the coring depth objective was reached, enough core had been recovered to convince researchers that the décollement had been crossed; however, recovery was insufficient to reveal the décollement's nature or exact depth. Absolutely no hole trouble had been experienced until some minor torquing and overpull occurred after the final XCB core (Core 156-949B-24X) had been laid out from 456 mbsf. A final WSTP temperature run then was made at 456 mbsf.

Following the WSTP run, one final effort was made to obtain an APC core adequate for age dating and identification of lithologic units. While the APC coring assembly was run down the drill string, the rig crew drilled 2 m of new hole so that any core obtained would not be affected by disturbance from the WSTP probe. When the APC was fired, indication of an incomplete stroke was noted; however, the barrel was withdrawn without excessive overpull. A 5.1-m core was recovered, of which more than 50% was later determined to be flow-in material.

Hydrologic interference with the nearby planned sealed reentry hole was a concern, and a borehole plug was requested. After the core bit had been pulled to 321 mbsf, a cement slurry was mixed to 1.9 kg/L (15.5 lb/gal) and emplaced from 321 to 101 mbsf. The pipe was then pulled clear of the seafloor, flushed of cement residue, and tripped to the surface, ending Hole 949B at 0915 EST on 3 July.

Sub-bottom Depth Adjustment at Hole 949B

A situation occurred when coring Core 156-949B-14X that requires that the procedures for determining sample sub-bottom depth be adjusted. Although the drill bit was advanced only from 354.9 to 359.9 mbsf (5.0 m) for Core 156-949B-14X, a total of 9.83 m of sediment was retrieved, yielding 197% recovery (Table 1). When the bit was then advanced from 359.9 to 369.5 mbsf (9.6 m), 9.6 m of sediment was recovered in Core 156-949B-15X, yielding 100% recovery. This results in ambiguity in the account of the sub-bottom depths for the interval between 359.9 and 364.73 mbsf (Fig. 4). Samples from both the lower half of Core 156-949B-14X and the upper half of Core 156-949B-15X were assigned identical "curatorial" depths, following the standard conversion of sample identifier to sub-bottom depth (see "Explanatory Notes" chapter, this volume). To correct this unsatisfactory situation, the "curatorial" depths for Core 156-949B-14X were recalculated to "corrected" depths by scaling the recovered length of 9.83 m to the cored interval of 5.0 m using the following "transfer function":

$$\text{depth}_{corr} = 354.9 + [(\text{depth}_{cur} - 354.9)/1.996],$$

where depth_{cur} refers to the "curatorial depth" and depth_{corr} to the "corrected depth" (Fig. 5). All plots of sample analyses in this chapter indicate whether the data were plotted vs. "curatorial" depths or "corrected" depths.

Hole 949C

For the reentry installation at Hole 949C, an identical hardware configuration to that of Hole 948D was used, except for the addition of a 4-m "cutoff" casing joint.

During the trip to install the reentry cone and conductor casing, the ship was moved back toward the offsets of Hole 949A. At 0645 EST on 4 July, Hole 949C was spudded in as jet-in of the conductor casing began. Jet-in was slowed by the unfavorable hydraulics of the bit/underreamer combination, as at Site 948; however, sediments at this site were softer. To avoid excessive erosion of the casing/hole annulus, the circulation rate was held to a maximum of 21 L/s (325 gpm). Slow, steady progress was made for about 3½ hr until the casing shoe reached 5062.5 mbrf, 4.5 m short of the target depth, based on the Hole 949A mud-line core. Even with full casing/cone weight applied, no further progress could be made, and it was decided to release the assembly at that depth.

Operation of the DrilQuip running tool was routine and, as soon as the underreamer arms were advanced past the casing shoe, the circulation rate was increased to 45.2 L/s (700 gpm), and drilling in a 44.4-cm (17½-in.) hole began. A good rate of penetration (ROP) was

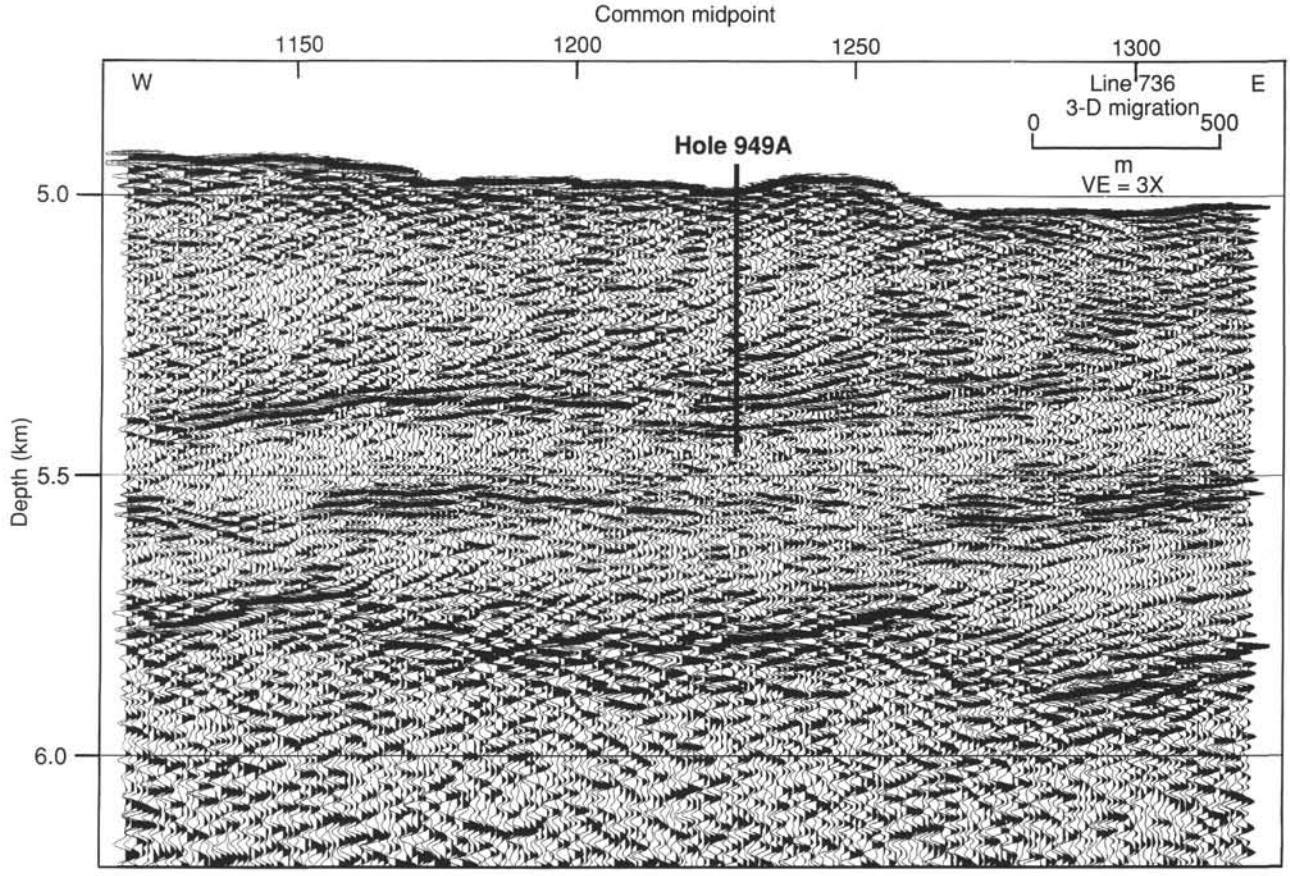

Figure 2. Seismic section illustrating reflection characteristics of the décollement. Section was converted to depth using a velocity function derived from Site 671 (Shipley et al., 1994). Specifically at Site 949, the prism velocity used was 1699 m/s; the underthrust section, 1743 m/s. Section gain was equalized with a 500-ms symmetric moving window. The location of seismic section is shown in Figure 1.

maintained, and the hole was drilled to the target depth of 398 mbsf in 8½ hr. Before the round trip for casing began, the hole was filled with mud with an average weight of 1.5 kg/L (12.8 lb/gal).

When the BHA for running 40.6-cm (16-in.) casing had been dismantled, the tool for running 34.0-cm (13⅜-in.) casing was made up to a stand of drill collars, while tools were assembled for running the surface-casing string. Thirty joints of range-3, 34.0-cm (13⅜-in.) casing were then assembled, with the casing hanger as the final joint. The drillers had to restrain the casing in the moonpool area with tugger lines to combat the effects of currents on the casing suspended below the ship. The casing-running tool, with cementing plug attached, was made up to the casing string, and the casing was run to reentry depth, with the drill string filled after every 20 stands.

The first reentry into the Hole 949C cone required more than 4 hr of maneuvering because of a combination of unfavorable currents, unfamiliarity with the orientation and "location offsets" of the cone, and marginal sonar performance. At the time of reentry, it was confirmed, by pipe measurement and video inspection, that the cone remained at the depth where it was released and that the mudskirt was landed at the seafloor. (A check of navigation records revealed that the Hole 949C cone actually had been emplaced about 30 m in an upslope direction from Hole 949A.) When the casing had been run to 89 mbsf, resistance was noted on the weight indicator. The rig crew did not know whether the weight was being taken by an obstruction in the hole or the effect was merely buoyancy of the casing in heavy mud; thus, the top drive was deployed and the casing was "washed" in through the remaining hole interval.

No difficulty was encountered when advancing the casing with the top drive and fluid circulation. As at Hole 948D, returns were noted to be reaching the seafloor via the conductor casing/hole annulus. As the casing shoe was lowered, with circulation, to its setting depth, no fill or resistance was noted, indicating a clean hole. Surprisingly, the string was lowered through the expected landing point with only a momentary indication of "taking weight." No further change in string weight was seen until the casing was set down abruptly when the shoe reached 5414.2 mbrf, which coincided exactly with the total depth of the hole. The string was raised to check if the casing hanger had latched in. A 9000-kg (20,000-lb) overpull was taken, and a TV picture showed relative motion between the pipe and the reentry cone. To avoid disturbing the minimal reconstitution of sediment around the conductor casing, no additional tension was applied.

A discrepancy of about 7.5 m between the depth of the 34-cm (13⅜-in.) casing hanger and its intended seat was disturbing because that spacing was critical for placing the seal sub of the subsequent 27.3-cm (10¾-in.) casing string opposite the sealing bore of the 34-cm (13⅜-in.) casing hanger. The vertical dimensions were known exactly with all three components latched together, but there was considerable uncertainty about whether the 34-cm (13⅜-in.) string was below its seat and resting at the bottom of the hole. Without a positive annular seal, the packer-permeability experiments and long-term CORK pressure monitoring either would be compromised seriously or be completely ineffective. There was also concern that the 34-cm (13⅜-in.) casing, when set in compression, would begin to buckle and "helix" in the hole to the extent that the 27.3-cm (10¾-in.) string (or the 31.1-cm [12¼-in.] bit) would not pass through it. To compound the riddle, the nature of the failure was not understood. Without a major dimensional error in one or both components, it should not have been possible for the casing hanger to pass through its seat in the adapter sub. That left the possibility that the 40.6-cm (16-in.) casing had parted below the reentry cone and either had fallen

Table 1. Coring summary, Site 949.

Core no.	Date (1994)	Time (UTC)	Depth (mbsf)	Length cored (m)	Length recovered (m)	Recovery (%)	Age
156-949A-							
1H	30 June	0530	0.0–3.0	3.0	2.95	98.3	
Coring totals				3.0	2.95	98.3	
			****** Drilled from 0.0 to 244.1 mbsf ******				
156-949B-							
1X	30 June	1930	244.1–253.8	9.7	2.29	23.6	lower to middle Miocene
2X	30 June	2115	253.8–263.5	9.7	9.61	99.1	
3X	1 July	0025	263.5–273.1	9.6	8.98	93.5	
4X	1 July	0145	273.1–282.8	9.7	1.94	20.0	
5X	1 July	0300	282.8–292.4	9.6	9.88	103.0	
6X	1 July	0440	292.4–302.1	9.7	0.12	1.2	
7X	1 July	0625	302.1–311.6	9.5	9.65	101.0	
8X	1 July	1000	311.6–321.3	9.7	0.00	0.0	
9X	1 July	1115	321.3–330.9	9.6	0.00	0.0	
10X	1 July	1245	330.9–340.6	9.7	0.00	0.0	
11X	1 July	1415	340.6–345.4	4.8	0.00	0.0	
12X	1 July	1555	345.4–350.2	4.8	0.00	0.0	
13X	1 July	2020	350.2–354.9	4.7	3.92	83.4	
14X	1 July	2225	354.9–359.9	5.0	9.83	196.0	
15X	2 July	0040	359.9–369.5	9.6	9.53	99.3	
16X	2 July	0220	369.5–379.1	9.6	0.10	1.0	
17X	2 July	0410	379.1–388.8	9.7	0.29	3.0	
18X	2 July	0610	388.8–398.8	10.0	0.00	0.0	
19X	2 July	0910	398.8–408.1	9.3	5.11	54.9	
20X	2 July	1115	408.1–417.7	9.6	0.00	0.0	
21X	2 July	1400	417.7–427.4	9.7	0.00	0.0	
22X	2 July	1615	427.4–437.1	9.7	9.57	98.6	
23X	2 July	1800	437.1–446.7	9.6	0.15	1.6	
24X	2 July	2030	446.7–456.4	9.7	0.00	0.0	
			****** Drilled from 0.0 to 244.1 mbsf ******				
25H	2 July	2355	458.4–464.2	5.8	5.83	100.0	
Coring totals				218.1	86.80	39.8	
Drilled				246.1			
Total				464.2			
			****** Drilled from 0.0 to 401.0 mbsf ******				
156-949C-							
1R	11 July	2025	401.0–405.9	4.9	0.00	0.0	
2R	11 July	2145	405.9–415.6	9.7	0.10	1.0	
3R	11 July	2350	415.6–425.2	9.6	0.00	0.0	
4R	12 July	0135	425.2–434.9	9.7	0.68	7.0	
5R	12 July	0330	434.9–444.5	9.6	0.14	1.5	
6R	12 July	0525	444.5–454.1	9.6	0.15	1.6	
7R	12 July	0710	454.1–463.8	9.7	1.11	11.4	
Coring totals				62.8	2.18	3.5	
Drilled				401.0			
Total				463.8			

down the 44.5-cm (17½-in.) hole or had been pulled down with the 34-cm (13⅜-in.) string after engagement.

Because there was resistance to raising the casing string from its position, there was little choice but to proceed with cementing and releasing the casing at that depth. A special lightweight cement slurry was mixed to 1.7 kg/L (14 lb/gal) using 1.2% (by weight) bentonite prehydrated in fresh mix water. The slurry was pumped into the drill string, circulation then was switched to the mud pump, and the cement was displaced with seawater. Circulating pressure built only to 3.8 MPa (550 psi) during the displacement and failed to rise during the final phase of displacement, again indicating that the formation had broken down and cement had not filled the entire annular column. No returns could be seen by TV either inside or outside the reentry cone during the entire cementing/displacing operation. When the top plug "bumped," the standpipe bleedoff valve was opened. Only a brief backflow was noted, indicating that the float valve in the casing shoe was holding and that cement slurry was not flowing back inside the casing.

A round trip and routine reentry then were made for a 31.1-cm (12¼-in.) bit and drilling BHA. The bit traveled unimpeded past the 34-cm (13⅜-in.) casing hanger and through the entire casing string, allaying concerns about any parting of the 40.6-cm (16-in.) casing, an off-center casing hanger, or "helixed" casing. No resistance whatever was encountered until 5413 mbrf. The plug and shoe were drilled out in just 1 hr. Three meters of new hole then were drilled, and the hole was flushed with extra-high-viscosity mud to clear it of debris.

The bit was pulled clear of the reentry cone and released onto the seafloor. During the tripping and releasing operations, the vibration-isolated TV (VIT) had been run to reentry depth, so that another routine reentry placed the drill string into logging position. Logging sheaves then were rigged, and the cement-bonding log (CBL) tool was made up to the logging cable and run down the pipe.

Results of the CBL showed that some cement bonding extended over the lowermost 108 m of the casing string, but that no sign of cement was evident over the remainder of the string, which "rang" as free pipe. Indications of signal from the 40.6-cm (16-in.) casing collars and shoe were seen through the uncemented 34-cm (13⅜-in.) casing and indicated that the 40.6-cm (16-in.) string was in its proper position. An interval of several meters of low-amplitude signal between the 34-cm (13⅜-in.) hanger and the point where the CBL originally entered the drill string was interpreted as open hole, but later was concluded to be the effect of centralization and the distance to the 40.6-cm (16-in.) pipe.

After recovery of the CBL, it was replaced with the Schlumberger array seismic imager (ASI), which was lowered a short distance down the pipe. The traveling block then was raised to its highest position, pulling the end of the drill string about 22 m clear of the reentry cone.

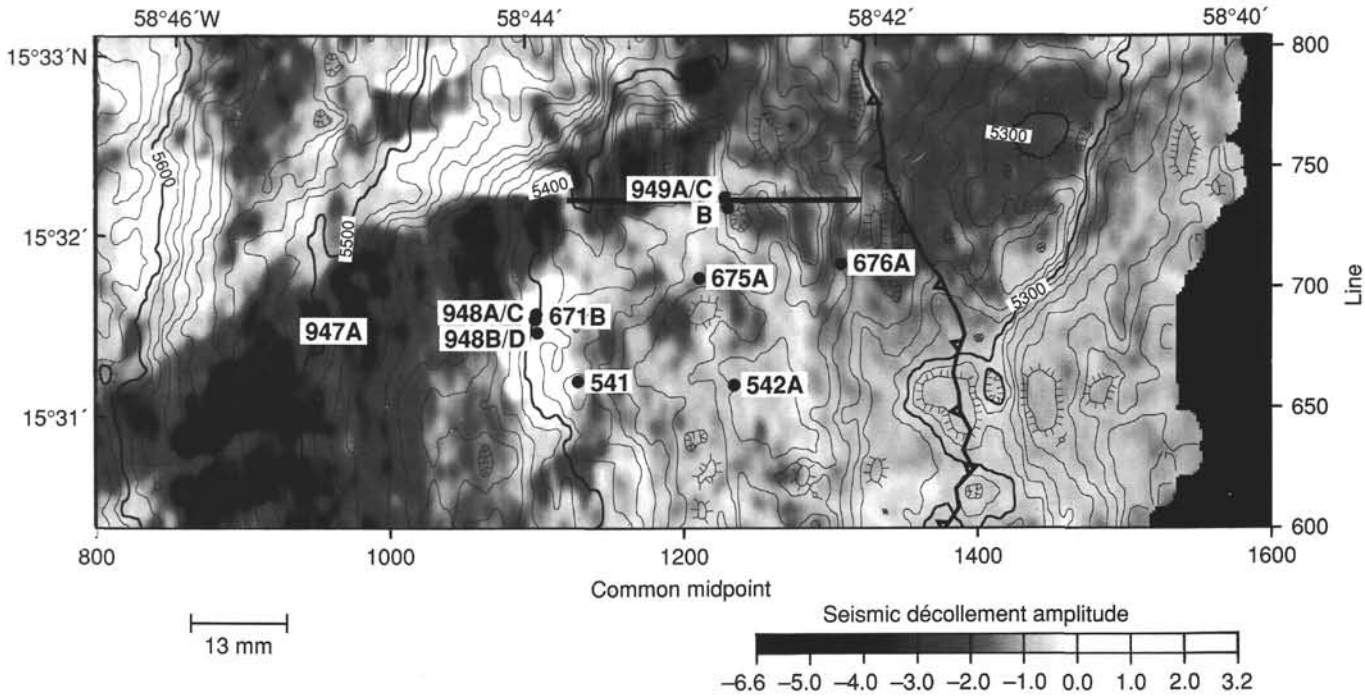

Figure 3. Map of area around the Leg 156 drill sites, showing the structure on the décollement and the peak amplitude of the reflection. Map is based on correlation of the lower fault as the décollement. Section is equivalent to a three-dimensional horizon crop map of the décollement. Structural contours are at 10-m intervals. Black line locates seismic section in Figure 2.

In preparation for deploying explosive charges, all sources of electromagnetic radiation and extraneous electrical fields were secured.

The vessel then was offset about 1200 m to the northwest to begin deployment of charges for the shear-wave VSP (SWVSP) experiment. In total, 21 charges were laid in a fan-shaped array to the north of Site 949. Because it was necessary to maintain ship's heading into the current to carry the charges clear of all propellers, the explosives were deployed in three subparallel traverses that were roughly west-to-east. Despite some positioning complications from variable currents and threats of rain showers, which would have required securing the explosives, conditions remained generally favorable, and the deployment was completed in 11 hr.

When the last of the explosives had been released, the vessel returned to normal operating mode, offset back to Hole 949C, the VIT (which had been held just below the ship) was lowered down the drill string, and the ASI was lowered down the inside of the pipe. A quick reentry was made, and the ASI was run into open hole. Because deployment and reentry had gone smoothly, about 5 hr was available before detonations were scheduled to commence. Air guns and hydrophones were rigged so that shooting could begin on the scheduled standard VSP. The first (lowermost) station of the VSP was completed before interruption for the SWVSP.

About 1 hr before explosive detonations were to begin, the Schlumberger seismic system was converted to the mode for recording the SWVSP. The first charge failed to detonate, but 19 of the remaining 20 shots were detected successfully and recorded over the ensuing 4 hr.

Recording of the standard VSP then resumed and was completed in the next 5½ hr. The ASI was recovered, the logging sheaves were rigged down, and the pipe was tripped by 2200 EST on 9 July.

Because of the detachment of the surface-casing string, accurate measurements were needed to adjust the spacing of the seal sub in the 27.3-cm (10¾-in.) casing string. The casing string was to be landed in the reentry cone, but the seal sub had to mate with a reduced-diameter section in the 34-cm (13⅜-in.) casing hanger that was only 16 in. long vertically. To obtain the needed measurements, a dedicated round trip was made with a BHA that featured the 40.6-cm (16-in.) DrilQuip running tool, with the 34-cm (13⅜-in.) running tool directly beneath it.

During preparations to deploy the VIT, we discovered that the reentry sonar was not operating. There was little prospect for repair in a reasonable time period, so the VIT was run with only the TV operating. The ensuing reentry required 6 hr because the reentry cone could not be tracked outside the TV's field of view, which is about 15 m in diameter.

When reentry finally was accomplished (with the top drive), the drill string was lowered a few meters until the 40.6-cm (16-in.) running tool landed in the 40.6-cm (16-in.) casing hanger. With the motion compensator holding about 2300 kg (5000 lb) of weight down on the hanger, the pipe was marked at the rotary table. The string then was rotated to the right to release it from the running-tool bushing and allow it to advance until the 34-cm (13⅜-in.) running tool was seated in the other casing hanger. The rig personnel used a lefthand rotation to engage the casing hanger, and tension was measured to verify that the running tool had reached a seat in the hanger. After 2300 kg (5000 lb) of weight again had been applied, a second mark was made on the pipe, and the running tool was released with clockwise rotation. Because the dimensions of all hardware components were known, the distance between the marks provided the needed information to determine that the 27.3-cm (10¾-in.) seal sub should be spaced 7.04 m lower than normal. The drill string then was tripped for a coring BHA.

In an attempt to supplement the low core recovery of Hole 949B through the zone of greatest scientific interest, an RCB BHA was assembled to core the interval below the surface-casing shoe and extending through the décollement. The combination of the RCB coring system and the antiwhirl polycrystalline diamond compact (PDC) core bit was chosen because it had outperformed the other rotary systems in terms of core recovery and quality during recent cruises.

Reentry was made in 1¾ hr with the aid of a barely functioning sonar. No resistance was met as the bit was run to total depth 3 m below the casing shoe, where continuous RCB coring began.

Seven cores were attempted over an interval of 62.8 m (401.0–463.8 mbsf). Unfortunately, this coring performance was even worse

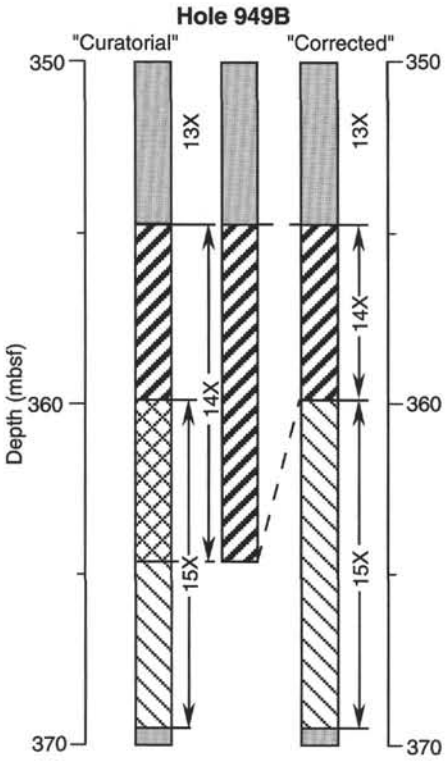

Figure 4. Depth ambiguities between Cores 156-949B-14X and -15X.

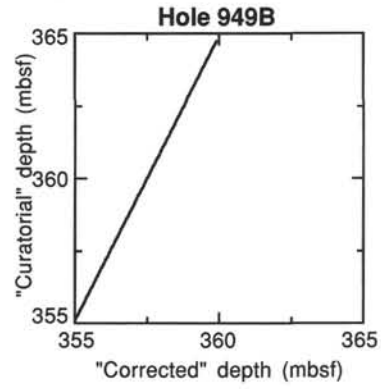

Figure 5. Graph of "transfer function" used to recalculate "corrected" depths for Core 156-949B-14X by scaling the recovered length of 9.83 m to the cored interval of 5.0 m.

than that using the XCB system in Hole 949B; average core recovery was only 3.5%, with several zero-recovery cores (Table 1). Again, various combinations of coring parameters and core catchers were tried without success. Core 156-949C-7R had the highest recovery (11.4%) and was from the more-recoverable lithology recognized as occurring below the décollement. Further coring was judged to be of little value, so the drill string was tripped for a third casing string.

During coring, the necessary hardware changes had been made to produce a "production" casing string with an annular seal. A joint of casing had been cut to length and welded onto the 27.3-cm (10¾-in.) casing hanger to extend it to 8.49 m from its standard length of 1.45 m. In addition, the seal sub had been modified by adding more seal grooves and seals to increase the length over which an effective seal could be achieved.

The total string, including 34 joints of casing, the seal sub, and the hanger, was assembled in 8 hr. The four joints immediately above the shoe joint were special perforated joints that were covered with a gravel-pack screen. An additional 5 hr was required to make up the "stinger" BHA terminated by the PDM and underreamer. After the trip to reentry depth, reentry was made in 1¼ hr, with the sonar performing at a marginal level. Rig personnel noted that the arms of the underreamer were in a partially open position during the reentry trip.

Following reentry, the bit/underreamer assembly would not pass the approximate depth of the 34-cm (13⅜-in.) casing hanger. It was difficult to determine whether the edge of the hanger was being contacted by the underreamer arms or by the sharp-edged casing shoe because of their close spacing. After other attempts failed, rig personnel found it necessary to pick up the top drive and rotate the entire string slowly to the left as it was lowered past the hanger to move the edges past the obstruction.

The casing string was run to 371 mbsf, 27 m above the surface casing shoe, before the top drive was picked up. No resistance had been felt to that point, but the drill string was found to be plugged when circulation was attempted. More pipe was added to advance the bit below the casing shoe, where full pump circulation could be applied without concern of opening the underreamer. "Soft" fill was encountered within a few meters, however, and the string was stopped about 4 m short of the shoe. When additional attempts to unplug the drill string were unsuccessful, the pipe was pulled back to the reentry cone in the hope that it would be cleared by the surge of tripping. The string remained blocked, so the pipe was swabbed at the surface with a wireline swab cup in a final attempt to establish circulation by applying a negative pressure differential across the bit. These efforts did not succeed, and a round trip was necessary to clear the pipe. This trip was slow because it was "wet," with 30 m of water gushing from each stand of pipe as its connection was broken.

When the BHA arrived at the rig floor, the casing string was detached and hung off in the moonpool. The stinger then was recovered, and muddy water was found in the pipe more than 300 m above the bit. As more BHA components were set aside, sand and silt had to be cleaned from the lowermost few meters above the PDM; the upper portion of the PDM was found to be packed with clean, fine sand. About 2 hr was required to clean the sand from the motor and to restore normal operation.

During the recovery pipe trip, adapters had been fabricated in the rig's machine shop to fit a float valve to the cavity of a coring top sub. The improvised float sub was placed above the PDM when the BHA was reassembled, with a 305-cm (10-ft) drill-pipe pup joint replaced by a 152-cm (5-ft) pup to preserve spacing. In addition, the underreamer arms had been taped in a closed position to avoid fouling the 34-cm (13⅜-in.) casing hanger. The casing string then was reattached to the BHA and run back to reentry depth at a slower-than-normal pace because of the requirement to fill the pipe periodically (imposed by the float valve). With the sonar completely inoperative, the TV-only reentry took 4¾ hr.

Again, the lower assembly failed to pass the 34-cm (13⅜-in.) casing hanger, and the rig crew had to use the top drive to "rotate past" the shoulder. The casing shoe was lowered to 345 mbsf before the top drive was deployed. When fill was tagged at 374 mbsf (24 m inside the surface casing), slow circulation of 6.5 L/s (100 gpm) was used to turn the PDM and wash out the fill without opening the underreamer arms. At 400 mbsf, the underreamer was in open hole, and the circulation rate was increased to clean the hole and drill/ream ahead.

The drilling-in operation with casing proceeded remarkably smoothly over the interval of the pre-drilled (cored) hole, with little weight required and a high ROP. The casing shoe was advanced from 401 to 463 mbsf in only 1½ hr. An additional 2¾ hr was required to penetrate the final 2.5 m and land the casing hanger in the 40.6-cm (16-in.) hanger. During that interval, the casing began to "pack off" and weight and depth indications became ambiguous. The assembly appeared to be landing at a point about 2 m short of the expected depth; however, latch-in was not achieved because the casing string could be pulled free, indicating that the snap ring of the casing hanger had not engaged. Circulating pressure increased whenever the string

was lowered and appeared to hold formation pressure when the pump was stopped. Rig personnel could not determine whether that was the effect of the hole packing off or of the annular seal sub reaching its seat in the 34-cm (13⅜-in.) casing hanger. On two or three occasions, the casing was thought to be latched in, and attempts were made to release it. Those efforts resulted only in apparent rotation of the entire casing string and freeing it vertically. Finally, weight (36,000 kg; 80,000 lb) far in excess of the casing weight was set down, and all aspects of latch-in were noted.

Releasing the casing string also proved difficult. Weight approximately equivalent to that of the casing was set down and rotation was attempted, but the string would not rotate. High torque was held on the string while string weight was varied to find the "neutral point." Only after the seemingly excessive weight of 36,000 kg (80,000 lb) was set down did the drill string spin free and separation occur.

As the pipe trip was begun, the actuation ball for the circulating sub was dropped and allowed to fall until the seafloor was cleared. Pressure then was applied to open the sub and allow the trip to continue "dry." Upon recovery and disassembly of the stinger BHA, the PDM and underreamer were flushed with freshwater by circulation through the top drive. Before the top drive was set back, it again was blanked off for a test of rig surface equipment to 15.2 MPa (2200 psi) in preparation for the permeability experiment.

To complete the casing installation for the final phase of experiments and emplacement of the CORK sensor string, blockage of the bottom of the casing was desired. A mechanical-set packer, or bridge plug, had been delivered by helicopter for that purpose. The bridge plug and its running tool were attached to a BHA of three drill-collar stands and a drilling jar. Because of the possible presence of sand in the hole, the improvised top/float sub also was included. The pipe trip again was slowed for filling the pipe. The reentry took 15 min with the aid of a repaired sonar tool.

When the bridge plug had reached 382 mbsf, the top drive was picked up. At 410 mbsf, an obstruction was contacted. Some fill had been anticipated, and the plan was to wash the plug to just above the casing shoe with pump circulation. However, circulation proved completely ineffective at removing the blockage or advancing the plug downhole. Pump rates as high as 54.9 L/s (850 gpm) were tried, with weight to 11,000 kg (25,000 lb) applied (rotation was not an option with the rotation-set plug). Progress was barely measurable. After more than 2 hr of pumping and working the unfamiliar plug in the hole, attempts at cleaning the hole were abandoned in consideration of the possibility of junking it. At that time, the nature of the solid obstruction was questionable, and failure of the plug or running tool was considered to be possible. The bridge plug was tripped back out of the hole.

At 0330 EST on 17 July, the bridge plug arrived on the rig floor. It was in excellent condition, but its concave base was packed solid with a mixture of clay, silt, and fine sand. Embedded in the sediment were several large chunks of black rubber, apparently pieces of the plugs used on the surface-casing cement operation. The sediment was a positive indication that the impediment was fill, not a mechanical problem with the casing, plug, or running tool. Unknown factors included the reason for the crew's inability to circulate out the relatively soft sediment, the mechanism by which the rubber found its way to the top of the fill, and the route by which sediment had entered the casing. Several options for the next step were considered before a tricone drill bit was made up to a short BHA and run in to clean out the hole.

During the pipe trip, the design of the lower portion of the bridge plug was studied and additional information about it was located. It became apparent that the lowermost portion, an integral "junk pusher," was designed to retain debris in the hole below the plug when fluid circulation is used by means of a hydraulic "curtain" formed by the location and attitude of the jet nozzles and by the skirt beneath them. To provide the capability of "washing" through sediment in the hole, the plug was modified in the ship's machine shop. The skirt was removed with a hacksaw, and short lengths of pipe were welded into the nozzle ports to orient them vertically and to extend them to the bottom of the plug.

Even with the sonar operational, the reentry took 2¼ hr. No sign of flow from the hole was noted. The top drive was picked up when the bit had been lowered to 374 mbsf and fill was contacted at 395 mbsf, 11 m higher than on the previous day.

Only 1 hr was required to wash the fill from the hole with a 200-gpm pump rate and no rotation. The bit was stopped 2.5 m above the casing shoe to avoid washing out any material that might be plugging the annulus around the shoe. A 20-bbl sweep of sepiolite drilling mud was circulated through the hole to ensure complete cleaning before the drill string was withdrawn. The bit was back on deck at 0500 EST on 18 July.

With the modified bridge plug, the pipe again was run back to reentry depth. Just as the search for the reentry cone began, the underwater TV signal was lost. Good sonar function was retained, but rig personnel considered it too risky to attempt a sonar reentry with the somewhat fragile cast-iron bridge plug. In all, 4¾ hr was spent to recover the VIT, to troubleshoot and rectify the TV problem, and to run the VIT back to reentry depth. The sonar failed after rig personnel started to search for the cone again. The tedious TV-only reentry then required an additional 2¼ hr, during which time the hole appeared to be flowing.

After the top drive was deployed at 378 mbsf, fill was found at 431 mbsf, with just 32 m of sediment accumulating in the 27 hr since the hole had been cleaned out. The modified plug was an improved wash-down tool, and the hole was cleaned to plug-setting depth at 463 mbsf in 1¼ hr. After 35 clockwise revolutions to set the upper slips, tension was applied in 6,800-kg (15,000-lb) and 14,000-kg (30,000-lb) steps to set the mechanical packer element and the lower slips. Tension then was increased to 23,000 kg (50,000 lb) to part the tension sleeve and to release the plug. To augment the mechanical locking and to verify integrity, a BHA weight of 11,000 kg (25,000 lb) was set down on the plug momentarily. Fifteen minutes of seawater circulation at 32.2 L/s (500 gpm) with the pipe at 460 mbsf then cleaned the casing/pipe annulus before the drill string was pulled.

As soon as the plug-running tool and float sub had been removed, the logging/packer BHA was assembled and run to reentry depth. A 2-hr TV reentry was made into a cone that showed no sign of flow. The TAM straddle-packer (TSP) was run to 376 mbsf, where the top drive was deployed.

Permeability tests began by running in the instrumented inflation go-devil at 2015 EST on 19 July. While the go-devil was pumped down the pipe, the TSP was positioned at 392 mbsf, and the motion compensator was actuated. A series of successful measurements was conducted and was in its concluding stages when the packer began to "climb" in the hole. Apparently, it was losing inflation pressure and was being pushed up the hole by confined test pressure. After the TSP was unseated and the go-devil retrieved for data, the coring-line sinker bars were run to test hole depth, at which time 15 m of fill was found. While data were being checked, the drill string was lowered, with circulation, to 3 m off the plug to wash the fill from the hole. After 30 min of circulation at 19.4 L/s (300 gpm), the TSP was pulled back to setting depth above the screened casing interval. The second packer set was at 388 mbsf, just below a casing connection that rig personnel hoped would retard slippage of the element up the hole. Several tries were required to obtain a good set, as the element was sealing hydraulically and ship's heave caused the sliding control valve to dump pressure into the borehole. When a satisfactory set was achieved, it held through 2 hr of testing before it again began to climb during a constant-rate injection test. The full BHA weight of 14,500 kg (32,000 lb) was required to hold the packer down while pressure was monitored. It was necessary to bleed off drill string pressure at the standpipe to unseat the packer because trapped pressure in the borehole pushed it up the hole when the pipe was raised. The go-devil arrived on deck at 1530 EST on 20 July to conclude the packer experiments.

In preparation for the VSP experiment, 10 stands of drill pipe were laid out to raise the BHA to just below the seafloor. A second "sounding" was taken with the sinker bars; no fill was encountered in the

hole. The logging sheaves were rigged, and the Schlumberger ASI tool was deployed for an air-gun VSP over the cased-hole section below the surface casing. Most of the 12 hr it took for the VSP experiment was in rigging and running the ASI. Air-gun shots were recorded at stations in the interval below the surface-casing shoe, which had not been drilled at the time of the earlier VSP experiment. The logging sheaves were rigged down, while the coring-line sinker bars again were run to check if fill was in the hole. The bars came to rest at 458 mbsf, just 4 m short of the bridge plug.

The drill string was recovered, and the rig was prepared for the final phase of site operations. A "stinger" BHA of three used 8¼-in. drill collars and five used 7½-in. drill collars was assembled and hung off at the rig floor. The CORK and its running tool then were incorporated into the drill string, and an upper BHA of two stands of drill collars completed the assembly.

Following the trip to the seafloor with the CORK assembly, another television-only reentry took 2¼ hr. The end of the stinger was run 58 m into the hole, where it was held for installing the sensor string and data logger.

The hole depth was verified again with the small-diameter sinker bars to check for progressive fill in the hole. Set-down was noted at 5455 m (439 mbsf), so a last-minute alteration was performed to change the length of the thermistor string from 445 to 435 m. When the coring line had been recovered, the U.S.-Canadian sensor-string/data-logger assembly was lowered into the drill string. A 7-m-long geochemical fluid sampler array was attached to the Kevlar sensor string, and the data logger was engaged by the overshot on the coring line for lowering to the CORK.

Normal indications of landing at the CORK were seen, but no positive indication of latch-in was noted. An overpull to about 2000 lb would fall off to about 1000 lb as more line was taken in. The resistance to full seating and the drag upon raising the data logger were interpreted to be the result of seal friction. Latching efforts twice resulted in sheared overshot pins, and wireline trips were made to redress the overshot. On the third wireline trip, a heavier 1700-lb sinker bar was assembled with the intention of using weight to force the seals of the data logger far enough into their seat to permit latching. There was no change in results upon engaging the data logger, however. As a precaution, the data logger and sensor string were recovered with the sinker bars for inspection. No damage was visible to either the data logger body or the Kevlar line. Before the assembly was run back to the CORK, the lower set of seals (which had no function in the current application) were ground away with the intent of reducing resistance to insertion.

Upon landing, the familiar pattern of overpull followed by slippage again was experienced. As a final measure, rig personnel tried a 200-gpm pump circulation in an effort to apply additional force down on the data logger. The measure apparently was effective, as the data logger held firm against a 3000-lb overpull. Then, several minutes were spent in working and jarring the sinker bars to shear the overshot pin and to release it from the data logger. When this release had been achieved, the sinker bars were recovered, only to reveal that the data logger and thermistor string were still attached. Now, the Kevlar line and conductors of the sensor string were damaged, apparently as a result of being pinched between the data logger and its seat.

Operating time was passing rapidly, and chances for completing the CORK installation successfully were fading. The damage to the uppermost part of the sensor string suggested that slack in the buoyant line had become fouled in the latch/seal area. Before another sensor string could be tailored to the hole's depth, the coring line again was reheaded for the slim sinker bars, and the bars were run into the hole. These came to rest at the same depth as during the previous run, indicating that fill in the hole had not been the problem when landing the logger.

In a frenzy of activity, a large group of technicians, scientists, and crew unpacked and modified a 715-m sensor array, folding and lashing the Kevlar cable (Fig. 6; Table 2). The new array and data logger were run to the CORK and landed. As before, no positive indication was seen of latching, only the temporary "sticking." No time remained for protracted latching efforts, so the sinker bars were "worked" only a few times before the wireline was recovered. The anticipated task of laying down and repacking the thermistor string proved to be unnecessary, as the overshot cleared the top of the pipe without the data logger attached. Despite the uncertainty of latching, there was little choice but to proceed with setting the CORK and ending the cruise.

When the drill string had been lowered to land the CORK in the base of the reentry cone, the actuating ball was pumped down to finally latch in the CORK assembly. Pressure was held after landing the ball until the latch ring was hydraulically extended into its mating groove in the 10¾-in. casing hanger. Rig personnel verified the latching by measuring tension on the drill string. During pumping and latching, the ROV landing platform had been dropped through the moonpool and allowed to fall freely down the pipe.

Table 2. Final thermistor locations in Hole 949C.

Thermistor number[a]	Depth[b] (mbsf)
1	200.4
4	279.5
5	299.4
6	319.0
3	327.1
7	338.7
8	358.5
9	377.6
2	398.4
10	407.9

[a] Thermistor numbering is based on original string configuration.
[b] Depths are based on the assumption that the base of the CORK data logger is at 1.0 mbsf.

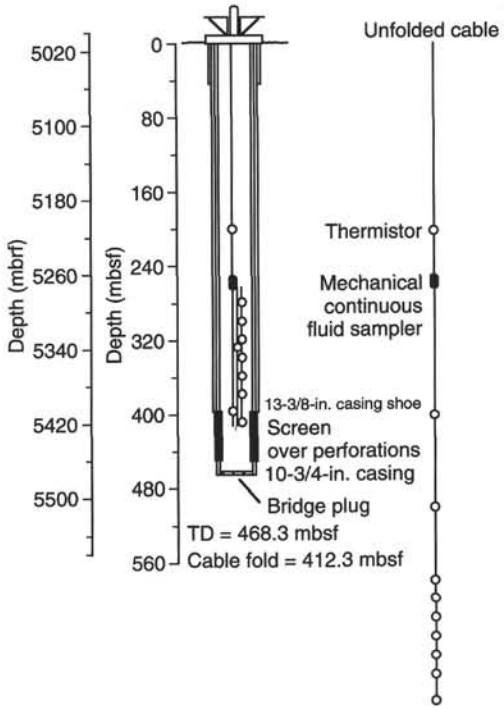

Figure 6. Schematic of final CORK sensor string in Hole 949C. The original, unfolded geometry is shown for reference. As illustrated, the string was folded twice to shorten it and to place two thermistors in the screened interval. Thermistor locations are indicated with open circles. The location of the osmotic fluid sampler is indicated with a solid oval.

Table 3. Summary of lithologic units and subunits recovered at Site 949.

Lithologic unit/subunit	Depth (mbsf)	Core interval (cm)	Age	General lithology	Depositional processes
I	0–2.95	948A-1H	Pleistocene	Light brownish gray clay with nannofossils and foraminifers; minor volcanic ash.	Hemipelagic settling; air-fall ash
IIB	244.10–255.40 and 302.10–353.88	948B-1X to 949B-2X-2, 10, and 949B-7X to 949B-13X-2, 68	early Pliocene to late middle Miocene	Light brownish gray and light olive gray claystone with nannofossils; rare volcanic ash.	Hemipelagic settling; air-fall ash
IIC	255.40–302.10 and 353.88–388.80	949B-2X-2, 10, to 949B-6X and 949B-13X-2, 68, to 949B-17X	Indeterminate	Mottled light olive gray claystone; rare volcanic ash; local discoloration.	Hemipelagic settling; air-fall ash
IIE	398.80–430.92	949B-19X to 949B-22X-3, 52, and 949C-2R to 949C-4R	middle to early Miocene	Pale yellowish brown and light brownish gray claystone with radiolarians; local discoloration.	Hemipelagic settling
III	430.92–464.20	949B-22X-3, 52, to 949B-25H and 949C-5R to 949C-7R	early Miocene to late Oligocene	Mottled variegated claystone interbedded with graded and laminated siltstone, greenish gray clayey siltstone, and gray claystone with nannofossils.	Hemipelagic settling; turbidity currents

Insufficient operating time remained for deploying the VIT to observe the platform and the unlatching operations. As soon as sufficient time had been allowed for the platform to land, the drill string was slacked and turned slightly to unjay the running tool from the CORK. The string was pulled free at 1100 EST on 23 July.

Because of the operational setbacks, some end-of-leg maintenance activities had been canceled; thus, only the pipe trip remained before the vessel could depart for Barbados. During the trip, both positioning beacons for Site 949 were recovered, the vessel was offset in DP mode to Site NBR-1, and that beacon was activated and recovered. The drilling assembly was on board at 1900 hr, and the *JOIDES Resolution* was under way at 1915 hr.

Site 949 to Barbados

We departed from the site 4 hr behind schedule, but with a short transit to Barbados. Rapid transit was aided by moderate sea conditions, light trade winds from abaft the beam, and a shallow draft. The first mooring line was put over in Bridgetown Harbor on 24 July, ending Leg 156.

LITHOSTRATIGRAPHY AND SEDIMENTOLOGY

Lithologic Units

The sedimentary strata recovered at Site 949 are similar to those at Site 948. In spite of miserable core recovery and complications imparted by stratigraphic repetitions across thrust faults, we were able to recognize the same three lithologic units as defined at Site 948 (Table 3; Fig. 7). Divisions between units and subunits are based on visual core descriptions, smear slide analyses, fossil content, carbonate content, and bulk X-ray mineralogy. The depth intervals cored at Site 949 include 0 to 2.95 mbsf (Core 156-949A-1H), 244.10 to 464.20 mbsf (Cores 156-949B-1X through -25H), and 401.00 to 463.80 mbsf (Cores 156-949C-1R through -7R). The percentage of recovery was 98.3% for Hole 949A and 39.8% for Hole 949B, but only 3.5% for Hole 949C.

Unit I (0–2.95 mbsf; 156-949A-1H)

The top 2.95 m of Unit I was sampled as a mud-line core. Based on comparisons with cores recovered at Site 676 (Shipboard Scientific Party, 1988), which is located 1.4 km southeast of Site 949, Unit I probably is about 160 m thick and ranges in age from early Pleistocene to late Miocene. The most common type of sediment is light brownish gray, mottled and moderately bioturbated clay, with trace to abundant amounts of nannofossils and foraminifers. Thin interbeds and irregular patches of light and dark gray volcanic ash are common. Carbonate content in this clay ranges from 7.8 to 31.8 wt% (Fig. 8; Table 4).

Unit II (244.10–430.92 mbsf; 156-949B-1X through -22X-3, 52 cm; and 949C-2R through -4R)

The cored interval of Unit II measures 186.82 m in structural thickness. Three of the subunits defined at Site 948 occur without ambiguity at Site 949; traces of Subunit IIA may exist within one of the fault zones encountered at this site, but we failed to recognize the other two subunits (IID and IIF). Two of the subunits (IIB and IIC) are repeated by thrust faults that splay off the basal décollement of the accretionary prism. Subunits IIA through IIC at Site 949 are equivalent to Unit II identified at Site 676 (Shipboard Scientific Party, 1988); our Subunit IIE is basically the same as Unit III at Site 676.

Nannofossil-bearing claystones of Subunit IIB are distinctive and repeated at least once by thrust faulting. The upper of the two cored intervals extends from 156-949B-1X to -2X-2, 10 cm (244.10–255.40 mbsf). The lower cored interval begins at the top of Core 156-949B-7X and extends to -13X-2, 68 cm (302.10–353.88 mbsf). A major

thrust fault, which is well defined on seismic reflection records at a depth of approximately 298 mbsf, forms the upper boundary of this interval. Because of poor core recovery within the fault zone (Core 156-949B-6X), as well as the possibility of additional faulting between Cores 156-949B-7X and -13X, the true stratigraphic thickness of Subunit IIB remains unknown.

Claystone color within Subunit IIB is mottled and ranges from light brownish gray to light olive gray. Coccoliths and discoasters are abundant and range in age from early Pliocene to late middle Miocene. Bioturbation is common. Volcanic ash occurs sporadically, both as discrete layers and as dark fragments dispersed by bioturbation. Carbonate content ranges widely (0.2–30.4 wt%, average of 13.1 wt%), but is consistently higher than that which characterizes adjacent subunits (Fig. 8). Consequently, both the upper and lower subunit boundaries are defined by sharp changes in carbonate, which are products of changes in nannofossil abundance.

Subunit IIC is composed of mottled gray, light olive gray, and light brownish gray claystone. Thin layers of volcanic ash are rare. Irregular fragments of claystone ("mud chips") are scattered throughout, and trace fossils (*Zoophycos* and *Chrondrites*) are common. The claystone is barren of nannofossils and radiolarians, but contains scattered foraminifers of indeterminate age. Angular fragments of darker greenish-gray claystone occur sporadically, and several intervals have sediment- and mineral-filled veins. Forty-eight samples were analyzed for carbonate content; the mean value is 0.4 wt%, and the range is 0.1 to 5.5 wt% (Table 4).

Subunit IIC is repeated at least once by thrusting. Local discoloration (to light brown and reddish brown) occurs in the vicinity of one fault zone. The upper of two cored intervals (255.40–302.10 mbsf) extends from 156-949B-2X-2, 10 cm, to -6X, where the carbonate-poor claystone overlies Subunit IIB (Fig. 7). In reality, stratigraphic assignment within the entire interval between 255.4 and 298 mbsf is ambiguous because of lithologic similarities between Subunits IIA and IIC and an absence of diagnostic microfossils. The vertical component of displacement on this particular thrust appears to be substantial (more than 50 m), based on offsets displayed by pore-water and physical-property gradients (e.g., bulk density, water content, lithium). Consequently, assignment of ambiguous strata to Subunit IIC is more consistent with seismic interpretations and other shipboard measurements.

Interpretation of the lower of the two cored intervals is more straightforward; Subunit IIC begins at 156-949B-13X-2, 68 cm, and ends at 949B-17X (353.88–388.80 mbsf). The upper limit of this interval, however, is also truncated by a fault zone, and the lower boundary cannot be located accurately because of zero core recovery in Core 156-949B-18X (Fig. 7). The true stratigraphic thickness of Subunit IIC, therefore, remains unknown.

Subunit IIE (398.80–430.92 mbsf; Core 156-949B-19X through -22X-3, 52 cm; and 949C-2R through -4R) is easy to recognize on the basis of radiolarian content. Some intervals contain unusually large and partially recrystallized radiolarians that are clearly visible on the split core surface. Claystone color ranges from pale yellowish brown to light brownish gray, and rare layers of volcanic ash are present. Carbonate content is consistently low, with an average of 0.1 wt% (Table 4). The exact stratigraphic top of the subunit is ill-defined owing to poor core recovery; calculation of a true stratigraphic thickness also is complicated by a thrust repetition at 402.82 mbsf, which places lower lower Miocene strata over upper lower Miocene deposits (Fig. 7). Some of the claystones in the vicinity of the fault are discolored to shades of orange, or stained by manganese. The base of Subunit IIE in Hole 949B coincides with the first occurrence of siltstone interbedded with variegated claystone (949B-22X-3, 52 cm). Unlike in Hole 948C, however, the boundary between Units II and III is gradational over a thickness of approximately 1.25 m; light brown claystones with radiolarians extend below the siltstone bed to 949C-22X-4, 26 cm (432.16 mbsf). Well-preserved radiolarians also were recovered from the core-catcher sample of Core 156-949C-7R.

Table 4. Ranges and mean values of total carbonate ($CaCO_3$) for lithologic units and subunits recovered at Holes 949A and 949B.

Unit/ subunit	Number	Range (wt%)	Average (wt%)
I	4	7.8–31.8	18.8
IIB	33	0.2–30.4	13.1
IIC	97	0.1–5.5	0.4
IIE	19	0.1–0.2	0.1
III	15	0.1–34.3	2.4

Notes: Measurements were performed with a Coulometrics analyzer. See Tables 5 through 13 for individual sample results and comparable estimates of relative percentages of calcite derived from X-ray diffraction analyses.

Unit III (430.92–464.20 mbsf; 156-949B-22X-3, 52 cm, through -25H; and 949C-5R through -7R)

The cored interval of Unit III is a meager 33.28 m thick in Hole 949B. Previous drilling at Site 676 (Leg 110) stopped before penetrating into the equivalent lithologies (Shipboard Scientific Party, 1988), and because of poor core recovery in Holes 949B and 949C, any subdivision of Unit III would be dubious. The background lithology is mottled variegated claystone, ranging in color from gray to light brownish gray, light olive gray, and greenish gray. Interbeds are generally less than 10 cm thick and consist of sandy siltstone, siltstone, clayey siltstone, claystone with nannofossils, and micrite. Most of the interbeds display sharp bases and normal size-grading; tops are either sharp or diffuse from bioturbation. Horizontal laminae and ripple cross-laminae are common near the bases. Carbonate content is generally low; with the exception of one nannofossil-rich bed (34.3 wt% carbonate), the claystones and silty claystones range from 0.1 to 0.8 wt% (Table 4). Results from Site 948 indicate that calcium carbonate is sharply partitioned within Unit III.

Inferred Depositional Environments

Our interpretations of depositional environment for the lithologic units cored at Site 949 are identical to those for Site 948. Unit I is a heavily bioturbated, hemipelagic clay deposit. Interbeds of volcanic ash are fairly common and were deposited either by air fall or by turbidity currents emanating from the nearby Lesser Antilles island arc. Relatively high contents of nannofossils and foraminifers show that suspension fall-out during the Pleistocene accumulated above the calcite compensation depth (CCD).

Unit II is likewise hemipelagic. The bioturbated claystones are generally homogeneous and change primarily in response to fossil preservation; volcanic ash is comparatively rare. Most of the depositional history of Unit II took place on the Atlantic abyssal plain below the CCD, thereby promoting dissolution of carbonate content to trace levels. Appreciable amounts of middle Miocene to early Pliocene age nannofossils have been preserved, but only within Subunit IIB, which records a time of depressed CCD. The abundance of radiolarians within Subunit IIE is consistent with settling of biogenic constituents and suspended silt and clay below the CCD during early to middle Miocene time.

Unit III is composed of fine-grained, thin-bedded turbidites. Hemipelagic background deposition during late Oligocene and the beginning of early Miocene time was punctuated by incursions of graded siltstone, clayey siltstone, and nannofossil-rich claystone. Internal sedimentary structures are consistent with base-missing Bouma sequences (T_{c-e} and T_{de}). Although core recovery in this unit was limited, many of the turbidites are coarser grained than the material recovered from Unit III at Site 948. Sharp partitioning of calcium carbonate into remobilized nannofossil-rich claystones indicates that abyssal-plain deposition occurred below the CCD during the late Oligocene. Carbonate preservation occurred only when deposition and burial of turbidites was rapid enough to inhibit dissolution.

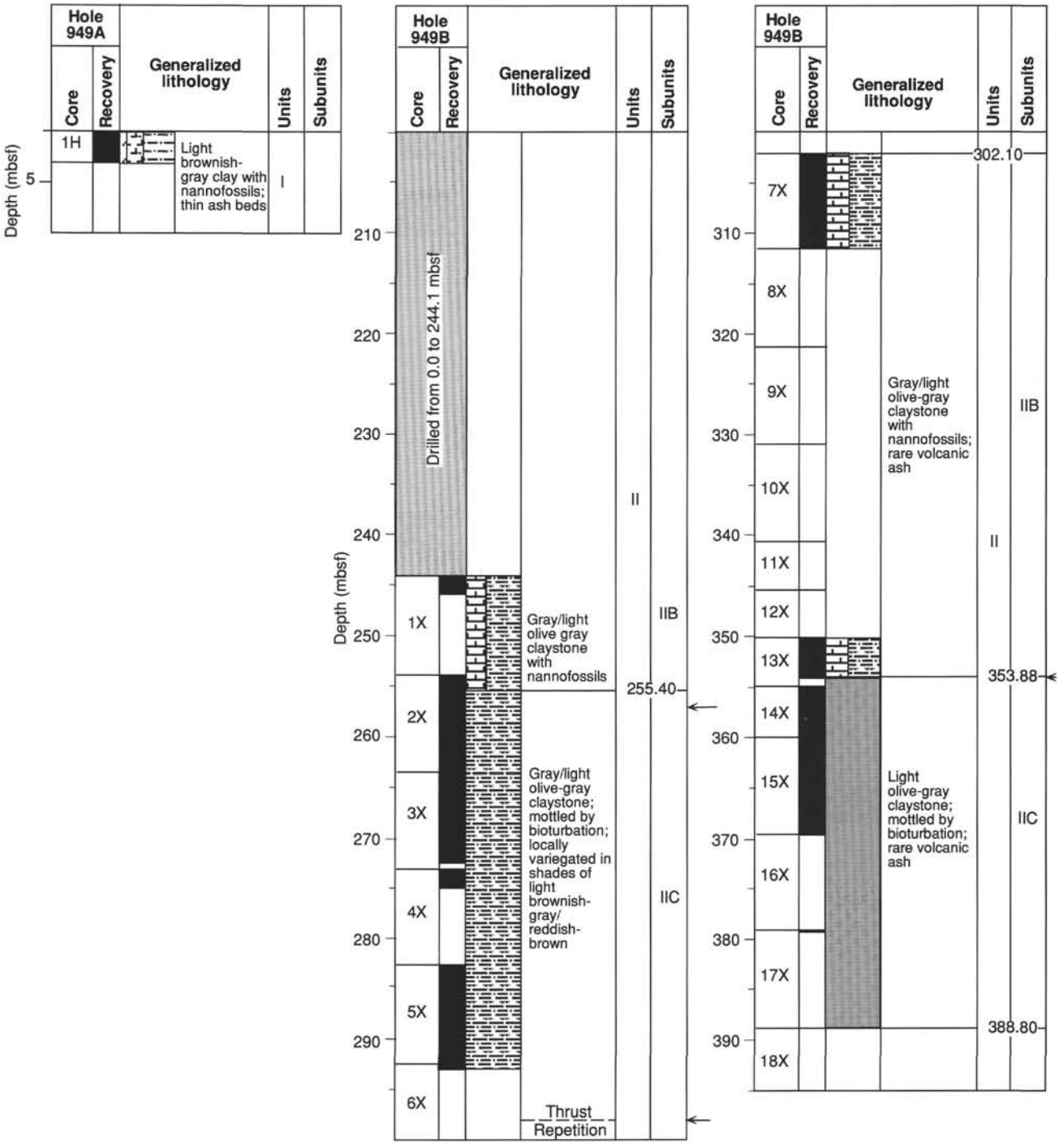

Figure 7. Lithostratigraphic summary for Site 949, showing core recovery, generalized lithology, boundaries between units and subunits, and locations of major faults (arrows).

Bulk Mineralogy

Relative proportions of quartz, plagioclase, calcite, and total clay minerals were calculated from X-ray diffraction (XRD) analysis of air-dried, randomly oriented bulk powders, following the techniques of Fisher and Underwood (this volume). Samples were taken from the trimmings of interstitial-water "squeeze cakes" (Tables 5–7), trimmings from whole-round specimens (Tables 8–10), and residues of selected physical properties specimens (Tables 11–13). Peak intensities (counts/s), integrated peak areas (total counts), and normalized mineral abundances (wt%) are presented separately for each type of specimen. All data for Hole 949C are grouped together in Table 14. We made no attempt to quantify the amount of amorphous solids or minerals other than those of the four primary constituent groups.

The total clay-mineral contents reported here are based on the sum of the values for individual clay minerals (smectite, illite, and [kaolinite + chlorite]). Error analysis and rigorous comparisons among different sets of peak-intensity and peak-area weighting factors are discussed by Fisher and Underwood (this volume). To obtain an independent measure of accuracy, we plotted the estimates of the

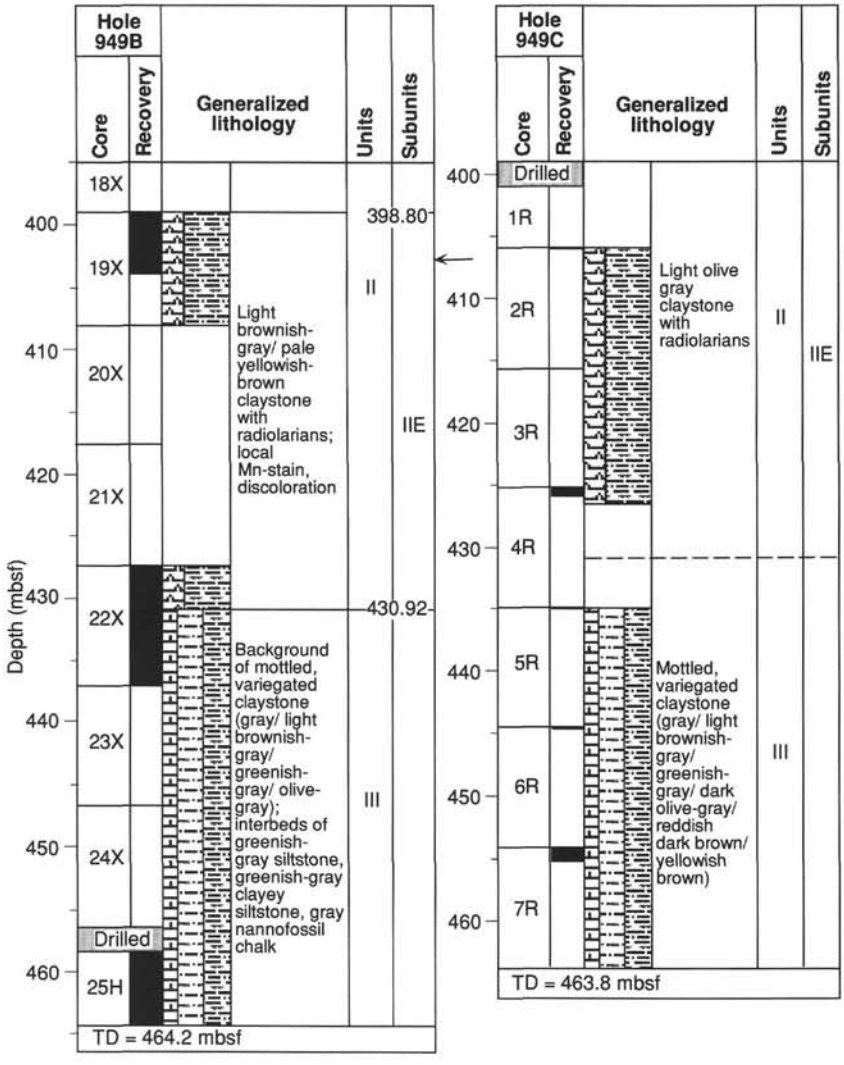

Figure 7 (continued).

percentage of calcite from XRD vs. the weight percent of total carbonate from Coulometrics analyses (Fig. 9). As with the data from Site 948, the differences are generally less than 5 wt%. We caution again, however, that the respective estimates of weight percent for individual clay minerals probably suffer from significant inaccuracies. In addition to the inherent problems of peak interference with untreated random powders, physical-property and whole-round residues were analyzed after measurement of water content and dry bulk density had finished; laboratory procedures include oven drying to 105°C for approximately 24 hr. This degree of heating causes incomplete dehydration and partial collapse of smectite interlayers, thereby further obscuring the true illite/smectite ratio. All of the data, therefore, should be viewed as semiquantitative estimates of relative, rather than absolute, abundances.

The sediment composition within Unit I, Hole 949B, is fairly consistent (Fig. 10). The relative percentages of total clay minerals, for example, range from 42% to 56%. The relative percentage of quartz is 21% to 27%, and plagioclase ranges between 7% and 16%. Estimates for calcite (6%–28%) agree with total carbonate data from Coulometrics measurements.

Depth-dependent trends in claystone compositions at Site 949 are not clearly defined owing to large gaps in core recovery and limited penetration into Unit III. Figure 11 illustrates the composite of relative mineral abundances for Units II and III at Hole 949B. The overall pattern is in reasonable agreement with previous XRD analyses of samples from Site 676 (Shipboard Scientific Party, 1988), although one-to-one comparisons are not possible because of differences in structural thickness within the toe of the accretionary prism.

Unlike at Site 948, no dramatic changes in mineralogic character occur across the lower boundary of Unit II. Calcite percentages are effectively zero, except within the nannofossil-rich claystone of Subunit IIB and carbonate turbidites of Unit III, where the maxima are 28% and 37%, respectively (Fig. 10). Quartz content is fairly constant throughout Hole 949B, generally falling between 22% and 30% (Fig. 10). Plagioclase content ranges from trace amounts to 14%, and generally, less plagioclase occurs in claystones below about 425 mbsf (Fig. 10). Total clay-mineral content scatters from 56% to 74% within carbonate-free claystones and drops to values of 36% to 56% within the nannofossil-rich claystones. The total clay-mineral content appears to increase slightly as one approaches the décollement zone (Fig. 11).

STRUCTURAL GEOLOGY

Introduction

Site 949 is located about 1.8 km west of the deformation front of the accretionary prism and, hence, occupies an intermediate position between Sites 671 and 948, which lie about 4.1 km to the west of the deformation front, and Site 676, which is situated just 0.9 km west of the deformation front. Sites 542 and 675, both of which are about 2.4 km arcward of the deformation front, suffered from poor core recovery in the vicinity of the décollement. The décollement in the area around Site 949 cannot be unambiguously defined using MCS data,

Table 5. Values of X-ray diffraction peak intensity for specimens trimmed from interstitial-water "squeeze cakes," Hole 949B.

Core, section, interval (cm)	Depth (mbsf)	Code	$CaCO_3$	Peak intensity above background (counts/s)					
				Smec.	Ill.	Kaol.	Qtz.	Plag.	Calc.
156-949B-									
1X-1, 120–150	245.30	IW	1.3	21.8	10.7	18.1	241.7	41.1	27.7
2X-5, 110–150	260.90	IW	0.2	34.2	6.8	23.6	301.0	37.3	0.0
3X-5, 110–150	270.60	IW	1.0	32.2	4.7	20.1	308.3	29.5	0.0
4X-1, 125–150	274.35	IW	0.8	53.9	8.1	24.7	296.6	26.6	0.0
5X-2, 110–150	285.40	MK	0.2	57.0	8.21	8.92	42.4	119.6	0.0
5X-4, 110–150	288.40	IW	0.5	28.4	10.4	14.0	291.8	57.9	14.1
7X-2, 110–150	304.70	IW	22.8	24.4	13.4	19.8	302.6	18.6	767.9
7X-6, 110–150	310.70	IW	7.4	26.2	6.1	8.1	233.0	36.9	188.8
13X-1, 110–150	351.30	IW	3.1	49.5	6.82	7.8	283.8	61.2	93.4
14X-2, 0–40	356.40	MK	0.2	30.7	11.7	26.5	284.3	107.0	0.0
14X-5, 110–150	362.00	IW	0.2	34.4	13.1	26.5	280.1	25.2	0.0
15X-2, 110–150	362.50	IW	0.3	45.7	6.73	0.4	302.2	20.9	0.0
15X-5, 110–150	367.00	IW	0.9	29.9	6.5	14.8	232.2	33.4	0.0
17X-CC, 2–8	379.12	IW	0.4	39.9	9.4	3.9	129.4	486.2	0.0
19X-2, 60–100	400.90	IW	0.2	72.4	15.4	38.4	300.5	46.1	0.0
22X-5, 110–150	434.50	IW	0.1	55.2	20.6	47.1	522.3	28.3	0.0
25H-3, 110–150	462.50	IW	NA	25.9	7.4	49.4	321.8	18.2	0.0

Notes: Smec. = smectite; Ill. = illite; Kaol. = kaolinite + chlorite; Qtz. = quartz; Plag. = plagioclase; Calc. = calcite. Sub-bottom depths for Core 156-949B-14X are curatorial depths (see "Operations" section, this chapter).

Table 6. Values of X-ray diffraction integrated peak areas for specimens trimmed from interstitial-water "squeeze cakes," Hole 949B.

Core, section, interval (cm)	Depth (mbsf)	Code	$CaCO_3$	Integrated area after peak fitting (total counts)					
				Smec.	Ill.	Kaol.	Qtz.	Plag.	Calc.
156-949B-									
1X-1, 120–150	245.30	IW	1.3	96.7	13.8	7.0	42.0	34.1	4.7
2X-5, 110–150	260.90	IW	0.2	153.5	0.8	12.6	47.7	33.1	0.0
3X-5, 110–150	270.60	IW	1.0	134.7	2.0	9.5	46.9	39.9	0.0
4X-1, 125–150	274.35	IW	0.8	173.6	2.8	12.5	41.8	48.0	0.0
5X-2, 110–150	285.40	MK	0.2	170.5	2.5	8.0	39.4	38.9	0.0
5X-4, 110–150	288.40	IW	0.5	128.2	8.9	5.9	50.4	51.2	0.0
7X-2, 110–150	304.70	IW	22.8	112.2	4.6	9.1	54.2	18.0	116.2
7X-6, 110–150	310.70	IW	7.4	155.7	3.7	4.6	51.1	29.6	38.9
13X-1, 110–150	351.30	IW	3.1	188.9	2.3	12.7	41.1	27.0	13.0
14X-2, 0–40	356.40	MK	0.2	187.3	7.3	14.2	49.3	46.4	0.0
14X-5, 110–150	362.00	IW	0.2	146.8	0.1	14.3	41.0	18.7	0.0
15X-2, 110–150	362.50	IW	0.3	228.3	1.5	15.2	45.2	12.9	0.0
15X-5, 110–150	367.00	IW	0.9	114.2	3.5	6.5	33.2	26.5	0.0
17X-CC, 2–8	379.12	IW	0.4	146.0	0.4	1.8	23.0	65.6	0.0
19X-2, 60–100	400.90	IW	0.2	222.9	4.1	18.7	49.2	28.4	0.0
22X-5, 110–150	434.50	IW	0.1	224.7	6.4	20.6	86.1	5.6	0.0
25H-3, 110–150	462.50	IW	NA	95.0	5.7	24.1	49.0	13.7	0.0

Notes: See Table 5 for explanation of abbreviations. Sub-bottom depths for Core 156-949B-14X are curatorial depths (see "Operations" section, this chapter).

Table 7. Estimates of relative mineral abundances for specimens trimmed from interstitial-water "squeeze cakes," Hole 949B.

Core, section, interval (cm)	Depth (mbsf)	Code	$CaCO_3$	Relative mineral abundance (wt%)						
				Smec.	Ill.	Kaol.	Clay	Qtz.	Plag.	Calc.
156-949B-										
1X-1, 120–150	245.30	IW	1.3	37.2	24.6	3.2	64.9	26.1	7.7	1.2
2X-5, 110–150	260.90	IW	0.2	51.9	2.6	7.1	61.6	30.3	8.1	0.0
3X-5, 110–150	270.60	IW	1.0	49.6	4.6	5.9	60.1	29.4	10.5	0.0
4X-1, 125–150	274.35	IW	0.8	50.7	5.0	5.9	61.7	28.3	10.1	0.0
5X-2, 110–150	285.40	MK	0.2	53.3	4.8	3.9	62.1	29.6	8.3	0.0
5X-4, 110–150	288.40	IW	0.5	43.6	14.6	2.8	61.0	27.5	11.5	0.0
7X-2, 110–150	304.70	IW	22.8	37.3	8.1	5.3	50.8	26.9	4.6	17.7
7X-6, 110–150	310.70	IW	7.4	49.8	6.5	2.4	58.6	30.3	6.2	4.9
13X-1, 110–150	351.30	IW	3.1	53.5	4.3	5.7	63.5	30.1	5.2	1.2
14X-2, 0–40	356.40	MK	0.2	48.3	9.8	5.6	63.7	28.2	8.1	0.0
14X-5, 110–150	362.00	IW	0.2	53.7	1.5	8.7	64.0	31.1	4.9	0.0
15X-2, 110–150	362.50	IW	0.3	57.3	3.1	5.9	66.3	32.0	1.7	0.0
15X-5, 110–150	367.00	IW	0.9	50.2	8.2	4.4	62.7	29.5	7.7	0.0
17X-CC, 2–8	379.12	IW	0.4	53.2	1.9	1.4	56.6	26.5	17.0	0.0
19X-2, 60–100	400.90	IW	0.2	52.8	5.8	6.9	65.5	30.0	4.5	0.0
22X-5, 110–150	434.50	IW	0.1	51.3	8.1	7.4	66.8	33.2	tr	0.0
25H-3, 110–150	462.50	IW	NA	38.0	12.9	16.9	67.8	27.9	4.3	0.0

Notes: "tr" indicates that traces of the mineral were detected, but calculated abundance is less than 0%. Clay = total relative abundances of clay minerals. Significant errors may exist in the percentages of individual clay minerals, and particularly in the illite/smectite ratio. See Fisher and Underwood (this volume) for a complete description of how calculations were performed. See Table 5 for explanation of other abbreviations. Sub-bottom depths for Core 156-949B-14X are curatorial depths (see "Operations" section, this chapter).

Table 8. Values of X-ray diffraction peak intensity for specimens trimmed from whole-round samples, Hole 949B.

Core, section, interval (cm)	Depth (mbsf)	Code	$CaCO_3$	Peak intensity above background (counts/s)					
				Smec.	Ill.	Kaol.	Qtz.	Plag.	Calc.
156-949B-									
2X-1, 28–42	254.08	AM	9.7	13.4	14.7	25.4	309.4	26.5	258.4
2X-1, 60–74	254.40	AM	9.4	17.2	12.7	17.6	245.7	36.0	225.5
2X-2, 72–88	256.02	WB	0.4	24.8	11.1	23.0	300.6	35.5	0.0
2X-6, 10–25	261.40	GZ	0.2	21.7	9.0	26.0	296.8	21.1	0.0
3X-2, 87–101	265.87	AF	0.5	24.3	16.0	27.1	237.0	32.7	0.0
3X-4, 16–32	268.16	HT	0.2	28.5	9.6	12.3	284.5	40.6	0.0
5X-1, 94–110	283.74	WB	0.6	22.7	9.1	12.0	226.0	23.4	0.0
5X-4, 43–56	287.73	JA	0.2	24.6	12.7	11.5	258.9	74.9	0.0
5X-6, 78–94	291.08	GZ	1.1	25.8	14.6	10.9	208.2	126.0	8.2
5X-6, 114–130	291.44	HT	0.4	23.5	13.4	21.4	335.8	29.2	0.0
7X-3, 14–25	305.24	PH	17.2	12.6	10.9	16.8	316.4	28.6	474.0
7X-4, 42–55	307.02	JA	19.2	16.0	13.7	17.1	321.6	188.1	589.4
7X-4, 119–135	307.79	HT	14.0	13.5	13.4	15.4	377.8	28.0	399.7
7X-5, 118–134	309.28	GZ	19.2	13.3	11.6	15.9	313.8	33.7	496.3
7X-6, 62–77	310.22	WB	5.3	19.5	13.8	15.5	351.9	37.5	152.0
13X-1, 50–66	350.70	PB	22.1	16.4	11.3	12.7	176.0	42.3	493.1
14X-1, 105–121	355.95	PB	0.2	19.3	4.1	21.1	285.1	47.8	0.0
14X-2, 54–70	356.94	GZ	0.2	25.3	6.5	17.8	215.9	33.6	0.0
14X-4, 33–45	359.73	JA	0.2	20.0	15.4	24.8	260.2	19.5	0.0
14X-4, 62–78	360.02	HT	0.3	16.5	18.6	18.4	242.9	33.1	14.3
15X-3, 84–100	363.74	HT	0.1	20.8	10.8	16.1	290.4	35.3	0.0
15X-3, 122–138	364.12	PB	0.1	37.0	8.7	17.3	222.5	15.5	0.0
15X-4, 41–57	364.81	GZ	1.1	24.3	10.5	21.8	315.7	28.2	0.0
15X-5, 28–44	366.18	WB	0.1	31.9	6.1	12.0	163.6	42.0	0.0
15X-5, 65–76	366.55	PH	0.1	48.3	3.5	0.0	115.5	238.0	0.0
15X-6, 57–65	367.97	SP	2.2	23.5	10.0	17.9	250.7	30.2	0.0
15X-6, 119–135	368.59	WB	1.7	16.7	17.6	13.9	219.7	31.0	0.0
19X-1, 33–50	399.13	WB	0.1	33.3	7.0	20.7	247.6	49.8	0.0
19X-2, 32–48	400.62	HT	0.1	29.6	7.2	22.9	257.9	50.0	0.0
19X-3, 34–50	401.64	GZ	0.1	30.9	6.7	23.2	264.4	26.2	0.0
19X-3, 95–106	402.25	JA	0.1	29.1	8.5	22.7	315.8	28.8	0.0
22X-1, 130–146	428.70	WB	0.1	23.9	9.9	29.3	395.2	20.9	0.0
22X-2, 0–16	428.90	GZ	0.1	23.2	8.2	24.7	283.0	22.9	0.0
22X-3, 0–13	430.40	SP	0.1	15.9	15.8	27.4	383.9	20.8	0.0
22X-4, 38–54	432.28	HT	0.1	22.9	18.2	24.3	459.2	20.8	0.0
25H-2, 84–93	460.74	JA	0.2	12.3	15.6	35.6	426.1	15.8	0.0

Notes: See Table 5 for explanation of abbreviations. Sub-bottom depths for Core 156-949B-14X are curatorial depths (see "Operations" section, this chapter).

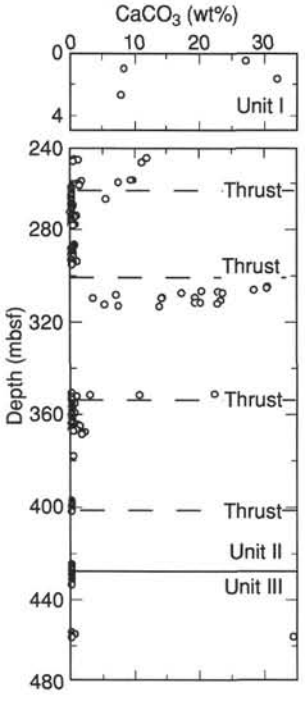

Figure 8. $CaCO_3$ content vs. depth for Holes 949A and 949B. Measurements were performed with a Coulometrics analyzer (see "Explanatory Notes" chapter, this volume). Sub-bottom depths for Core 156-949B-14X are "corrected" depths (see "Operations" section, this chapter).

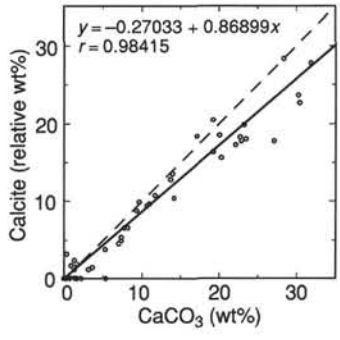

Figure 9. Linear regression of relative percentage of calcite from XRD analyses and weight percent of $CaCO_3$ from Coulometrics analyses. r = correlation coefficient. Dashed line shows a reference slope equal to 1:1.

with two sets of strong negative-polarity reflectors, each representing potential detachment zones, separated by a vertical distance of about 50 m. We hoped to provide structural control in this region, and in the section of confused reflectors higher in the accretionary prism, from a study of the cored section at this site.

Coring at Hole 949B began at 244.1 mbsf and extended to 464.2 mbsf (see "Operations" section, this chapter). Unfortunately, total core recovery was poor (Fig. 12; Table 1), with major intervals of no recovery between 311.6 mbsf (base of Core 156-949B-7X) and 350.2 mbsf (base of Core 156-949B-12X) and only 0.39 m total recovered between 369.5 mbsf (base of Core 156-949B-15X) and 398.8 mbsf (base of Core 156-949B-18X). In addition, there was no recovery from Cores 156-949B-20X through -21X (408.1–427.4 mbsf) and -24X (446.7–456.4 mbsf), and only 0.15 m from 949B-23X (437.1–

Table 9. Values of X-ray diffraction integrated peak areas for specimens trimmed from whole-round samples, Hole 949B.

Core, section, interval (cm)	Depth (mbsf)	Code	$CaCO_3$	Integrated peak area (total counts)					
				Smec.	Ill.	Kaol.	Qtz.	Plag.	Calc.
156-949B-									
2X-1, 28–42	254.08	AM	9.7	51.6	18.5	12.3	43.6	16.1	44.0
2X-1, 60–74	254.40	AM	9.4	85.3	18.4	10.9	44.5	9.0	45.8
2X-2, 72–88	256.02	WB	0.4	151.6	9.7	12.7	46.1	25.8	0.0
2X-6, 10–25	261.40	GZ	0.2	119.2	8.6	13.9	49.0	14.8	0.0
3X-2, 87–101	265.87	AF	0.5	107.4	23.1	14.5	41.0	11.6	0.0
3X-4, 16–32	268.16	HT	0.2	103.0	11.7	6.1	36.1	45.8	0.0
5X-1, 94–110	283.74	WB	0.6	129.0	11.5	6.7	43.5	25.3	0.0
5X-4, 43–56	287.73	JA	0.2	110.9	16.1	6.2	44.6	50.8	0.0
5X-6, 78–94	291.08	GZ	1.1	141.1	16.7	4.8	43.2	64.5	0.0
5X-6, 114–130	291.44	HT	0.4	115.4	14.6	11.2	62.3	14.2	0.0
7X-3, 14–25	305.24	PH	17.2	50.6	10.7	8.3	54.7	12.8	83.1
7X-4, 42–55	307.02	JA	19.2	75.0	8.0	7.9	59.1	37.8	96.2
7X-4, 119–135	307.79	HT	14.0	58.6	10.9	8.9	60.9	18.1	65.8
7X-5, 118–134	309.28	GZ	19.2	50.0	6.5	7.1	59.1	19.6	89.4
7X-6, 62–77	310.22	WB	5.3	97.0	8.4	10.4	68.0	26.8	25.6
13X-1, 50–66	350.70	PB	22.1	90.3	13.1	6.7	28.6	21.9	104.9
14X-1, 105–121	355.95	PB	0.2	85.2	3.6	10.6	55.8	33.0	0.0
14X-2, 54–70	356.94	GZ	0.2	132.2	3.2	9.7	41.4	34.6	0.0
14X-4, 33–45	359.73	JA	0.2	106.8	20.2	13.0	42.5	7.2	0.0
14X-4, 62–78	360.02	HT	0.3	66.6	32.8	10.5	38.3	8.2	0.4
15X-3, 84–100	363.74	HT	0.1	92.4	11.6	7.8	39.0	29.0	0.0
15X-3, 122–138	364.12	PB	0.1	173.5	4.9	8.1	34.5	5.2	0.0
15X-4, 41–57	364.81	GZ	1.1	130.1	11.2	10.4	45.3	18.5	0.0
15X-5, 28–44	366.18	WB	0.1	116.0	4.8	5.7	28.0	46.4	0.0
15X-5, 65–76	366.55	PH	0.1	151.9	0.2	0.0	15.6	29.2	0.0
15X-6, 57–65	367.97	SP	2.2	97.4	7.5	6.5	37.2	39.7	0.0
15X-6, 119–135	368.59	WB	1.7	82.5	23.1	6.6	31.3	33.9	0.0
19X-1, 33–50	399.13	WB	0.1	168.1	3.6	11.5	54.3	31.4	0.0
19X-2, 32–48	400.62	HT	0.1	119.8	4.7	9.2	47.3	32.2	0.0
19X-3, 34–50	401.64	GZ	0.1	139.7	2.6	11.6	50.3	23.6	0.0
19X-3, 95–106	402.25	JA	0.1	144.6	1.9	11.3	49.9	22.9	0.0
22X-1, 130–146	428.70	WB	0.1	131.9	8.9	13.9	63.9	20.2	0.0
22X-2, 0–16	428.90	GZ	0.1	129.0	5.2	12.8	58.5	25.2	0.0
22X-3, 0–13	430.40	SP	0.1	79.8	15.4	13.3	61.5	17.4	0.0
22X-4, 38–54	432.28	HT	0.1	146.2	13.6	11.4	84.1	7.8	0.0
25H-2, 84–93	460.74	JA	0.2	48.4	12.8	17.9	57.9	3.3	0.0

Notes: See Table 5 for explanation of abbreviations. Sub-bottom depths for Core 156-949B-14X are curatorial depths (see "Operations" section, this chapter).

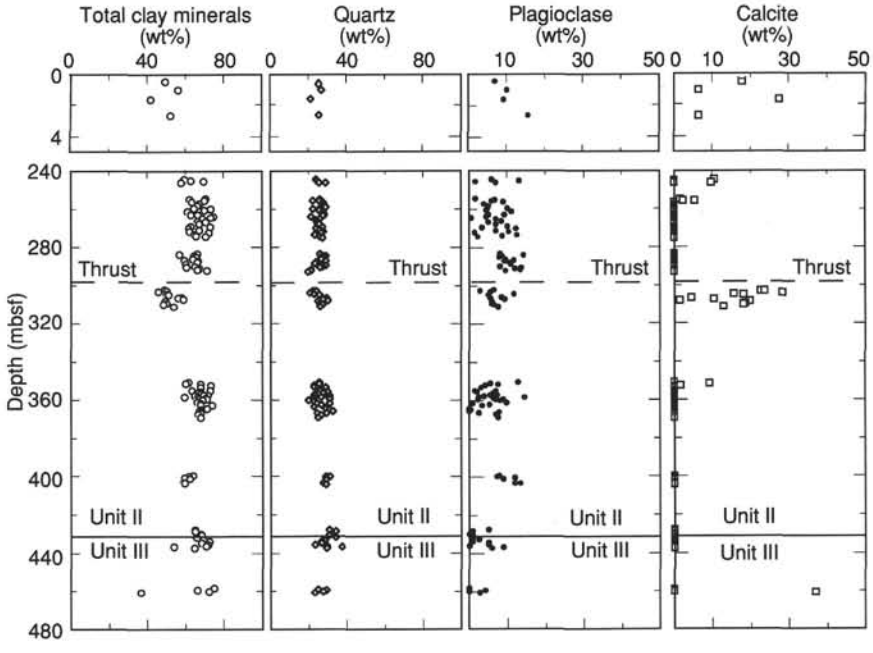

Figure 10. Values of relative abundance for major mineral groups at Holes 949A and 949B. Estimates were calculated from bulk-powder XRD data, following the technique of Fisher and Underwood (this volume). Sub-bottom depths for Core 156-949B-14X are "corrected" depths (see "Operations" section, this chapter).

446.7 mbsf). In an attempt to mitigate this situation, Hole 949C was cored using the rotary core-barrel system, from just below the second casing string at 401.0 to 463.8 mbsf. From the seven cores from this hole, a total of only 2.18 m of section was recovered (3.5% total recovery; Table 1).

Ample time allowed us to document in detail structures from Holes 949B and 949C and to make a complete catalog of measurements and VCDs of all recovered sections. Deformation structures at Site 949 are similar to those at Site 948: inclined bedding, core-scale faults commonly with slickensided surfaces and slickenlines, mineral veins, sediment-filled veins, brecciated zones, fracture networks, stratal disruption, and scaly fabric. All these structures are defined in the "Explanatory Notes" chapter (this volume), with the exception of fracture networks. This term is one we found increasingly useful during core

Table 10. Estimates of relative mineral abundances for specimens trimmed from whole-round samples, Hole 949B.

Core, section, interval (cm)	Depth (mbsf)	Code	$CaCO_3$	Relative mineral abundance (wt%)						
				Smec.	Ill.	Kaol.	Clay	Qtz.	Plag.	Calc.
156-949B-										
2X-1, 28–42	254.08	AM	9.7	20.9	37.0	6.7	64.6	22.4	3.2	9.9
2X-1, 60–74	254.40	AM	9.4	30.1	30.9	4.6	65.6	25.2	0.4	8.8
2X-2, 72–88	256.02	WB	0.4	46.3	14.7	5.5	66.5	28.9	4.6	0.0
2X-6, 10–25	261.40	GZ	0.2	43.9	15.9	7.7	67.4	29.8	2.8	0.0
3X-2, 87–101	265.87	AF	0.5	34.2	34.2	5.3	73.7	26.0	0.3	0.0
3X-4, 16–32	268.16	HT	0.2	39.6	20.9	2.9	63.4	25.4	11.3	0.0
5X-1, 94–110	283.74	WB	0.6	44.8	18.9	2.7	66.4	28.9	4.7	0.0
5X-4, 43–56	287.73	JA	0.2	37.4	24.7	2.2	64.3	25.3	10.5	0.0
5X-6, 78–94	291.08	GZ	1.1	40.4	21.7	1.2	63.3	25.2	11.5	0.0
5X-6, 114–130	291.44	HT	0.4	39.6	23.9	5.0	68.5	30.0	1.5	0.0
7X-3, 14–25	305.24	PH	17.2	22.3	24.6	6.0	53.0	25.0	3.6	18.4
7X-4, 42–55	307.02	JA	19.2	28.1	15.3	5.2	48.6	24.2	11.0	16.3
7X-4, 119–135	307.79	HT	14.0	25.2	23.9	6.2	55.2	26.2	5.0	13.5
7X-5, 118–134	309.28	GZ	19.2	23.5	16.4	6.4	46.3	25.9	7.4	20.4
7X-6, 62–77	310.22	WB	5.3	37.3	16.2	6.4	59.9	29.5	6.7	3.8
13X-1, 50–66	350.70	PB	22.1	31.1	21.6	2.9	55.6	22.3	4.9	17.3
14X-1, 105–121	355.95	PB	0.2	40.8	9.3	8.8	58.9	29.6	11.6	0.0
14X-2, 54–70	356.94	GZ	0.2	49.3	6.7	5.8	61.8	29.1	9.0	0.0
14X-4, 33–45	359.73	JA	0.2	36.0	31.8	5.1	72.9	27.1	tr	0.0
14X-4, 62–78	360.02	HT	0.3	22.9	49.0	2.5	74.3	22.6	tr	3.1
15X-3, 84–100	363.74	HT	0.1	38.9	22.9	4.2	65.9	26.8	7.3	0.0
15X-3, 122–138	364.12	PB	0.1	56.0	8.4	3.5	67.9	32.1	tr	0.0
15X-4, 41–57	364.81	GZ	1.1	44.5	18.5	4.7	67.7	29.2	3.1	0.0
15X-5, 28–44	366.18	WB	0.1	47.2	9.9	3.5	60.6	26.4	13.1	0.0
15X-5, 65–76	366.55	PH	0.1	60.4	1.7	0.0	62.1	30.4	7.6	0.0
15X-6, 57–65	367.97	SP	2.2	42.2	15.7	4.0	61.8	26.7	11.5	0.0
15X-6, 119–135	368.59	WB	1.7	30.9	37.8	1.7	70.4	23.3	6.3	0.0
19X-1, 33–50	399.13	WB	0.1	51.1	6.3	5.6	63.0	30.7	6.3	0.0
19X-2, 32–48	400.62	HT	0.1	46.8	9.6	5.7	62.0	29.5	8.5	0.0
19X-3, 34–50	401.64	GZ	0.1	50.6	5.6	6.8	63.1	31.2	5.7	0.0
19X-3, 95–106	402.25	JA	0.1	51.9	4.5	6.6	63.0	31.5	5.5	0.0
22X-1, 130–146	428.70	WB	0.1	43.8	14.9	7.0	65.7	30.6	3.7	0.0
22X-2, 0–16	428.90	GZ	0.1	46.2	9.9	7.4	63.4	30.7	5.9	0.0
22X-3, 0–13	430.40	SP	0.1	31.7	29.6	7.4	68.7	28.2	3.1	0.0
22X-4, 38–54	432.28	HT	0.1	43.3	19.5	4.6	67.3	32.7	tr	0.0
25H-2, 84–93	460.74	JA	0.2	23.3	33.9	14.7	71.8	28.2	tr	0.0

Notes: "tr" indicates that traces of the mineral were detected, but calculated abundance is less than 0%. See Fisher and Underwood (this volume) for a complete description of how calculations were performed. See Tables 5 and 7 for explanation of abbreviations. Sub-bottom depths for Core 156-949B-14X are curatorial depths (see "Operations" section, this chapter).

analysis for describing intervals where the sediment had been broken into angular fragments by narrow fractures having no clear preferred orientation and that are typically spaced at distances of about 5 to 10 mm. Individual fractures rarely extend for more than 10 mm and end at either a fracture of different orientation or at a point where several fractures terminate. The fractures are mostly planar and rarely show slickensides or slickenveins. Fracture networks are closely associated with zones of scaly fabric, and we consider that they may pass gradationally into the latter, with progressive development of fractures having a restricted range of orientations and that, like scaly fabric, are commonly polished and may show slickenlines. Fracture networks may be equivalent to stratal disruption in intervals where bedding is not visible. Both occur typically in the same settings, close to zones of intense scaly fabric. It is possible that some fracture networks are enhanced or even generated during drilling, but their close and apparently gradational relationship with scaly fabric, and the common coincidence of the latter with faults independently indicated as being natural by other evidence, convinced us that they are natural structural discontinuities. If these findings are confirmed by planned shore-based studies, then the term fracture network should be added to the list of standardized terms used for deformation structures in ODP cores (see "Explanatory Notes" chapter, this volume).

The long intervals of no core recovery made it difficult for us to delineate closely domains having common structural attributes in the way possible in more completely recovered cored sections (see "Structural Geology" section, "Site 948" chapter, this volume). However, we recognized sufficient structural similarities in particular intervals to permit a tentative subdivision, and the structural geology of the cores from Hole 949B are described in terms of three domains, with the uppermost domain being divided into two subdomains. Subdomain IA includes Cores 156-949B-1X through -7X (244.1–311.6 mbsf), Subdomain IB includes Cores 156-949B-13X through -15X (350.2–369.5

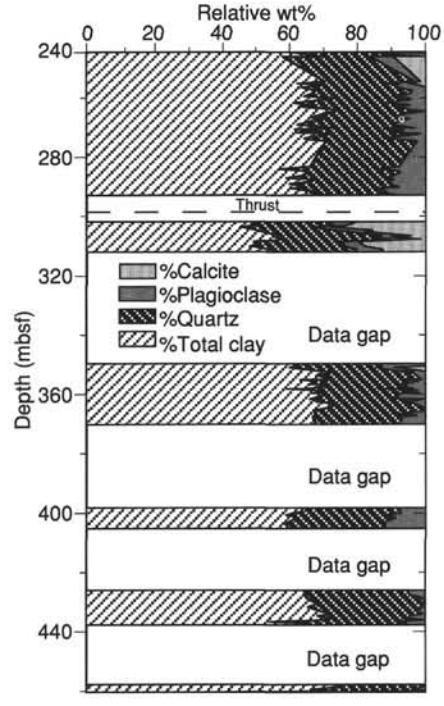

Figure 11. Cumulative relative mineral abundances for Units II and III, Hole 949B, based on XRD analyses of bulk powders.

Table 11. Values of X-ray diffraction peak intensity for residues of physical-properties specimens, Holes 949A and 949B.

Core, section, interval (cm)	Depth (mbsf)	$CaCO_3$	Peak intensity above background (counts/s)					
			Smec.	Ill.	Kaol.	Qtz.	Plag.	Calc.
156-949A-								
1H-1, 50–52	0.50	27.1	16.4	17.8	17.7	301.2	55.7	571.9
1H-1, 100–102	1.00	8.3	13.4	13.7	20.9	379.9	75.2	191.5
1H-2, 15–17	1.65	31.8	11.5	8.7	12.7	220.4	76.2	669.9
1H-2, 117–119	2.67	7.8	10.9	13.0	14.2	306.6	91.3	198.2
156-949B-								
1X-1, 36–38	244.46	11.8	15.2	10.2	15.8	212.0	33.2	259.8
1X-1, 82–84	244.92	0.7	14.0	12.5	23.7	309.7	62.8	9.6
1X-2, 18–20	245.78	0.4	19.3	13.3	21.6	273.1	21.8	0.0
1X-CC, 26–28	246.20	11.0	19.6	8.1	17.5	228.3	40.9	325.9
2X-1, 90–92	254.70	1.7	18.2	15.9	23.7	286.9	22.7	13.5
2X-1, 139–141	255.19	7.4	22.7	9.6	21.1	230.5	30.0	189.9
2X-2, 18–20	255.48	1.3	17.3	19.5	17.9	210.6	41.8	24.1
2X-2, 106–108	256.36	0.7	27.9	11.3	23.4	285.4	61.7	0.0
2X-3, 65–67	257.45	0.2	30.5	11.4	29.5	321.8	29.7	0.0
2X-4, 28–30	258.58	0.2	19.0	12.6	26.6	412.7	23.9	0.0
2X-4, 143–145	259.73	0.2	17.5	15.6	22.1	336.9	44.0	0.0
2X-5, 31–33	260.11	0.2	17.5	16.2	18.9	301.4	19.4	0.0
2X-5, 81–83	260.61	0.2	25.5	15.4	17.7	262.0	41.0	0.0
2X-6, 1–3	261.31	0.2	22.0	6.7	18.6	226.8	33.0	0.0
2X-6, 140–142	262.70	5.5	18.0	9.7	26.1	299.8	23.3	0.0
2X-7, 18–20	262.98	0.2	28.2	4.9	21.8	252.5	27.9	0.0
3X-1, 27–29	263.77	0.2	17.2	22.2	21.0	231.0	35.5	0.0
3X-1, 116–118	264.66	0.2	16.2	16.1	25.3	260.2	24.0	0.0
3X-2, 31–33	265.31	0.2	16.8	16.4	32.5	291.8	28.6	0.0
3X-2, 140–142	266.40	0.2	22.8	11.8	21.9	247.2	27.2	0.0
3X-3, 50–52	267.00	0.2	18.0	20.3	21.9	264.3	32.1	0.0
3X-3, 110–112	267.60	0.2	19.5	14.2	18.7	272.2	39.3	0.0
3X-4, 113–115	269.13	0.0	25.4	9.1	15.9	243.1	35.8	0.0
3X-5, 25–27	269.75	0.2	17.0	20.1	18.6	207.2	21.9	0.0
3X-5, 86–88	270.36	0.3	24.4	9.7	20.4	322.1	24.3	0.0
3X-6, 14–16	271.14	0.6	19.9	16.8	16.4	273.6	31.2	0.0
3X-6, 63–65	271.63	0.2	27.9	10.9	20.4	241.4	36.4	0.0
3X-CC, 10–12	272.24	0.2	27.6	12.8	8.8	184.7	31.4	0.0
4X-1, 20–22	273.30	0.1	12.6	23.3	17.4	299.1	32.4	0.0
4X-1, 108–110	274.18	0.2	19.6	13.7	16.8	224.1	24.4	0.0
4X-2, 12–14	274.72	0.5	19.3	16.6	17.7	287.4	24.5	0.0
5X-1, 35–37	283.15	0.7	30.3	11.7	9.2	185.4	40.8	0.0
5X-1, 133–135	284.13	0.5	24.9	0.0	8.3	168.8	44.0	0.0
5X-2, 21–23	284.51	0.4	29.2	12.8	13.4	276.1	39.2	0.0
5X-2, 84–86	285.14	0.2	23.3	12.5	10.8	335.4	49.0	0.0
5X-3, 17–19	285.97	0.3	25.3	9.9	17.8	280.5	72.3	0.0
5X-3, 111–113	286.91	0.4	25.6	6.3	11.4	255.9	47.7	0.0
5X-4, 18–20	287.48	0.3	21.6	13.5	13.4	307.8	55.4	0.0
5X-4, 67–69	287.97	0.2	18.7	12.6	7.0	238.6	103.6	0.0
5X-5, 42–44	289.22	0.4	31.6	7.9	13.5	236.0	96.4	0.0
5X-5, 136–138	290.16	0.2	20.8	15.4	16.2	404.3	86.5	0.0
5X-6, 23–25	290.53	0.2	24.5	8.3	10.1	233.3	134.1	0.0
5X-6, 104–106	291.34	0.3	16.0	21.7	9.6	202.1	164.3	0.0
5X-7, 11–13	291.91	0.3	15.0	21.0	10.4	211.1	98.8	0.0
5X-CC, 18–20	292.46	0.3	14.5	24.5	9.6	224.7	117.0	0.0
7X-1, 31–33	302.41	30.4	15.9	9.3	10.7	215.0	118.6	842.4
7X-1, 86–88	302.96	30.3	14.5	18.3	16.2	298.4	18.9	823.8
7X-2, 4–6	303.64	28.3	10.6	10.4	12.7	219.8	43.2	682.2
7X-2, 76–78	304.36	20.3	13.4	11.6	15.3	272.6	170.2	561.0
7X-3, 8–10	305.18	23.5	18.0	16.3	17.8	321.4	20.9	706.7
7X-3, 127–129	306.37	7.1	20.6	8.4	20.4	370.4	46.4	239.5
7X-4, 32–34	306.92	14.2	22.0	19.3	21.6	348.5	44.2	383.9
7X-4, 81–83	307.41	3.6	22.6	13.7	24.5	401.4	59.4	124.2
7X-5, 25–27	308.35	23.2	15.4	14.8	16.5	304.3	28.8	660.9
7X-5, 136–138	309.46	20.0	16.6	11.6	14.6	297.9	24.7	593.1
7X-6, 22–24	309.82	22.7	17.1	11.4	15.1	279.2	31.0	518.3
7X-7, 11–13	311.21	13.7	15.7	14.1	16.3	306.8	35.1	363.8
13X-1, 18–20	350.38	0.2	19.7	10.2	16.4	222.8	83.5	0.0
13X-1, 98–100	351.18	10.7	18.7	10.7	20.6	199.2	26.9	219.0
13X-2, 27–29	351.97	1.0	17.3	12.3	13.1	244.4	57.0	17.8
13X-2, 88–90	352.58	0.2	11.5	19.2	25.1	318.0	19.6	0.0
13X-3, 26–28	353.46	0.1	26.8	10.2	23.7	276.9	21.2	0.0
14X-1, 39–41	355.29	0.3	16.6	13.2	27.3	341.5	19.8	0.0
14X-1, 58–60	355.48	0.6	23.0	7.7	22.8	267.1	20.2	0.0
14X-1, 122–124	356.12	0.2	23.4	12.9	28.1	369.9	23.9	0.0
14X-2, 123–125	357.63	0.1	26.7	10.3	17.5	181.3	166.8	0.0
14X-3, 48–50	358.38	0.1	17.9	15.1	18.1	224.1	97.4	0.0
14X-3, 127–129	359.17	0.2	21.5	14.4	21.0	268.8	29.6	0.0
14X-4, 16–18	359.56	0.1	21.5	19.0	17.2	165.5	74.5	0.0
14X-4, 130–132	360.70	0.2	24.2	7.6	18.0	249.8	26.3	0.0
14X-5, 41–43	361.31	0.2	33.7	6.7	16.8	228.6	42.7	0.0
14X-5, 86–88	361.76	0.2	31.3	8.8	24.0	264.7	45.6	0.0
14X-6, 22–24	362.62	0.2	16.5	20.0	30.5	292.2	27.4	0.0
14X-6, 114–116	363.54	0.7	25.9	5.0	26.9	274.2	19.2	0.0
14X-7, 10–12	364.00	0.2	15.3	17.2	21.4	266.9	35.0	0.0
14X-CC, 10–12	364.53	0.2	13.8	17.4	16.2	175.6	59.7	0.0
15X-1, 39–41	360.29	0.2	14.6	15.0	19.6	233.3	33.0	0.0
15X-1, 144–146	361.34	0.2	13.9	13.3	17.6	272.9	37.6	0.0
15X-2, 18–20	361.58	0.2	27.6	8.4	24.8	277.8	17.7	0.0
15X-2, 94–96	362.34	0.2	17.2	14.9	19.7	304.5	28.0	0.0
15X-3, 23–25	363.13	0.1	13.1	21.0	17.7	287.0	21.8	0.0
15X-3, 148–150	364.38	0.1	24.4	13.1	16.6	221.9	24.4	0.0

Table 11 (continued).

Core, section, interval (cm)	Depth (mbsf)	$CaCO_3$	Peak intensity above background (counts/s)					
			Smec.	Ill.	Kaol.	Qtz.	Plag.	Calc.
15X-4, 60–62	365.00	1.4	22.6	9.5	18.7	300.2	19.8	0.0
15X-4, 133–135	365.73	0.4	17.8	12.0	14.2	1023.6	24.8	0.0
15X-5, 56–58	366.46	0.1	21.2	15.0	13.0	195.6	38.3	0.0
15X-5, 95–97	366.85	0.7	22.0	9.6	18.5	226.7	21.2	0.0
15X-6, 9–11	367.49	0.5	24.4	16.8	17.2	237.0	36.1	0.0
15X-7, 6–8	368.96	1.7	17.6	10.9	8.8	254.4	34.8	0.0
19X-1, 84–86	399.64	0.1	28.1	7.8	16.4	266.3	50.4	0.0
19X-1, 135–137	400.15	0.1	21.5	5.7	21.1	359.0	56.4	0.0
19X-2, 23–25	400.53	0.1	21.5	7.3	17.8	343.7	30.3	0.0
19X-3, 8–10	401.38	0.1	31.5	7.6	22.4	255.3	54.0	0.0
19X-4, 48–50	403.28	0.1	26.9	4.3	17.5	205.9	108.9	0.0
19X-4, 85–87	403.65	0.1	20.9	5.8	14.1	198.8	40.5	0.0
22X-1, 31–33	427.71	0.1	26.7	9.2	30.3	384.0	20.1	0.0
22X-1, 102–104	428.42	0.1	18.6	9.4	21.6	369.2	15.5	0.0
22X-2, 102–104	429.92	0.1	20.5	11.8	26.1	430.2	17.8	0.0
22X-3, 27–29	430.67	0.1	16.1	9.6	25.9	388.5	24.6	0.0
22X-3, 114–116	431.54	0.1	20.6	12.8	20.7	345.8	15.5	0.0
22X-4, 113–115	433.03	0.1	16.9	15.1	26.4	353.2	20.4	0.0
22X-5, 47–49	433.87	0.1	17.6	16.6	32.0	376.1	21.8	0.0
22X-5, 91–93	434.31	0.1	16.0	19.6	30.0	439.0	29.7	0.0
22X-6, 73–75	435.63	0.1	10.6	22.3	21.7	434.7	26.1	0.0
22X-6, 118–120	436.08	0.1	15.9	12.6	21.0	398.0	12.5	0.0
22X-7, 13–15	436.53	0.1	18.1	20.1	39.0	1163.0	45.2	0.0
23X-CC, 2–4	437.12	0.1	17.6	12.6	29.6	341.4	18.6	0.0
25H-1, 23–25	458.63	0.1	11.3	22.3	40.1	430.9	16.8	0.0
25H-1, 96–98	459.36	0.7	16.1	20.1	44.6	621.6	24.5	0.0
25H-2, 13–15	460.03	0.1	14.9	18.7	31.0	333.9	17.8	0.0
25H-2, 69–71	460.59	34.3	9.5	5.8	30.8	318.1	12.0	636.1

Notes: See Table 5 for explanation of abbreviations. Sub-bottom depths for Core 156-949B-14X are curatorial depths (see "Operations" section, this chapter).

mbsf), Domain II includes Core 949B-19X (398.8–408.1 mbsf), and -22X (427.4–437.1 mbsf), and Domain III includes Core 949B-25H (458.4–464.2 mbsf). The distribution of major structural features is summarized in Figure 12, and a detailed record of structures and their orientation is presented in Table 15. Figures 13 and 14 show variations in the dip of bedding, and the distribution and thickness of intense scaly fabric (shear zones), respectively, with depth.

Subdomain IA: Accretionary Prism (244.1–311.6 mbsf)

Cores 156-949B-1X through -7X consist of variably bioturbated, gray to light olive gray claystone with sparse thin ash beds. The subdomain is characterized by bedding that is generally inclined and ranges in dip up to 68° (Fig. 13). Many bedding readings are based on the assumption that this orientation is indicated by planar *Zoophycos* discs (Ekdale et al., 1984), an assumption supported in places by the parallelism of the discs to subtle changes in color or texture. Both grading in ash layers and the sense of asymmetry in *Zoophycos* spreiten indicate that the sediments are oriented the right way up. Bedding orientations derived from paleomagnetic determinations of geographic coordinates (see "Paleomagnetism" section, this chapter) suggest that the rocks are folded on a scale of 1 m or more, with those between Sections 156-949B-1X-2 and -2X-3 striking about north-south, whereas those from Section 156-949B-2X-5 through -5X-3 are of more variable orientation and have an overall northwest-southeast strike (Fig. 15).

A complex interval of deformation occurs from 156-949B-2X-3, 129 cm, through -2X-5, 15 cm. Zones of intense scaly fabric up to 11 cm thick with boundaries dipping between 22° and 62° alternate with undeformed intervals and others showing fracture networks. Discrete faults having scaly margins 1 to 2 mm wide bound an intensely fractured and scaly brown claystone interval that occurs throughout the interval 156-949B-2X-3, 129–144 cm. The geometric relationships of the scaly fabric to the faults indicate thrust movement, as do the boundary-fabric relationships in several of the scaly fabric zones. Intense scaly fabric in a brown-stained, 10-cm-thick, inclined zone is present in the interval 156-949B-2X-6, 48–61 cm (Fig. 16).

Several small faults, one of which indicates normal movement, occur in Core 156-949B-3X. A fault extending through interval 156-949B-3X-6, 89–100 cm, is surrounded by a fracture network zone that extends through interval 156-949B-3X-6, 70–107 cm. A small fault of uncertain sense of displacement is seen in interval 156-949B-4X-4, 102–112 cm.

Core 156-949B-5X is notable for the presence of widespread and well-developed sediment-filled veins and veins of phillipsite and rhodochrosite, as determined by XRD analysis (Table 16). The sediment-filled veins occur in approximately horizontal zones, particularly in Sections 949B-5X-3 through -5X-7. Individually, these are mostly steeply dipping, commonly anastomosing veins, that range in width from <1 to 2 mm wide (Fig. 17). Some are at least 18 cm long. Most veins have diffuse boundaries, and small displacements occur across a few of the veins.

The rhodochrosite veins are mostly less than 1 mm thick. Although some small horizontal sets occur along fractures and fissility, many of the veins dip steeply and can be continuous for distances of up to at least 14 cm. Most rhodochrosite veins are planar or slightly undulating; many show fibers aligned in the dip direction and some have acted as normal faults. One example, in interval 156-949B-5X-3, 80–90 cm, shows a 1-cm offset of a shallowly dipping alteration band. Steep, open fractures, some of which show dip-slip striations, are closely associated with these veins. A subhorizontal phillipsite vein about 5 mm thick, with irregular boundaries, occurs in Sample 156-949B-5X-2, 3–6 cm (Fig. 18). It crosses undeformed sediment and is not associated with any other structural feature. Scaly fabric in Core 156-949B-5X is confined to two centimeter-scale, shallowly dipping zones (Samples 156-949B-5X-4, 55–65 cm, and -5X-5, 61–65 cm). Although the former scaly fabric zone contains a rhodochrosite vein, the relative age of the scaly fabric and the vein could not be determined.

Micropaleontological data indicate a stratigraphic inversion in Subdomain IA, with late middle Miocene nannofossils at 156-949B-2X-2, 4 cm, and early early Pliocene nannofossils at 156-949B-7X-1, 7 cm (see "Biostratigraphy" section, this chapter). Recovered cores between 156-949B-2X-2, 4 cm, and -7X-1, 7 cm, are barren of fossils. Discontinuities in index properties (bulk density and porosity), acoustic impedance (see "Core Physical Properties" section, this chapter), and pore-water composition (see "Inorganic Geochemistry" section, this chapter) suggest the presence of a fault in the unrecovered

Table 12. Values of X-ray diffraction integrated peak areas for residues of physical-properties specimens, Holes 949A and 949B.

Core, section, interval (cm)	Depth (mbsf)	$CaCO_3$	Integrated area after peak fitting (total counts)					
			Smec.	Ill.	Kaol.	Qtz.	Plag.	Calc.
156-949A-								
1H-1, 50–52	0.50	27.1	102.7	7.5	8.2	59.3	28.3	121.3
1H-1, 100–102	1.00	8.3	62.4	10.1	12.4	72.9	33.2	37.2
1H-2, 15–17	1.65	31.8	61.4	6.9	7.2	46.1	27.6	148.5
1H-2, 117–119	2.67	7.8	51.5	5.6	7.5	50.1	36.5	31.3
156-949B-								
1X-1, 36–38	244.46	11.8	79.9	12.3	10.1	41.0	22.9	57.5
1X-1, 82–84	244.92	0.7	64.1	13.0	12.2	55.9	44.1	1.6
1X-2, 18–20	245.78	0.4	92.3	12.5	12.3	50.3	11.6	0.0
1X-CC, 26–28	246.20	11.0	100.7	8.0	8.8	40.7	26.5	56.7
2X-1, 90–92	254.70	1.7	91.4	18.6	14.7	51.4	14.1	3.7
2X-1, 139–141	255.19	7.4	119.0	11.8	12.1	43.2	31.5	35.3
2X-2, 18–20	255.48	1.3	87.8	31.2	13.4	46.8	39.5	4.1
2X-2, 106–108	256.36	0.7	143.9	8.5	11.9	50.2	42.8	0.0
2X-3, 65–67	257.45	0.2	164.4	10.2	15.7	45.9	24.2	0.0
2X-4, 28–30	258.58	0.2	96.7	10.7	13.1	58.6	21.7	0.0
2X-4, 143–145	259.73	0.2	76.6	13.8	12.1	58.1	37.9	0.0
2X-5, 31–33	260.11	0.2	90.0	38.5	9.6	42.6	40.3	0.0
2X-5, 81–83	260.61	0.2	138.6	22.9	11.6	41.1	32.7	0.0
2X-6, 1–3	261.31	0.2	126.3	6.2	10.3	49.5	45.9	0.0
2X-6, 140–142	262.70	5.5	71.0	6.4	13.8	43.0	14.3	0.0
2X-7, 18–20	262.98	0.2	134.4	4.4	11.1	39.4	36.7	0.0
3X-1, 27–29	263.77	0.2	69.1	36.6	11.2	39.1	34.4	0.0
3X-1, 116–118	264.66	0.2	69.2	18.9	12.0	43.6	10.1	0.0
3X-2, 31–33	265.31	0.2	60.1	13.5	17.9	46.1	23.4	0.0
3X-2, 140–142	266.40	0.2	93.5	12.9	11.8	39.7	33.4	0.0
3X-3, 50–52	267.00	0.2	106.6	27.5	10.7	48.8	35.3	0.0
3X-3, 110–112	267.60	0.2	98.8	15.1	9.9	40.7	32.5	0.0
3X-4, 113–115	269.13	0.0	107.0	6.7	8.3	40.6	36.3	0.0
3X-5, 25–27	269.75	0.2	68.3	22.5	9.1	36.4	20.5	0.0
3X-5, 86–88	270.36	0.3	95.6	8.0	10.8	46.9	43.4	0.0
3X-6, 14–16	271.14	0.6	93.1	15.4	7.7	38.6	31.4	0.0
3X-6, 63–65	271.63	0.2	117.3	6.6	9.3	45.1	39.9	0.0
3X-CC, 10–12	272.24	0.2	150.6	24.2	3.8	27.5	20.7	0.0
4X-1, 20–22	273.30	0.1	50.3	14.7	10.0	48.7	40.0	0.0
4X-1, 108–110	274.18	0.2	102.9	14.7	10.0	48.7	40.0	0.0
4X-2, 12–14	274.72	0.5	98.7	15.1	12.7	41.8	15.1	0.0
5X-1, 35–37	283.15	0.7	177.2	16.8	5.3	34.8	52.9	0.0
5X-1, 133–135	284.13	0.5	133.6	0.0	4.1	37.9	49.8	0.0
5X-2, 21–23	284.51	0.4	152.1	13.9	5.4	45.6	49.3	0.0
5X-2, 84–86	285.14	0.2	120.2	18.6	5.0	55.2	44.5	0.0
5X-3, 17–19	285.97	0.3	139.9	13.7	8.1	49.8	49.8	0.0
5X-3, 111–113	286.91	0.4	124.6	5.3	7.1	60.1	46.8	0.0
5X-4, 18–20	287.48	0.3	88.4	22.5	5.6	48.5	47.8	0.0
5X-4, 67–69	287.97	0.2	88.2	22.1	3.9	41.1	52.3	0.0
5X-5, 42–44	289.22	0.4	159.6	2.3	5.8	41.1	48.0	0.0
5X-5, 136–138	290.16	0.2	125.2	15.6	8.1	57.0	43.3	0.0
5X-6, 23–25	290.53	0.2	131.1	9.9	4.4	44.2	62.9	0.0
5X-6, 104–106	291.34	0.3	77.1	26.8	2.5	34.5	60.8	0.0
5X-7, 11–13	291.91	0.3	65.9	25.5	3.5	41.2	62.5	0.0
5X-CC, 18–20	292.46	0.3	66.8	44.0	3.7	43.4	68.2	0.0
7X-1, 31–33	302.41	30.4	92.5	8.9	4.9	34.8	25.3	142.9
7X-1, 86–88	302.96	30.3	84.1	9.4	8.2	46.3	11.8	141.3
7X-2, 4–6	303.64	28.3	43.1	11.2	6.7	46.2	17.2	135.8
7X-2, 76–78	304.36	20.3	78.3	8.2	7.2	48.3	40.1	92.1
7X-3, 8–10	305.18	23.5	97.5	7.9	9.5	58.5	20.2	116.1
7X-3, 127–129	306.37	7.1	128.2	5.2	9.9	65.0	34.8	35.9
7X-4, 32–34	306.92	14.2	117.8	8.2	11.6	72.3	26.1	75.2
7X-4, 81–83	307.41	3.6	123.6	5.4	10.7	71.5	37.9	17.5
7X-5, 25–27	308.35	23.2	74.7	7.2	9.1	53.3	18.9	107.4
7X-5, 136–138	309.46	20.0	80.0	6.2	8.0	54.2	19.2	100.8
7X-6, 22–24	309.82	22.7	93.3	4.1	8.3	61.5	21.5	108.6
7X-7, 11–13	311.21	13.7	71.7	8.9	7.3	56.9	25.7	68.0
13X-1, 18–20	350.38	0.2	86.6	7.1	8.4	37.3	39.9	0.0
13X-1, 98–100	351.18	10.7	90.3	11.0	10.9	46.9	22.6	52.9
13X-2, 27–29	351.97	1.0	71.6	24.2	8.0	45.0	39.4	2.1
13X-2, 88–90	352.58	0.2	40.2	21.0	14.1	46.7	19.3	0.0
13X-3, 26–28	353.46	0.1	148.9	13.0	12.4	51.0	21.0	0.0
14X-1, 39–41	355.29	0.3	70.5	20.6	15.2	53.4	13.2	0.0
14X-1, 58–60	355.48	0.6	144.5	5.7	11.8	54.3	32.0	0.0
14X-1, 122–124	356.12	0.2	118.6	9.9	15.0	57.9	12.4	0.0
14X-2, 123–125	357.63	0.1	127.8	8.5	10.1	34.5	28.7	0.0
14X-3, 48–50	358.38	0.1	89.9	20.0	9.7	46.7	35.1	0.0
14X-3, 127–129	359.17	0.2	84.8	27.5	12.6	44.7	35.2	0.0
14X-4, 16–18	359.56	0.1	112.9	26.9	11.3	44.7	46.2	0.0
14X-4, 130–132	360.70	0.2	118.1	2.4	11.0	39.2	13.7	0.0
14X-5, 41–43	361.31	0.2	135.3	2.9	7.7	33.5	55.2	0.0
14X-5, 86–88	361.76	0.2	179.6	5.1	11.8	42.3	15.9	0.0
14X-6, 22–24	362.62	0.2	90.2	25.3	16.3	49.1	37.5	0.0
14X-6, 114–116	363.54	0.7	126.1	4.9	11.5	40.4	10.8	0.0
14X-7, 10–12	364.00	0.2	75.2	24.9	10.9	38.9	36.5	0.0
14X-CC, 10–12	364.53	0.2	62.4	33.8	7.2	38.5	51.6	0.0
15X-1, 39–41	360.29	0.2	53.5	16.2	10.3	36.8	28.2	0.0
15X-1, 144–146	361.34	0.2	61.4	15.8	8.1	45.3	35.4	0.0
15X-2, 18–20	361.58	0.2	132.6	6.2	11.3	43.6	7.5	0.0
15X-2, 94–96	362.34	0.2	74.9	16.5	11.0	57.4	25.3	0.0
15X-3, 23–25	363.13	0.1	39.2	22.4	10.4	40.4	18.0	0.0
15X-3, 148–150	364.38	0.1	133.9	14.9	8.1	38.3	6.7	0.0

Table 12 (continued).

Core, section, interval (cm)	Depth (mbsf)	$CaCO_3$	Integrated area after peak fitting (total counts)					
			Smec.	Ill.	Kaol.	Qtz.	Plag.	Calc.
15X-4, 60–62	365.00	1.4	97.1	8.6	10.2	47.6	6.4	0.0
15X-4, 133–135	365.73	0.4	79.1	17.8	6.9	92.3	11.0	0.0
15X-5, 56–58	366.46	0.1	96.6	18.0	6.9	36.2	37.7	0.0
15X-5, 95–97	366.85	0.7	119.9	10.6	8.0	42.6	15.4	0.0
15X-6, 9–11	367.49	0.5	120.3	16.4	10.1	49.5	37.2	0.0
15X-7, 6–8	368.96	1.7	74.0	15.1	4.3	31.6	29.6	0.0
19X-1, 84–86	399.64	0.1	167.1	7.8	7.8	45.1	41.4	0.0
19X-1, 135–137	400.15	0.1	101.5	3.6	10.7	57.3	23.5	0.0
19X-2, 23–25	400.53	0.1	84.1	4.3	7.4	48.2	33.8	0.0
19X-3, 8–10	401.38	0.1	125.6	4.3	10.6	44.7	34.0	0.0
19X-4, 48–50	403.28	0.1	128.5	2.5	8.2	42.5	49.5	0.0
19X-4, 85–87	403.65	0.1	96.6	3.5	7.5	45.6	36.7	0.0
22X-1, 31–33	427.71	0.1	139.6	6.6	14.5	62.0	23.7	0.0
22X-1, 102–104	428.42	0.1	81.4	5.9	11.5	65.2	6.5	0.0
22X-2, 102–104	429.92	0.1	92.4	10.2	13.6	70.5	5.2	0.0
22X-3, 27–29	430.67	0.1	72.9	11.9	10.8	60.2	8.8	0.0
22X-3, 114–116	431.54	0.1	87.0	9.0	11.2	77.4	8.7	0.0
22X-4, 113–115	433.03	0.1	87.1	16.7	12.3	64.5	17.0	0.0
22X-5, 47–49	433.87	0.1	74.2	18.7	15.2	54.2	11.0	0.0
22X-5, 91–93	434.31	0.1	74.1	18.6	16.4	70.7	25.5	0.0
22X-6, 73–75	435.63	0.1	25.6	26.3	10.1	63.7	25.4	0.0
22X-6, 118–120	436.08	0.1	80.6	15.2	10.3	55.7	6.3	0.0
22X-7, 13–15	436.53	0.1	90.2	14.0	19.1	220.2	49.8	0.0
23X-CC, 2–4	437.12	0.1	78.3	9.5	14.0	66.5	21.4	0.0
25H-1, 23–25	458.63	0.1	50.5	28.5	20.5	71.5	5.4	0.0
25H-1, 96–98	459.36	0.7	71.5	13.0	22.3	90.9	18.6	0.0
25H-2, 13–15	460.03	0.1	65.3	18.2	14.8	62.6	3.1	0.0
25H-2, 69–71	460.59	34.3	39.8	1.4	16.7	58.4	2.4	140.2

Note: See Table 5 for explanation of abbreviations. Sub-bottom depths for Core 156-949B-14X are curatorial depths (see "Operations" section, this chapter).

Core 156-949B-6X which is probably responsible for the biostratigraphic inversion.

Several slickenlined, steeply dipping faults cut Core 156-949B-7X. We could determine a movement sense on only one of these fractures (Sample 156-949B-7X-2, 43–52 cm); it shows 1.5-cm normal displacement on the split core face. Zones of fracture networks and scaly fabric up to 14 cm thick occur at widely spaced intervals.

Subdomain IB: Accretionary Prism (350.2–369.5 mbsf)

This subdomain is characterized by shallow bedding dips. The highest values we recorded were 12° and 16°, with all other measurements being less than 10° (Fig. 13). The sediments are light olive gray claystone with nannofossils, mottled by bioturbation. The assemblage of deformation structures is similar to that in Subdomain IA.

We recognized two major shear zones in this subdomain (intervals 156-949B-13X-2, 68–136 cm, and -14X-1, 28–75 cm). In these intervals, zones of intense scaly fabric alternate with thinner zones of less intense shearing with fracture networks (Fig. 19). Individual scaly fabric zones mostly dip around 30°, with the internal foliation inclined at a high angle. Relationships between the zone boundaries and the scaly foliation indicate thrust movements on the boundary. The near-horizontal attitude of bedding in the sediments immediately overlying interval 156-949B-13X-2, 68–136 cm, indicates that here the thrust is ramping through the section.

Domain II: Décollement Zone (398.8–437.1 mbsf)

Cores 156-949B-19X and -22X are included in the same domain because they contain rocks that share lithological and deformational characteristics with those from the closely defined décollement zone at Site 948. The boundary between lithologic Units II and III, which is probably the primary control on the level of the décollement beneath shallow parts of the prism, occurs in Core 156-949B-22X.

Most of Core 156-949B-19X is light brownish gray to pale yellowish brown claystone with radiolarians. Deformation in Sections 156-949B-19X-1 and -19X-2 is restricted to minor faults with narrow zones of scaly fabric and of uncertain sense of displacement. Black diagenetic manganese oxide stains narrow (<2 cm) horizontal zones in Section 156-949B-19X-3, commonly preferentially concentrated in bioturbation structures. Scaly foliation zones occur in intervals 156-949B-19X-3, 73–80 cm, and -19X-3, 119 cm, through -19X-4, 3 cm. Whereas the brownish claystone just above the deeper scaly foliation zone contains early early Miocene radiolarians, a sharp-bounded, near-horizontal zone of blue-gray claystone extending from interval 156-949B-19X-4, 3–21 cm, contains radiolarians of late early Miocene age, some three or four zones younger (see "Biostratigraphy" section, this chapter). The scaly fabric zone above the blue-gray claystone thus marks a low dipping thrust, probably located at the sharp lower boundary of the zone.

We did not identify unequivocal bedding in Core 156-949B-19X, but several observations suggest that it is nearly horizontal. Thus, diagenetic manganese oxide occurs in horizontally elongate, flat lenses whose shape probably was controlled by subtle differences in lithology; subhorizontal bioturbation discs (not *Zoophycos*) occur in the core, and ash from Sample 156-949B-19X-4, 8–12 cm, although it is much disturbed by bioturbation, occupies an approximately horizontal zone.

Brown, radiolarian-bearing claystone of lithologic Unit II is found from Section 156-949B-22X-1 to -22X-3, 52 cm, where the top of a dark gray silty layer marks the Unit II/III boundary. There is no indication at the core-scale that this is anything other than a normal stratigraphic contact. The only deformation structures in Core 156-949B-22X above the boundary are associated with two steeply dipping normal faults; one, from interval 156-949B-22X-1, 113–131 cm, is marked by a 2.5-cm scaly fabric zone (Fig. 20), and the other, from interval 156-949B-22X-3, 14–20 cm, is associated with a parallel scaly fabric zone only 2 mm wide.

Below the lithologic Unit II/III boundary, three steeply dipping normal faults having adjacent, parallel, scaly fabric zones ranging from 1 mm to 3 cm thick occur between 156-949B-22X-3, 66 cm, and -22X-4, 15 cm. A sharp-bounded, horizontal zone of scaly fabric 1 cm wide is present at 949B-22X-5, 109 cm; and at 949B-22X-6, 6 cm, the top of a zone of more widespread deformation is marked by an interval of thin, intense scaly fabric zones, less deformed phacoids, and stratal disruption that extends to 949B-22X-6, 27 cm. From 949B-22X-6, 27 cm, to the bottom of 22X are intervals individually several decimeters thick that are variously intact, moderately to locally intensely fractured, and affected by scaly foliation and stratal disruption that mostly involves a normal sense of movement (Fig. 21).

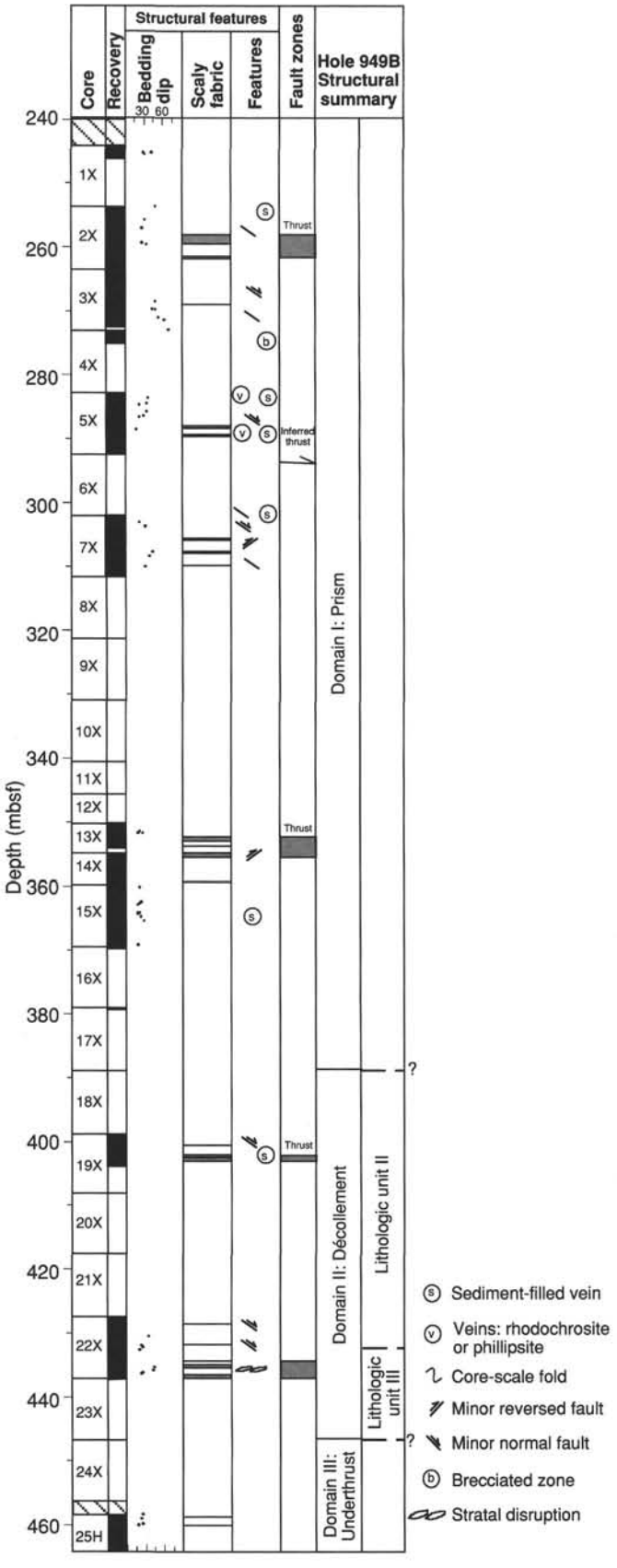

Figure 12. Summary diagram of major structural features recorded from Hole 949B. See Table 15 for data.

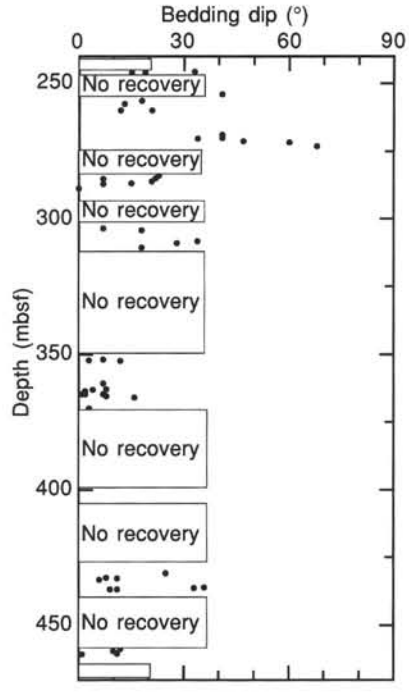

Figure 13. Graph of bedding dip vs. sub-bottom depth for Hole 949B.

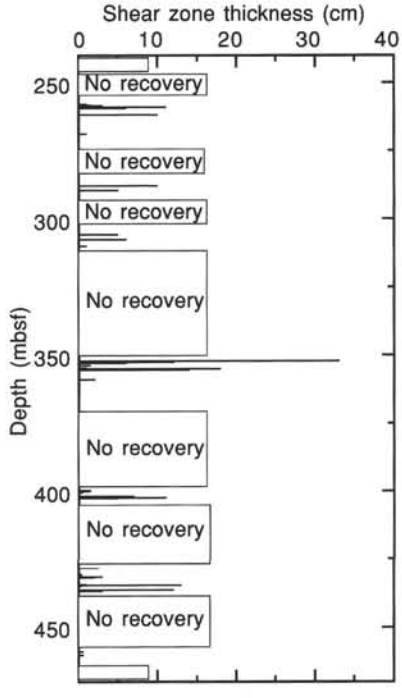

Figure 14. Frequency and thickness of shear zones (zones of intense scaly fabric) vs. sub-bottom depth for Hole 949B.

As at Site 948, the sediments of lithologic Unit III are softer, of more plastic consistency, and show clearer stratal disruption than do the overlying lithologic Unit II claystones. Neither lithologic unit displays the overall intensity of deformation recorded in the décollement zone at Site 948 (see "Site 948" chapter, this volume) and zeolite and carbonate veins, present in the upper part of the décollement zone at Site 948, were not recovered from the equivalent zone at Site 949. However, several shallowly dipping, decimeter-scale intervals

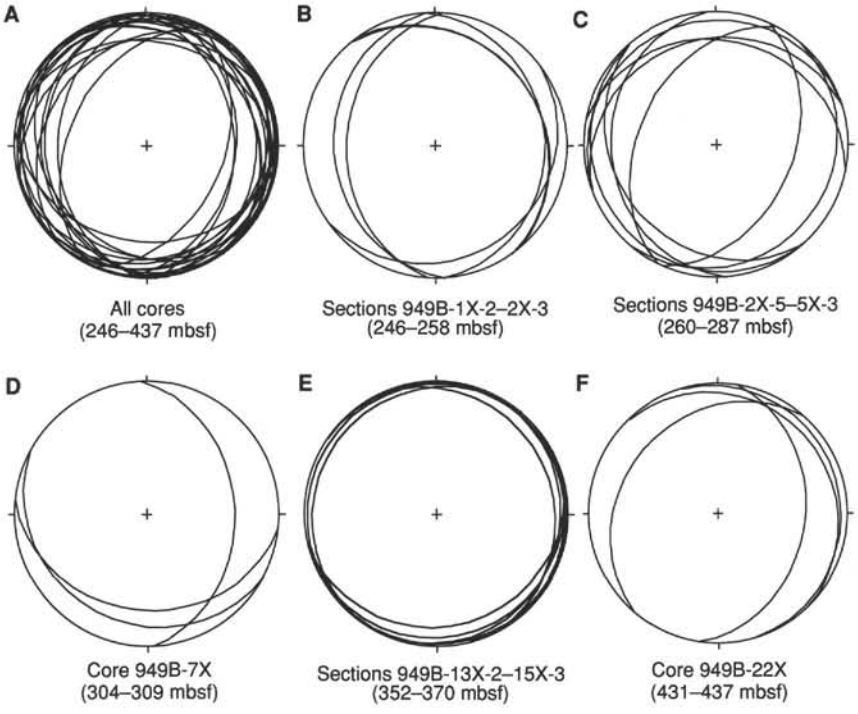

Figure 15. Bedding orientations (lower hemisphere, equal-area projection) after orientation in the geographic reference frame using paleomagnetic remanence data, Hole 949B (see "Explanatory Notes" chapter, this volume). **A.** All planes from the cored section. **B.** Subdomain IA above the fault zone in Section 156-949B-2X-4. **C.** Subdomain IA, Sections 156-949B-2X-5 to -5X-3. **D.** Subdomain IA, Core 156-949B-7X. **E.** Subdomain IB (Sections 156-949B-13X-2 through -15X-3). **F.** Domain III (Core 156-949B-22X).

of intense scaly fabric, fracture networks, and stratal disruption indicate that Cores 949B-19X and -22X represent parts of the décollement domain.

Domain III: Underthrust Section (458.4–464.2 mbsf)

Depths calculated from MCS data indicate that Core 156-949B-25H is from below the likely décollement reflector set and within the section being underthrust below the front of the accretionary prism. This accords with the shallow dip of the rocks (maximum 12°; Fig. 13) and the presence of only two millimeter-scale subhorizontal zones of scaly fabric. Unfortunately, severe deformation induced by flow-in during coring prevented useful structural observations below 156-949B-25H-2, 114 cm.

Magnetic Anisotropy

Anisotropy of magnetic susceptibility (AMS) was measured from 119 samples from Site 949 to determine mineral preferred orientation fabrics. Of the samples, 91 could be oriented into geographic coordinates using paleomagnetic data. Maximum susceptibility axes in Subdomain IA are well clustered, with a mean of 339°/1° (declination/inclination) and confidence limits (α_{95}) = 9° (Fig. 22A). The minimum axes are less well-clustered, with a mean of 245°/56°, and α_{95} = 17°. The AMS orientations from Subdomain IB are similar to those of Subdomain IA (Fig. 22B). The maximum susceptibility axes have a mean of 341°/2° and α_{95} = 11°. The minimum susceptibility axes have a mean of 253°/47° and α_{95} = 16°. Samples from the décollement and the underthrust section (Domains II and III) have AMS orientations with subvertical minimum susceptibility axes and maximum susceptibility axes scattered about a subhorizontal plane (Fig. 22C, -D). The change from moderately inclined, west-southwest–trending minimum susceptibility axes in the accretionary prism to steeply inclined minimum susceptibility axes in the décollement is similar to that observed at Site 948 (compare Fig. 22 with fig. 28 in the "Site 948" chapter, this volume). The shapes of susceptibility ellipsoids range between weakly prolate and weakly oblate in the prism and décollement samples (Fig. 23A–C). Samples from the underthrust section have more highly anisotropic susceptibility ellipsoids with more oblate shapes (Fig. 19D).

Conclusions

Poor core recovery from Site 949, especially over the critical interval of the décollement, greatly inhibited our independent interpretation of the structural geology at this site. However, comparison of the assemblage of structures and their distribution with the similar, but much more complete, data from Site 948 has allowed us to divide Hole 949B into prism, décollement, and underthrust domains, with boundaries consistent with those indicated by magnetic and MCS studies.

Despite the poor recovery, it seems clear that the intensity of deformation at Site 949 is weaker and more diffuse than that at Site 948. This difference probably results from the smaller differential movement across the décollement at Site 949, which is closer to the deformation front and at an earlier stage of development.

BIOSTRATIGRAPHY

A summary of the Site 949 calcareous nannofossil, foraminifer, and radiolarian biostratigraphy is given in Figure 24. The biostratigraphy described here is based on shipboard investigations.

In spite of the poor core recovery at Site 949, biostratigraphic information from Hole 949B indicates four sedimentary sequences bound by thrust fault zones. The uppermost thrust fault is documented by calcareous nannofossil markers, the lower two by radiolarian markers.

A section of late middle Miocene age containing calcareous nannofossils occurs in Cores 156-949B-1X through Sample 156-949B-2X, 2–3 cm. Below is a barren interval of claystone that extends through Core 156-949B-6X. A major biostratigraphic reversal was recognized, on the basis of nannofossils, in Core 156-949B-7X, where sediments of late Miocene to early Pliocene age lie below those of middle Miocene age in Cores 156-949B-1X and -2X. Geochemical and structural evidence suggests that the thrust probably occurs within Core 156-949B-6X (see "Inorganic Geochemistry" and "Structural Geology" sections, this chapter).

Radiolarian occurrences indicate two biostratigraphic reversals within Cores 156-949B-19X through -22X. These reversals document thrust faults, one in Section 156-949B-19X-4 and the other within the unrecovered portion of Core 156-949B-21X. Both reversals coincide with intervals of recrystallization of radiolarian tests. In

Table 13. Estimates of relative mineral abundances for residues of physical-properties specimens, Holes 949A and 949B.

Core, section, interval (cm)	Depth (mbsf)	$CaCO_3$	Relative mineral abundance (wt%)						
			Smec.	Ill.	Kaol.	Clay	Qtz.	Plag.	Calc.
156-949A-									
1H-1, 50–52	0.50	27.1	33.0	12.3	4.5	49.8	25.5	6.9	17.8
1H-1, 100–102	1.00	8.3	25.8	21.7	8.9	56.5	26.9	10.2	6.5
1H-2, 15–17	1.65	31.8	23.0	13.8	5.2	42.0	21.2	9.2	27.7
1H-2, 117–119	2.67	7.8	28.7	16.0	7.5	52.2	25.5	15.6	6.6
156-949B-									
1X-1, 36–38	244.46	11.8	30.8	23.2	5.6	59.5	24.1	5.7	10.7
1X-1, 82–84	244.92	0.7	27.5	27.1	7.9	62.5	24.4	13.1	0.0
1X-2, 18–20	245.78	0.4	37.6	24.7	7.0	69.3	29.0	1.7	0.0
1X-CC, 26–28	246.20	11.0	37.8	14.9	5.0	57.7	25.8	6.9	9.6
2X-1, 90–92	254.70	1.7	32.1	31.3	6.8	70.2	26.5	1.6	1.8
2X-1, 139–141	255.19	7.4	38.3	18.5	5.6	62.3	25.7	6.6	5.4
2X-2, 18–20	255.48	1.3	25.6	40.5	3.8	69.9	22.1	5.7	2.3
2X-2, 106–108	256.36	0.7	44.6	13.2	5.5	63.3	27.8	8.9	0.0
2X-3, 65–67	257.45	0.2	46.5	14.4	6.4	67.3	28.7	4.0	0.0
2X-4, 28–30	258.58	0.2	37.7	20.6	7.7	66.1	29.0	4.9	0.0
2X-4, 143–145	259.73	0.2	30.7	26.6	7.0	64.3	25.9	9.9	0.0
2X-5, 31–33	260.11	0.2	25.5	46.3	1.4	73.2	22.1	4.7	0.0
2X-5, 81–83	260.61	0.2	37.9	28.7	3.3	69.9	25.7	4.4	0.0
2X-6, 1–3	261.31	0.2	44.3	11.1	5.7	61.1	27.7	11.2	0.0
2X-6, 140–142	262.70	5.5	37.1	17.5	11.8	66.4	28.6	4.9	0.0
2X-7, 18–20	262.98	0.2	47.9	8.4	6.2	62.6	28.2	9.2	0.0
3X-1, 27–29	263.77	0.2	22.1	49.8	2.5	74.4	21.3	4.4	0.0
3X-1, 116–118	264.66	0.2	29.4	37.7	6.1	73.2	26.2	0.6	0.0
3X-2, 31–33	265.31	0.2	26.2	30.4	12.4	68.9	24.2	6.9	0.0
3X-2, 140–142	266.40	0.2	36.2	23.9	6.3	66.4	25.4	8.2	0.0
3X-3, 50–52	267.00	0.2	31.4	36.2	2.9	70.6	24.6	4.9	0.0
3X-3, 110–112	267.60	0.2	36.6	26.1	4.6	67.2	25.7	7.0	0.0
3X-4, 113–115	269.13	0.0	43.7	13.6	5.1	62.4	27.6	10.0	0.0
3X-5, 25–27	269.75	0.2	28.0	41.2	3.5	72.7	24.1	3.2	0.0
3X-5, 86–88	270.36	0.3	38.7	16.0	6.8	61.5	26.2	12.3	0.0
3X-6, 14–16	271.14	0.6	36.4	27.6	3.4	67.3	25.8	6.9	0.0
3X-6, 63–65	271.63	0.2	44.1	12.5	5.4	62.0	27.8	10.2	0.0
3X-CC, 10–12	272.24	0.2	41.9	29.8	0.0	71.8	26.7	1.5	0.0
4X-1, 20–22	273.30	0.1	24.2	33.3	6.6	64.2	23.3	12.6	0.0
4X-1, 108–110	274.18	0.2	36.4	24.4	4.6	65.3	26.0	8.7	0.0
4X-2, 12–14	274.72	0.5	37.2	27.1	6.2	70.5	27.2	2.3	0.0
5X-1, 35–37	283.15	0.7	45.0	19.6	1.1	65.7	26.4	8.0	0.0
5X-1, 133–135	284.13	0.5	53.4	0.0	3.1	56.5	29.3	14.2	0.0
5X-2, 21–23	284.51	0.4	43.9	18.7	1.6	64.2	27.2	8.6	0.0
5X-2, 84–86	285.14	0.2	37.8	26.4	1.3	65.4	26.8	7.8	0.0
5X-3, 17–19	285.97	0.3	41.7	19.2	3.0	63.9	26.8	9.3	0.0
5X-3, 111–113	286.91	0.4	45.1	9.8	4.2	59.1	29.3	11.6	0.0
5X-4, 18–20	287.48	0.3	30.9	34.4	1.4	66.6	24.2	9.2	0.0
5X-4, 67–69	287.97	0.2	31.5	34.1	0.5	66.1	23.4	10.5	0.0
5X-5, 42–44	289.22	0.4	52.3	4.6	3.1	60.0	29.1	10.9	0.0
5X-5, 136–138	290.16	0.2	39.1	22.6	3.1	64.8	27.2	8.0	0.0
5X-6, 23–25	290.53	0.2	43.0	15.3	1.9	60.3	26.1	13.7	0.0
5X-6, 104–106	291.34	0.3	27.5	39.6	0.0	67.1	21.1	11.8	0.0
5X-7, 11–13	291.91	0.3	25.2	40.3	0.1	65.7	21.0	13.3	0.0
5X-CC, 18–20	292.46	0.3	20.1	51.0	0.0	71.1	19.5	9.5	0.0
7X-1, 31–33	302.41	30.4	31.2	14.8	2.5	48.6	22.4	6.5	22.6
7X-1, 86–88	302.96	30.3	28.7	16.4	4.5	49.7	23.8	2.9	23.6
7X-2, 4–6	303.64	28.3	16.9	23.9	4.5	45.4	20.8	5.5	28.3
7X-2, 76–78	304.36	20.3	29.6	15.5	4.6	49.7	23.1	11.6	15.6
7X-3, 8–10	305.18	23.5	32.4	13.5	5.3	51.2	25.8	5.0	18.0
7X-3, 127–129	306.37	7.1	43.1	9.2	5.6	57.8	29.5	8.2	4.5
7X-4, 32–34	306.92	14.2	36.7	13.1	6.0	55.8	28.2	5.6	10.3
7X-4, 81–83	307.41	3.6	42.9	9.8	6.3	59.0	30.3	9.2	1.5
7X-5, 25–27	308.35	23.2	28.8	14.5	6.2	49.5	25.0	5.7	19.8
7X-5, 136–138	309.46	20.0	31.5	12.7	5.5	49.7	26.1	5.8	18.5
7X-6, 22–24	309.82	22.7	34.4	8.1	5.7	48.2	27.3	6.3	18.2
7X-7, 11–13	311.21	13.7	30.0	18.6	4.9	53.5	26.2	7.5	12.8
13X-1, 18–20	350.38	0.2	39.7	15.9	5.8	61.4	25.9	12.7	0.0
13X-1, 98–100	351.18	10.7	33.5	20.2	6.0	59.7	25.6	5.5	9.3
13X-2, 27–29	351.97	1.0	26.3	39.0	2.5	67.9	22.8	7.6	1.7
13X-2, 88–90	352.58	0.2	18.2	46.3	8.4	73.0	22.9	4.1	0.0
13X-3, 26–28	353.46	0.1	44.3	18.7	4.9	67.9	29.1	3.0	0.0
14X-1, 39–41	355.29	0.3	27.1	38.0	7.6	72.7	26.0	1.3	0.0
14X-1, 58–60	355.48	0.6	47.4	9.8	6.0	63.2	29.8	7.0	0.0
14X-1, 122–124	356.12	0.2	42.2	17.7	8.0	67.8	30.3	1.9	0.0
14X-2, 123–125	357.63	0.1	45.8	15.0	5.1	65.8	27.8	6.5	0.0
14X-3, 48–50	358.38	0.1	32.0	32.4	3.8	68.3	24.9	6.8	0.0
14X-3, 127–129	359.17	0.2	27.3	39.8	4.2	71.3	23.1	5.6	0.0
14X-4, 16–18	359.56	0.1	32.0	34.2	3.1	69.3	23.7	7.1	0.0
14X-4, 130–132	360.70	0.2	51.1	6.1	7.6	64.9	31.4	3.8	0.0
14X-5, 41–43	361.31	0.2	48.6	6.0	4.5	59.1	26.7	14.3	0.0
14X-5, 86–88	361.76	0.2	53.2	8.2	5.1	66.5	31.0	2.5	0.0
14X-6, 22–24	362.62	0.2	27.9	36.3	6.2	70.4	23.2	6.4	0.0
14X-6, 114–116	363.54	0.7	49.8	10.2	6.9	66.8	31.0	2.1	0.0
14X-7, 10–12	364.00	0.2	26.9	39.8	3.9	70.6	22.5	6.9	0.0
14X-CC, 10–12	364.53	0.2	21.7	48.2	1.1	70.9	20.3	8.8	0.0
15X-1, 39–41	360.29	0.2	26.0	36.6	6.3	68.9	23.1	8.0	0.0
15X-1, 144–146	361.34	0.2	28.2	33.2	4.5	65.9	24.4	9.7	0.0
15X-2, 18–20	361.58	0.2	49.6	11.9	6.2	67.7	31.5	0.8	0.0
15X-2, 94–96	362.34	0.2	30.3	31.6	5.8	67.7	26.8	5.4	0.0
15X-3, 23–25	363.13	0.1	19.1	49.5	5.4	74.0	22.8	3.2	0.0
15X-3, 148–150	364.38	0.1	44.7	23.2	2.8	70.7	29.3	tr	0.0

Table 13 (continued).

Core, section, interval (cm)	Depth (mbsf)	$CaCO_3$	Relative mineral abundance (wt%)						
			Smec.	Ill.	Kaol.	Clay	Qtz.	Plag.	Calc.
15X-4, 60–62	365.00	1.4	43.1	18.8	6.5	68.4	31.2	0.4	0.0
15X-4, 133–135	365.73	0.4	31.3	32.8	3.1	67.2	32.8	0.0	0.0
15X-5, 56–58	366.46	0.1	35.4	29.7	2.4	67.5	24.8	7.8	0.0
15X-5, 95–97	366.85	0.7	45.0	19.0	3.8	67.8	29.7	2.5	0.0
15X-6, 9–11	367.49	0.5	38.3	24.4	3.9	66.6	26.6	6.9	0.0
15X-7, 6–8	368.96	1.7	34.6	31.4	1.5	67.5	25.1	7.5	0.0
19X-1, 84–86	399.64	0.1	48.9	11.4	3.2	63.5	28.8	7.8	0.0
19X-1, 135–137	400.15	0.1	44.9	8.7	7.9	61.5	31.4	7.1	0.0
19X-2, 23–25	400.53	0.1	42.0	11.0	6.1	59.2	29.0	11.8	0.0
19X-3, 8–10	401.38	0.1	47.2	8.7	6.4	62.2	28.9	8.9	0.0
19X-4, 48–50	403.28	0.1	48.1	5.5	5.2	58.8	27.9	13.3	0.0
19X-4, 85–87	403.65	0.1	44.7	8.6	5.8	59.1	28.9	12.0	0.0
22X-1, 31–33	427.71	0.1	45.8	11.3	7.5	64.6	30.6	4.9	0.0
22X-1, 102–104	428.42	0.1	40.4	15.2	9.4	65.1	34.0	0.9	0.0
22X-2, 102–104	429.92	0.1	38.0	21.1	8.6	67.6	32.4	tr	0.0
22X-3, 27–29	430.67	0.1	34.1	27.2	7.2	68.4	30.7	0.9	0.0
22X-3, 114–116	431.54	0.1	38.0	19.7	7.7	65.4	33.8	0.9	0.0
22X-4, 113–115	433.03	0.1	32.7	30.0	6.2	68.9	28.6	2.5	0.0
22X-5, 47–49	433.87	0.1	28.9	35.3	8.0	72.3	26.8	0.9	0.0
22X-5, 91–93	434.31	0.1	26.7	33.0	8.6	68.3	26.7	5.0	0.0
22X-6, 73–75	435.63	0.1	12.0	55.0	4.8	71.7	23.3	4.9	0.0
22X-6, 118–120	436.08	0.1	34.2	30.7	5.5	70.4	29.6	tr	0.0
22X-7, 13–15	436.53	0.1	23.7	20.1	10.1	53.9	37.2	9.0	0.0
23X-CC, 2–4	437.12	0.1	33.9	20.9	9.8	64.5	29.7	5.8	0.0
25H-1, 23–25	458.63	0.1	16.9	48.6	9.5	75.1	24.9	tr	0.0
25H-1, 96–98	459.36	0.7	26.0	25.9	14.3	66.2	29.7	4.2	0.0
25H-2, 13–15	460.03	0.1	26.7	36.7	8.4	71.8	28.2	tr	0.0
25H-2, 69–71	460.59	34.3	14.5	4.2	17.8	36.4	23.7	2.9	37.0

Notes: "tr" indicates that traces of the mineral were detected, but calculated abundance is less than 0%. See Fisher and Underwood (this volume) for a complete description of how calculations were performed. See Tables 5 and 7 for explanation of abbreviations. Sub-bottom depths for Core 156-949B-14X are curatorial depths (see "Operations" section, this chapter).

general, the ages of radiolarian assemblages recovered at this site are never as young as middle Miocene and never as old as Oligocene.

Calcareous Nannofossils

Hole 949A

Hole 949A was cored from 0 to 2.95 mbsf as a mud-line core (Core 156-949A-1H). The sediments contain few to abundant nannofossils of early Pleistocene age that are slightly older than those from the mud-line cores of Site 948 (see "Biostratigraphy" section, "Site 948" chapter, this volume). Nannofossils are moderately well preserved, except those found in the bottom of Sample 156-949A-1H-CC. Reworked Pliocene and Miocene discoasters were found throughout this core.

Sample 156-949A-1H-1, 63–64 cm, was placed in the *Pseudoemiliania lacunosa* Zone, based on the presence of *P. lacunosa* and the absence of *Helicosphaera sellii.* Samples 156-949A-1H-1, 110 cm, to -CC were assigned to the *H. sellii* Zone as a result of the occurrence of *H. sellii* and the absence of *Calcidiscus macintyrei.*

Hole 949B

Hole 949B was drilled without coring to a depth of 244.1 mbsf. Nannofossil-bearing sediments range in age from late Oligocene to early Pliocene (Fig. 24). Pliocene and Oligocene sediments generally contain common and moderately well-preserved calcareous nannofossils. Miocene sediments contain relatively few and often poorly to moderately preserved floras.

Sample 156-949B-1X-1, 5–6 cm, is barren. Sample 156-949B-1X-1, 89–90 cm, contains rare broken discoasters and was assigned to Zone CN7 because of a tentative identification of *Discoaster hamatus.* Samples 156-949B-1X-1-CC through -2X-2, 2–3 cm, contain *D. hamatus,* but lack *Catnaster calyculus* and *D. bollii;* therefore, this interval has been placed in Subzone CN7a, of late middle Miocene age. A barren interval between Samples 156-949B-2X-2, 38–39 cm, and -6X-CC may be the result of dissolution.

A major biostratigraphic reversal was identified in Section 156-949B-7X-1, where lower Pliocene to upper Miocene sediments of Core 156-949B-7X were found below those of the middle Miocene sediments recovered in Cores 156-949B-1X and -2X. Samples 156-949B-7X-1, 7 cm, and -7X-1, 24–25 cm, were assigned to Subzone CN10b of early early Pliocene age as a result of the presence of the range marker *Ceratolithus acutus.* Samples 156-949B-7X-1, 66–67 cm, through -7X-6, 25–26 cm, have been placed in Subzone CN10a owing to the absence of *Discoaster quinqueramus* and the presence of *Triquetrorhabdulus rugosus,* as well as the consistent presence of *Amaurolithus.* Samples 156-949B-7X-6, 57 cm, through -7X-7, 3–4 cm, were assigned to Subzone CN9b because of the co-appearance of *Discoaster quinqueramus, D. surculus, Amaurolithus primus,* and *A. delicatus.* Samples 156-949B-7X-7, 39 cm, through -7X-CC contain *Discoaster quinqueramus* and *D. surculus,* but lack *Amaurolithus,* and, therefore, this interval has been placed in Subzone CN9a.

Recovery in Cores 156-949B-8X through -12X was 0%, except for a small amount of sediment from Sample 156-949B-11X-CC (given entirely to the shipboard paleontological staff). This sample contains few poorly to moderately preserved *Discoaster berggrenii* and *D. quinqueramus.* It was assigned to Subzone CN9a because of the absence of *Amaurolithus.* Thereby, the whole interval from Cores 156-949B-8X through -11X might also belong to Subzone CN9a of late Miocene age. If this is the case, Subzone CN9a is slightly thicker than expected, which may be attributed to one of two possible reasons: either an additional undocumented fault lies between Cores 156-949B-8X and 156-949B-11X, resulting in structural thickening of the section, or the sedimentation rate increased during the late Miocene.

Sample 156-949B-13X-1, 23 cm, is barren. Samples 156-949B-13X-1, 46 cm, through -13X-2, 20 cm, contain six-rayed *Discoaster hamatus,* but lack *Catinaster calyculus,* so it was placed in Subzone CN7a of late middle Miocene age. *Discoaster neohamatus* and *D. bollii* are common in this interval. Discoasters are broken and less common in samples from Section 156-949B-13X-2. Samples 156-949B-13X-2, 59 cm, through -CC are barren.

A long barren interval persists from Cores 156-949B-14X through -24X that may have resulted from a shallowing of the carbonate compensation depth during the Miocene. The décollement zone is contained within this interval, so these sediments could not be dated by nannofossils.

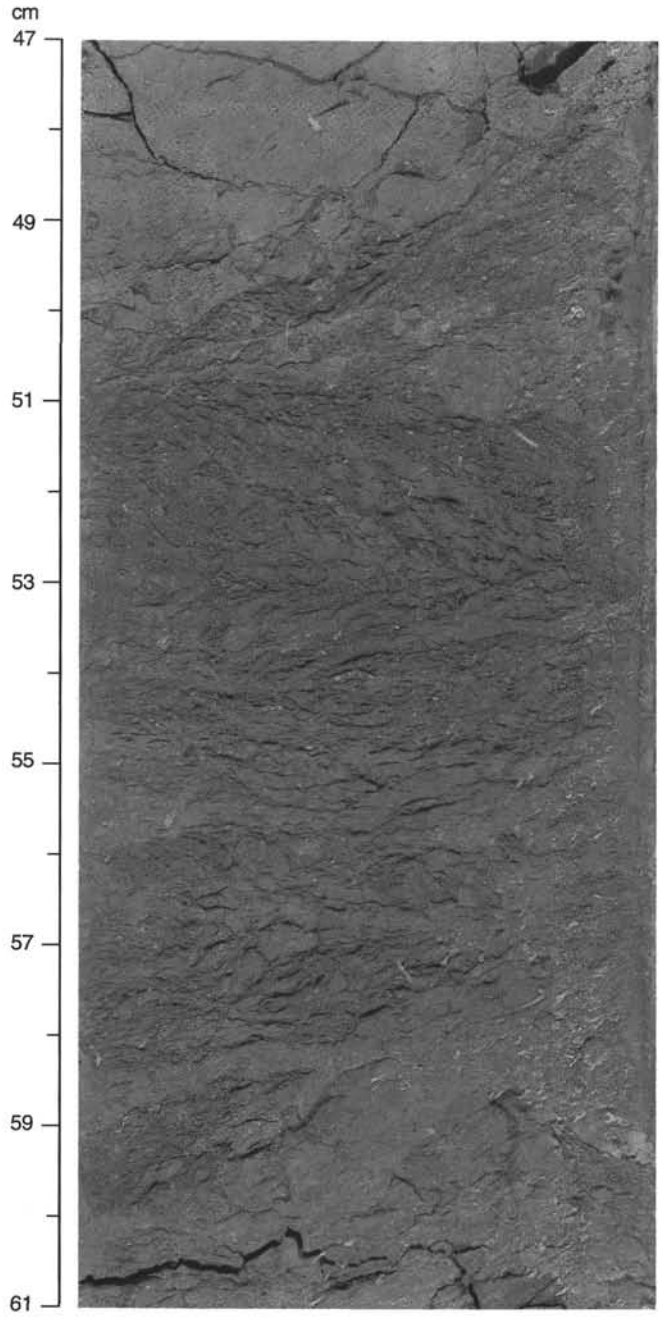

Figure 16. Moderately dipping zone of intense scaly fabric (interval 156-949B-2X-6, 47–61 cm).

Below the décollement zone, nannofossils are found in the brownish gray claystones and gray nannofossil chalk in Sections 156-949B-25H-1 and -25H-2, respectively. Samples 156-949B-25H-1, 106–107 cm, and -25H-2, 55–56 cm, were assigned to Zone CP19 of late Oligocene age, because they contain the range marker *Sphenolithus ciperoensis. Cyclicargolithus abisectus* is abundant.

Hole 949C

Core recovery in Hole 949C was extremely low, averaging only 3.5%. Samples 156-949C-2R-CC through -6R-CC are barren of nannofossils. Sample 156-949C-7R-CC was placed within Zone CP19 of late Oligocene age as a result of the occurrence of the range marker *Sphenolithus ciperoensis.*

Planktonic Foraminifers

Hole 949B

Planktonic foraminifers occur in mud-line Core 156-949B-1H. *Globorotalia truncatulinoides, Globorotalia menardii, Globorotalia tosaensis,* and *Globigerina ruber* are most common, indicating the *Globorotalia truncatulinoides* Zone (N22/N23) of Pleistocene age.

Core 156-949B-1X and Section 156-949B-2X-1 contain a well-preserved fauna of late middle Miocene age (Fig. 24). The association has been assigned to the *Globorotalia acostaensis* Zone (N16). Common species are *Globorotalia acostaensis* and *Globigerina nepenthes.*

Samples 156-949B-2X-CC through -6X-CC are barren. Planktonic foraminifers are abundant in Core 156-949B-7X. The assemblage is composed of broken specimens of large globigerinids, which cannot be determined, and smaller intact foraminifers of *Globorotalia* and *Sphaerodinellopsis* type. The fauna is mostly composed of *Sphaerodinellopsis seminulina, Neogloboquadrina humerosa,* and *Sphaerodinellopsis disjuncta,* indicating the *Neogloboquadrina humerosa* Zone (N17) of late Miocene age.

The interval from Cores 156-949B-8X through -12X had extremely poor recovery. In Section 156-949B-13X-1, an association of small planktonic foraminifers occurs that is similar to the fauna of Core 156-949B-1X. *Globigerina nepenthes* and *Globorotalia acostaensis* are predominant. The assemblage indicates an age of late middle Miocene and was assigned to the *Globorotalia acostaensis* Zone (N16).

Radiolarians

Hole 949B

Radiolarians occur only in Cores 156-949B-19X through -22X (Fig. 24). Sections 156-949B-19X-1 through -CC contain a well-preserved fauna of early Miocene age. A distinct color change at Sample 156-949B-19X-4, 2.5 cm, coincides with an age reversal. In Section 156-949B-19X-1 to the color change at -19X-4, 2.5 cm, pale yellowish brown claystones yield a continuous sequence of associations from the *Calocycletta costata* Zone (R9) through the *Cyrtocapsella tetrapera* Zone (R12). In the upper part of the sequence, radiolarian Zone R9 is indicated by the biostratigraphic markers *Didymocyrtis tubaria, Liriospyris stauropora, Stichocorys wolffii, Cyrtoapsella cornuta, Calocycletta costata, Calocycletta virginis,* and *Dorcadospyris forcipata.* The association in the lower part, assigned to radiolarian Zone R12, includes *Dorcadospyris ateuchus, Didymocyrtis prismatica, Calocycletta serrata, Cyclampterium pegetrum, Carpocanopsis cingulata,* and *Theocyrtis tuberosa.* Further shore-based studies will provide better information about the distribution of individual radiolarian zones from Sections 156-949B-19X-1 through -19X-3. Below the color change at Sample 156-949B-19X-4, 2.5 cm, greenish to greenish gray claystones are rich in radiolarians of the *Calocycletta costata* Zone (R9) again. Biostratigraphically important taxa are *Didymocyrtis violina, Didymocyrtis tubaria, Stichocorys wolffii, Liriospyris stauropora,* and *Cyrtocapsella cornuta.*

Sample 156-949B-19X-CC again contains well-preserved radiolarians of early early Miocene age. The association is composed mostly of *Calocycletta serrata, Eucyrtidium diaphanes, Dorcadospyris forcipata, Cyrtocapsella cornuta, Cyclampterium leptetrum, Lychnocanoma elongata, Stichocorys wolffii,* and *Calocycletta robusta,* indicating the *Cyrtocapsella tetrapera* Zone (R12).

Recovery in Core 156-949B-20X was extremely poor; only a small piece of rock could be analyzed. It contains a rich radiolarian fauna of early early Miocene age. *Calocycletta serrata, Calocycletta virginis, Tholospyris mamillaris, Dorcadospyris ateuchus, Cyrtocapsella cornuta,* and *Lychnocanoma elongata* can be assigned to a zonal range from the *Cyrtocapsella tetrapera* Zone (R12) to the *Lychnocanoma elongata* Zone (R13). The fauna is definitely younger than late Oligocene.

Recovery in Core 156-949B-21X was also extremely poor; nevertheless, strongly recrystallized radiolarians were found embedded in

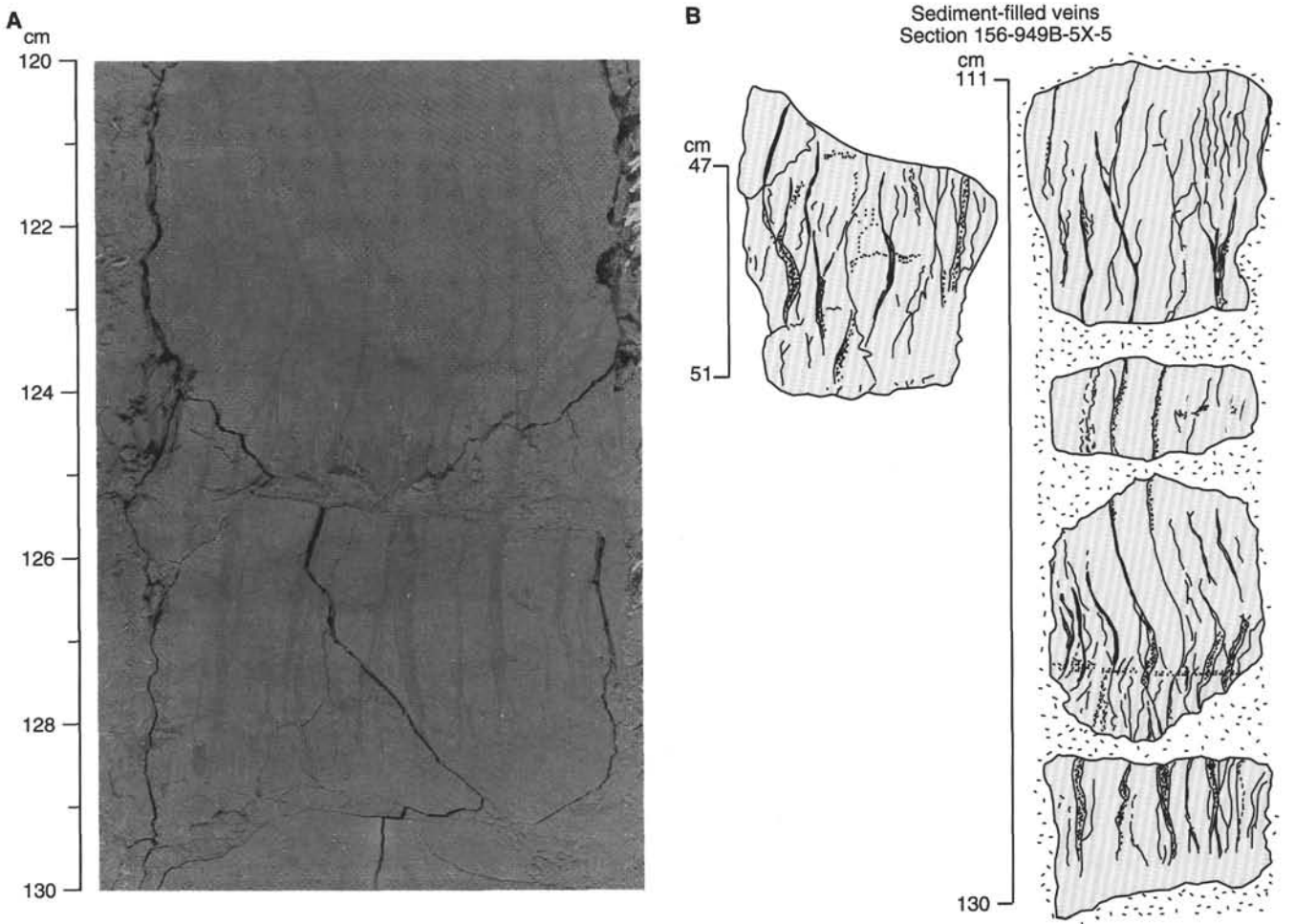

Figure 17. Examples of sediment-filled veins. **A.** Close-up core photograph, interval 156-949B-5X-5, 120–130 cm. **B.** Sketches showing prominent features of the veins.

small fragments of light brownish gray claystone in the core-catcher sample. The number of identified species is low because of recrystallization (Fig. 25). Biostratigraphic markers *Didymocyrtis prismatica, Dorcadospyris ateuchus, Calocycletta virginis, Tholospyris anthophora,* and *Dorcadospyris forcipata* indicate that this sample belongs to radiolarian zones in the range from the *Cyrtocapsella tetrapera* Zone (R12) to the *Lychnocanoma elongata* Zone (R13).

In Core 156-949B-22X, light brownish gray claystones similar to those in Core 156-949B-21X were recovered in the upper part and greenish gray claystones in the lower part. Radiolarians did not occur in the greenish gray claystone, which was identified as a turbidite (see "Lithostratigraphy and Sedimentology" section, this chapter). Strongly recrystallized forms occur in Section 156-949B-22X-1 through the upper part of Section 156-949B-22X-3. Here, one taxon could be identified, *Calocycletta* sp., which ranges from late Oligocene to Neogene in age.

The preservation of radiolarians is good in Sample 156-949B-22X-4, 15–18 cm. The association is partly pyritized and includes undeterminable spherical bodies. Determinable siliceous specimens are *Liriospyris stauropora, Cyrtocapsella cornuta, Tholospyris mamillaris, Calocycletta virginis*(?), *Calocycletta serrata*(?), and *Stichocorys wolffii.* Because of the poor preservation of the lower part of the *Calocycletta* tests, it was impossible to determine the species clearly. In view of the absence of *Calocycletta costata,* the association can be assigned to the *Stichocorys wolffii* Zone (R10) and to the *Cyrtocapsella tetrapera* Zone(?) (R12) of early Miocene age.

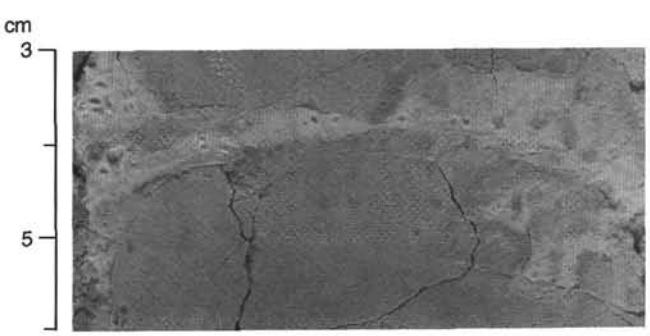

Figure 18. Subhorizontal phillipsite vein (Sample 156-949B-5X-2, 3–6 cm).

Hole 949C

Hole 949C was drilled adjacent to Hole 949B; Core 156-949C-1R, drilled from 401.0 to 405.9 mbsf, corresponds in depth to Core 156-949B-19X (Table 1). Cores 156-949C-1R through -3R had no recovery, except for two small rock fragments in Sample 156-949C-2R-CC both of which contain a well-preserved radiolarian assemblage with common *Calocycletta costata, Calocycletta virginis, Tholospyris mamillaris, Cyrtocapsella cornuta, Dorcadospyris dentata,* and *Liriospyris stauropora.* The age of the fauna is late early Miocene, indicating the *Calocycletta costata* Zone (R9).

Table 14. Values of X-ray diffraction peak intensity, integrated peak areas, and estimates of relative mineral abundances for residues of physical-properties specimens and trimmings from interstitial-water "squeeze-cakes," Hole 949C.

Core, section, interval (cm)	Depth (mbsf)	Smec.	Ill.	Kaol.	Qtz.	Plag.	Calc.
		Intensity above background (counts/s)					
156-949C-							
4R-1, 0–4	425.20	24.7	5.6	29.0	314.6	18.9	0.0
4R-1, 11–13	425.31	15.1	8.2	19.0	374.5	17.8	0.0
6R-CC, 0–7	444.50	18.3	22.3	34.5	1687.9	88.8	0.0
7R-1, 32–34	454.42	17.7	19.6	24.6	395.4	12.9	0.0
7R-1, 46–48	454.56	12.9	20.7	30.8	578.8	21.4	0.0
7R-1, 75–77	454.85	13.2	18.1	24.6	645.2	12.6	0.0
7R-1, 80–90	454.90	18.3	21.5	52.3	552.0	38.6	0.0
7R-CC, 6–8	455.06	11.5	7.8	44.8	419.4	13.9	790.6
		Area after peak fitting (total counts)					
156-949C-							
4R-1, 0–4	425.20	113.6	3.2	14.9	58.6	15.8	0.0
4R-1, 11–13	425.31	69.0	6.1	11.4	59.1	21.5	0.0
6R-CC, 0–7	444.50	100.5	10.7	16.5	219.4	35.5	0.0
7R-1, 32–34	454.42	99.6	19.0	13.0	69.1	3.9	0.0
7R-1, 46–48	454.56	65.1	17.5	15.8	81.7	6.2	0.0
7R-1, 75–77	454.85	51.7	13.5	11.7	87.0	3.0	0.0
7R-1, 80–90	454.90	81.7	15.1	26.3	87.9	3.2	0.0
7R-CC, 6–8	455.06	66.4	5.2	21.9	52.1	1.0	132.4
		Relative mineral abundance (wt%)					
156-949C-							
4R-1, 0–4	425.20	7.5	10.2	63.8	31.9	4.3	0.0
4R-1, 11–13	425.31	16.4	9.9	62.0	30.4	7.6	0.0
6R-CC, 0–7	444.50	16.2	9.3	53.8	40.2	6.0	0.0
7R-1, 32–34	454.42	30.8	5.6	70.4	29.6	tr	0.0
7R-1, 46–48	454.56	34.9	9.3	69.9	30.1	tr	0.0
7R-1, 75–77	454.85	33.1	8.8	66.6	33.4	tr	0.0
7R-1, 80–90	454.90	27.7	15.2	70.2	29.8	tr	0.0
7R-CC, 6–8	455.06	11.2	15.9	49.5	23.1	1.2	26.1

Notes: "tr" indicates that traces of the mineral were detected, but calculated abundance is less than 0%. See Fisher and Underwood (this volume) for a complete description of how calculations were performed. See Table 3 for explanation of abbreviations.

Strongly recrystallized radiolarians are abundant in Core 156-949C-4R. Some of these taxa could be determined as *Calocycletta* sp. and *Tholospyris mamillaris,* but further zonal assignment was not possible. According to the general biostratigraphic record of Site 949, the fauna is probably of early Miocene age.

Comparison of Holes 949B and 949C

Although core recovery in both holes was extremely poor, some interesting facts can be recognized by comparing the biostratigraphic data of Holes 949B and 949C:

1. The age of the radiolarian association in Core 156-949C-2R is younger than that in Core 156-949B-19X, although Core 156-949C-2R is from a greater sub-bottom depth (Fig. 26). *Calocycletta costata* is abundant in Core 156-949C-2R and less common in Section 156-949B-19X-1. The difference represents an unknown time interval within the *Calocycletta costata* Zone (R9).
2. Recrystallized radiolarians occur in Cores 156-949B-21X and -22X as well as in Core 156-949C-4R. Large spherical radiolarians of *Orosphera* type are abundant in Core 156-949C-4R. These are comparable to the "fat rads" in Hole 948C (see "Biostratigraphy" section, "Site 948" chapter, this volume). The recrystallized radiolarians in Hole 949B are larger, but appear to be delicate and "soft," so that the washing procedure generated an abrasive effect and a decrease in size of the "fat rads" in the residue. It seems, however, that the large size of these radiolarians results not only from special recrystallization effects, but also from a real biologic event of large radiolarians that developed during the early Miocene. The presence of numerous, well-preserved large specimens of the genus *Oropagis* in Core 156-949B-19X supports this interpretation.

PALEOMAGNETISM

Shipboard paleomagnetic work at this site was hindered by the poor recovery throughout most of the cored section. A total of 136 discrete samples were measured for both natural remanence and magnetic susceptibility. In addition, all split-core sections longer than 40 cm were measured in the cryogenic magnetometer and put through the MST (see "Explanatory Notes" chapter, this volume).

Natural Remanence

After removal of the drill-induced magnetization between the 3- and 5-mT alternating-field (AF) steps, characteristic remanence directions could usually be obtained from Site 949 discrete samples (Fig. 27). Both normal and reversed polarities were measured throughout the section (Fig. 28), and in general, the reversed-polarity directions (e.g., Fig. 27B, -E) are less well-resolved than the normal-polarity directions (e.g., Figs. 27A, -C, -D, and -F). The discrete sample data show a trend toward lower remanence intensities with increasing depth; in particular, lithologic Unit III (430.92 mbsf total depth) is marked by uniformly low remanence intensities (Fig. 28C). As at Site 948, the stable remanence from discrete samples can be used with confidence to reorient portions of the cores into geographic coordinates at this site.

Using the biostratigraphic ages (see "Biostratigraphy" section, this chapter), several tentative correlations between the magnetic polarity time scale (Cande and Kent, 1992) and portions of the magnetostratigraphy at this site have been made (Fig. 29). Core 156-949A-1H is of entirely normal polarity and has been assigned to the Jaramillo Subchron. The only other confidently identified portion of the polarity time scale is Chron 3r, from 305.6 to 311 mbsf within Core 156-949B-7X. Because both the onset (5.7 Ma) and termination (5.05 Ma) of Chron 3r are present, a sedimentation rate of 8.3 m/m.y. can be calculated for this interval. The presence of the termination of Chron 3r also indicates that the Miocene/Pliocene boundary occurs in Core 156-949B-7X. The other correlations with the polarity time scale presented in Figure 29 are less trustworthy and should be used with caution.

Magnetic Susceptibility

MST and discrete sample magnetic susceptibility measurements indicate a good correlation between susceptibility and lithology (Fig.

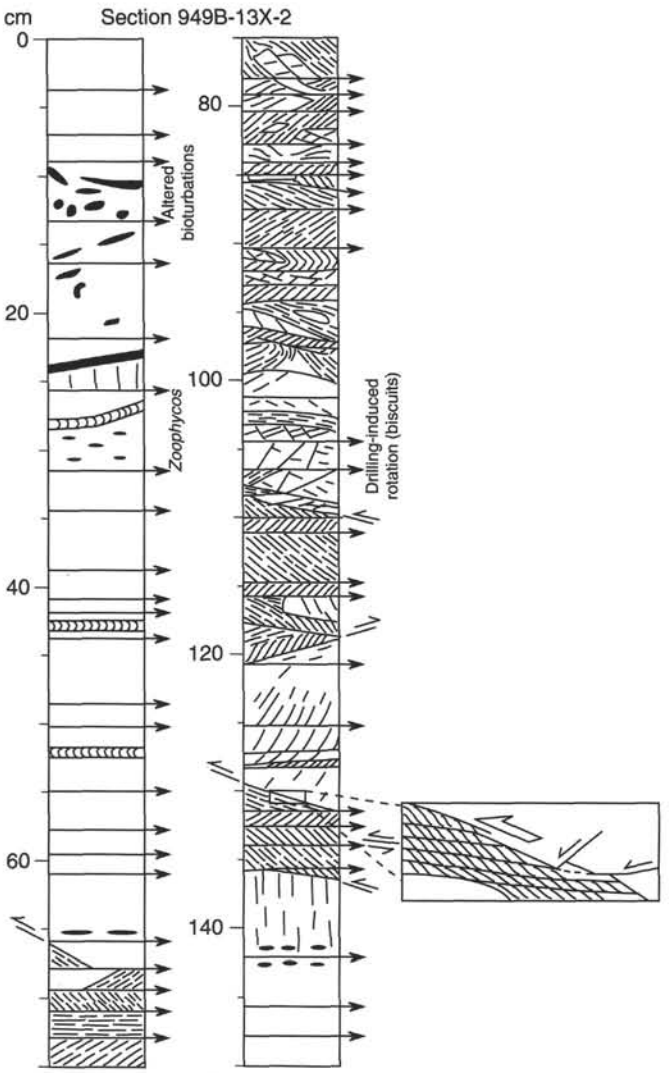

Figure 19. Detailed sketch of Section 156-949B-13X-2 showing a major shear zone in the lower part of the prism domain. The relationship of scaly fabric zone boundaries to scaly foliation (inset) indicates upward movement of the hanging wall. The horizontal stratification in rocks immediately above the shear zone indicates that the inferred thrust fault ramps across its hanging wall.

30). Lithologic Unit II (240–430.92 mbsf) is characterized by relatively high (>1×10^{-3} SI) susceptibilities. Lithologic Unit III (430.92–464.2° mbsf) has much lower ($1–6 \times 10^{-4}$ SI) susceptibilities. Post-cruise work will be devoted to correlations between the incomplete susceptibility stratigraphy at this site and the more detailed susceptibility stratigraphy at Site 948.

ORGANIC GEOCHEMISTRY

Overview

The concentrations of methane in Site 949 sediments found by headspace analyses were below 20 ppm by volume and do not show any trend with depth. Trace quantities of ethane and occasionally propane were found, with a methane-to-ethane ratio of 20 to 200.

The organic carbon content of the sediments is low, mostly below 0.2 wt%, in the cores from 244 to 436 mbsf. Below 436 mbsf, higher organic carbon contents were found occasionally, mainly associated with gray to dark gray intervals, presumably turbidite deposits. Extracts from these layers contain low concentrations of hydrocarbons and have a characteristic pattern of double peaks and a strong

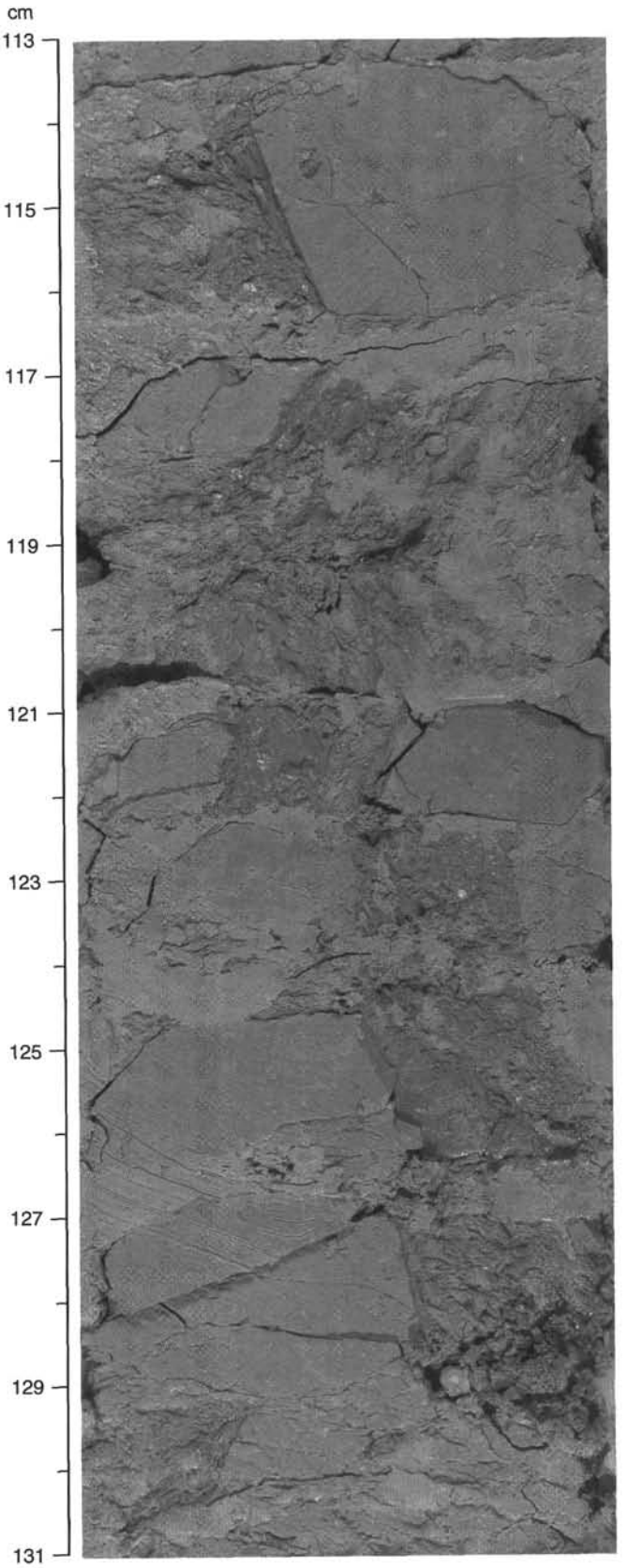

Figure 20. Normal fault with intense scaly fabric (interval 156-949B-22X-1, 113–131 cm).

Table 15. Structural measuremensts performed on cores from Hole 949B.

Core, section, interval (cm)	Depth (mbsf)	ID	Thickness (cm)	Intensity	Apparent dip (°)	Apparent trend (°)	Strike (°)	Dip (°)	Reorient.	Geo. strike (°)	Geo. dip (°)	Comments
156-949B-												
1X-2, 10–12	245.7	B					0	33	Paleomag.	183	33	*Zoophycos*
1X-2, 22–23	245.82	B					157	15	Paleomag.	54	15	*Zoophycos*
1X-2, 31–33	245.91	B					30	19	Paleomag.	322	19	*Zoophycos*, right way up
2X-1, 28–28	254.08	B					17	41	Paleomag.	325	41	
2X-1, 58–58	254.38	B			38	90						*Zoophycos*
2X-2, 46–49	255.76	SV										
2X-2, 106–107	256.36	B					123	18	Paleomag.	357	18	*Zoophycos*
2X-3, 12–15	256.92	B					216	24	Paleomag.	176	24	
2X-3, 75–75	257.55	B					292	13				*Zoophycos*
2X-3, 89–94	257.69	F					317	44				
2X-3, 129–133	258.09	SFZ	0.2				161	48				Thrust
2X-3, 129–133	258.09	SF		3								
2X-3, 129–144	258.09	F										Fracture network
2X-3, 141–144	258.21	SFZ	1		25	270						Thrust
2X-3, 141–144	258.21	SF		2								
2X-3, 143–147	258.23	F			32	270						Thrust
2X-4, 13–18	258.43	SFZ	1.5		40	270						Thrust
2X-4, 13–18	258.43	SF		3								
2X-4, 30–41	258.6	SFZ	3				13	61				Thrust
2X-4, 30–41	258.6	SF		3			114	62				
2X-4, 52–64	258.82	F										Fracture network
2X-4, 70–83	259	SFZ	11				28	22				Probable thrust
2X-4, 70–83	259	SF		3			8	52				
2X-4, 81–85	259.11	F	2									Fracture network
2X-4, 84–85	259.14	SFZ	0.3				226	30				Probable thrust
2X-4, 84–85	259.14	SF		3								
2X-4, 85–87	259.15	F	1.5									Fracture network
2X-4, 87–87	259.17	SFZ	0.5				99	30				Probable thrust
2X-4, 87–87	259.17	SF		3								
2X-4, 102–112	259.32	F					340	44				Probably reverse
2X-4, 126–129	259.56	SFZ	1		20	90						Probable thrust
2X-4, 126–129	259.56	SF		3								
2X-4, 129–130	259.59	F		3								Fracture network
2X-4, 130–132	259.6	SFZ	2									Low dip
2X-4, 130–132	259.6	SF		3								
2X-4, 132–134	259.62	F		3								Fracture network
2X-4, 134–142	259.64	SFZ	6				26	37				Probable thrust
2X-4, 134–142	259.64	SF		3			299	44				
2X-5, 17–18	259.97	B					118	12	Paleomag.	40	12	
2X-5, 21–23	260.01	B					19	21	Paleomag.	253	21	
2X-6, 48–61	261.78	SFZ	10				141	45				
2X-6, 48–61	261.78	SF		3			146	57				
3X-3, 93–104	267.43	Fn					347	51				1-mm-thick SF
3X-4, 93–102	268.93	SFZ	1				196	44				
3X-4, 93–102	268.93	SF		2								
3X-4, 100–100	269	B					353	41				Aligned bioturbations
3X-5, 62–69	270.12	F					29	58				
3X-5, 65–68	270.15	B					335	41	Paleomag.	207	41	*Zoophycos*
3X-5, 75–78	270.25	B					54	41	Paleomag.	24	41	
3X-5, 82–84	270.32	B					340	34				
3X-6, 45–45	271.45	B					204	47				
3X-6, 70–107	271.7	F										Fracture network
3X-6, 78–80	271.78	F					230	25				
3X-6, 89–100	271.89	F					4	70				
3X-6, 90–93	271.9	B					129	60				Planar bioturbation
4X-1, 20–30	273.3	B					150	68				Ash(?) layer
4X-1, 90–95	274	V	1				9	41				Phillipsite
4X-CC, 14–20	274.95	BZ										Green alteration halo (phillipsite?)
5X-1, 128–130	284.08	B					207	23	Paleomag.	139	23	Planar bioturbation
5X-2, 3–6	284.33	V	0.5									Subhorizontal, phillipsite
5X-2, 9–12	284.39	SV										Steep dip
5X-2, 12–26	284.42	F										Fracture network
5X-2, 26–32	284.56	V	<0.1				220	88				Rhodochrosite V, fibers 270-87
5X-2, 35–37	284.65	SV										Subhorizontal
5X-2, 50–75	284.8	F		3								Fracture network
5X-2, 68–69	284.98	B					0	22	Paleomag.	282	22	*Zoophycos*
5X-2, 90–100	285.2	F		3								Fracture network
5X-2, 99–100	285.29	B					180	7	Paleomag.	137	7	Planar bioturbation
5X-3, 7–10	285.87	SV										Steep dip
5X-3, 24–52	286.04	SV										Steep dip
5X-3, 44–48	286.24	B					190	21	Paleomag.	176	21	
5X-3, 59–69	286.39	F					40	70				Green alteration halo (phillipsite)
5X-3, 82–93	286.62	Fn					42	69				Offset on core face 1 cm
5X-3, 82–93	286.62	V	<0.1				42	69				Rhodochrosite V along Fn
5X-3, 118–119	286.98	B					130	15				Planar bioturbation
5X-3, 127–131	287.07	V	<0.1				183	68				Set of rhodochrosite V, fibers 270-68
5X-3, 134–135	287.14	B					262	7	Paleomag.	150	7	*Zoophycos*
5X-3, 135–143	287.15	SV										Steep dip
5X-4, 11–14	287.41	SV										Steep dip
5X-4, 25–36	287.55	SV										Steep dip
5X-4, 55–65	287.85	SFZ	10				180	20				Bottom boundary (top not visible, WRS)
5X-4, 55–65	287.85	SF		3			242	64				Fragments of rhodochrosite V in SF
5X-4, 68–77	287.98	V	<0.1									Set of rhodochrosite V
5X-4, 69–69	287.99	V	<0.1				277	57				Rhodochrosite, fibers 000-57
5X-4, 70–70	288	V	<0.1				92	80				Rhodochrosite, fibers 182-82
5X-4, 77–77	288.07	V	<0.1				252	71				Rhodochrosite, fibers 000-70
5X-4, 95–102	288.25	V	<0.1									Set of rhodochrosite V
5X-4, 96–96	288.26	V	<0.1				126	75				Rhodochrosite, fibers 190-77
5X-4, 100–100	288.3	V	<0.1				292	85				Rhodochrosite, fibers 090-77

Table 15 (continued).

Core, section, interval (cm)	Depth (mbsf)	ID	Thickness (cm)	Intensity	Apparent dip (°)	Apparent trend (°)	Strike (°)	Dip (°)	Reorient.	Geo. strike (°)	Geo. dip (°)	Comments
5X-4, 96–96	288.26	V	<0.1				126	75				Rhodochrosite, fibers 190-77
5X-4, 100–100	288.3	V	<0.1				292	85				Rhodochrosite, fibers 090-77
5X-4, 104–105	288.34	V	<0.1									Rhodochrosite, subhorizontal
5X-5, 15–16	288.95	B						0				Aligned bioturbation
5X-5, 16–21	288.96	F		2								Fracture network
5X-5, 21–52	289.01	SV										Steep dip
5X-5, 50–52	289.3	B										Aligned bioturbation
5X-5, 61–65	289.41	SFZ	5		0	90						
5X-5, 61–65	289.41	SF		3								
5X-5, 69–73	289.49	SV										Steep dip
5X-5, 73–80	289.53	V	<0.1									Rhodochrosite, subvertical
5X-5, 90–100	289.7											
5X-5, 100–150	289.8	SV										Several sets, steep dip
5X-6, 2–6	290.32	SV										Steep dip
5X-6, 67–78	290.97	SV										Steep dip
5X-6, 97–110	291.27	SV										Steep dip
5X-6, 130–136	291.6	SV										Steep dip
5X-6, 144–150	291.74	V										Steep dip
5X-7, 40–45	292.2	SV										Steep dip
5X-CC, 3–13	292.31	V	<0.1				133	85				Set of rhodochrosite V, adjacent SL 270-82
5X-CC, 17–31	292.45	SV										Steep dip
5X-CC, 31–40	292.58	F		2								Fracture network
7X-1, 48–72	302.58	F					161	85				At 51–54 cm
7X-1, 51–54	302.61	SL					327	72				At 51–54 cm
7X-1, 141–141	303.51	B					270	7				
7X-2, 18–30	303.78	SV										
7X-2, 42–44	304.02	SV										
7X-2, 43–52	304.03	F					175	65				Probably normal
7X-2, 43–52	304.03	SL					325	53				
7X-2, 60–64	304.2	Fn					30	63				Offset 1.5 cm on core face
7X-2, 60–64	304.2	SL					150	57				
7X-2, 65–65	304.25	B					154	18	Paleomag.	154	18	
7X-2, 89–92	304.49	F					350	67				
7X-2, 95–98	304.55	F					325	58				
7X-3, 68–75	305.78	SFZ	5				144	46				
7X-3, 68–75	305.78	SF		2								
7X-3, 134–148	306.44	F		2								Fracture network, incipient SF
7X-3, 134–136	306.44	F					23	16				Probably reverse
7X-3, 136–138	306.46	SFZ	0.1		18	90						Thrust
7X-3, 136–138	306.46	SF		3								
7X-4, 103–109	307.63	SFZ	6		0	90						
7X-4, 103–109	307.63	SF		3								
7X-5, 16–16	308.26	B					162	34	Paleomag.	358	34	*Zoophycos* and parallel CTV
7X-5, 70–82	308.8	F					173	47				
7X-5, 88–91	308.98	B					173	28	Paleomag.	96	28	
7X-5, 108–112	309.18	F					180	32				
7X-6, 38–87	309.98	F		1								Fracture network
7X-6, 50–53	310.1	SFZ	1									Low dip
7X-6, 50–53	310.1	SF		3								
7X-6, 108–108	310.68	B					9	18				*Zoophycos*
13X-2, 10–10	351.8	CTV					129	6				Black (Mn oxide) bands
13X-2, 28–28	351.98	B					27	7				*Zoophycos*
13X-2, 43–43	352.13	B					45	3	Paleomag.	220	3	*Zoophycos*
13X-2, 53–53	352.23	B					48	12	Paleomag.	334	12	*Zoophycos*
13X-2, 67–100	352.37	SFZ	33				21	39				Top boundary
13X-2, 67–100	352.37	SF		3			257	69				At 81 cm
13X-2, 100–102	352.7	F		2								Fracture network
13X-2, 102–103	354.7	SFZ	1									Low dip
13X-2, 102–103	352.72	SF		3								
13X-2, 103–110	352.73	F		3								Fracture network
13X-2, 107–119	352.77	SFZ	12				293	27				Upper boundary
13X-2, 107–119	352.77	SF		3			303	62				At 114 cm
13X-2, 119–131	352.89	F		3								Fracture network
13X-2, 130–137	353	SFZ	6				321	34				Upper boundary
13X-2, 130–137	353	SF		3			293	71				At 134 cm
13X-2, 136–140	353.06	F		2								Fracture network
13X-CC, 27–32	353.93	SFZ	1.5				313	23				
13X-CC, 27–32	353.93	SF		2								
14X-1, 15–29	355.05	F		3								Fracture network
14X-1, 27–30	355.17	Fr					153	46				Offset 1 cm SFZ upper boundary
14X-1, 29–47	355.19	SFZ	18				45	3				Upper boundary
14X-1, 29–47	355.19	SF		3			10	63				At 35 cm
14X-1, 45–49	355.35	Fr					25	56				Offset 1 cm lower SFZ boundary
14X-1, 46–63	355.36	F		3								Fracture network
14X-1, 60–74	355.5	SFZ	14									
14X-1, 60–74	355.5	SF		3			307	62				At 68 cm
14X-1, 74–80	355.64	F		3								Fracture network grades downward into drilling disturbance
14X-6, 72–74	359.09	SFZ	2									Low dip
14X-6, 72–74	359.09	SF		3			0	90				
15X-1, 69–70	360.59	B					236	7				*Zoophycos*
15X-2, 76–84	362.16	Fiss						0				With yellowish alteration
15X-3, 4–5	362.94	B					225	8	Paleomag.	216	8	*Zoophycos*
15X-3, 20–21	363.1	B					297	4				*Zoophycos*
15X-3, 52–53	363.42	B					63	2	Paleomag.	57	2	*Zoophycos* right way up
15X-3, 139–144	364.29	SV										
15X-3, 149–150	364.39	B			0	90						
15X-4, 22–23	364.62	B					0	1				*Zoophycos* right way up
15X-4, 25–28	364.65	B					180	7	Paleomag.	20	7	
15X-4, 40–43	364.8	B					0	2	Paleomag.	304	2	

Table 15 (continued).

Core, section, interval (cm)	Depth (mbsf)	ID	Thickness (cm)	Intensity	Apparent dip (°)	Apparent trend (°)	Strike (°)	Dip (°)	Reorient.	Geo. strike (°)	Geo. dip (°)	Comments
15X-4, 90–91	365.3	B					180	8	Paleomag.	62	8	*Zoophycos* right way up
15X-4, 146–148	365.86	B					143	16	Paleomag.	74	16	
15X-6, 74–78	368.14	SV										
15X-7, 27–28	369.68	B			12	90						*Zoophycos*
15X-7, 36–37	369.77	B					135	3	Paleomag.	346	3	*Zoophycos*
19X-1, 140–145	400.2	SFZ	0.2				11	54				
19X-1, 140–145	400.2	SF		3								
19X-2, 45–53	400.75	SFZ	0.5				180	82				Probably normal
19X-2, 45–53	400.75	SF		1								
19X-3, 14–20	401.44	F										
19X-3, 53–55	401.83	CTV					24	10				MnO staining
19X-3, 73–80	402.03	SFZ	7									Low dip
19X-3, 73–80	402.03	SF		2			114	69				At 76 cm
19X-3, 119–120	402.49	SFZ	1									Low dip
19X-3, 119–120	402.49	SF		3								
19X-3, 120–123	402.5	F	3	2								Fracture network
19X-3, 122–133	402.52	SFZ	11									Low dip
19X-3, 122–133	402.52	SF		3								
19X-3, 133–143	402.63	F		2								Fracture network, incipient SF
19X-3, 140–143	402.7	SFZ	3									Low angle
19X-3, 140–143	402.7	SF		2								
19X-3, 145–150	402.75	SFZ	5									Low angle
19X-3, 145–150	402.75	SF		2								
19X-4, 0–3	402.8	SFZ	3				30	8				Base = thrust with stratigraphic invertion
19X-4, 0–3	402.8	SF		3								
19X-4, 43–52	403.23	SV										Steep dip
22X-1, 113–131	428.53	SFZ	2.5				202	75				At 130 cm, lower boundary, normal fault
22X-1, 113–131	428.53	SL					54	74				At 130 cm, along lower boundary of SFZ
22X-1, 113–131	428.53	SF		3			153	45				At 123 cm
22X-3, 14–20	430.54	SFZ	0.2				204	63				Normal fault
22X-3, 14–20	430.54	SF		3								
22X-3, 51–55	430.91	B					237	25	Paleomag.	221	25	
22X-3, 66–80	431.06	SFZ	0.4				254	80				At 68 cm, normal fault
22X-3, 66–80	431.06	SL					241	83				At 68 cm
22X-3, 66–80	431.06	SFZ	0.4				0	87				At 76 cm, same fault as above
22X-3, 66–80	431.06	SF		3								
22X-3, 111–117	431.51	F					180	65				At 114 cm, probably normal
22X-3, 119–144	431.59	SFZ	0.1				149	74				At 128 cm, probably normal fault
22X-3, 119–144	431.59	SF		3								
22X-3, 119–144	431.59	SL					240	85				At 128 cm
22X-3, 119–144	431.59	SFZ	0.1				0	90				At 140 cm
22X-3, 119–144	431.59	SF		3								
22X-3, 147–150	431.87	SFZ	3				186	75				Normal fault, offset >8 cm on core face
22X-3, 147–150	431.87	SF		3								
22X-4, 0–2	431.9	SFZ	1									Steep dip, same normal fault as above
22X-4, 0–2	431.9	SF		3								
22X-4, 2–11	431.92	F		3								Fracture network, brecciation
22X-4, 11–15	432.01	SFZ	2				197	57				Probably normal
22X-4, 11–15	432.01	SF		3								
22X-4, 63–63	432.53	B					346	8				Silty turbidite
22X-4, 73–73	432.63	B					319	11				
22X-4, 120–120	433.1	B					0	6	Paleomag.	344	6	Silty turbidite
22X-5, 108–109	434.48	SFZ	1				0	3				
22X-5, 108–109	434.48	SF		3								
22X-6, 4–17	434.94	SFZ	13				45	11				Upper boundary (is base of overlying turbidite)
22X-6, 4–17	434.94	SF		3								Irregularly developed (fractured phacoids)
22X-6, 17–19	435.07	F		3								Fracture network
22X-6, 18–19	435.08	SFZ	0.3									
22X-6, 18–16	435.08	SF		3								
22X-6, 19–28	435.09	F		3								Fracture network, incipient SF
22X-6, 34–67	435.24	F		2								Fracture network, SD
22X-6, 55–60	435.45	Fn					348	85				SD of silty turbidite
22X-6, 90–130	435.8	F		2								Fracture network, SD
22X-6, 101–104	435.91	B					322	36				
22X-6, 136–140	436.26	B					21	33	Paleomag.	9	33	Silty turbidite
22X-7, 2–3	436.42	Fr					47	21				Causes dip of overlying turbidite
22X-7, 3–4	436.43	SFZ	1				97	24				Upper boundary (is base of overlying turbidite)
22X-7, 3–4	436.43	SF		3								
22X-7, 3–10	436.43	F		3								Fracture network
22X-7, 10–12	436.5	SFZ	2									Low dip
22X-7, 10–12	436.5	SF		3								
22X-7, 12–13	436.52	F		3								Fracture network
22X-7, 13–25	436.53	SFZ	12									Low dip
22X-7, 13–25	436.53	SF		3								Irregularly developed (fractured phacoids)
22X-7, 25–45	436.65	SD										SD of silty turbidite and fracture network in clay
22X-7, 39–40	436.79	B					338	11	Paleomag.	317	11	Silty turbidite affected by SD
22X-CC, 0–4	436.84	SD										In silty turbidite
22X-CC, 0–4	436.84	B					206	9				Silty turbidite affected by SD
22X-CC, 4–5	436.88	SFZ	0.5				206	9				Between two silty turbidites
22X-CC, 4–5	436.88	SF		3								In silty turbidite
22X-CC, 5–8	436.89	SD										
22X-CC, 8–11	436.92	SFZ	3									Low dip
22X-CC, 8–11	436.92	SF		3								
25H-1, 41–41	458.81	B					99	12				Mud turbidite
25H-1, 64–65	459.04	SFZ	0.6				270	5				Parallel to bedding
25H-1, 64–65	459.04	SF		3								

Table 15 (continued).

Core, section, interval (cm)	Depth (mbsf)	ID	Thickness (cm)	Intensity	Apparent dip (°)	Apparent trend (°)	Strike (°)	Dip (°)	Reorient.	Geo. strike (°)	Geo. dip (°)	Comments
25H-1, 108–108	459.48	B					90	10				Silty turbidite
25H-2, 44–45	460.34	SFZ	0.6				94	15				Parallel to bedding
25H-2, 44–45	460.34	SF										
25H-2, 48–48	460.38	B					95	11				Mud turbidite
25H-2, 75–75	460.65	B					0	1				Silty turbidite

Notes: ID = structural identifier; thickness = thickness of structure measured normal to boundaries on the cut core face; intensity = intensity of development of scaly fabric. Intensity is indicated by a 3-point numerical scale: 1 (incipient), 2 (moderate), and 3 (intense). For more detailed information see "Explanatory Notes" chapter (this volume).

Table 16. X-ray diffraction mineralogy of veins from Hole 949B.

Core, section, interval (cm)	Depth (mbsf)	Sampled feature	Calcite	Feldspar	Illite	Kaolinite/ chlorite	Phillipsite	Quartz	Rhodochrosite	Smectite
156-949B-										
4X-1, 40–42	273.5	White, soft mineral patch				#	###	##		###
5X-2, 4–5	284.34	White, soft mineral vein					###			###
5X-2, 5–6	284.35	Light green halo in sediment around vein sampled at 4–5 cm					###	#		###
5X-2, 20–21	284.5	Encasing sediment of vein sampled at 4–5 cm			#	###		###		###
5X-3, 61–62	286.41	Green/blue halo in sediment around fracture			#	##	####	##		##
5X-3, 71–72	286.51	Brown halo in sediment around the same fracture as above			#	###		###		###
5X-3, 130–131	287.1	Pink mineral vein + matrix			#	#		#	####	##
7X-2, 59–60	304.19	Light green halo around ash layer sampled at 64–65 cm	###		#	#	##	##		###
7X-2, 64–65	304.24	Ash layer			#	#	###	###		##
13X-2, 47–48	352.17	Encasing sediment of zone of scaly fabric (see below)	##		#	###		###		###
13X-2, 83–84	352.53	Green band in zone of scaly fabric		##	#	##		###		##
13X-2, 86–87	352.56	Reddish band in zone of scaly fabric				###		###		##
13X-2, 103–104	352.73	Brownish band in zone of scaly fabric (coarse fraction)			#	###		####		##
13X-2, 103–104	352.73	Brownish band in zone of scaly fabric (fine fraction)		#	#	###		###		###
13X-2, 122–123	352.92	Brownish-reddish band in zone of scaly fabric			#	###		####		##

Note: Relative major peak intensities are indicated as follows: # = very low; ## = low; ### = high; #### = very high.

predominance of odd over even alkanes, indicating an immature source. Thirty organic-poor samples were examined for migrated hydrocarbons, and very low concentrations of hydrocarbons were observed in the extracts of three samples from 282 to 290 mbsf. However, no conclusion as to the origin of these hydrocarbons could be made because of the very low concentrations.

Hydrocarbon Gases

Headspace gas analyses were performed on every section (1.5 m) of the cores from Site 949. The usual sampling frequency for headspace analyses at ODP is one per core. Information obtained during Leg 110 at the northern Barbados Ridge suggested that the maximum methane concentration exists near the décollement zone (Mascle, Moore, et al., 1988), and we intended to define this maximum methane concentration better by increasing the sampling frequency for headspace analyses.

Samples for headspace analysis were taken at the bottom of each core section, just after the core was cut into sections. The analysis of the headspace gas was conducted as described in the "Explanatory Notes" chapter (this volume). Concentrations of methane are low, less than 20 ppm by volume in all samples (Table 17). Most methane concentrations are between 5 and 15 ppm, and no clear trend in these concentrations occurs with depth (Fig. 31). Very low concentrations of ethane and occasionally propane were also found in the headspace analyses (Table 17). The methane-to-ethane ratio varies from 20 to 100 in most samples, indicating a slight general decrease with depth. The large scatter in methane-to-ethane ratios is partly attributable to analytical uncertainties of low concentrations.

Higher methane concentrations might be suspected in the more organic-rich layers. However, headspace analysis of one such layer (Sample 156-949B-22X-6, 145–150 cm) did not give higher methane concentrations compared to the organic-poor samples (Table 17).

The very low concentrations of hydrocarbon gases and the scatter in methane concentrations with depth do not allow us to make an interpretation with respect to the origin of the hydrocarbon gases at Site 949.

Organic Carbon

Organic carbon content, defined as the difference between total carbon and carbonate carbon (see "Explanatory Notes" chapter, this volume), was determined in all samples taken for interstitial-water analysis and in most samples for physical properties analyses (Table 18). The organic carbon content of the sediments is low, mostly below 0.2 wt%, in the cores from 244 to 436 mbsf (Fig. 32). Below 436 mbsf, higher organic carbon contents were found occasionally, mainly associated with gray to dark gray intervals. These layers have been interpreted as turbidite deposits (see "Lithostratigraphy and Sedimentology" section, this chapter).

A number of samples from both organic-rich and organic-poor sediments were collected for further organic geochemical analysis (Fig. 32). Organic carbon was also determined by Rock-Eval pyrolysis on these samples, and the results of the two methods show reasonably good agreement for samples having organic carbon contents above 0.2 wt% (Fig. 33). For samples containing less than 0.2 wt%, the Rock-Eval analyses tend to give higher results compared to the results of total carbon minus inorganic carbon (Table 18).

Nitrogen and Sulfur

Total nitrogen was determined (see "Explanatory Notes" chapter, this volume) on the samples that were analyzed for organic carbon (Table 18). Most nitrogen results are between 0.02 to 0.05 wt% and show no correlation with organic carbon content for the low organic carbon samples.

Reliable sulfur results were obtained on only four samples (Table 18), owing to the analytical problems discussed in the "Organic Geochemistry" section, "Site 948" chapter (this volume). The highest sulfur content was found in the sample with the highest organic content.

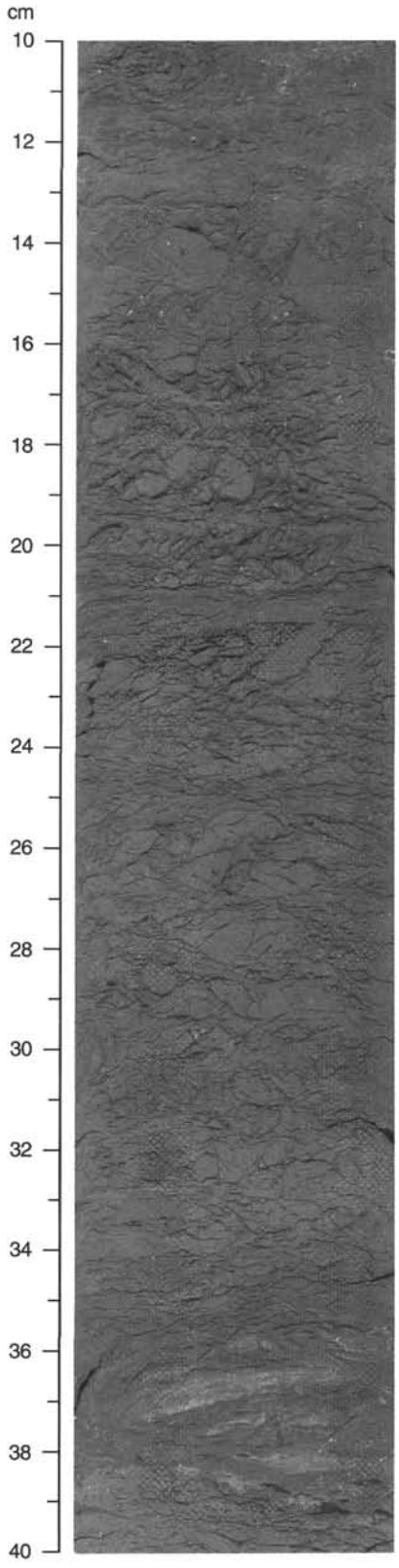

Figure 21. Interval of intense deformation in the décollement (Domain II), showing the association of intense scale fabric, fracture networks, and stratal disruption in lithologic Unit III (interval 156-949B-22X-7, 10–40 cm).

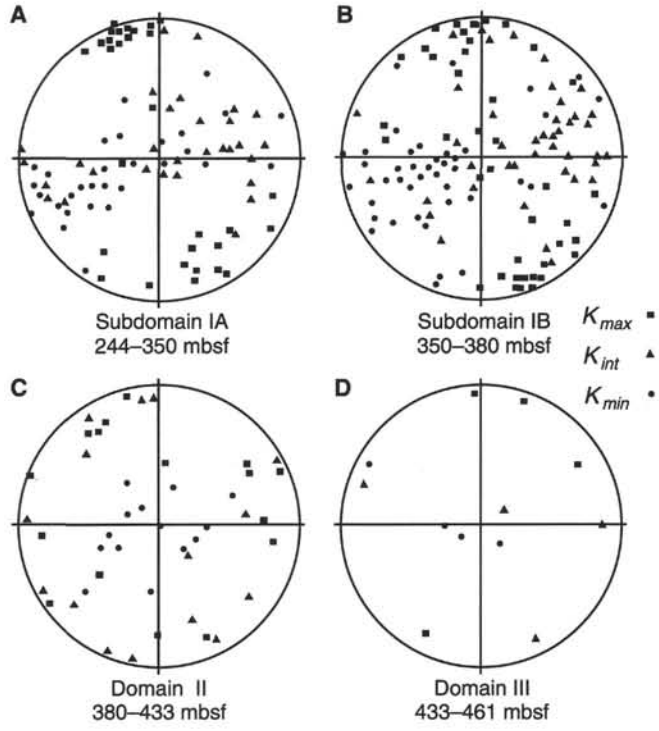

Figure 22. Equal-area, lower hemisphere projections of the principal AMS axes from Site 949 samples. Solid squares = maximum susceptibility axes, solid triangles = intermediate stress axes, and solid circles = minimum susceptibility axes. The axes have been oriented into geographic coordinates using paleomagnetic results. **A.** Axes from Subdomain IA (Cores 156-949B-1X to -7X). **B.** Axes from Subdomain IB (Cores 156-949B-13X to -17X). **C.** Axes from Domain II (Cores 156-949B-19X to -22X). **D.** Axes from Domain III (Cores 156-949B-23X to -25X). The sub-bottom depths for some domains have a wider range than can be defined from the structural data because useful magnetic data could be extracted from cores having poor recovery.

Kerogen Analyses

Thirty-four samples were analyzed with respect to kerogen type and maturity using the Rock-Eval pyrolysis technique (see "Explanatory Notes" chapter, this volume). Unlike at Site 948, samples were not taken explicitly from the organic-rich layers (compare Fig. 32 and Fig. 43 in the "Site 948" chapter, this volume), since no information about organic carbon content was available before selecting the samples.

Generally, Rock-Eval data are not considered reliable for sediments having low organic carbon contents because of matrix effects. Therefore, only the data for three samples have been plotted on the diagram used to characterize the type of organic matter. The organic matter in these samples appears to consist of mixtures of type II + type III kerogen (Fig. 34). However, the hydrogen index for whole-rock samples (as opposed to isolated kerogen) of clay-rich sediments having relatively low organic carbon contents, such as the ones in this study, may be underestimated because of adsorption of pyrolyzates on the clays (Peters, 1986).

One further complication with respect to interpretation of organic matter type based on Rock-Eval data is that the amounts of hydrocarbons released by cracking of the kerogen S_2 do not appear to be dependent on the total organic content (TOC) of the samples from Hole 949B (Table 19). Contrary to what might have been expected, the S_2 is slightly higher for a number of the organic-poor samples (TOC <0.1 wt%) compared to samples having higher organic carbon content (TOC >0.5 wt%). Furthermore, the shape of the S_2 peak of most samples does not differ much. It is not clear what phenomenon causes the S_2 peak of the organic-poor samples, but S_2 is not likely to

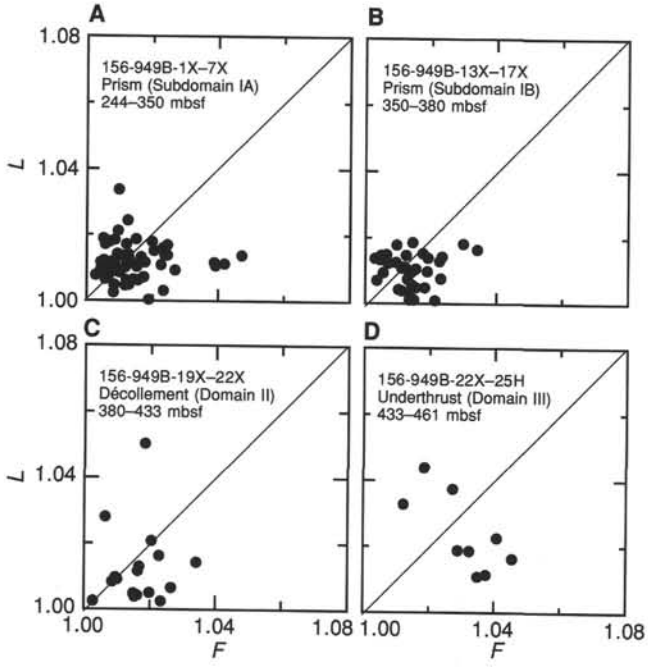

Figure 23. Flinn-type diagrams showing the shape of the susceptibility ellipsoids for Site 949 samples. Vertical axes are magnetic lineations ($L = K_{max}/K_{int}$) and horizontal axes are magnetic foliations ($F = K_{int}/K_{min}$). Prolate ellipsoids have $L > F$, and plot in the upper left corner of the diagrams; oblate ellipsoids have $L < F$, and plot in the lower right portion of the diagrams. **A.** Axes from Subdomain IA. **B.** Axes from Subdomain IB. **C.** Axes from Domain II. **D.** Axes from Domain III. The sub-bottom depths for some domains have a wider range than can be defined from the structural data because useful magnetic data could be extracted from some cores having poor recovery.

result from pyrolyzable organic matter in those samples. Similar problems with the Rock-Eval data were encountered during Leg 110 (Mascle, Moore, et al., 1988), although they were not specifically mentioned. Thus, it appears that Rock-Eval data for samples having low S_2 values are not useful for determining the type of organic matter in the kinds of sediments we dealt with for this study.

Bitumen Analyses

Extractable organic matter was analyzed in the 34 samples that were also analyzed by Rock-Eval pyrolysis (Table 19). Hydrocarbons were extracted from approximately 500 mg of dry sediment using a dichloromethane/methanol mixture (see "Explanatory Notes" chapter, this volume), and the concentrated extract in hexane was analyzed by gas chromatography (GC).

The concentration of most hydrocarbons is low and the *n*-alkanes that could be identified mostly are below approximately 20 ng/g of sediment for most samples having low organic carbon content. Considerably higher hydrocarbon concentrations were found in the more organic-rich samples from Cores 156-949B-22X and -25H. The chromatograms of these sediments show a characteristic pattern with double peaks from C_{25} to C_{31}, with the tallest peak in the doublet being an *n*-alkane (Fig. 35). Identification of the second peak in the doublets was not possible in the shipboard laboratory. The *n*-alkanes of the chromatograms of the three samples from Cores 156-949B-22X and -25H show a strong odd over even predominance (Fig. 36) with a carbon preference index (CPI) (Waples, 1985) of 2.8 to 3.2. The concentration of *n*-alkanes with low carbon atomic numbers is generally low; this is probably a result of evaporation during drying, since the samples from Hole 949B were dried in an oven at 40°C, not in a freeze drier (see "Explanatory Notes" chapter, this volume).

Table 17. Hydrocarbons in headspace gas at Hole 949B.

Core, section, interval (cm)	Depth (mbsf)	C_1 (ppm)	C_2 (ppm)	C_3 (ppm)	C_1/C_2
156-949B-					
1X-1, 0–5	244.13	13.4	0.18		74
2X-1, 145–150	255.28	10.3	0.07		147
2X-2, 145–150	256.78	7.8	0.16		49
2X-3, 145–150	258.28	7.6	0.18		42
2X-4, 145–150	259.78	8.3	0.14		59
2X-5, 145–150	261.28	10.4	0.20		52
2X-6, 145–150	262.78	10.7	0.20		54
3X-1, 145–150	264.98	12.2	0.09		136
3X-2, 145–150	266.48	10.6	0.18		59
3X-3, 145–150	267.98	8.9	0.15		59
3X-4, 145–150	269.48	9.0	0.12		75
3X-5, 105–110	270.58	11.5	0.26		44
4X-1, 120–125	274.33	10.5	0.17		62
5X-1, 145–150	284.28	14.0	0.23		61
5X-2, 105–110	285.38	10.1	0.20		51
5X-3, 145–150	287.28	12.5	0.20		63
5X-4, 105–110	288.38	7.8	0.16		49
5X-5, 145–150	290.28	10.5	0.05		210
7X-1, 145–150	303.58	10.3	0.15		69
7X-2, 105–110	304.68	8.3	0.15		55
7X-3, 145–150	306.58	8.6	0.14		61
7X-4, 145–150	308.08	3.7			
7X-5, 145–150	309.58	5.6	0.11		51
7X-6, 105–110	310.68	8.4	0.10		84
13X-1, 145–150	351.68	6.8	0.23		30
13X-2, 145–150	353.18	7.1	0.19		37
15X-1, 145–150	361.38	11.8	0.29		41
15X-2, 105–110	362.48	10.2	0.34		30
15X-3, 145–150	364.38	10.3	0.32		32
15X-4, 145–150	365.88	6.9	0.23		30
15X-5, 105–110	366.98	2.2			
15X-6, 145–150	368.88	13.2	0.42	0.36	31
19X-1, 145–150	400.28	11.1	0.45	0.16	25
19X-2, 145–150	401.78	15.2	0.67	0.17	23
19X-3, 145–150	403.28	10.2	0.51		20
22X-2, 105–110	429.98	7.4	0.28		26
22X-2, 145–150	430.38	8.3	0.28		30
22X-3, 145–150	431.88	5.0			
22X-4, 145–150	433.38	5.9	0.13		45
22X-5, 105–110	434.48	7.0			
22X-6, 145–150	436.38	8.5	0.11		77
25H-1, 145–150	459.88	5.3			
25H-2, 145–150	461.38	5.6			
25H-3, 105–110	462.48	6.1			
25H-4, 98–103	463.91	6.0			

Hydrocarbon analyses on the organic-poor samples mainly were performed to detect the presence of migrated hydrocarbons in the sediments, since it had been suggested that fluids from deeper levels containing mature organic matter flow through the sediments of the décollement (Mascle, Moore, et al., 1988). As mentioned above, the concentrations of hydrocarbons are low in the organic-poor samples, and except for three samples (Fig. 36) it was not possible to determine the distribution of *n*-alkanes, since many of them were below detection limit. The three samples from Core 156-949B-5X were taken from above and within a fault zone (see "Structural Setting" chapter, this volume). For these samples, the low-carbon-numbered alkanes are also missing, probably because of evaporation during drying. The distribution of the heavier alkanes shows a slight odd over even predominance, with a CPI of 1.3 for all three samples.

Given the low concentrations of hydrocarbons in these samples and the fact that shipboard procedures and the laboratory are not constructed for trace hydrocarbon analyses, it is too early to make any definitive conclusion as to the origin of these hydrocarbons. An interpretation about whether the sediments at Hole 949B contain any migrated hydrocarbons awaits further shore-based analyses.

INORGANIC GEOCHEMISTRY

Overview of Results

Interstitial waters were squeezed and analyzed for the same components described in the "Inorganic Geochemistry" section, "Site 948" chapter (this volume). Recovery was poor at this site: 39.8% in Hole 949B and 3.5% in Hole 949C. The chloride concentration-depth

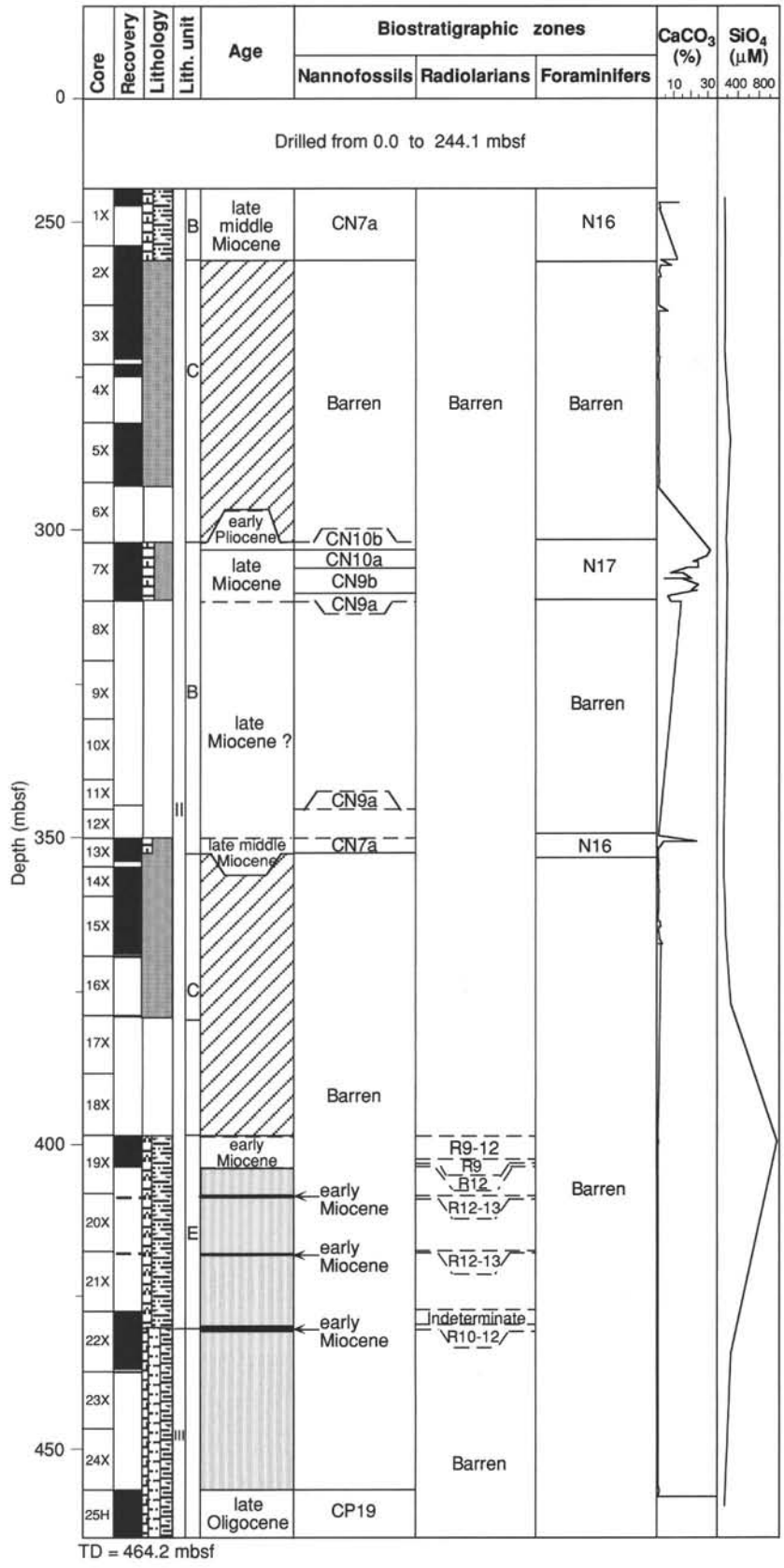

Figure 24. Biostratigraphic summary for Hole 949B.

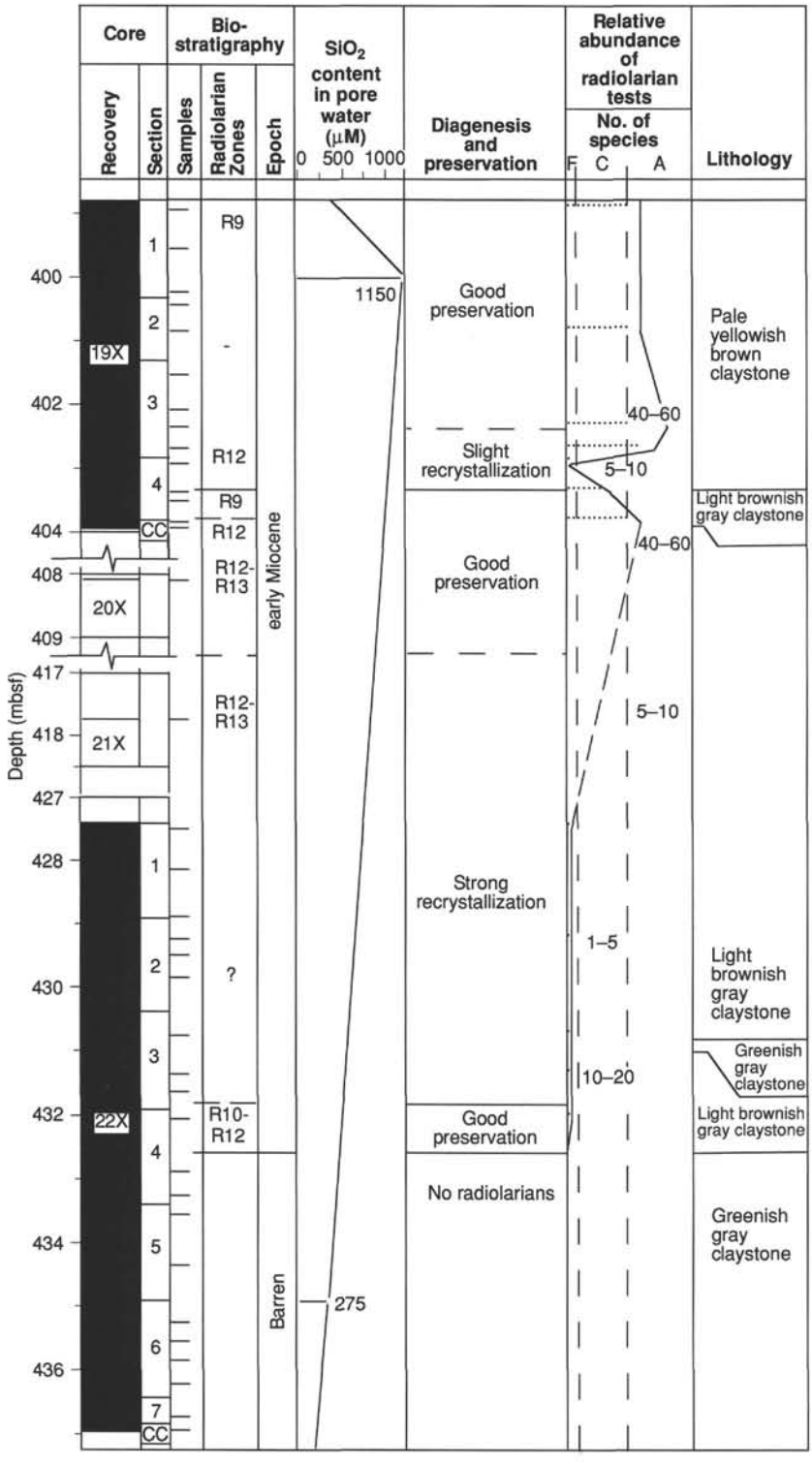

Figure 25. Radiolarian preservation compared with lithologic units, silica content, abundance of radiolarian tests (F = few, C = common, A = abundant), and taxonomic diversity in the décollement of Hole 949B.

profile indicates that the whole section drilled has been diluted by a freshwater source. Two distinct focused fluid conduits, characterized by lower than seawater Cl concentrations, were intercepted at ~360 and ~425 mbsf. The former is within the accretionary complex and the latter in the décollement zone, and both are associated with faults. The concentration-depth profiles also indicate the importance of lateral fluid advection at this site. Concentration reversals in the depth range of about 270 to 350 mbsf, associated with the thrust fault and intersected at ~300 mbsf, suggest vertical displacement of approximately 80 m, observed in all concentration-depth profiles. No diffusive exchange was observed across the thrust fault zone. Based on the physical and chemical properties across this thrust, its calculated maximum age is approximately 36,000 yr. Diagenesis is widespread, generally similar but overall less intense than that at Site 948.

Regionally, dilution of the interstitial waters by a considerably fresher than seawater advected fluid and the intensity of water-rock reactions increase from east to west, from the Leg 110 "reference" Site 672, through the thrust front, toward the arc. Accordingly, at this

Table 18. Carbon, nitrogen, and sulfur data from Holes 949A and 949B.

Core, section, interval (cm)	Depth (mbsf)	Inorg. C (%)	$CaCO_3$ (%)	Total C (%)	Org. C (%)	Nitrogen (%)	Sulfur (%)
156-949A-							
1H-1, 50–52	0.50	3.25	27.07	3.40	0.15	0.04	NA
1H-1, 100–102	1.00	1.00	8.33	1.14	0.14	0.05	NA
1H-1, 143–150	1.43	NA	NA	NA	NA	NA	NA
1H-2, 15–17	1.65	3.82	31.82	3.90	0.08	0.03	NA
1H-2, 117–119	2.67	0.94	7.83	1.03	0.09	0.03	NA
156-949B-							
1X-1, 36–38	244.46	1.42	11.83	1.48	0.06	0.03	NA
1X-1, 82–84	244.92	0.09	0.75	0.13	0.04	0.03	NA
1X-1, 120–150	245.30	0.16	1.33	0.21	0.05	0.02	NA
1X-2, 18–20	245.78	0.05	0.42	0.11	0.06	0.04	NA
1X-CC, 26–28	246.20	1.32	11.00	1.38	0.06	0.03	NA
1X-CC, 38–40	246.32	1.36	11.33	1.40	0.04	0.02	NA
2X-1, 28–42	254.08	1.16	9.66	1.23	0.07	0.04	NA
2X-1, 60–74	254.40	1.13	9.41	1.20	0.07	0.04	NA
2X-1, 90–92	254.70	0.21	1.75	0.27	0.06	0.04	NA
2X-1, 139–141	255.19	0.89	7.41	0.96	0.07	0.03	NA
2X-2, 18–20	255.48	0.16	1.33	0.21	0.05	0.03	NA
2X-2, 55–61	255.85	0.07	0.58	0.12	0.05	0.03	NA
2X-2, 72–88	256.02	0.05	0.42	0.12	0.07	0.04	NA
2X-2, 106–108	256.36	0.08	0.67	0.00	NA	0.03	NA
2X-3, 0–40	256.80	0.17	1.42	0.24	0.07	0.02	NA
2X-3, 65–67	257.45	0.02	0.17	0.09	0.07	0.04	NA
2X-3, 83–89	257.63	0.41	3.42	0.52	0.11	0.03	NA
2X-4, 28–30	258.58	0.02	0.17	0.10	0.08	0.05	NA
2X-4, 53–59	258.83	0.03	0.25	0.11	0.08	0.04	NA
2X-4, 143–145	259.73	0.02	0.17	0.08	0.06	0.04	NA
2X-5, 31–33	260.11	0.02	0.17	0.10	0.08	0.04	NA
2X-5, 81–83	260.61	0.02	0.17	0.07	0.05	0.03	NA
2X-5, 110–150	260.90	0.02	0.17	0.09	0.07	0.03	NA
2X-6, 1–3	261.31	0.02	0.17	0.10	0.08	0.04	NA
2X-6, 10–26	261.40	0.03	0.25	0.11	0.08	0.05	NA
2X-6, 82–88	262.12	0.04	0.33	0.10	0.06	0.03	NA
2X-6, 140–142	262.70	0.66	5.50	0.72	0.06	0.04	NA
2X-7, 9–14	262.89	0.04	0.33	0.09	0.05	0.03	NA
2X-7, 18–20	262.98	0.02	0.17	0.07	0.05	0.03	NA
3X-1, 27–29	263.77	0.02	0.17	0.09	0.07	0.03	NA
3X-1, 86–91	264.36	0.02	0.17	0.08	0.06	0.03	NA
3X-1, 116–118	264.66	0.02	0.17	0.08	0.06	0.04	NA
3X-2, 31–33	265.31	0.02	0.17	0.10	0.08	0.04	NA
3X-2, 87–101	265.87	0.06	0.50	0.12	0.06	0.04	NA
3X-2, 140–142	266.40	0.03	0.25	0.08	0.05	0.04	NA
3X-3, 50–52	267.00	0.02	0.17	0.09	0.07	0.04	NA
3X-3, 63–68	267.13	0.04	0.33	0.09	0.05	0.04	NA
3X-3, 110–112	267.60	0.02	0.17	0.09	0.07	0.03	NA
3X-4, 16–32	268.16	0.03	0.25	0.08	0.05	0.03	NA
3X-4, 60–66	268.60	0.05	0.42	0.10	0.05	0.03	NA
3X-4, 113–115	269.13	0.03	0.03	0.08	0.05	0.05	NA
3X-5, 25–27	269.75	0.02	0.17	0.07	0.05	0.03	NA
3X-5, 86–88	270.36	0.04	0.33	0.07	0.03	0.03	NA
3X-5, 110–150	270.60	0.12	1.00	0.17	0.05	0.04	NA
3X-6, 14–16	271.14	0.07	0.58	0.13	0.06	0.03	NA
3X-6, 63–65	271.63	0.02	0.17	0.07	0.05	0.03	NA
3X-6, 100–106	272.00	0.02	0.17	0.07	0.05	0.03	NA
3X-CC, 10–12	272.24	0.02	0.17	0.06	0.04	0.02	NA
4X-1, 20–22	273.30	0.01	0.08	0.12	0.11	0.03	NA
4X-1, 95–101	274.05	0.02	0.17	0.07	0.05	0.03	NA
4X-1, 108–110	274.18	0.03	0.25	0.09	0.06	0.04	NA
4X-1, 125–150	274.35	0.10	0.83	0.17	0.07	0.01	NA
4X-2, 12–14	274.72	0.06	0.50	0.11	0.05	0.04	NA
5X-1, 7–13	282.87	0.05	0.42	0.11	0.06	0.03	NA
5X-1, 35–37	283.15	0.08	0.67	0.11	0.03	0.03	NA
5X-1, 94–110	283.74	0.07	0.58	0.11	0.04	0.03	NA
5X-1, 133–135	284.13	0.06	0.50	0.07	0.01	0.08	NA
5X-2, 21–23	284.51	0.05	0.42	0.07	0.02	0.03	NA
5X-2, 84–86	285.14	0.02	0.17	0.05	0.03	0.02	NA
5X-2, 110–150	285.40	0.02	0.17	0.05	0.03	0.01	NA
5X-3, 17–19	285.97	0.04	0.33	0.07	0.03	0.03	NA
5X-3, 111–113	286.91	0.05	0.42	0.09	0.04	0.04	NA
5X-4, 18–20	287.48	0.04	0.33	0.05	0.01	0.06	NA
5X-4, 43–56	287.73	0.03	0.25	0.05	0.02	0.06	NA
5X-4, 67–69	287.97	0.03	0.25	0.05	0.02	0.03	NA
5X-4, 110–150	288.40	0.06	0.50	0.11	0.05	0.02	NA
5X-5, 6–12	288.86	0.17	1.42	0.23	0.06	0.03	NA
5X-5, 42–44	289.22	0.05	0.42	0.07	0.02	0.03	NA
5X-5, 136–138	290.16	0.03	0.25	0.07	0.04	0.05	NA
5X-6, 23–25	290.53	0.02	0.17	0.05	0.03	0.03	NA
5X-6, 57–63	290.87	0.06	0.50	0.08	0.02	0.03	NA
5X-6, 78–94	291.08	0.13	1.08	0.16	0.03	0.03	NA
5X-6, 104–106	291.34	0.04	0.33	0.08	0.04	0.03	NA
5X-6, 114–130	291.44	0.05	0.42	0.09	0.04	0.04	NA
5X-7, 6–8	291.86	0.02	0.17	0.05	0.03	0.04	NA
5X-7, 11–13	291.91	0.04	0.33	0.08	0.04	0.03	NA
5X-CC, 18–20	292.46	0.04	0.33	0.07	0.03	0.03	NA
7X-1, 31–33	302.41	3.65	30.40	3.73	0.08	0.00	NA
7X-1, 86–88	302.96	3.64	30.32	3.74	0.10	0.04	NA
7X-2, 4–6	303.64	3.40	28.32	3.47	0.07	0.04	NA
7X-2, 76–78	304.36	2.44	20.33	2.55	0.11	0.04	NA
7X-2, 110–150	304.70	2.74	22.82	2.95	0.21	0.04	NA
7X-3, 8–10	305.18	2.82	23.49	2.91	0.09	0.04	NA
7X-3, 14–25	305.24	2.07	17.24	2.16	0.09	0.04	NA
7X-3, 127–129	306.37	0.85	7.08	0.92	0.07	0.04	NA
7X-4, 32–34	306.92	1.71	14.24	1.81	0.10	0.04	NA
7X-4, 42–55	307.02	2.31	19.24	2.41	0.10	0.04	NA
7X-4, 81–83	307.41	0.43	3.58	0.51	0.08	0.04	NA
7X-4, 119–135	307.79	1.68	13.99	1.75	0.07	0.04	NA
7X-5, 25–27	308.35	2.79	23.24	2.90	0.11	0.04	NA
7X-5, 54–59	308.64	0.32	2.67	0.32	0.00	0.00	0.16
7X-5, 118–134	309.28	2.31	19.24	2.38	0.07	0.04	NA
7X-5, 136–138	309.46	2.40	19.99	2.50	0.10	0.04	NA
7X-6, 22–24	309.82	2.73	22.74	2.83	0.10	0.04	NA
7X-6, 62–77	310.22	0.64	5.33	0.71	0.07	0.04	NA
7X-6, 110–150	310.70	0.89	7.41	0.95	0.06	0.03	NA
7X-7, 11–13	311.21	1.64	13.66	1.72	0.08	0.04	NA
13X-1, 15–18	350.35	0.03	0.25	0.08	0.05	0.04	NA
13X-1, 18–20	350.38	0.02	0.17	0.07	0.05	0.03	NA
13X-1, 52–66	350.72	2.65	22.07	2.67	0.02	0.03	NA
13X-1, 98–100	351.18	1.29	10.75	1.39	0.10	0.04	NA
13X-1, 110–150	351.30	0.37	3.08	0.43	0.06	0.01	NA
13X-2, 22–26	351.92	0.16	1.33	0.22	0.06	0.04	NA
13X-2, 27–29	351.97	0.12	1.00	0.18	0.06	0.03	NA
13X-2, 88–90	352.58	0.03	0.25	0.10	0.07	0.04	NA
13X-3, 26–28	353.46	0.01	0.08	0.11	0.10	0.04	NA
14X-1, 39–41	355.29	0.04	0.33	0.13	0.09	0.04	NA
14X-1, 58–60	355.48	0.07	0.58	0.18	0.11	0.05	NA
14X-1, 105–121	355.95	0.03	0.25	0.09	0.06	0.04	NA
14X-1, 122–124	356.12	0.02	0.17	0.12	0.10	0.05	NA
14X-2, 0–40	356.40	0.03	0.25	0.10	0.07	0.02	NA
14X-2, 54–70	356.94	0.02	0.17	0.08	0.06	0.04	NA
14X-2, 123–125	357.63	0.01	0.08	0.07	0.06	0.03	NA
14X-2, 130–136	357.70	0.02	0.17	0.05	0.03	0.03	NA
14X-3, 13–19	358.03	0.02	0.17	0.08	0.06	0.04	NA
14X-3, 48–50	358.38	0.01	0.08	0.07	0.06	0.03	NA
14X-3, 127–129	359.17	0.02	0.17	0.09	0.07	0.04	NA
14X-4, 16–18	359.56	0.01	0.08	0.08	0.07	0.04	NA
14X-4, 33–45	359.73	0.02	0.17	0.10	0.08	0.04	NA
14X-4, 62–78	360.02	0.04	0.33	0.08	0.04	0.04	NA
15X-1, 39–41	360.29	0.03	0.25	0.08	0.05	0.04	NA
15X-1, 76–82	360.66	0.01	0.08	0.06	0.05	0.04	NA
14X-4, 130–132	360.70	0.03	0.25	0.08	0.05	0.04	NA
14X-4, 143–149	360.83	0.02	0.17	0.06	0.04	0.04	NA
14X-5, 22–27	361.12	0.02	0.17	0.07	0.05	0.04	NA
14X-5, 41–43	361.31	0.02	0.17	0.06	0.04	0.02	NA
15X-1, 144–146	361.34	0.02	0.17	0.07	0.05	0.03	NA
15X-2, 18–20	361.58	0.02	0.17	0.08	0.06	0.07	NA
14X-5, 86–88	361.76	0.02	0.17	0.08	0.06	0.04	NA
14X-5, 110–150	362.00	0.02	0.17	0.09	0.07	0.02	NA
15X-2, 94–96	362.34	0.03	0.25	0.09	0.06	0.06	NA
15X-2, 110–150	362.50	0.04	0.33	0.10	0.06	0.01	NA
14X-6, 22–24	362.62	0.02	0.17	0.11	0.09	0.04	NA
15X-3, 23–25	363.13	0.01	0.08	0.09	0.08	0.06	NA
15X-3, 53–60	363.43	0.02	0.17	0.06	0.04	0.04	NA
14X-6, 114–116	363.54	0.08	0.67	0.13	0.05	0.04	NA
15X-3, 84–100	363.74	0.01	0.08	0.06	0.05	0.02	NA
14X-7, 1–3	363.91	0.02	0.17	0.09	0.07	0.05	NA
14X-7, 10–12	364.00	0.03	0.25	0.08	0.05	0.04	NA
15X-3, 122–130	364.12	0.01	0.08	0.08	0.07	0.05	NA
15X-3, 148–150	364.38	0.01	0.08	0.07	0.06	0.04	NA
14X-CC, 10–12	364.53	0.02	0.17	0.06	0.04	0.03	NA
15X-4, 41–57	364.81	0.13	1.08	0.20	0.07	0.06	NA
15X-4, 60–62	365.00	0.17	1.42	0.24	0.07	0.05	NA
15X-4, 133–135	365.73	0.05	0.42	0.12	0.07	0.05	NA
15X-5, 3–10	365.93	0.03	0.25	0.08	0.05	0.04	NA
15X-5, 28–44	366.18	0.01	0.08	0.06	0.05	0.04	NA
15X-5, 56–58	366.46	0.01	0.08	0.06	0.05	0.04	NA
15X-5, 65–76	366.55	0.01	0.08	0.04	0.03	0.03	NA
15X-5, 95–97	366.85	0.09	0.75	0.15	0.06	0.05	NA
15X-5, 110–150	367.00	0.11	0.92	0.16	0.05	0.03	NA
15X-6, 9–11	367.49	0.06	0.50	0.12	0.06	0.05	NA
15X-6, 57–65	367.97	0.26	2.17	0.33	0.07	0.05	NA
15X-6, 91–98	368.31	0.15	1.25	0.18	0.03	0.05	NA
15X-6, 119–135	368.59	0.20	1.67	0.26	0.06	0.04	NA
15X-7, 6–8	368.96	0.21	1.75	0.27	0.06	0.03	NA
17X-CC, 0–6	379.10	0.05	0.42	0.08	0.03	0.02	NA
19X-1, 33–50	399.13	0.01	0.08	0.07	0.06	0.04	NA
19X-1, 84–86	399.64	0.01	0.08	0.06	0.05	0.04	NA
19X-1, 135–137	400.15	0.01	0.08	0.07	0.06	0.06	NA
19X-2, 23–25	400.53	0.01	0.08	0.05	0.04	0.04	NA
19X-2, 32–48	400.62	0.01	0.08	0.06	0.05	0.04	NA
19X-2, 60–100	400.90	0.02	0.17	0.05	0.03	0.04	NA
19X-3, 8–10	401.38	0.01	0.08	0.06	0.05	0.04	NA
19X-3, 26–32	401.56	0.12	1.00	0.06	0.00	0.04	NA
19X-3, 34–50	401.64	0.01	0.08	0.05	0.04	0.04	NA
19X-3, 95–106	402.25	0.01	0.08	0.05	0.04	0.02	NA
19X-4, 48–50	403.28	0.01	0.08	0.06	0.05	0.01	NA

site, which is closer to the thrust front and where the sediments have average higher porosities than those at Site 948, for example, the Cl dilution is lower, as seen in Figure 37C. However, because of no recovery, we have no record of the actual extent of dilution of the interstitial waters at and immediately above the décollement at this site.

A mechanical continuous fluid sampler, driven by osmotic pumping, was deployed by attaching it to the CORK thermistor string within the décollement zone. It is designed to sample in situ formation fluid continuously for more than 2 yrs.

Methods

For sample retrieval and preparation procedures, see "Inorganic Geochemistry" section, "Site 948" chapter (this volume).

Table 18 (continued).

Core, section, interval (cm)	Depth (mbsf)	Inorg. C (%)	$CaCO_3$ (%)	Total C (%)	Org. C (%)	Nitrogen (%)	Sulfur (%)
19X-4, 54–60	403.34	0.02	0.17	0.05	0.03	0.02	NA
19X-4, 85–87	403.65	0.01	0.08	0.18	0.17	0.02	NA
22X-1, 31–33	427.71	0.01	0.08	0.06	0.05	0.03	NA
22X-1, 102–104	428.42	0.01	0.08	NA	NA	NA	NA
22X-1, 130–146	428.70	0.01	0.08	0.06	0.05	0.03	NA
22X-2, 0–16	428.90	0.01	0.08	0.07	0.06	0.03	NA
22X-2, 102–104	429.92	0.01	0.08	0.05	0.04	0.02	NA
22X-2, 110–150	430.00	0.01	0.08	0.05	0.04	0.03	NA
22X-3, 0–13	430.40	0.01	0.08	0.08	0.07	0.03	NA
22X-3, 27–29	430.67	0.01	0.08	0.08	0.07	0.03	NA
22X-3, 114–116	431.54	0.01	0.08	0.06	0.05	0.03	NA
22X-3, 129–136	431.69	0.02	0.17	0.06	0.04	0.04	NA
22X-4, 38–54	432.28	0.01	0.08	0.06	0.05	0.04	NA
22X-4, 113–115	433.03	0.01	0.08	0.07	0.06	0.03	NA
22X-4, 125–132	433.15	0.02	0.17	0.08	0.06	0.05	NA
22X-5, 47–49	433.87	0.01	0.08	0.09	0.08	0.04	NA
22X-5, 91–93	434.31	0.01	0.08	0.09	0.08	0.03	NA
22X-5, 110–150	434.50	0.01	0.08	0.11	0.10	0.05	NA
22X-6, 73–75	435.63	0.01	0.08	0.08	0.07	0.03	NA
22X-6, 118–120	436.08	0.01	0.08	0.11	0.10	0.04	NA
22X-6, 145–150	436.35	0.02	0.17	0.72	0.70	0.06	0.88
22X-7, 13–15	436.53	0.01	0.08	0.11	0.10	0.03	NA
23X-CC, 2–4	437.12	0.01	0.08	0.10	0.09	0.04	NA
25H-1, 23–25	458.63	0.01	0.08	0.42	0.41	0.05	NA
25H-1, 43–50	458.83	0.02	0.17	0.54	0.52	0.07	0.33
25H-1, 96–98	459.36	0.09	0.75	0.54	0.45	0.06	NA
25H-2, 13–15	460.03	0.01	0.08	0.09	0.08	0.05	NA
25H-2, 35–42	460.25	0.02	0.17	0.37	0.35	0.16	0.17
25H-2, 69–71	460.59	4.12	34.32	4.69	0.57	0.04	NA
25H-2, 84–93	460.74	0.03	0.25	0.21	0.18	0.05	NA
25H-3, 110–150	462.50	NA	NA	NA		NA	NA

Notes: NA = not analyzed. Depths determined for Core 949B-14X are "curatorial" depths (see "Operations" section, this chapter).

Analyses

Essentially the same methods as described in Gieskes et al. (1991) were used for the interstitial-water analyses, except for dissolved manganese, which was analyzed by atomic absorption spectroscopy. At this site Mn analysis included matrix matching. As at Site 948, the concentrations of each of the dissolved components, Cl, Ca, Mg, K, and Na, were determined by the two methods discussed in the "Explanatory Notes" chapter (this volume). The results from the more accurate and precise method are reported in Table 20. Interstitial waters from the three samples marked by an asterisk were sealed in special gas-tight Cu tubes for shore-based analysis of helium isotope ratios. When available, excess interstitial water was used for a partial or complete set of shipboard chemical analyses. The one interstitial-water sample marked by two asterisks was partially contaminated by drilling fluid, as is clearly indicated by its high sulfate concentration.

Results

The shipboard interstitial-water chemical data are given in Table 20 and have been plotted vs. depth (mbsf) in Figures 37–41.

Chloride and Salinity

The concentration-depth profile of dissolved chloride (Fig. 37A) is characterized (1) by lower than seawater Cl concentrations, except (a) in the lower Pliocene sediment of Core 949B-7X, situated beneath the main fault intercepted at this site, at ~300 mbsf, and (b) in the underthrust section below the second prominent negative polarity seismic reflector, at ~450 mbsf (see "Vertical Seismic Profiles" section, this chapter); and (2) by its nonsteady-state nature. The near-seawater Cl concentration in the lower Pliocene section is from material that has been displaced by a fault from a shallower depth, as also is indicated by a biostratigraphic repetition (see "Biostratigraphy" section, this chapter). Based on Leg 110 results, the advected fresher-than-seawater fluid has not permeated the uppermost 200 m of the accretionary complex. Faulting must have been recent enough not to allow diffusive exchange to erase the Cl-concentration reversal. The underthrust sediment section also is characterized by near-seawater dissolved Cl-concentration. A similar division between low Cl above the décollement and approximately seawater Cl in the décollement and underthrust section was observed at Site 948.

Distinct dissolved-Cl minima occur at ~290, ~360, and ~425 mbsf. All three are associated with fault zones (see "Structural Geology" section, this chapter). Although on average the dissolved-Cl concentration of the section drilled is only 4% to 5% fresher than seawater dissolved-Cl concentration, in situ production of enough freshwater at 60% to 65% porosity (see "Physical Properties" section, this chapter) and at just 20° to 35°C (see "In Situ Temperature Measurements" section, this chapter) is implausible. Therefore, as discussed in the "Inorganic Geochemistry" section, "Site 948" chapter (this volume), a solution having significantly lower than seawater Cl concentration must have been advected from deeper in the accretionary complex. An origin for this solution was originally proposed by Gieskes et al. (1990) based on Leg 110 geochemical results and will be determined by shore-based geochemical, especially isotopic, analyses. Unlike at Site 948, the Cl minima at this site are not accompanied by methane maxima, most probably because of the less distinct dissolved Cl minima and the generally low dissolved-methane concentrations. (For a more detailed discussion of methane concentrations, see "Organic Geochemistry" section, this chapter.)

Based on preliminary calculations of a sediment diffusion coefficient at ~360 mbsf of 5×10^{-6} cm^2/s, using the wireline resistivity log of Site 948 at "equivalent" depth and lithology (see "Downhole Logging" section, "Site 948" chapter, this volume) and the porosity measurements at this site (see "Physical Properties" section, this chapter), the low-Cl fluid has advected into the narrow (<7 m) distinct dissolved-Cl minimum at ~360 mbsf, less than 500 yr ago.

Because of the sparse core recovery between ~370 and 450 mbsf, assumptions and interpretations about the asymmetry and nature of the dissolved-Cl concentration profile above and below the Cl minimum at ~425 mbsf are premature. The slightly higher than seawater Cl concentrations in Sections 156-949B-7X-2 and 156-949C-6R-CC (see Table 20 and Fig. 37A) suggest in situ hydration reactions, probably involving volcanic ash.

Overall, the salinity depth profile (Fig. 37B) is mostly similar to that of chlorinity, indicating that in this section the Cl concentration controls the salinity. A narrow horizon of relatively high salinity at ~430 mbsf, within the generally low salinity décollement zone, may reflect the existence of a thrust fault at the fault zone shown in Figure 12 (see "Structural Geology" section, this chapter). Unfortunately, because the sample from this level was collected for He analysis, it was analyzed only for salinity.

Calcium and Magnesium

Dissolved calcium concentrations are three to four times higher than those of seawater, and dissolved magnesium concentrations are 50% to 70% of those of seawater (Table 20). As discussed in the "Inorganic Geochemistry" section, "Site 948" chapter (this volume), the high Ca concentrations are especially notable in view of the incomplete bacterial sulfate reduction and, thus, moderate alkalinity production. The origin of the high Ca concentrations also is discussed in the "Inorganic Geochemistry" section, "Site 948" chapter (this volume).

Dissolved-Ca concentrations increase slightly with depth toward the décollement zone and do not vary much within it and in the underthrust section (Fig. 38A), while dissolved-Mg concentrations decrease toward the décollement and are offset to slightly higher, but more or less constant, concentrations in the décollement and underthrust section (Fig. 38B). The basement alteration signal of steep increases in Ca concentrations and decreases in Mg (and Na) concentrations, so strongly manifested in the dissolved-Ca and -Mg (and -Na) concentration-depth profiles of the underthrust section at Site 948, were not encountered at this site, except for the Li profile discussed below. This is most probably because of the minimal penetration into and recovery of the underthrust section at this site, and

Table 19. Summary of Rock-Eval pyrolysis data for Hole 949B.

Core, section, interval (cm)	Depth (mbsf)	T_{max}	S_1	S_2	S_3	PI	PC	HI	OI	TOC
156-949B										
1X-CC, 38–40	246.32	358	0.19	0.14	1.76	0.59	0.02	155	1955	0.09
2X-2, 55–61	255.85	462	0.22	0.74	0.78	0.23	0.08	740	780	0.10
2X-3, 83–89	257.63	513	0.14	0.81	2.01	0.15	0.07	736	1827	0.11
2X-4, 53–59	258.83	461	0.16	1.05	0.15	0.13	0.10	875	125	0.12
2X-6, 82–88	262.12	464	0.15	1.04	0.14	0.13	0.09	945	127	0.11
2X-7, 9–14	262.89	465	0.16	1.22	0.12	0.12	0.11	938	92	0.13
3X-1, 86–91	264.36	460	0.18	0.79	0.44	0.19	0.08	790	440	0.10
3X-3, 63–68	267.13	462	0.24	0.74	0.38	0.24	0.08	822	422	0.09
3X-4, 60–66	268.60	467	0.25	1.25	0.16	0.17	0.12	961	123	0.13
3X-6, 100–106	272.00	458	0.12	0.94	0.29	0.11	0.08	940	290	0.10
4X-1, 95–100	274.05	464	0.07	0.88	0.30	0.07	0.07	977	333	0.09
5X-1, 7–13	282.87	471	0.07	0.93	0.38	0.07	0.08	1033	422	0.09
5X-5, 6–12	288.86	483	0.11	0.62	0.42	0.15	0.06	1033	700	0.06
5X-6, 57–63	290.87	471	0.13	0.85	0.44	0.13	0.08	1062	550	0.08
5X-7, 6–8	291.86	467	0.12	0.72	0.36	0.14	0.07	1028	514	0.07
7X-5, 54–59	308.64	591	0.12	0.31	1.11	0.29	0.03	1033	3700	0.03
13X-1, 15–18	350.35	465	0.08	1.17	0.24	0.06	0.10	1170	240	0.10
13X-6, 22–26	351.92	524	0.19	0.70	0.63	0.22	0.07	1000	900	0.07
14X-2, 130–136	357.70	463	0.13	1.57	0.21	0.08	0.14	1121	150	0.14
14X-3, 13–19	358.03	463	0.10	1.12	0.27	0.08	0.10	1120	270	0.10
15X-1, 76–82	360.66	463	0.09	1.28	0.14	0.07	0.11	1163	127	0.11
14X-4, 143–149	360.83	463	0.07	1.01	0.21	0.06	0.09	0	262	0.08
14X-5, 22–27	361.12	466	0.08	1.05	0.27	0.07	0.09	1166	300	0.09
15X-3, 53–60	363.43	463	0.07	1.00	0.09	0.07	0.08	1111	100	0.09
14X-7, 1–3	363.91	469	0.09	1.07	0.09	0.08	0.09	1188	100	0.09
15X-5, 3–10	365.93	461	0.09	1.00	0.09	0.08	0.09	714	64	0.14
15X-6, 91–98	368.31	464	0.16	0.97	0.33	0.14	0.09	1077	366	0.09
19X-3, 26–32	401.56	449	0.20	0.70	0.16	0.22	0.07	1000	228	0.07
19X-4, 54–60	403.34	457	0.20	1.11	0.09	0.15	0.10	1110	90	0.10
22X-3, 129–136	431.69	452	0.03	0.46	0.20	0.06	0.04	0	666	0.03
22X-4, 125–132	433.15	449	0.04	0.57	0.21	0.07	0.05	0	525	0.04
22X-6, 145–150	436.35	416	0.14	0.57	0.41	0.20	0.05	91	66	0.62
25H-1, 43–50	458.83	448	0.16	0.77	0.31	0.17	0.07	145	58	0.53
25H-2, 35–42	460.25	451	0.11	0.65	0.33	0.14	0.06	162	82	0.40

Notes: S_1 and S_2 in milligrams hydrocarbons per gram of dry sediment, S_3 in milligrams carbon dioxide per gram of dry sediment; PI = production index; PC = pyrolyzed carbon, HI = hydrogen index; OI = oxygen index; TOC = total organic carbon. Depths determined for Core 156-949B-14X are "curatorial" depths (see "Operations" section, this chapter).

probably also because less time was available to develop diffusion profiles in this section for all the chemical components, regardless of their diffusion coefficients.

Throughout the entire section drilled, the Mg/Ca ratios are below 0.9 (Table 20; Fig. 38C), which is outside the stability field of dolomite. This, together with the oxidation state at this section, could explain the presence of manganese carbonates, such as rhodochrosite and kutnahorite, in the veins above the décollement, instead of the more common diagenetic carbonates, for example, dolomite or siderite (see "Structural Geology" section, this chapter).

Figure 38D indicates that the diagenetic Ca and Mg(+Na) exchange reactions differ in lithologic Unit I through Subunit IIB in the accretionary complex, from those in Subunit IIC and in Unit III in the décollement and underthrust section (see "Lithostratigraphy and Sedimentology" section, this chapter). In the former, the exchange reaction Ca ↔ Mg dominates, while in the latter the exchange reaction Ca ↔ Mg + Na becomes more important. The increased role of Na in the diagenesis of the sediments with burial depth may have been caused by a decrease in the amount of admixed volcanic ash and/or by an increase in temperature. The sediment of Core 156-949B-22X, at 430–435 mbsf, however, is geochemically more similar to that of the accretionary complex Subunit IIB sediments rather than to the underthrust sediments. Interestingly, a fault zone marks this interval (see "Structural Geology" section, this chapter), and the dissolved-Cl profile (Fig. 37A) indicates the presence of a fluid conduit along this fault.

Sulfate, Ammonia, and Alkalinity

At this site, as well as at Site 948, sulfate reduction is incomplete in the depth intervals drilled, most likely because of the very low sedimentation rates combined with the very low total organic carbon (TOC) content, mostly <0.2 wt%, and probably also because of the nature of the organic matter (see "Organic Geochemistry" section, this chapter). Except for the reversal in dissolved sulfate concentrations at the fault in Core 156-949B-6X, sulfate concentrations decrease only slightly between 240 and 360 mbsf (Fig. 39A). Below the thrust fault at ~360 mbsf (see "Structural Geology" section, this chapter), the dissolved-sulfate concentration profile is diffusional and sulfate decreases linearly with depth. This implies the existence of a much more depleted dissolved-sulfate horizon, even possibly a zero sulfate horizon, at greater burial depth. Extrapolation to zero sulfate concentration is ~320 m deeper, at 770 mbsf, just above oceanic basement. As at Site 948, sediments having higher concentrations of organic matter probably exist at greater depth.

The thrust fault at ~360 mbsf, which is also a fluid conduit, as clearly seen in the dissolved-Cl profile (Fig. 37A), seems to act as a geochemical boundary not only for dissolved sulfate, but also for dissolved ammonia and, especially, for alkalinity (Figs. 39B and -C, respectively). The considerably stronger gradient in dissolved-ammonia concentrations in the décollement and underthrust sections, lithologic Unit III, may be related to the change in clay mineralogy in this unit (see "Lithostratigraphy and Sedimentology" section, this chapter).

Although alkalinity increases linearly with depth below ~360 mbsf, the low overall alkalinity, only 25% of the expected alkalinity production by sulfate reduction alone, suggests close coupling among several diagenetic reactions that produce and consume alkalinity, as discussed in the "Inorganic Geochemistry" section, "Site 948" chapter (this volume).

Sodium, Potassium, and Lithium

Overall, the dissolved concentration-depth profiles of Na and Cl are similar, except between 370 and 430 mbsf, within the structurally defined décollement zone, where dissolved Na concentrations increase while dissolved Cl concentrations decrease with depth, as seen

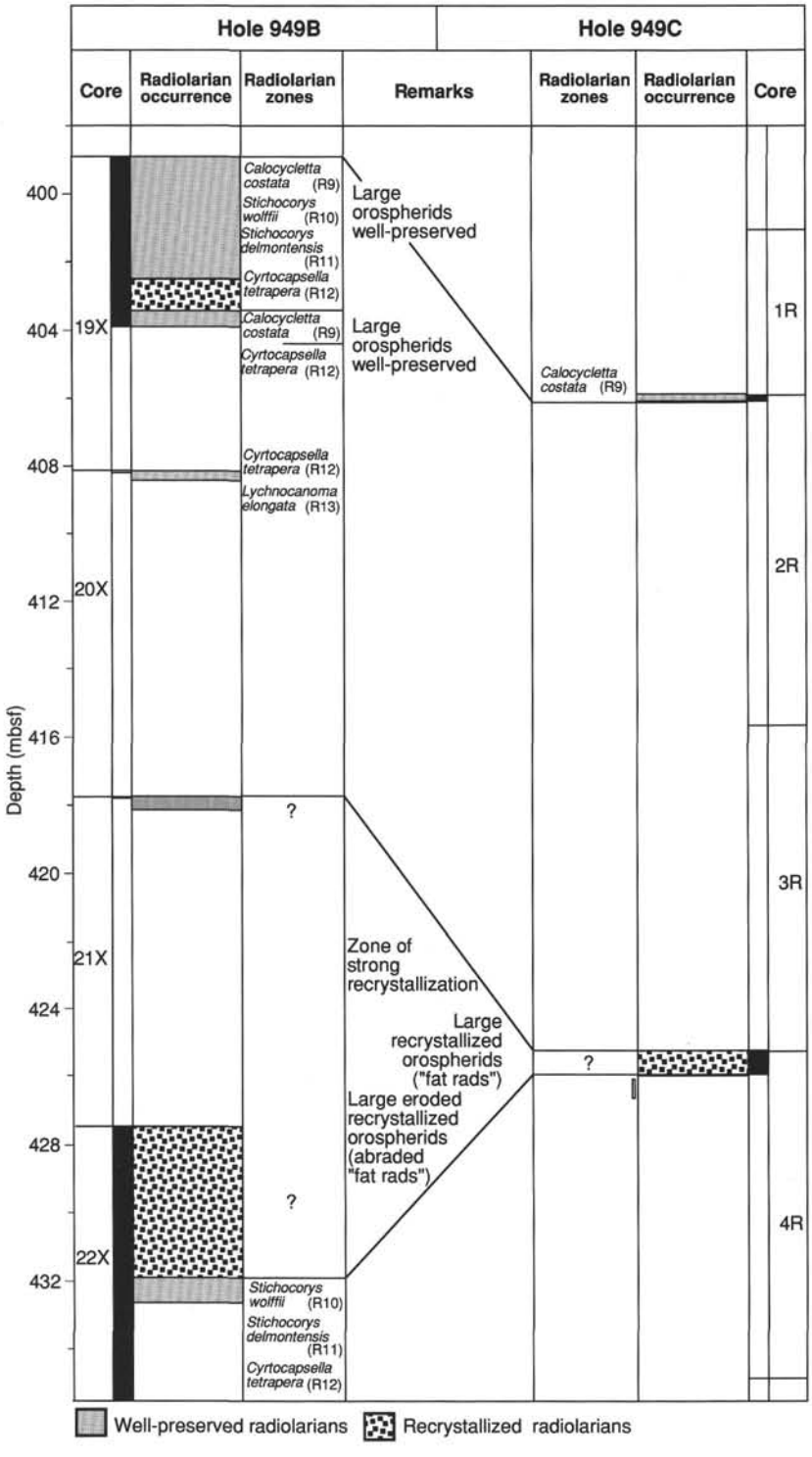

Figure 26. Comparison of biostratigraphic summaries of Holes 949B and 949C.

clearly in the Na/Cl depth profile of Figure 40B. Unlike Cl, the nonconservative behavior of Na is important for unraveling diagenetic processes. The observed increases in Na concentrations are significant, because within this same depth interval some Na is consumed by the diagenetic exchange reaction between Ca and Mg + Na, discussed above. Ion exchange with ammonia is most likely the responsible reaction for the increase in dissolved-Na concentrations within this depth interval, where the dissolved-ammonia concentration profile is steepest (see Fig. 39B). Dissolved-K concentrations, however, are almost constant at the same depth interval (Fig. 40C), as also indicated by the K/Cl ratios. Potassium concentrations are low throughout the section, at about 35% to 40% of seawater dissolved-K concentration. As with Mg, K is being consumed by volcanic-matter alteration reactions at low temperatures.

The observation that Li concentrations increase with depth (Fig. 40D) is most interesting, because at low temperatures Li is taken up by alteration of both volcanic ash and oceanic basement. However, at moderate and high temperatures, it is released into the fluid phase. Although

Table 20. Interstitial-water chemical data of major constituents, Holes 949A, 949B, and 949C.

Core, section, interval (cm)	Depth (mbsf)	IW volume (mL)	pH	Alk. (mM) (Gran.)	Sal. (Refr.)	Cl^- (mM) (Titrn.)	Ca^{2+} (mM) (Titrn.)	Mg^{2+} (mM) (Titrn.)	Mg/Ca	SO_4^{2-} (mM) (IC)	NH_4^+ (μM) (Spec.)	SiO_2 (μM)	Li^+ (μM) (AES)	K^+ (mM) (AES)	Na^+ (mM)	Na/Cl	Mn^{2+} (μM) (AES)
156-949A-																	
1H-1, 143-150	1.5	65	7.44	2.99	35.1	559	11.2	51.5	4.61	28.2	17	485	31.0	10.9	482	0.86	2.0
156-949B-																	
1X-1, 120–150	245.5	19	7.31	0.80	33.0	539	37.7	32.4	0.86	16.5	231	137	59.5	4.1	429	0.80	82.3
2X-3, 00–040	257.0	15			33.5	547	38.0	32.6	0.86	16.1	220	161	68.0	4.1	434	0.79	131.1
2X-5, 110–150	261.1	10			33.8	547	38.3	31.5	0.82	16.3		152	73.0	4.2	436	0.80	132.5
3X-5, 110–150	270.8	15	7.43	1.23	33.8	545	38.2	31.6	0.83	15.8	209	156	81.0	4.1	434	0.80	148.5
4X-1, 125–150	274.5	6			33.8	542	38.3	31.5	0.82	16.0	235	151	85.0	3.9	430	0.79	146.3
5X-2, 110–150[a]	285.6	19			33.2												
5X-4, 110–150	288.6	9			32.8	535	38.1	30.6	0.80	16.0	235	252	89.0	3.9	426	0.80	195.4
7X-2, 110–150	304.9	30	7.45	0.53	35.0	563	37.7	27.5	0.73	17.4	272	184	39.0	4.9	463	0.82	72.8
7X-6, 110–150	310.9	24	7.26	0.63	34.0	549	38.2	27.7	0.72	17.1	261	201	39.0	4.5	448	0.82	94.7
13X-1, 110–150	351.5	19	7.60	0.72	33.8	544	39.0	29.7	0.76	16.2	261	139	72.0	4.3	435	0.80	112.1
14X-2, 0–40[a,b]	355.8	19			34.0	547											
14X-5, 110–150	358.6	9			32.7	530	38.5	30.3	0.79	16.4	249	134	82.0	4.1	421	0.79	128.1
15X-2, 110–150	362.7	18	7.60	1.23	33.5	541	40.2	30.3	0.75	16.0	250	157	86.0	4.0	429	0.79	163.8
15X-5, 110–150	367.2	18	7.65	1.16	33.5	538	39.5	30.0	0.76	15.7	260	164	94.0	4.1	428	0.79	155.1
17X-CC, 2–8	378.6	3			33.0	535	43.0	34.4	0.80	15.2		267		3.8	407	0.76	176.6
19X-2, 60–100	401.1	16	7.31	1.74	32.2	532	38.7	34.3	0.89	15.0	190	1154	167.0	3.9	414	0.78	546.1
22X-2, 110–150[a]	430.2	19			34.2												
22X-5, 110–150	434.7	23	7.49	2.35	32.5	540	37.8	32.3	0.85	14.0	314	267	190.0	3.9	427	0.79	228.1
25H-3, 110–150	460.7	29	7.74	2.83	34.8	559	41.6	36.0	0.87	12.3	363	140	207.0	3.3	428	0.77	56.8
156-949C-																	
2R-CC, 5–10	415.0	2			32.8	530											
4R-1, 0–4	425.2	2			32.2	527											
6R-CC, 8–15[c]	453.6	4			34.0	546	37.2	34.6	0.93	16.2							
7R-1, 80–90	455.0	34			34.4	563	40.1	35.3	0.88	12.7							

Notes: Abbreviations for methods used: Gran. = Gran titration; Refr. = hand-held refractometer; Titrn. = titration; IC = ion chromatograph; Spec. = spectrophotometer; AES = atomic emission spectrometry; AAS = atomic absorption spectrometry. Sub-bottom depths for Core 156-949B-14X are "corrected" depths (see "Operations" section, this chapter).

[a] He samples.

[b] Some extra sample available.

[c] Contaminated by drill water.

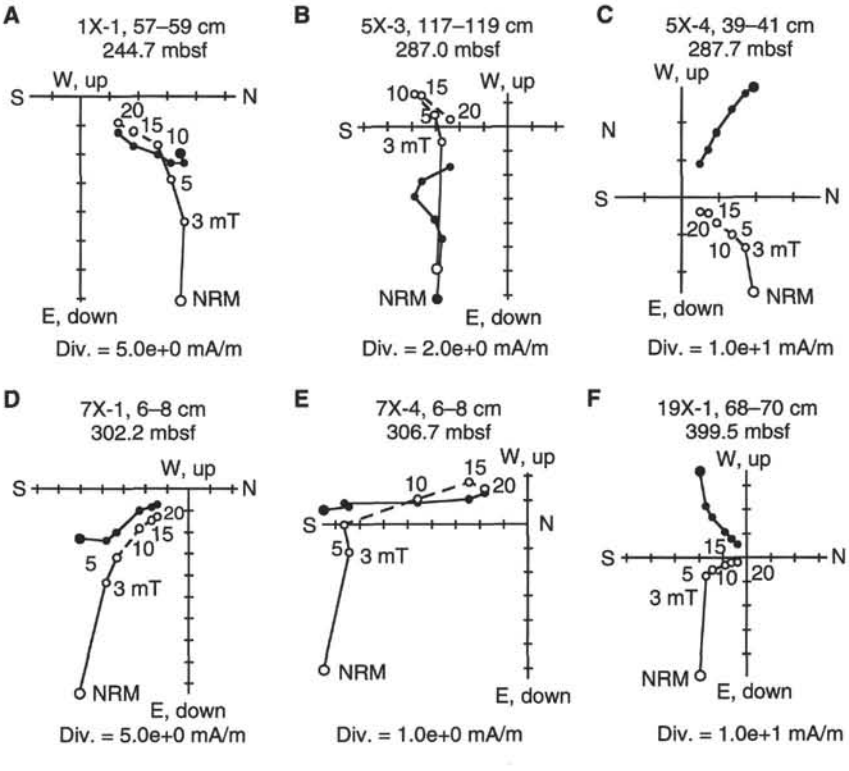

Figure 27. Orthogonal vector projections of demagnetization behavior of representative discrete samples from Hole 949B. Solid circles = projections of the remanence vector on the horizontal plane; open circles = projections of the remanence vector on the vertical plane. The intensity of remanence (mA/m) of each axis is denoted, and the AFs used for each demagnetization step are given next to the open circles. Samples in **A**, **C**, **D**, and **F** have normal polarity after removal of the drilling overprint by the 5-mT step. Samples **B** and **E** have reversed polarity.

the exact crossover temperature is not known as yet, it is at or below 70°C. The concentration-depth profile of Figure 40D thus may suggest that the crossover temperature is at about 30°C. But if this were so, Li production within the section drilled would be linear with depth, which is most unlikely diagenetically. Alternatively, and more likely, the dissolved-Li concentration-depth profile provides the only clear indication of communication with oceanic basement at this site. Based on a geothermal gradient of 8°C/100 m (see "In Situ Temperature Measurements" section, this chapter), the temperature at the sediment/oceanic basement interface beneath this site should be approximately 80°C, which is higher than the crossover temperature for Li release from clay minerals, oceanic basement, or volcanic-ash alteration.

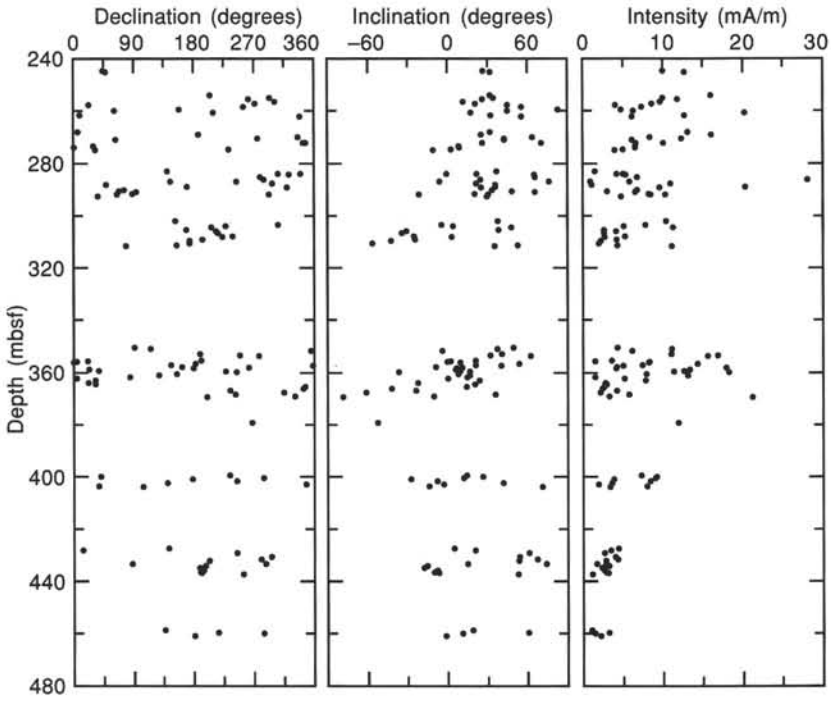

Figure 28. Remanence results vs. depth from the Hole 949B discrete samples after 20-mT AF demagnetization.

Silica and Manganese

The dissolved-silica and -manganese concentration-depth profiles are similar to the corresponding profiles at Site 948 (see "Inorganic Geochemistry" section, "Site 948" chapter, this volume). Silica concentration is high immediately below the décollement seismic reflection at ~400 mbsf (see "Vertical Seismic Profiles" section, this chapter) in the radiolarian-rich claystone of Subunit IIE (see "Lithostratigraphy and Sedimentology" section, this chapter) (Fig. 41A). The Si concentration is identical to that observed at Site 948 in Unit I, 140 µM (Table 20), indicating saturation with respect to amorphous silica (opal-A) solubility at the ambient temperature.

The maximum dissolved-Mn concentration of 612 µM (Fig. 41B), at the same depth as maximum Si concentration, mostly reflects a depositional feature, as discussed in the "Inorganic Geochemistry" section, "Site 948" chapter (this volume). As seen in Figure 41C, the Mn/Si depth profile has two maxima that correspond to the depth intervals of the two most distinct Cl minima at this site, at ~360 and ~425 mbsf (Fig. 37A), and is elevated at the low-Cl horizon above the main thrust fault, at ~300 mbsf.

Thrust Fault

Matching chemical-concentration reversals in the depth range of 250 to 360 mbsf (see Figs. 37–41) suggests a vertical displacement of about 80 m across the thrust fault located at ~300 mbsf (see "Vertical Seismic Profiles" section, this chapter). The concentration-depth profiles across the fault are mostly symmetrical, suggesting that in situ diagenetic reactions have not altered the pre-fault interstitial-water chemistries as yet, and that the sediment emplacement from deeper in the section above the lower Pliocene sediments of Core 156-949C-7X (see "Biostratigraphy" section, this chapter) has been recent enough so that diffusive exchange did not erase the original geochemical signatures. Assuming that the vertical gradients of the various parameters measured in this section do not change laterally, preliminary calculations of a sediment diffusion coefficient of 5.4×10^{-6} cm^2/s, based on the resistivity logging data at Site 948, together with porosity and temperature data at this site (see "Downhole Logging" section, "Site 948" chapter, this volume, and "Core Physical Properties" and "In Situ Temperature Measurements" sections, this chapter) indicate that the fault is younger than 36,000 yr.

Mechanical Continuous Fluid Sampler

The mechanical continuous fluid sampler (MCFS) was deployed at Hole 949C by attaching it to the thermistor string within the décollement zone (see "Operations" section, this volume). A schematic diagram of the MCFS is shown in Figure 42. The objective for deploying the MCFS was to continuously obtain in situ formation fluid for about 2 yr over the period of deployment of the CORK string. The heart of the MCFS is the osmotic pump, a semipermeable membrane filled with a salt-saturated solution. Water diffusing across the membrane creates a negative pressure gradient in the annulus surrounding the membrane, thereby pulling fluid through the sample tube. By using a constant osmotic pressure differential across a rigid, semipermeable membrane, a constant flow rate through the capillary sample tube is maintained. This is achieved by having a sufficiently large reservoir of NaCl on the high-salinity side to keep it NaCl-saturated, thus maintaining a constant osmotic pressure gradient. The flow rate of the pump is calibrated to fill the capillary tube by the end of the deployment. The capillary tubing used is of 0.8-mm internal diameter (to allow clay and fine silt particles through) and 400 m long, a length sufficient to contain the fluid pumped for more than 2.1 yr. The tubing is attached to the low-pressure side of the osmotic pump and has been wound onto modular sample coil assemblies, each containing 100 m of tubing; the assemblies are connected in series to one another. Thus, this modular system consists of pumps, sample coils, and connections.

The capillary tubing was pre-filled with degassed distilled water. As this water will be drawn into the osmotic-pump housing, maintaining the pressure differential, fluid from the décollement horizon will be drawn into the capillary tubing, replacing the distilled water. The calculated constant pumping rate will yield a time series of the formation fluid sampled over the length of the capillary tubing.

Upon retrieval, the filled capillary sample tubing will be divided into sections containing 3.5–5.1 mL representing 2–3-week intervals and analyzed as discrete samples for various major, minor, and trace

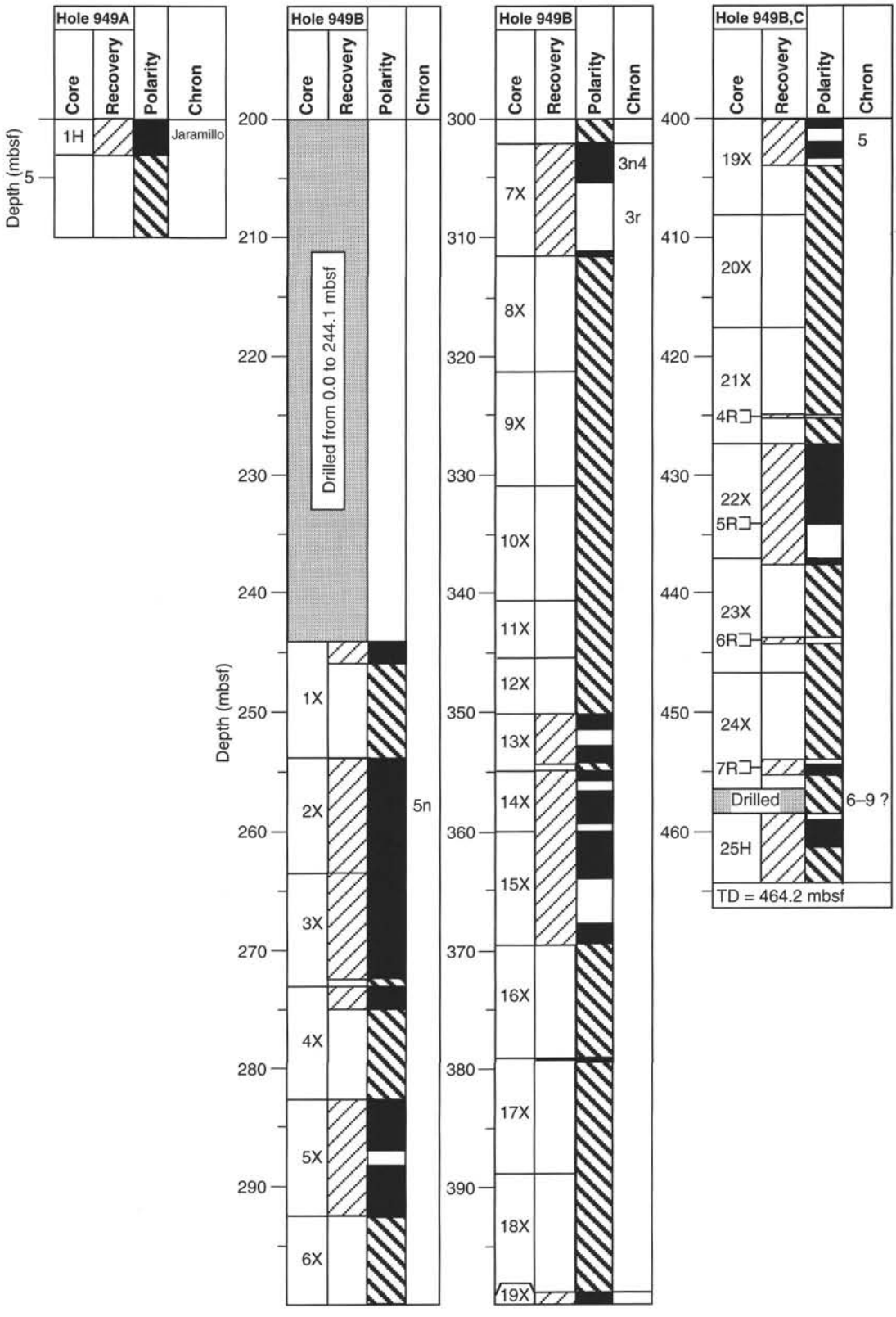

Figure 29. Summary magnetostratigraphy for Site 949. Black intervals denote normal polarity, white intervals reversed polarity, and the heavily striped intervals polarity of indeterminate nature. All XCB cores are from Hole 949B, and all RCB cores are from Hole 949C. The interval from 305.6 to 311 mbsf within Core 156-949B-7X has been assigned to Chron 3r (5.05–5.7 Ma).

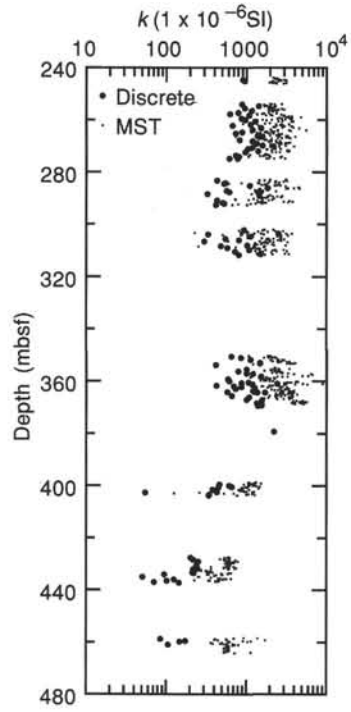

Figure 30. Magnetic susceptibility from the MST (small dots) and from discrete samples (solid circles). Susceptibilities have been plotted in 1×10^{-6} SI volume units. High ($>1 \times 10^{-3}$ SI units) susceptibilities characterize lithologic Unit II, while Unit III is characterized by much lower susceptibilities.

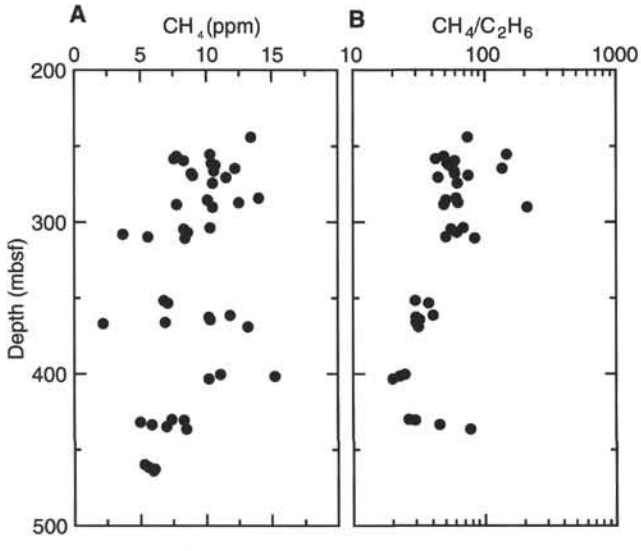

Figure 31. Results of headspace gas analyses vs. depth in Hole 949B. **A.** Methane. **B.** Methane/ethane ratio.

chemical components and isotopic compositions. At 37°C, the temperature at the décollement at this site, the osmotic pump will draw in 88 mL of fluid per year.

CORE PHYSICAL PROPERTIES

Introduction

The objective of the physical properties group for Site 949 was to provide a comprehensive downhole profile of measurements from the lower part of the accreted section through the décollement into the top of the underthrust section. This information was expected to be important for selecting a suitable interval for the screened casing (see "Background and Scientific Objectives" section, this chapter). This goal could not be accomplished owing to the very low core recovery. Our data set is limited to a series of windows over small depth intervals, precluding any detailed analysis of the downhole trends in physical properties. Still, this will be expected to serve as a background for evaluating thermal and chemical measurements from the instrumented hole over the next several years. The physical-property data set from this site adds to the existing geotechnical database available from DSDP Leg 78A and ODP Leg 110 and, together with post-cruise studies, will eventually help to constrain the consolidation history of sediment in the early stages of accretion.

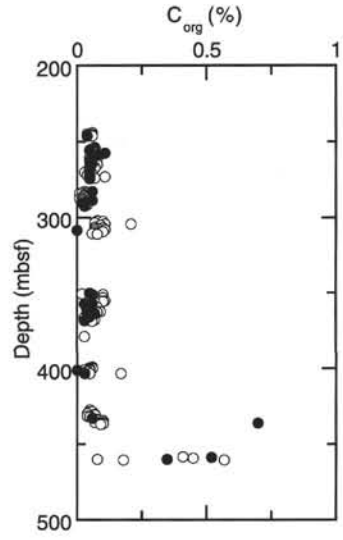

Figure 32. Organic carbon content, determined as total carbon minus carbonate carbon by Coulometric analysis, vs. depth in Hole 949B. Open circles = samples for physical properties and interstitial water. Solid circles = samples for organic geochemical analyses. Depths determined for Core 949B-14X are "curatorial" depths (see "Operations" section, this chapter).

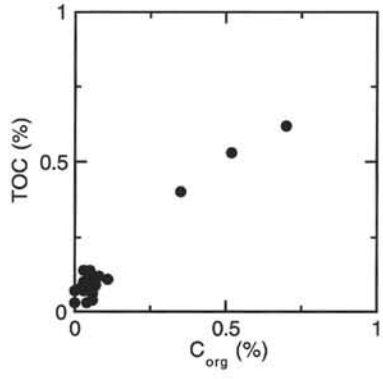

Figure 33. Crossplot of organic carbon content determined by two methods in Hole 949B: total carbon minus inorganic carbon (TC – IC) and Rock-Eval (TOC).

Density and Porosity

Because of the generally poor quality of the GRAPE data from XCB cores, and particularly of those collected at Site 948, the GRAPE device was turned off for all MST measurements on Site 949 cores. The discontinuous core recovery at Site 949 precludes any interpretation of downhole trends for most of the index-property measurements performed on core sediment samples.

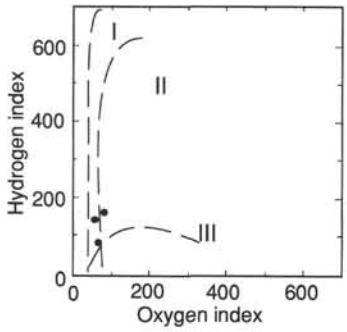

Figure 34. Hydrogen and oxygen indices (HI and OI) obtained from Rock-Eval analyses of samples from Hole 949B, plotted on a modified van Krevelen diagram (Tissot and Welte, 1984). Kerogen type: I = highly oil prone; II = oil prone; III = gas prone.

The Hole 949A mud-line core showed bulk densities increasing from 1.4 to 1.5 g/cm^3 and porosities decreasing from 77% to 70% over a 2-m interval (Table 21; Fig. 43A, -C). Over the depth interval from 244 to 292 mbsf (Cores 156-949B-1X through -5X), a decrease in bulk density from an average of 1.72 to 1.63 g/cm^3 coincides with an increase in porosity from 60% to 66% (Fig. 43B, -D). The observed trend in density and porosity is sharply offset in Core 156-949B-7X (302–311 mbsf), which is characterized by an average bulk density of 1.86 g/cm^3 and an average porosity of 55%. This offset is probably related to a structural discontinuity that occurs between 290 and 300 mbsf (see "Structural Setting" chapter, this volume, and "Biostratigraphy" section, this chapter).

The index-property data set for the remainder of the cored section in Holes 949B and 949C is characterized by an apparently linear downhole trend of increasing bulk density and decreasing porosity that extends over large gaps in recovery in the section. This apparent continuity is probably an artifact of the sparse data record.

Between 350 and 369 mbsf (Cores 156-949B-13X through -15X), bulk density ranges from 1.59 to 1.85 g/cm^3, with an average of 1.68 g/cm^3, while porosity ranges from 59.2% to 69.5%, with an average of 64.8%. Core 156-949B-19X sampled the upper part of the décollement zone and has an average bulk density of 1.70 g/cm^3 and an average porosity of 61.6%; Cores 156-949B-22X and -23X at the lower boundary of the décollement zone have an average bulk density of 1.90 g/cm^3 and an average porosity of 55.4%. Cores 156-949B-25H and 949C-4R through -7R represent the top of the underthrust section with an average bulk density of 1.90 g/cm^3 and an average porosity of 52.1%.

Compressional-wave Velocity

P-wave velocity was measured at this site using the digital sonic velocimeter (DSV) and the Hamilton Frame velocimeter (see "Explanatory Notes" chapter, this volume).

Both measurements of *P*-wave velocity obtained from the mud-line core in Hole 949A using the DSV (1432 and 1481 m/s) showed velocities well below those found at similar depths in Hole 948B (Table 22). These measurements are likely to be faulty, resulting from Core 156-949A-1H having been unevenly split, which made it difficult to insert both DSV transducers completely into the sediment.

As with all other shipboard data sets, the velocity data display a discontinuous downhole profile related to the poor recovery in Hole 949B. The velocity data set can be divided into three continuous groups of measurements (Table 22; Fig. 44B). The longest coherent downhole record extends from 244 to 311 mbsf (Cores 156-949B-1X through -7X) and has velocities that range from 1532 to 1629 m/s. Despite large scatter, a slight downhole increase in the average velocity is evident.

Between 350 and 369 mbsf (Cores 156-949B-13X through -15X), velocities vary from 1522 m/s in the shallower part to 1608 m/s in the deeper part of the interval, delineating a moderately scattered trend of increasing velocity with depth. The limited recovery within the presumed décollement zone between 390 and 445 mbsf allowed us to obtain only a few *P*-wave measurements. Data from Core 156-949B-19X in the upper part of this zone range from 1525 to 1554 m/s over an interval of only a few meters. Velocities in Cores 156-949B-22X and -23X at the bottom of the décollement zone are significantly higher, ranging from 1576 to 1684 m/s.

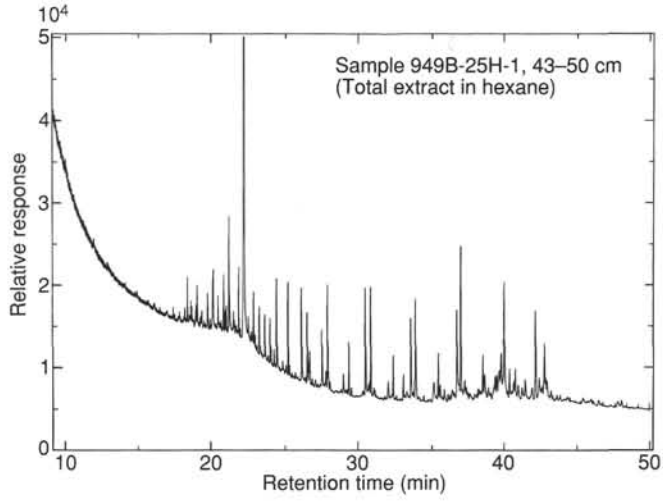

Figure 35. Gas chromatogram of total extract of Sample 156-949B-25H-1, 43–50 cm, in hexane.

Only two reliable *P*-wave measurements were obtained in the top of the underthrust sediments (in Cores 156-949B-25H and 949C-7R), yielding an average velocity of 1618 m/s, comparable to those determined in Hole 948C at the same stratigraphic position.

The downhole profile of transverse *P*-wave anisotropy displays an equally large degree of scatter without an apparent trend throughout all cored intervals in Hole 949B (Fig. 44F). The scatter is largest in the topmost interval (Cores 156-949B-1X through -7X), with anisotropy ranging from –3.76% to 5.14%. It ranges from –1.7% to 2.3% in Cores 156-949B-13X through -15X, from –2.2% to 3.57% within the décollement zone, and from 0.1% to 5.4% in the underthrust section.

The downhole acoustic-impedance profile based on the longitudinal compressional-wave velocities from Hamilton Frame measurements (Fig. 44H) clearly delineates a trend of decreasing values in most of the uppermost interval: from an average 2.6 (at 244 mbsf) to an average of 2.45 Mg/m^{2}s · 10^3 (at 292 mbsf). With an average value of 2.77 Mg/m^{2}s · 10^3 in Core 156-949B-7X, a large impedance contrast occurs between 292 and 300 mbsf. Cores 156-949B-14X and -15X again display a lower average impedance of 2.47 Mg/m^{2}s · 10^3. Another impedance contrast is found again within the décollement zone, with an average value of 2.51 Mg/m^{2}s · 10^3 at the top and 2.87 Mg/m^{2}s · 10^3 at the bottom of this zone.

Shear-wave Velocities

The mud-line core indicates low shear-wave velocities (36–41 m/s) and anisotropy, with horizontal velocities faster than vertical (Table 23). The deeper cores show velocities of 500 to 900 m/s, with no evidence of consistent anisotropy (Table 24; Fig. 44E). Low velocities coincide with high bulk densities (Fig. 43B).

Thermal Conductivity

Thermal conductivity data were collected from unsplit cores once per section. After the cores were split, drilling disturbance at the measurement points was checked. Measurements performed on small biscuits or drilling-disturbed sediment tended to be low and were discarded. Higher values obtained from the "flow-in" sections of Core 156-949B-25H may be the result of mechanical consolidation during flow-in and also were discarded.

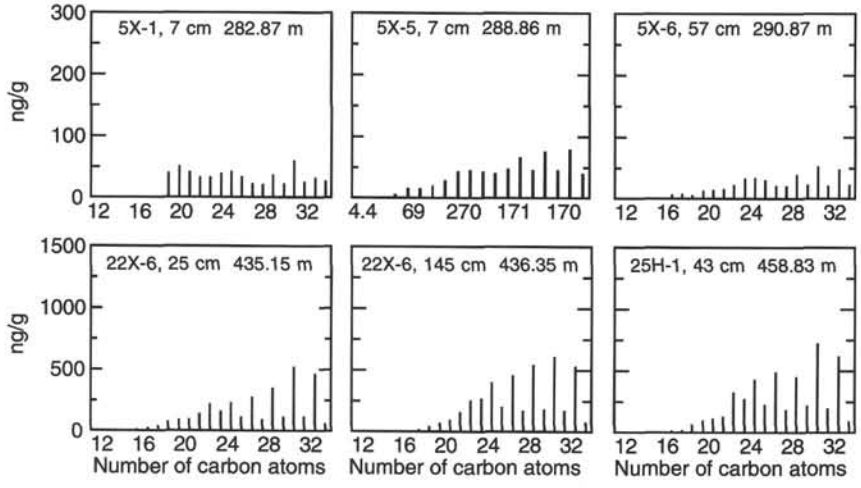

Figure 36. Concentrations of *n*-alkanes in Hole 949B sediments (ng/g), based on GC flame ionization detector (FID) analysis of total sediment extracts. Note the two different scales on the *Y* axes.

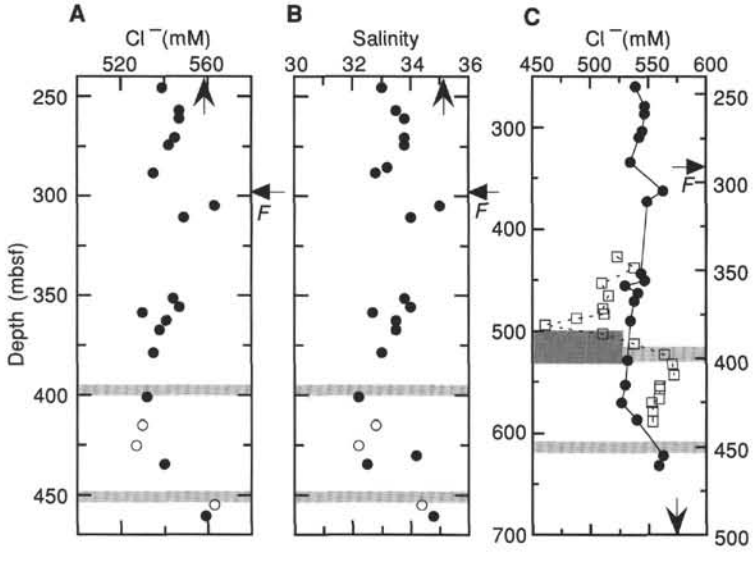

Figure 37. Concentration-depth profiles of (**A**) Cl; (**B**) salinity; and (**C**) Cl at Sites 948 and 949. Hole 949B data are represented by solid circles, Hole 949C data by open circles, and Site 948 data by open squares. In all plots, the arrow indicates seawater concentration, the arrow plus *F* indicates the major thrust fault intercepted, and the light-gray shaded areas delineate the depth intervals of the two negative-polarity seismic reflections; the upper one is the décollement reflector. The darker shaded area delineates the décollement zone at Site 948.

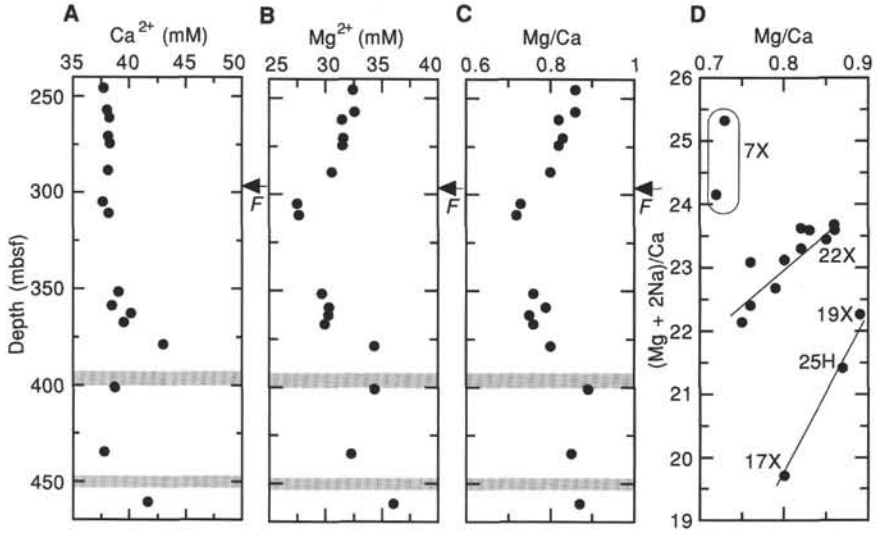

Figure 38. Concentration-depth profiles of (**A**) Ca; (**B**) Mg; (**C**) Mg/Ca; and (**D**) Mg + 2Na/Ca vs. Mg/Ca. For explanation of shaded areas and arrows, see Figure 37 caption.

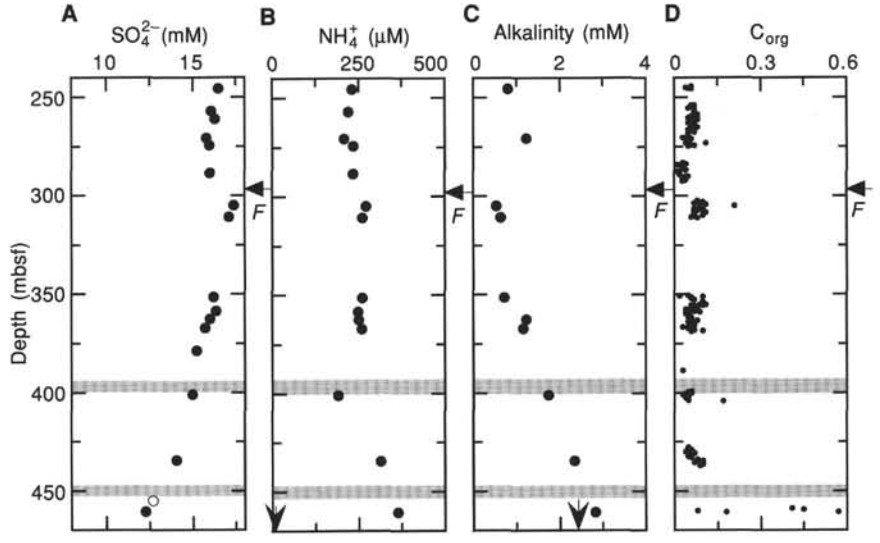

Figure 39. Concentration-depth profiles of (**A**) sulfate; (**B**) ammonia; (**C**) alkalinity; and (**D**) sediment organic carbon. For explanation of shaded areas and arrows, see Figure 37 caption.

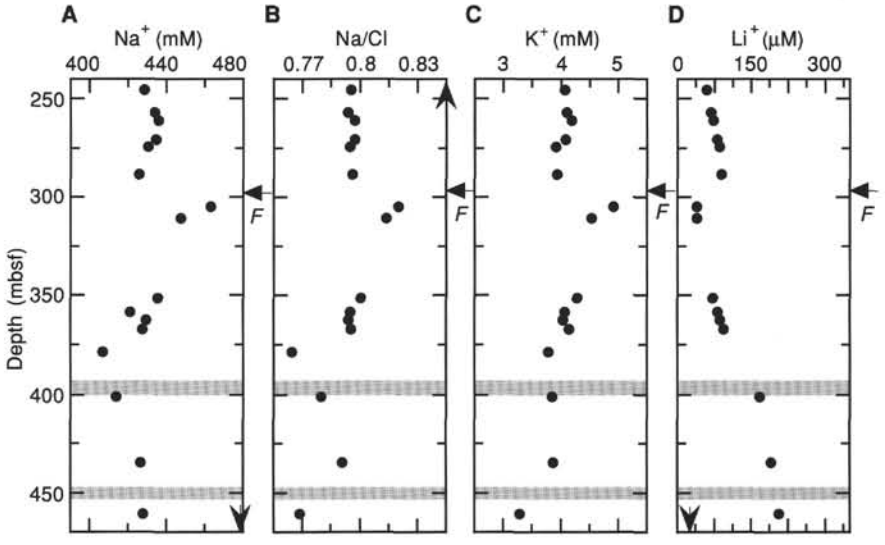

Figure 40. Concentration-depth profiles of (**A**) Na; (**B**) Na/Cl; (**C**) K; and (**D**) Li. For explanation of shaded areas and arrows, see Figure 37 caption.

Thermal conductivity values are given in Table 25 and have been plotted as a function of depth in Figure 45A. Thermal conductivity decreases with depth from about 1.17 W/(m·K) at 244 mbsf to about 1.08 W/(m·K) at 293 mbsf and is offset to higher values between 293 and 302 mbsf. Below 302 mbsf, data available are insufficient to define any obvious trends. Overall changes of thermal conductivity seem to correlate with porosity (Figs. 45B).

Resistivity and Formation Factor

The formation factor of mud-line Core 156-949A-1H averages 2.1. This value is higher than that obtained at Site 948, but may reflect the use of a different probe and an improved calibration technique, rather than a true change in sediment properties (see "Explanatory Notes" chapter, this volume).

Formation factors in Holes 949B and 949C range from 4 to 11 (Table 26). In lithologic Unit III, formation factors range from 6 to 11, and for a given porosity also tend to be higher than measurements at Site 948. The variation with depth follows some, but not all, of the porosity trends (Fig. 46). In particular, the decrease in formation factor between a depth of 260 and 290 mbsf correlates with the porosity increase in lithologic Subunit IIB, which is fairly homogeneous claystone. The formation factor also reflects lithologic changes; in particular, the base of calcareous lithologic Subunit IIB (Cores 156-

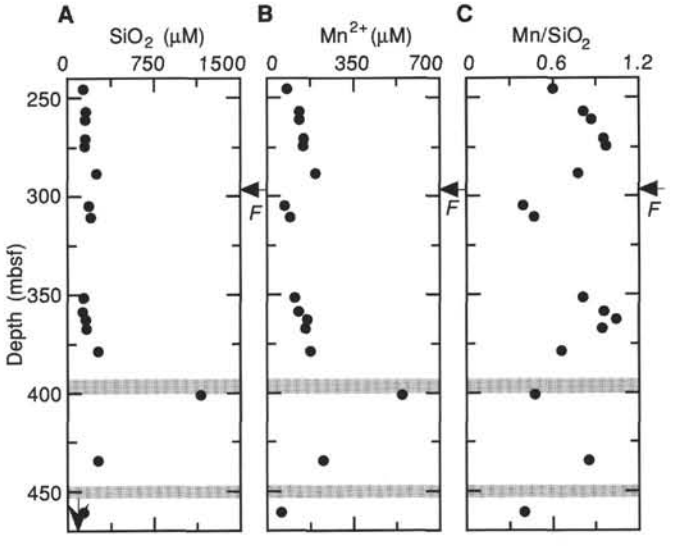

Figure 41. Concentration depth profiles of (**A**) silica; (**B**) Mn; and (**C**) Mn/SiO_2. For explanation of shaded areas and arrows, see caption to Figure 37.

Table 21. Index properties data for Holes 949A, 949B, and 949C.

Core, section, interval (cm)	Depth (mbsf)	Water content B (%wet wt)	Water content C (%dry wt)	Bulk density B (g/cm^3)	Bulk density C (g/cm^3)	Grain density (g/cm^3)	Dry density (g/cm^3)	Porosity (vol%)	Void ratio	Notes
156-949A-										
1H-1, 50–52	0.50	55.98	127.19	1.42	1.41	2.69	0.62	77.0	3.34	
1H-1, 100–102	1.00	55.61	125.28	1.42	1.41	2.65	0.62	76.4	3.24	
1H-2, 15–17	1.65	50.71	102.89	1.48	1.47	2.67	0.73	72.8	2.68	
1H-2, 117–119	2.67	48.10	92.69	1.51	1.49	2.60	0.78	70.2	2.35	
156-949B-										
1X-1, 36–38	244.46	36.60	57.72	1.75	1.68	2.65	1.06	59.9	1.49	
1X-1, 82–84	244.92	40.06	66.84	1.68	1.63	2.69	0.98	63.7	1.76	
1X-2, 18–20	245.78	36.90	58.49	1.75	1.66	2.61	1.05	59.9	1.49	
1X-CC, 26–28	246.20	37.82	60.81	1.71	1.67	2.69	1.04	61.5	1.60	
2X-1, 28–30	254.08	37.91	61.07	1.71	1.68	2.74	1.04	62.1	1.64	WR
2X-1, 60–62	254.40	44.49	80.13	1.60	1.56	2.67	0.86	67.6	2.09	WR
2X-1, 90–92	254.70	37.13	59.07	1.77	1.66	2.61	1.04	60.1	1.51	
2X-1, 139–141	255.19	39.75	65.97	1.74	1.62	2.63	0.98	62.8	1.69	
2X-2, 18–20	255.48	41.95	72.25	1.67	1.58	2.58	0.92	64.6	1.82	
2X-2, 72–74	256.02	41.10	69.78	1.68	1.61	2.69	0.95	64.7	1.83	WR
2X-2, 106–108	256.36	40.88	69.15	1.69	1.61	2.65	0.95	64.2	1.79	
2X-3, 65–67	257.45	34.73	53.21	1.81	1.72	2.68	1.12	58.2	1.39	
2X-4, 28–30	258.58	35.51	55.05	1.80	1.69	2.62	1.09	58.4	1.41	
2X-4, 143–145	259.73	38.68	63.07	1.78	1.63	2.61	1.00	61.6	1.60	
2X-5, 31–33	260.11	40.00	66.66	1.68	1.61	2.62	0.97	63.0	1.70	
2X-5, 81–83	260.61	43.48	76.92	1.64	1.56	2.61	0.88	66.2	1.96	
2X-6, 1–3	261.31	39.40	65.02	1.75	1.62	2.60	0.98	62.2	1.65	
2X-6, 24–26	261.54	37.68	60.46	1.74	1.67	2.71	1.04	61.5	1.60	WR
2X-6, 140–142	262.70	37.07	58.92	1.77	1.66	2.63	1.05	60.2	1.51	
2X-7, 18–20	262.98	41.85	71.97	1.68	1.58	2.58	0.92	64.4	1.81	
3X-1, 27–29	263.77	43.90	78.26	1.62	1.51	2.38	0.84	64.5	1.82	D
3X-1, 116–118	264.66	41.07	69.68	1.66	1.53	2.33	0.90	61.3	1.58	D
3X-2, 31–33	265.31	35.88	55.95	1.76	1.67	2.59	1.07	58.5	1.41	D
3X-2, 100–102	266.00	36.77	58.16	1.75	1.67	2.63	1.06	59.9	1.49	WR
3X-2, 140–142	266.40	39.72	65.89	1.71	1.61	2.60	0.97	62.6	1.67	
3X-3, 50–52	267.00	41.09	69.76	1.67	1.60	2.64	0.94	64.3	1.80	
3X-3, 110–112	267.60	42.43	73.69	1.69	1.57	2.59	0.90	65.0	1.86	
3X-4, 31–33	268.31	45.85	84.68	1.60	1.54	2.67	0.83	68.8	2.21	WR
3X-4, 113–115	269.13	43.94	78.38	1.63	1.53	2.52	0.86	65.8	1.93	
3X-5, 25–27	269.75	45.54	83.64	1.66	1.52	2.55	0.83	67.6	2.09	
3X-5, 86–88	270.36	40.19	67.20	1.74	1.60	2.56	0.96	62.7	1.68	
3X-6, 14–16	271.14	42.31	73.34	1.70	1.58	2.63	0.91	65.3	1.88	
3X-6, 63–65	271.63	42.14	72.83	1.67	1.56	2.54	0.90	64.3	1.80	
3X-CC, 10–12	272.24	48.20	93.06	1.60	1.50	2.66	0.78	70.7	2.42	
4X-1, 20–22	273.30	45.13	82.24	1.63	1.53	2.56	0.84	67.2	2.05	
4X-1, 108–110	274.18	41.19	70.03	1.72	1.62	2.74	0.95	65.2	1.87	
4X-2, 12–14	274.72	37.69	60.48	1.73	1.64	2.58	1.02	60.3	1.52	
5X-1, 35–37	283.15	49.25	97.05	1.55	1.50	2.70	0.76	71.9	2.56	
5X-1, 109–111	283.89	47.40	90.13	1.61	1.46	2.38	0.77	67.7	2.10	WR
5X-1, 133–135	284.13	48.17	92.94	1.56	1.50	2.62	0.78	70.4	2.38	
5X-2, 21–23	284.51	45.66	84.01	1.65	1.51	2.50	0.82	67.2	2.05	
5X-2, 84–86	285.14	45.23	82.60	1.62	1.55	2.67	0.85	68.3	2.16	
5X-3, 17–19	285.97	41.90	72.11	1.67	1.56	2.53	0.91	64.0	1.78	
5X-3, 111–113	286.91	41.93	72.22	1.67	1.58	2.58	0.92	64.5	1.82	
5X-4, 18–20	287.48	43.58	77.26	1.67	1.54	2.54	0.87	65.7	1.91	
5X-4, 43–45	287.73	44.39	79.81	1.67	1.52	2.47	0.84	65.8	1.92	WR
5X-4, 67–69	287.97	44.98	81.74	1.61	1.53	2.56	0.84	67.1	2.04	SF
5X-5, 42–44	289.22	44.03	78.67	1.65	1.53	2.48	0.85	65.6	1.91	
5X-5, 136–138	290.16	43.65	77.45	1.65	1.56	2.64	0.88	66.6	1.99	
5X-6, 23–25	290.53	45.59	83.80	1.61	1.54	2.65	0.84	68.5	2.17	
5X-6, 93–95	291.23	44.26	79.41	1.62	1.56	2.68	0.87	67.5	2.08	WR
5X-6, 104–106	291.34	46.41	86.59	1.60	1.52	2.64	0.82	69.1	2.23	
5X-6, 129–131	291.59	38.27	62.00	1.71	1.62	2.51	1.00	60.3	1.52	WR
5X-7, 11–13	291.91	43.44	76.80	1.64	1.57	2.68	0.89	66.7	2.01	
5X-CC, 18–20	292.46	42.63	74.31	1.66	1.58	2.66	0.91	65.8	1.93	
7X-1, 31–33	302.41	36.74	58.08	1.76	1.68	2.68	1.06	60.3	1.52	
7X-1, 86–88	302.96	28.13	39.14	1.92	1.85	2.71	1.33	50.9	1.04	
7X-2, 4–6	303.64	33.15	49.60	1.85	1.75	2.70	1.17	56.7	1.31	
7X-2, 76–78	304.36	33.05	49.37	1.83	1.75	2.68	1.17	56.3	1.29	
7X-3, 8–10	305.18	31.50	45.99	1.88	1.78	2.69	1.22	54.7	1.21	
7X-3, 24–26	305.34	30.05	42.96	1.91	1.80	2.68	1.26	52.9	1.12	WR
7X-3, 127–129	306.37	34.28	52.16	1.83	1.72	2.65	1.13	57.4	1.35	
7X-4, 32–34	306.92	31.03	44.99	1.88	1.79	2.69	1.23	54.2	1.18	
7X-4, 54–56	307.14	27.83	38.56	1.94	1.86	2.71	1.34	50.5	1.02	WR
7X-4, 81–83	307.41	33.73	50.90	1.81	1.73	2.68	1.15	57.1	1.33	
7X-4, 134–136	307.94	28.91	40.66	1.89	1.84	2.73	1.31	52.0	1.08	WR
7X-5, 25–27	308.35	31.58	46.17	1.86	1.78	2.71	1.22	55.0	1.22	
7X-5, 133–135	309.43	30.35	43.58	1.86	1.82	2.74	1.27	53.8	1.17	WR
7X-5, 136–138	309.46	31.63	46.27	1.85	1.79	2.73	1.22	55.2	1.23	
7X-6, 22–24	309.82	30.12	43.11	1.88	1.80	2.68	1.26	53.0	1.13	
7X-6, 62–64	310.22	31.72	46.46	1.89	1.76	2.65	1.20	54.6	1.20	WR
7X-7, 11–13	311.21	33.24	49.79	1.82	1.74	2.68	1.16	56.5	1.30	
13X-1, 18–20	350.38	42.39	73.57	1.66	1.59	2.66	0.91	65.6	1.91	
13X-1, 50–52	350.70	42.34	73.42	1.63	1.59	2.66	0.92	65.6	1.91	WR
13X-1, 98–100	351.18	36.97	58.65	1.77	1.67	2.64	1.05	60.2	1.51	
13X-2, 27–29	351.97	42.39	73.59	1.66	1.58	2.63	0.91	65.4	1.89	SF
13X-2, 88–90	352.58	38.25	61.94	1.72	1.67	2.72	1.03	62.2	1.65	
13X-3, 26–28	353.46	37.34	59.59	1.74	1.66	2.63	1.04	60.4	1.53	
14X-1, 39–41	355.29	37.86	60.93	1.73	1.67	2.72	1.04	61.8	1.62	SF
14X-1, 58–60	355.48	39.79	66.07	1.69	1.64	2.72	0.99	63.7	1.75	

Table 21 (continued).

Core, section, interval (cm)	Depth (mbsf)	Water content B (%wet wt)	Water content C (%dry wt)	Bulk density B (g/cm^3)	Bulk density C (g/cm^3)	Grain density (g/cm^3)	Dry density (g/cm^3)	Porosity (vol%)	Void ratio	Notes
14X-1, 105–107	355.95	40.49	68.03	1.66	1.61	2.63	0.96	63.6	1.75	WR
14X-1, 122–124	356.12	36.99	58.71	1.78	1.68	2.68	1.06	60.6	1.54	
14X-2, 69–71	357.09	42.92	75.19	1.64	1.57	2.61	0.89	65.7	1.91	WR
14X-2, 123–125	357.63	43.27	76.26	1.71	1.57	2.66	0.89	66.4	1.98	
14X-3, 48–50	358.38	43.40	76.69	1.65	1.56	2.60	0.88	66.1	1.95	
14X-3, 127–129	359.17	41.56	71.11	1.85	1.55	2.45	0.91	63.0	1.70	
14X-4, 16–18	359.56	44.32	79.59	1.67	1.55	2.62	0.86	67.1	2.04	
14X-4, 44–46	359.84	40.71	68.67	1.67	1.62	2.70	0.96	64.4	1.81	WR
14X-4, 77–79	360.17	44.82	81.21	1.60	1.53	2.57	0.85	67.0	2.03	WR
14X-4, 130–132	360.70	41.19	70.05	1.77	1.59	2.60	0.94	64.0	1.78	
14X-5, 41–43	361.31	45.60	83.82	1.63	1.54	2.64	0.84	68.4	2.16	
14X-5, 86–88	361.76	41.69	71.51	1.74	1.58	2.58	0.92	64.3	1.80	
14X-6, 22–24	362.62	36.46	57.39	1.75	1.66	2.59	1.06	59.2	1.45	
14X-6, 114–116	363.54	40.49	68.05	1.75	1.59	2.56	0.95	63.0	1.70	
14X-7, 10–12	364.00	41.34	70.47	1.66	1.61	2.68	0.94	64.8	1.84	
14X-CC, 10–12	364.53	44.77	81.07	1.62	1.55	2.66	0.86	67.8	2.10	
15X-1, 39–41	360.29	43.51	77.03	1.65	1.56	2.62	0.88	66.4	1.97	
15X-1, 144–146	361.34	42.04	72.54	1.68	1.60	2.69	0.93	65.6	1.90	
15X-2, 18–20	361.58	41.19	70.03	1.66	1.61	2.69	0.95	64.7	1.84	
15X-2, 94–96	362.34	38.72	63.19	1.77	1.64	2.66	1.01	62.1	1.64	
15X-3, 23–25	363.13	42.46	73.78	1.68	1.57	2.59	0.90	65.1	1.87	
15X-3, 99–101	363.89	42.14	72.82	1.63	1.59	2.66	0.92	65.4	1.89	WR
15X-3, 137–139	364.27	45.22	82.55	1.60	1.55	2.69	0.85	68.4	2.16	WR
15X-3, 148–150	364.38	43.81	77.96	1.64	1.57	2.66	0.88	66.9	2.02	
15X-4, 56–58	364.96	39.31	64.77	1.70	1.63	2.63	0.99	62.5	1.66	WR
15X-4, 60–62	365.00	39.62	65.61	1.71	1.65	2.74	0.99	63.7	1.75	
15X-4, 133–135	365.73	43.72	77.68	1.63	1.56	2.64	0.88	66.6	2.00	
15X-5, 28–30	366.18	46.10	85.54	1.59	1.54	2.73	0.83	69.5	2.28	WR
15X-5, 56–58	366.46	44.48	80.13	1.61	1.56	2.69	0.87	67.8	2.10	
15X-5, 75–77	366.65	44.48	80.13	1.61	1.54	2.58	0.86	66.9	2.02	WR
15X-5, 95–97	366.85	38.27	61.99	1.75	1.65	2.67	1.02	61.7	1.61	
15X-6, 9–11	367.49	41.29	70.34	1.69	1.60	2.67	0.94	64.7	1.83	
15X-6, 64–66	368.04	43.65	77.47	1.63	1.56	2.64	0.88	66.6	2.00	WR
15X-6, 119–121	368.59	43.16	75.93	1.64	1.57	2.61	0.89	65.9	1.94	WR
15X-7, 6–8	368.96	42.50	73.90	1.67	1.59	2.70	0.92	66.1	1.95	
19X-1, 49–51	399.29	38.61	62.91	1.71	1.66	2.70	1.02	62.4	1.66	WR
19X-1, 84–86	399.64	41.17	70.00	1.66	1.61	2.69	0.95	64.8	1.84	
19X-1, 135–137	400.15	37.17	59.16	1.73	1.66	2.61	1.04	60.1	1.51	
19X-2, 23–25	400.53	38.62	62.92	1.70	1.64	2.65	1.01	61.9	1.63	
19X-2, 47–49	400.77	37.98	61.25	1.72	1.63	2.56	1.01	60.5	1.53	WR
19X-3, 8–10	401.38	37.25	59.36	1.76	1.66	2.62	1.04	60.3	1.52	
19X-3, 49–51	401.79	36.31	57.00	1.74	1.66	2.58	1.06	58.9	1.44	WR
19X-3, 105–107	402.35	34.26	52.12	1.79	1.69	2.57	1.11	56.7	1.31	WR
19X-4, 48–50	403.28	43.05	75.59	1.63	1.57	2.62	0.89	65.9	1.93	
19X-4, 85–87	403.65	41.41	70.68	1.68	1.61	2.68	0.94	64.9	1.85	
22X-1, 31–33	427.71	33.80	51.06	1.79	1.72	2.63	1.14	56.7	1.31	
22X-1, 102–104	428.42	32.32	47.75	1.87	1.77	2.71	1.20	55.8	1.26	
22X-1, 145–147	428.85	32.93	49.10	1.80	1.76	2.71	1.18	56.5	1.30	WR
22X-2, 15–17	429.05	32.67	48.52	1.83	1.77	2.73	1.19	56.4	1.29	WR
22X-2, 102–104	429.92	31.67	46.35	1.89	1.75	2.60	1.20	54.1	1.18	
22X-3, 12–14	430.52	32.45	48.05	1.83	1.76	2.70	1.19	55.9	1.27	WR
22X-3, 27–29	430.67	32.56	48.29	1.84	1.77	2.72	1.19	56.2	1.28	
22X-3, 114–116	431.54	31.60	46.21	1.86	1.77	2.68	1.21	54.7	1.21	
22X-4, 53–55	432.43	31.31	45.59	1.83	1.79	2.73	1.23	54.8	1.21	WR
22X-4, 113–115	433.03	32.15	47.38	1.88	1.75	2.64	1.19	55.0	1.22	
22X-5, 47–49	433.87	32.91	49.06	1.83	1.74	2.65	1.17	55.9	1.27	
22X-5, 91–93	434.31	32.35	47.82	1.86	1.77	2.71	1.20	55.9	1.27	
22X-6, 73–75	435.63	32.47	48.07	1.88	1.76	2.70	1.19	55.9	1.27	
22X-6, 118–120	436.08	34.39	52.40	1.83	1.71	2.63	1.12	57.4	1.35	
22X-7, 13–15	436.53	26.45	35.96	1.95	1.89	2.70	1.39	48.7	0.95	
23X-CC, 2–4	437.12	32.24	47.58	1.89	1.77	2.72	1.20	55.8	1.26	
25H-1, 23–25	458.63	30.61	44.12	1.95	1.77	2.61	1.23	52.9	1.13	
25H-1, 96–98	459.36	28.23	39.34	1.97	1.84	2.66	1.32	50.6	1.02	
25H-2, 13–15	460.03	29.63	42.10	1.92	1.82	2.71	1.28	52.7	1.11	
25H-2, 69–71	460.59	25.30	33.87	1.98	1.92	2.73	1.43	47.4	0.90	
25H-2, 92–94	460.82	28.56	39.98	1.90	1.87	2.78	1.33	52.0	1.08	WR
156-949C										
4R-1, 11–13	425.31	32.82	48.85	1.84	1.76	2.70	1.18	56.30	1.29	
7R-1, 32–34	454.42	34.04	51.61	1.86	1.74	2.71	1.15	57.68	1.36	
7R-1, 46–48	454.56	31.72	46.46	1.89	1.79	2.74	1.22	55.44	1.24	
7R-1, 75–77	454.85	27.55	38.03	2.05	1.87	2.74	1.36	50.39	1.02	
7R-CC, 6–8	455.06	23.73	31.12	2.06	1.94	2.70	1.48	45.05	0.82	

Notes: B = from wet volume and wet weight; C = calculated using dry volume; WR = whole-round sample; D = drill breccia; SF = scaly fabric.

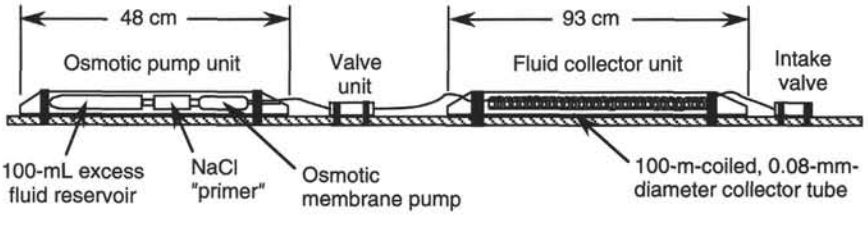

Figure 42. A schematic diagram of the MCFS.

Table 22. *P*-wave velocity measurements for Holes 949A, 949B, and 949C.

Core, section, interval (cm)	Depth (mbsf)	*P*–wave velocity (m/s)			Transverse anisotropy (%)	Acoustic impedance, longitudinal (MPa·s/m)
		V_{pl}	V_{pt1}	V_{pt2}		
156-949A-						
1H-2, 14–16	1.64	1481.2	1464.0	1464.0	–1.17	
1H-2, 120–122	2.70	1463.8	1432.0	1432.0	–2.20	2.19
156-949B-						
1X-1, 36–38	244.46		1600.0	1599.5		
1X-1, 82–84	244.92	1573.6	1531.0	1574.7	–1.31	2.56
1X-CC, 26–28	246.20	1579.7	1580.0	1582.6	0.11	2.63
2X-1, 139–141	255.19	1573.1	1505.0	1534.2	–3.47	2.55
2X-2, 18–20	255.48	1587.6	1576.0	1611.2	0.37	2.50
2X-2, 65–67	255.95	1541.5	1559.0	1617.4	3.00	2.48
2X-2, 106–108	256.36	1533.4	1545.0	1542.9	0.70	2.47
2X-5, 31–33	260.11	1566.2	1541.0	1559.7	–1.02	2.53
2X-5, 81–83	260.61	1557.7	1585.0	1585.4	1.74	2.43
2X-6, 140–142	262.70	1567.2	1542.0	1581.7	–0.33	2.61
2X-7, 18–20	262.98	1564.3	1528.0	1613.2	0.40	2.47
3X-2, 139–141	266.39	1583.0				2.55
3X-3, 50–52	267.00	1539.8	1559.0	1569.9	1.58	2.47
3X-3, 110–112	267.60	1531.7	1541.0	1540.5	0.57	2.41
3X-5, 86–88	270.36	1560.5	1543.0	1584.2	0.21	2.49
3X-6, 63–65	271.63	1570.1	1512.0	1512.1	–3.76	2.46
4X-1, 108–110	274.18	1547.2	1532.0	1539.9	–0.75	2.51
5X-1, 35–37	283.15	1555.4	1545.0	1548.3	–0.55	2.33
5X-1, 33–135	284.13	1583.3	1521.0	1569.8	–2.43	2.37
5X-2, 84–86	285.14	1539.9	1552.0	1470.2	–1.88	2.38
5X-5, 136–138	290.16	1549.4	1552.0	1568.2	0.68	2.42
5X-6, 23–25	290.53	1539.1	1574.0	1588.6	2.70	2.37
5X-6, 104–106	291.34	1562.4	1563.0	1552.3	–0.31	2.38
5X-7, 11–13	291.91	1542.8	1560.0	1575.9	1.61	2.43
5X-CC, 18–20	292.46	1578.0	1593.0	1601.7	1.23	2.50
7X-1, 31–33	302.41	1628.9	1593.0	1576.3	–2.77	2.74
7X-1, 86–88	302.96	1607.9	1625.0	1645.1	1.68	2.98
7X-2, 4–6	303.64	1551.9	1561.0	1560.8	0.57	2.72
7X-2, 76–78	304.36	1599.5	1583.0	1573.2	–1.36	2.79
7X-3, 8–10	305.18	1564.3	1557.0	1583.9	0.38	2.78
7X-3, 127–129	306.37	1584.6	1580.0	1554.2	–1.11	2.72
7X-4, 32–34	306.92	1560.8	1530.0	1561.6	–0.98	2.79
7X-4, 81–83	307.41	1567.2	1584.0	1572.1	0.68	2.72
7X-5, 136–138	309.46	1501.1	1574.0	1586.8	5.14	2.68
7X-6, 22–24	309.82	1570.4	1582.0	1604.2	1.43	2.83
7X-7, 11–13	311.21	1584.5	1535.0	1551.3	–2.64	2.76
13X-1, 18–20	350.38	1530.8	1581.0	1577.9	3.13	2.43
13X-1, 98–100	351.18	1557.8	1574.0	1572.0	0.98	2.60
13X-2, 27–29	351.97	1539.0	1539.0	1601.8	2.02	2.43
13X-3, 26–28	353.46	1522.2	1547.0	1537.8	1.30	2.52
14X-1, 122–124	356.12		1480.0	1556.8		
14X-3, 48–50	358.38	1531.8	1559.0	1572.3	2.18	2.39
14X-4, 16–18	359.56	1521.1	1532.0	1571.6	1.98	2.36
14X-5, 41–43	361.31		1552.0	1580.2		
14X-6, 114–116	363.54			1538.1		
14X-CC, 10–12	364.53	1608.4	1570.0	1590.4	–1.76	2.49
15X-1, 144–146	361.34	1570.8	1557.0	1561.2	–0.76	2.51
15X-2, 18–20	361.58	1564.0	1563.0	1585.3	0.66	2.52
15X-2, 94–96	362.34	1523.2	1572.0	1547.0	2.36	2.50
15X-3, 148–150	364.38	1551.9	1556.0	1567.7	0.63	2.43
15X-4, 60–62	365.00	1532.7	1561.0	1559.2	1.78	2.52
15X-4, 133–135	365.73	1568.1	1594.0	1548.2	0.20	2.45
15X-5, 56–58	366.46	1558.1	1582.0	1533.2	–0.04	2.43
15X-5, 95–97	366.85		1541.0	1569.1		0.00
15X-7, 6–8	368.96	1585.8	1606.0	1579.3	0.44	2.53
19X-1, 84–86	399.64	1558.6	1635.0	1595.6	3.57	2.51
19X-1, 135–137	400.15	1524.7	1563.0	1532.7	1.52	2.53
19X-2, 23–25	400.53	1568.4	1540.0	1528.5	–2.20	2.58
19X-3, 8–10	401.38	1528.6	1546.0	1531.9	0.68	2.54
19X-4, 48–50	403.28	1543.2	1533.0	1519.8	–1.08	2.42
19X-4, 85–87	403.65	1552.0	1548.0	1548.2	–0.25	2.49
22X-1, 102–104	428.42		1590.0	1589.8		
22X-3, 27–29	430.67	1578.4	1597.0	1599.6	1.26	2.79
22X-4, 113–115	433.03		1640.0	1640.3		0.00
22X-5, 47–49	433.87	1576.0	1590.0	1599.6	1.17	2.74
22X-5, 91–93	434.31	1596.3	1617.0	1624.4	1.52	2.83
22X-6, 118–120	436.08		1549.0	1549.3		
22X-7, 13–15	436.53	1683.7	1687.0	1695.0	0.43	3.17
23X-CC, 2–4	437.12	1610.0	1578.0	1584.2	–1.83	2.85
25H-2, 69–71	460.59	1609.1	1707.0	1677.2	5.03	3.09
156-949C-						
R7-1, 75–77	454.87	1622.0	1583.0	1658.0	–0.10	3.30
R7-CC, 6–8	455.06	1624.0	1727.0	1708.0	5.40	3.30

Table 23. *S*-wave measurements for Hole 949A.

Core, section, interval (cm)	Depth (mbsf)	Shear-wave velocity (m/s)	
		Horizontal	Vertical
156-949A-			
1H-1, 58–60	0.58	37.10	36.08
1H-1, 112–114	1.12	38.99	37.64
1H-2, 9.5–11.5	1.60	40.37	38.08
1H-2, 126.5–128.5	2.77	36.89	36.08

949B-2X and -13X) is associated with an increase from about 6 to about 7, while porosity remains constant.

Data from samples that cracked when penetrated by the probe were not plotted, but are still listed in Table 26. Sometimes, a quick and imprecise reading was possible before opening of the crack; in other cases, the final reading was recorded after opening of the crack. Core pieces brecciated by drilling have a resistivity lower than or, in some cases, equal to that of the remaining intact biscuits (tops of Cores 156-949B-3X and -14X).

Measurements performed in scaly fabric zones often plot outside the scatter of measurements from undisturbed sediment: sometimes above, sometimes below. A lower resistivity may simply mean that cracks opened in the foliation during drilling. The high values may indicate desaturation of open cracks; however, the readings were stable and reproducible, unlike those from specimens that cracked when the probe was inserted.

Shear Strength

Undrained shear strengths were measured on APC core samples from the mud-line core only (Table 27) because of sample disturbance and biscuit formation in XCB cores. Measurements of shear strength also were attempted with a pocket penetrometer on intact biscuits of XCB cores. However, the hardness of the sediments exceeded the measurable limit of the pocket penetrometer (maximum 220.65 kPa).

Natural Gamma Ray

Natural gamma-ray radiation (NGR) was recorded on cores from Holes 949A, 949B, and 949C at a sampling frequency of five per section and a sampling time of 30 s. Results are presented in counts per seconds (cps), with no background correction (see "Explanatory Notes" chapter, this volume).

The sparsity of data for Holes 949A (Fig. 47A, -C) and 949C precludes a detailed correlation of lithological variation and natural gamma-ray counts. Four well-defined intervals can be distinguished in Hole 949B (Fig. 47B). The first interval extends from 240 to 295 mbsf and is characterized by constant low values (20–25 cps) and high scatter. Between 300 and 320 mbsf (Core 156-949B-7X and -8X), the data average around 30 cps. From 350 to 370 mbsf (Core 156-949B-13X to -15X) and around 400 mbsf (Core 156-949B-19X), the data cluster around 20 to 25 cps. The two intervals around 430 mbsf (Cores 156-949B-22X and -23X) and 460 mbsf (Cores 156-949B-25H and 949C-7R) show an increase in the count rate from 35 to 40 cps.

The data from energy Window 3 (1.1–1.59 MeV), which can be attributed to the variations in potassium content, mirror closely the variations in the total counts (Fig. 47D). High-amplitude variations in the total count rate near 260 mbsf may reflect a thrust zone in that same interval (see "Structural Setting" chapter, this volume). Two other thrust or fault zones, identified at 350 and 430 mbsf based on structural information, correlate with high-amplitude variations in the count rate. The sharp increase in potassium content in the interval corresponding to Core 156-949B-22X, at 430 mbsf, may reflect a lithological change. Because of the absence of data, the décollement zone is not well defined. The data for uranium and thorium are uniform from 240 to 400 mbsf. Between 430 and 464 mbsf (Cores 156-949B-22X through -25H), uranium and thorium count rates increase slightly to 1 cps, as does that for potassium over the same interval.

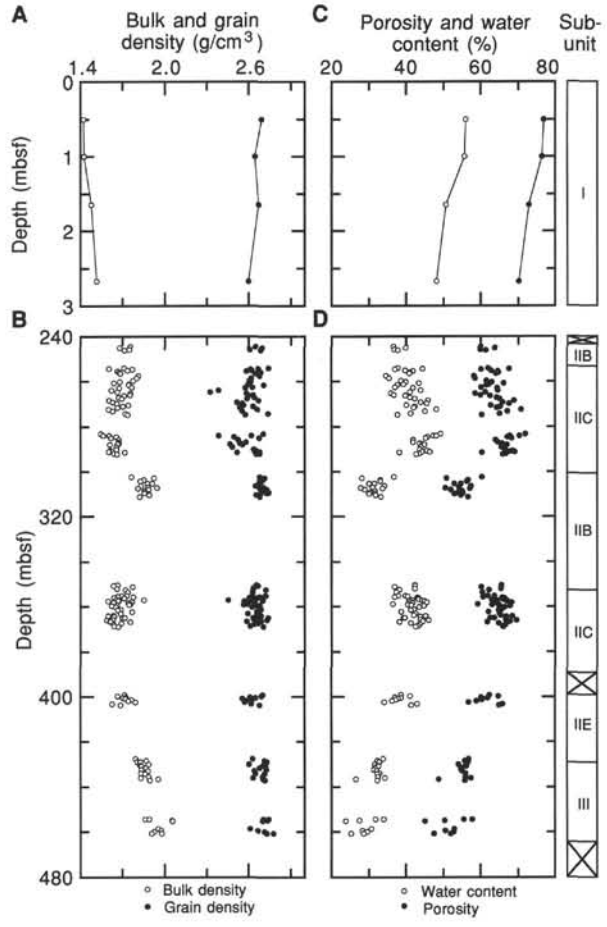

Figure 43. Density and porosity data from Site 949. **A.** Bulk and grain densities in mud-line Core 156-949A-1H. **B.** Bulk and grain densities combined from Holes 949B and 949C. **C.** Porosity and water content (percentage of wet weight) in mud-line Core 949A-1H. **D.** Porosity and water content (percentage of wet weight) in Holes 949B and 949C.

HEAT FLOW

WSTP Operations and Estimated Temperatures

The WSTP was deployed in temperature-only configuration four times in Hole 949B, yielding four equilibrium temperature values (Table 28). All deployments took place in calm seas, during breaks in coring after Hole 949B was washed from 0.0 to 244.1 mbsf. Individual measurements are referenced according to the identifier of the subsequent core.

The temperature of bottom water at this site was determined to be 2.35° ± 0.05°C, the same as that at Site 948, by holding the tools 20 m above the mud line for 5 to 10 min at the start of each deployment. Consistent results were obtained between successive deployments using the same sensor.

WSTP deployment 949B-3X (Core 156-949B-3X) at 264.6 mbsf provided a good equilibration curve following probe insertion (Fig. 48A), but the data logger was electrically "noisy," superimposing high-frequency, 0.3°C variations in temperature over the cooling curve (Fig. 49A). Examination of the recorder after the station revealed that (1) it was a different recorder from that run previously during Leg 156, and (2) a chip was loose on the main circuit board. Deck tests with the instrument during the next several hours, and comparison with results from a more stable recorder (used during the rest of the cruise), indicated that the noise was evenly distributed around the true signal. This interpretation is supported by a comparison of the equilibration temperature for this station (23.5° ± 0.5°C)

Table 24. *S*-wave measurements for Hole 949B.

Core, section, interval (cm)	Depth (mbsf)	Shear-wave velocity (m/s)					
		xy	*xz*	*yx*	*yz*	*zx*	*zy*
156-949B-							
1X-1, 36–38	244.46		617.68		517.59		458.61
1X-CC, 26–28	246.20	600.16			640.40		653.08
2X-5, 31–33	260.11		693.13		554.89		537.54
3X-3, 50–52	267.00	548.02			708.78		650.12
3X-1, 108–110	264.58		517.43			500.94	
5X-1, 133–135	284.13		776.79		658.80		870.87
5X-2, 84–86	285.14	635.86			583.60		619.32
5X-5, 136–138	290.16		837.85		599.66	562.77	
5X-CC, 18–20	292.46		714.42		590.61	559.49	
5X-6, 23–25	290.53	604.45			671.98		566.95
7X-5, 136–138	309.46	571.02			504.01		562.77
7X-6, 22–24	309.82	493.45			395.76		512.09
13X-1, 18–20	350.38		772.53	618.76		733.82	
13X-2, 27–29	351.97		763.10		732.44		759.55
14X-3, 48–50	358.38	670.95		756.42			784.18
23X-8, 2–4	437.12	794.02		573.68			906.80
19X-1, 135–137	400.15	712.70		708.22			609.33
22X-3, 27–29	430.67	547.19		596.87			499.07
25H-2, 69–71	460.59		557.62		494.16		573.85

Note: Polarization convention: *xy* means wave traveling in *x* direction, polarized in *y* direction; *z* direction is parallel to core axis.

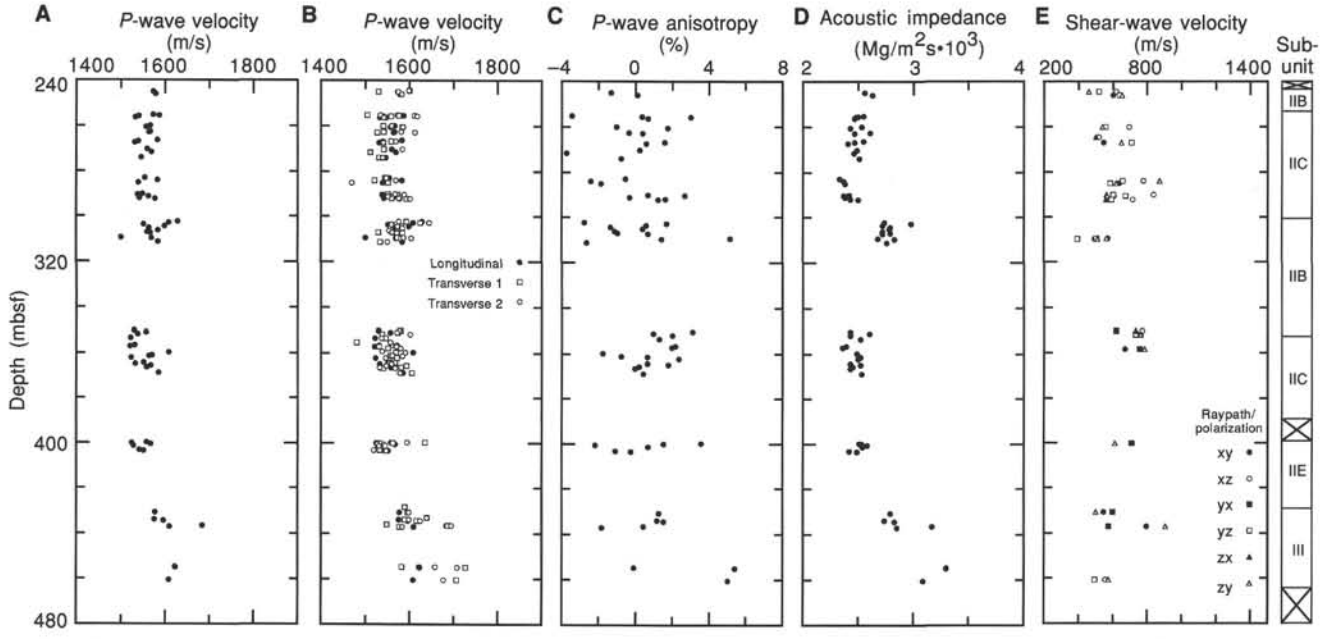

Figure 44. Velocity data from Site 949. **A.** Longitudinal *P*-wave velocities, measured with the Hamilton Frame velocimeter on XCB core samples from Holes 949B and 949C. **B.** Longitudinal and transverse *P*-wave velocities, measured with the Hamilton Frame velocimeter on XCB core samples from Holes 949B and 949C. **C.** Transverse *P*-wave velocity anisotropy in XCB cores from Holes 949B and 949C. **D.** Acoustic impedance, based on longitudinal compressional (*P*-wave) velocities, Holes 949B and 949C. **E.** Shear-wave velocities in pieces cut from Cores 156-949B-1X through -24X and Core 156-949-25H. Symbols indicate propagation and polarization directions, as defined in the inset diagram.

with those from successive stations and bottom water, as described later. Despite the noise, testing with a decade box indicated that the instrument was properly calibrated, both before and after the station.

Deployments 949B-8X and 949B-13X (Figs. 48B, -C), using a more stable data logger, yielded equilibrium temperatures of 27.1° ± 0.1° and 30.3° ± 0.3°C, respectively (Figs. 49B, -C). The greater uncertainty of the equilibrium temperature for station 949B-13X results from the probe shifting in the sediment during the first minutes of the station. Station 949B-25H was run at what had been the intended total depth for Hole 949B, but relatively soft and plastic mud that packed onto the probe tip after the run suggested that an APC core might recover some of the sediment below this depth. This deployment provided an excellent equilibration curve (Figs. 48D and 49D) and an estimated in situ temperature of 39.2°C. The good fit of all data to the theoretical model is shown in Figure 50.

Thermal Gradient and Heat Flow

Temperature values determined at Site 949 are plotted vs. depth in Figure 51. In combination with the bottom-water temperature of 2.35°C, the Hole 949B data yield a thermal gradient of 80°C/km over the upper 457.5 mbsf. The linear consistency of the data does not indicate constant heat flow (and thus probably is a coincidence), as an increase in thermal conductivity over the upper 450 mbsf of 50% is typical of seafloor sediments. A linear thermal gradient combined with an increase

Table 25. Thermal conductivity data for Holes 949A, 949B, and 949C.

Core, section, interval (cm)	Depth (mbsf)	Thermal conductivity (W/[m·K])
156-949A-		
1H-1, 113	1.13	0.96
156-949B-		
1X-1, 30	244.40	1.16
1X-2, 20	245.80	1.18
2X-1, 30	254.10	1.16
2X-4, 100	259.30	1.05
2X-5, 30	260.10	1.12
2X-7, 30	263.10	1.11
3X-3, 30	266.80	1.02
3X-4, 30	268.30	1.08
3X-5, 33	269.83	1.10
4X-1, 30	273.40	1.11
4X-2, 13	274.73	1.15
5X-1, 40	283.20	1.06
5X-4, 30	287.60	1.04
5X-5, 30	289.10	1.00
5X-6, 30	290.60	1.08
5X-7, 30	292.10	1.11
5X-CC, 30	292.58	1.05
7X-1, 30	302.40	1.19
7X-2, 30	303.90	1.25
7X-5, 30	308.40	1.27
7X-6, 30	309.90	1.24
7X-7, 30	311.40	1.21
7X-CC, 13	311.66	1.24
13X-1, 50	350.70	1.15
13X-2, 100	352.70	1.14
13X-3, 30	353.50	1.16
14X-1, 120	355.50	1.18
14X-4, 30	357.30	1.09
14X-5, 30	358.10	1.04
14X-6, 30	358.90	1.14
14X-7, 30	359.60	1.13
14X-CC, 15	359.80	1.08
15X-1, 30	360.20	1.07
15X-3, 30	363.20	1.16
15X-4, 30	364.70	1.17
15X-5, 30	366.20	1.07
22X-1, 30	427.70	1.17
22X-2, 30	429.20	1.25
22X-3, 30	430.70	1.21
22X-4, 30	432.20	1.29
22X-5, 30	433.70	1.19
22X-6, 30	435.20	1.22
22X-7, 30	436.70	1.27
25H-1, 30	458.70	1.15
25H-2, 30	460.20	1.19
156-949C-		
7R-1, 50	454.60	1.17
7R-CC, 15	455.15	1.45

in thermal conductivity would imply increasing heat flow with depth. Work will be done post-cruise to calculate the heat flow at Site 949.

VERTICAL SEISMIC PROFILES

Introduction

Both zero-offset and bottom-shot vertical seismic profiles (VSP) were acquired in Hole 949C. The objectives of the zero-offset VSP were to correlate the drilled section to the regional three-dimensional seismic reflection data set and to provide accurate interval velocity and time-depth functions for this part of the accretionary prism. The objective of the bottom-shot VSP was to characterize the shear-wave velocity structure and anisotropy within the prism, particularly near the décollement.

Zero-offset VSP

Acquisition

The acoustic source consisted of 2.0-L (120-in.^{3}) and 4.9-L (300-in.^{3}) air guns. Seismic arrivals were received by the five-element Schlumberger array seismic imager (ASI). A description of the ASI, as well as gun and receiver geometries, can be found in the "Explanatory Notes" chapter (this volume). We occupied 17 shot-firing stations from 458.20 to 39.10 mbsf. The VSP was run in three stages: (1) depths from

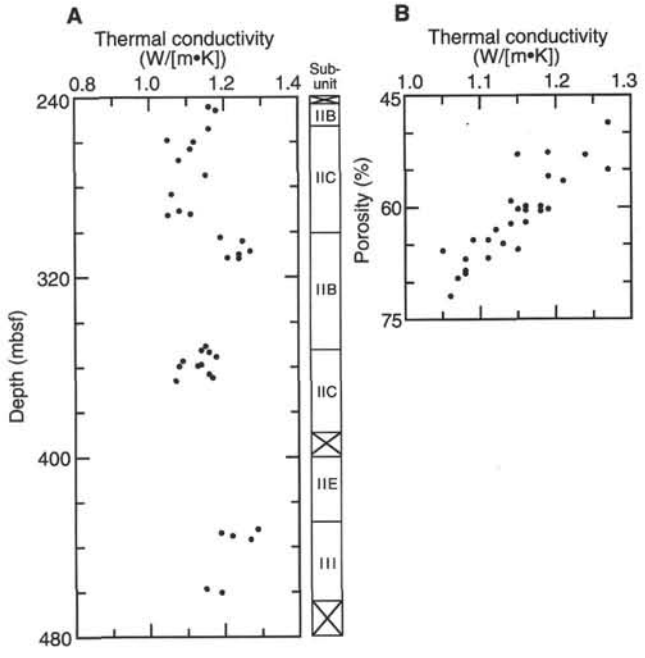

Figure 45. Thermal conductivity data for Site 949. **A.** Thermal conductivity vs. depth for Holes 949B and 949C, 240–480 mbsf. **B.** Thermal conductivity vs. porosity at Site 949.

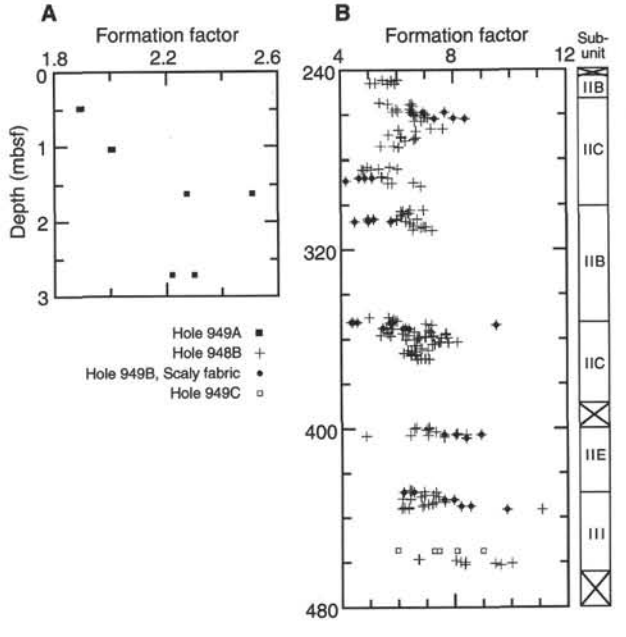

Figure 46. Formation factors from Site 949. **A.** Formation factor from resistivity measurements from mud-line Core 156-949A-1H. **B.** Formation factor from resistivity measurements, Holes 949B and 949C.

397.25 to 366.77 mbsf were shot before the bottom-shot VSP; (2) depths from 351.50 mbsf to the top of the hole were shot just after the bottom-shot VSP; (3) depths from 458.20 to 397.25 mbsf were shot in the third casing string several days later. We recorded data from 68 geophone clamping positions; several geophone positions were occupied twice (one was occupied three times) to overcome high noise levels near the top of the hole. A total of 6 to 35 shots were fired at each location to allow stacking of shots to increase signal-to-noise ratios. The ASI was moved up the hole to yield geophone clamping

Table 26. Resistivity measurements from Holes 949A, 949B, and 949C.

Core, section, interval (cm)	Depth (mbsf)	Measured resistance (Ω)	Orientation	Resistivity at 21°C (Ωm)	Formation factor	Notes
156-949A-						
1H-1, 49	0.49	32.0	T	0.388	1.90	
1H-1, 49	0.49	31.8	L	0.386	1.89	
1H-1, 104	1.04	33.8	T	0.411	2.01	
1H-1, 104	1.04	33.6	L	0.409	2.00	
1H-2, 12.5	1.63	42.0	T	0.512	2.51	
1H-2, 12.5	1.63	38.0	L	0.464	2.27	
1H-2, 121.5	2.72	38.4	T	0.470	2.30	
1H-2, 121.5	2.72	37.0	L	0.454	2.22	
156-949B-						
1X-1, 36	244.46	91	L	1.12	5.50	
1X-1, 38	244.48	100	T	1.23	6.03	
1X-1, 84	244.94	96	L	1.19	5.83	
1X-1, 85	244.95	96	T	1.19	5.82	
1X-2, 19	245.79	83	L	1.03	5.05	
1X-2, 20	245.80	87	T	1.07	5.25	
1X-CC, 26	246.20	98	T	1.22	5.96	
1X-CC, 26	246.20	93	L	1.16	5.69	
2X-1, 91	254.71	88	L	1.10	5.39	
2X-1, 137	255.17	107	T	1.34	6.55	
2X-1, 137	255.17	93	L	1.16	5.70	
2X-2, 20	255.50	106	L	1.32	6.46	
2X-2, 108	256.38	107	T_2	1.34	6.58	
2X-3, 68.5	257.49	105	L	1.32	6.48	
2X-3, 70	257.50	97	T	1.22	5.97	
2X-4, 32	258.62	98	T	1.24	6.05	
2X-4, 32	258.62	95	L	1.20	5.85	
2X-4, 73	259.03	112	S	1.42	6.94	SF
2X-4, 73	259.03	124	SO	1.57	7.70	SF
2X-4, 73	259.03	103	SO	1.33	6.51	SF
2X-5, 32	260.12	113	L	1.44	7.03	
2X-5, 33	260.13	106	T	1.35	6.60	
2X-5, 80	260.60	107	L	1.37	6.69	
2X-5, 80	260.60	106	T	1.36	6.64	
2X-6, 5	261.35	113	L	1.45	7.10	
2X-6, 5	261.35	111	T	1.43	6.99	
2X-6, 51	261.81	128	S	1.64	8.01	SF
2X-6, 53	261.83	117	S	1.50	7.33	SF
2X-6, 53	261.83	134	SO	1.72	8.41	SF
2X-7, 20	263.00	105	L	1.35	6.63	
2X-7, 21	263.01	109	T	1.40	6.87	
3X-2, 34	265.34	106	L	1.40	6.84	D
3X-2, 34	265.34	109	T	1.45	7.08	D
3X-2, 140	266.40	111	L	1.48	7.22	
3X-2, 140	266.40	117	T	1.56	7.62	
3X-3, 51	267.01	94	T_2	1.24	6.06	
3X-3, 111	267.61	103	L	1.37	6.69	
3X-4, 112	269.12	88	T	1.17	5.72	
3X-5, 42	269.92	95	T	1.26	6.15	
3X-5, 107	270.57	103	T	1.36	6.68	
3X-5, 107	270.57	95	L	1.26	6.17	
3X-6, 15	271.15	102	L	1.35	6.62	
3X-6, 64	271.64	97	T	1.29	6.30	
4X-1, 107	274.17	90	T	1.21	5.91	
4X-1, 109	274.19	83	L	1.11	5.44	
4X-2, 13	274.73	93	T	1.24	6.06	
5X-1, 37	283.17	80	T	1.10	5.40	C
5X-1, 38	283.18	74	L	1.01	4.95	
5X-1, 41	283.21	83		1.18	5.75	
5X-1, 134	284.14	89	T	1.23	6.03	
5X-1, 134	284.14	79	T	1.10	5.36	
5X-1, 135	284.15	71	L	0.97	4.77	
5X-1, 135	284.15	75	L	1.04	5.09	
5X-2, 5	284.35	80	T	1.13	5.54	
5X-2, 23	284.53	68	L	0.94	4.62	C
5X-2, 23	284.53	71		0.99	4.83	
5X-3, 18	285.98	90	T	1.25	6.13	C
5X-3, 18	285.98	90	L	1.25	6.14	C
5X-3, 137	287.17	96		1.36	6.67	C
5X-4, 19	287.49	80	T	1.12	5.47	
5X-4, 48	287.78	80	L	1.12	5.49	
5X-4, 58	287.88	68	S	0.95	4.66	SF
5X-4, 63	287.93	75	S	1.05	5.13	SF
5X-4, 63	287.93	71	SO	0.99	4.86	SF
5X-4, 72	288.02	82		1.16	5.69	
5X-5, 63	289.43	61	S	0.86	4.19	SF
5X-5, 137	290.17	95	L	1.35	6.61	
5X-6, 17	290.47	85	T	1.19	5.83	
5X-6, 24	290.54	83	T_2	1.16	5.69	
5X-7, 11	291.91	99		1.40	6.85	
7X-1, 31	302.41	93	L	1.32	6.48	
7X-1, 31	302.41	99	T_2	1.42	6.93	
7X-1, 87	302.97	90	T	1.26	6.14	
7X-1, 87	302.97	91	L	1.27	6.22	
7X-2, 8	303.68	95	L	1.31	6.42	
7X-2, 8	303.68	94	T	1.30	6.38	
7X-2, 76	304.36	90	L	1.26	6.17	

Table 26 (continued).

Core, section, interval (cm)	Depth (mbsf)	Measured resistance (Ω)	Orientation	Resistivity at 21°C (Ωm)	Formation factor	Notes
7X-3, 10	305.20	90	T_2	1.25	6.14	
7X-3, 128	306.38	87	L	1.22	6.00	
7X-3, 136	306.46	72	T	1.01	4.97	SF
7X-3, 142	306.52	97	T	1.37	6.70	
7X-3, 146	306.56	75	T	1.06	5.17	SF
7X-4, 34	306.94	86	T_2	1.22	5.98	
7X-4, 82	307.42	92	L	1.29	6.32	
7X-4, 104	307.64	66	S	0.92	4.50	SF
7X-4, 106	307.66	85	S	1.18	5.78	SF
7X-4, 106	307.66	73	SO	1.02	4.97	SF
7X-5, 24	308.34	93	L	1.32	6.44	
7X-5, 138	309.48	95	T_2	1.35	6.59	
7X-6, 24	309.84	100	L	1.41	6.91	
7X-6, 24	309.84	102	T	1.43	7.01	
7X-6, 93	310.53	97	T	1.40	6.83	
7X-7, 12	311.22	93	T_2	1.34	6.55	
7X-7, 39	311.49	104		1.48	7.24	
13X-1, 19	350.39	73	T_2	1.02	5.00	
13X-1, 19	350.39	83	L	1.16	5.69	
13X-1, 99	351.19	85	L	1.20	5.86	
13X-2, 29	351.99	86	T_2	1.22	6.00	
13X-2, 29	351.99	85	L	1.21	5.93	
13X-2, 65	352.35	85	T	1.19	5.82	
13X-2, 73	352.43	65	S	0.91	4.44	SF
13X-2, 73	352.43	64	SO	0.89	4.37	SF
13X-2, 90	352.60	67	L	0.93	4.57	SF
13X-2, 133	353.03	84	S	1.17	5.74	SF
13X-2, 133	353.03	85	SO	1.19	5.81	SF
13X-2, 142	353.12	90	L	1.26	6.16	C
13X-3, 27	353.47	101	L	1.43	6.99	
13X-CC, 27	353.93	104	T	1.47	7.20	
13X-CC, 30	353.96	137	T	1.94	9.49	SF
14X-1, 17	355.07	78		1.15	5.61	
14X-1, 33	355.23	76		1.12	5.48	SF
14X-1, 34	355.24	87		1.28	6.27	SF
14X-1, 54	355.44	81		1.19	5.84	
14X-1, 56	355.46	80		1.18	5.77	
14X-1, 68	355.58	89	S	1.31	6.42	
14X-1, 68	355.58	86	SO	1.27	6.20	SF
14X-1, 127	356.17	98	T	1.45	7.11	
14X-2, 124	357.64	93	T	1.35	6.59	
14X-2, 144	357.84	80		1.16	5.67	
14X-3, 49	358.39	99	L	1.46	7.16	
14X-3, 126	359.16	107	T	1.58	7.71	
14X-4, 26	359.66	86		1.26	6.18	
14X-4, 131	360.71	107		1.57	7.71	
14X-5, 41	361.31	89	L	1.31	6.39	
14X-5, 88	361.78	101	T	1.48	7.27	
14X-6, 22	362.62	100	T	1.47	7.21	
14X-6, 115	363.55	105	L	1.54	7.55	
14X-7, 10	364.00	94	45°	1.39	6.79	
15X-1, 37	360.27	88	L	1.29	6.31	
15X-1, 37	360.27	94	T	1.37	6.69	
15X-1, 145	361.35	113	L	1.66	8.11	
15X-1, 146	361.36	105	T	1.54	7.53	
15X-2, 19	361.59	109	L	1.59	7.80	
15X-2, 20	361.60	104	T	1.53	7.47	
15X-2, 95	362.35	102	L	1.49	7.31	
15X-2, 95	362.35	101	T	1.48	7.24	
15X-3, 22	363.12	92	L	1.35	6.59	
15X-3, 22	363.12	93	T	1.36	6.66	
15X-3, 145	364.35	95	L	1.39	6.80	
15X-3, 145	364.35	96	T	1.40	6.87	
15X-4, 58	364.98	89	T	1.30	6.36	
15X-4, 61	365.01	102	L	1.49	7.30	C
15X-4, 61	365.01	99	L	1.45	7.08	
15X-4, 133	365.73	91	T	1.33	6.50	
15X-4, 135	365.75	93	L	1.36	6.65	
15X-5, 60	366.50	91	L	1.33	6.50	
15X-5, 60	366.50	87	T	1.27	6.21	
15X-5, 99	366.89	93	L	1.36	6.63	
15X-5, 99	366.89	91	T	1.33	6.49	
15X-6, 8	367.48	93	L	1.35	6.63	
15X-6, 8	367.48	91	T	1.32	6.48	
15X-6, 136	368.76	98	L	1.43	6.97	
15X-6, 136	368.76	96	T	1.40	6.83	
15X-7, 10	369.00	94	L	1.37	6.71	
15X-7, 10	369.00	100	T	1.46	7.13	
19X-1, 85	399.65	95	T^2	1.35	6.63	
19X-1, 85	399.65	102	L	1.45	7.11	
19X-1, 136	400.16	102	L	1.45	7.08	
19X-1, 136	400.16	95	T_1	1.35	6.59	
19X-2, 37	400.67	105	T_2	1.49	7.28	C
19X-2, 39	400.69	101	L	1.43	6.99	
19X-3, 9	401.39	106	T_2	1.50	7.33	
19X-3, 93	402.23	117	L	1.65	8.09	
19X-3, 141	402.71	117	S	1.65	8.06	SF
19X-3, 141	402.71	130	SO	1.83	8.94	SF

Table 26 (continued).

Core, section, interval (cm)	Depth (mbsf)	Measured resistance (Ω)	Orientation	Resistivity at 21°C (Ωm)	Formation factor	Notes
19X-3, 141	402.71	111	S	1.56	7.63	SF
19X-3, 143	402.73	122	T	1.72	8.43	
19X-4, 13	402.93	103	T	1.44	7.06	
19X-4, 29	403.09	94		1.32	6.45	
19X-4, 49	403.29	71	L	1.00	4.87	
19X-4, 49	403.29	67	T	0.94	4.60	C
19X-4, 85	403.65	111		1.56	7.62	
19X-4, 141	404.21	123	SO	1.72	8.42	
22X-1, 30	427.70	95	L	1.32	6.47	
22X-1, 35	427.75	94	T	1.31	6.42	
22X-1, 103	428.43	101	L	1.41	6.91	
22X-1, 118	428.58	105	T	1.50	7.33	
22X-1, 118	428.58	94	S	1.34	6.55	SF
22X-1, 118	428.58	89	SO	1.27	6.20	SF
22X-2, 19	429.09	89	L	1.25	6.11	C
22X-2, 28	429.18	77	T	1.08	5.29	C
22X-2, 30	429.20	84	T	1.18	5.75	C
22X-2, 101	429.91	101	T	1.42	6.94	
22X-2, 103	429.93	105	L	1.48	7.23	
22X-3, 29	430.69	98	L	1.39	6.80	
22X-3, 29	430.69	107	T	1.52	7.42	
22X-3, 115	431.55	89	L	1.26	6.16	
22X-3, 122	431.62	93	T	1.31	6.43	
22X-4, 13	432.03	110	S	1.56	7.64	SF
22X-4, 13	432.03	115	S	1.63	7.97	SF
22X-4, 114	433.04	105	T	1.49	7.31	
22X-4, 114	433.04	110	L	1.56	7.65	
22X-5, 48	433.88	103	L	1.47	7.22	
22X-5, 92	434.32	100	L	1.44	7.05	
22X-5, 92	434.32	98	T	1.41	6.90	
22X-6, 13	435.03	116	S	1.68	8.22	
22X-6, 14	435.04	121	SO	1.75	8.56	
22X-6, 23	435.13	97	T	1.40	6.85	
22X-6, 73	435.63	88	T	1.30	6.36	
22X-6, 73	435.63	86	L	1.27	6.21	
22X-6, 123	436.13	86	L	1.25	6.13	
22X-6, 123	436.13	89	T	1.30	6.37	
22X-7, 9	436.49	141	T	2.01	9.86	SF
22X-7, 15	436.55	159	T	2.27	11.10	
25H-1, 24	458.64	100	L	1.37	6.73	
25H-1, 24	458.64	100	T	1.37	6.71	
25H-1, 95	459.35	120	T	1.64	8.04	
25H-1, 95	459.35	121	L	1.65	8.09	
25H-2, 15	460.05	127	L	1.71	8.38	
25H-2, 17	460.07	124	T	1.67	8.20	
25H-2, 70	460.60	141	L	1.93	9.43	
25H-2, 70	460.60	150	T	2.05	10.01	
25H-2, 138	461.28	100		1.36	6.65	D
156-949C-						
7R-1, 77	454.87	87	L	1.43	7.44	
7R-1, 75	454.85	85	T	1.39	7.26	
7R-1, 47	454.57	70	L	1.15	5.98	
7R-1, 50	454.60	70	L	1.15	5.98	
7R-CC, 10	455.10	107	T	1.75	9.00	
7R-CC, 10	455.10	96	L	1.57	8.08	

Notes: L, T_1, T_2 = orientation with respect to core (longitudinal or transverse); S, SO = respectively, parallel and orthogonal to foliation; SF = scaly fabric; C = sediment cracked during probe penetration, usually resulting in unstable readings; D = slight drilling disturbance (fractures), measurements from more disturbed zones have been removed.

Table 27. Vane shear strength data for Hole 949A.

Core, section, interval (cm)	Depth (mbsf)	Peak (kPa)	Residual (kPa)
156-949A-			
1H-1, 113	1.13	11.9	7.7
1H-2, 14	1.64	6.5	2.7
1H-2, 125	2.75	6.2	5.0

levels at 7.62-m intervals from 397.25 to 39.10 mbsf; the interval was decreased to 3.81 m for the lowermost 20 geophone positions.

During all three parts of the zero-offset VSP experiment, the air guns, ASI, and MAXIS recording system all performed flawlessly. The cement-bond log that was run just prior to the VSP experiment indicated that only the lowermost 50 to 100 m of the casing was well cemented. A combination of relatively high sea state and poor coupling of the casing to the prism sediments in the nonbonded part of the hole contributed to relatively low signal-to-noise ratios. The noise recorded on the horizontal geophones was excessive, and few coherent events can be identified. The sea state was much greater during the third shooting stage, and up to 35 shots were needed at each station to obtain acceptable stacks.

Shipboard Processing

Preliminary processing of the zero-offset VSP data was performed on board *JOIDES Resolution*. The following processing steps were performed for the interval 397.25 to 39.1 mbsf (only steps 1 to 6 applied to both vertical and horizontal components); the deepest 20 stations will be processed on shore:

1. Edit bad shots,
2. Separate vertical and horizontal component data,
3. Edit bad traces from each geophone level for each component,
4. Subtract firing delay from each shot,
5. Apply bandpass filter (3-5-80-92 Hz), and
6. Stack all shots at each level.

Table 28. Summary of WSTP deployments in Hole 949B.

Measurement	Depth (mbsf)	Quality	Temperature (°C)	Comments
156-949B-				
3X	264.6	Good	23.5 ± 0.5	Noisy recorder
8X	312.7	Excellent	27.1 ± 0.1	
13X	351.3	Good	30.3 ± 0.3	Probe shifted
25H	457.5	Excellent	39.2 ± 0.2	

Steps applied to the vertical component only:

7. Apply $t^{1.25}$ gain to correct for amplitude decay with depth,
8. Pick first-break times,
9. Subtract first-break times to flatten reflected arrivals to zero time,
10. Apply filter in frequency-wavenumber (F-K) domain to attenuate downgoing wavefield and enhance upgoing wavefield,
11. Shift to two-way traveltime by adding twice first-break time to each seismogram,
12. Select and apply corridor mute to eliminate noise approximately 0.5 s below first breaks, and
13. Stack all levels into a single trace (corridor stack).

Preliminary Results

A plot of the filtered and stacked vertical component of VSP data is shown in Figure 52 (the horizontal components are not shown here due to high noise levels). The most prominent arrivals are the direct arrivals (first breaks) and the oceanic crust reflection. All events dipping parallel to the first breaks are downgoing waves; those dipping parallel to the oceanic crust reflection are upgoing (reflected) waves. Some reflections are visible between the first breaks and the oceanic crust reflection on the vertical component, but the bubble pulse is large and obscures reflections within 250 ms of the first breaks. The eight shallowest traces have been contaminated by a high-amplitude, nearly flat first arrival (probably a tube wave) that completely obscures all other events. These traces were not processed further.

The first-break times provide a time-depth profile for the sampled interval (Fig. 53). The traveltime to the seafloor was determined by subtracting the height of the rig floor above sea level (11.3 m) and the depth of the air guns (7 m) from the depth to seafloor (referenced to the drill floor; 5016 m) and then dividing by the velocity of sound in seawater (1508 m/s). This yields (5016 – 11.3 – 7)/1508 = 3.3141 s. We have connected the calculated seafloor traveltime with the first reliable first-break time by a dashed line. The velocity implied by this line is 1617 m/s, which is our "best guess" for the velocity of the shallowest part of the prism. This velocity is heavily dependent on the choice of seafloor traveltime. Velocities deeper in the section were computed by fitting line segments to the data points via least-squares linear regression.

The processed vertical component shows upgoing (reflected) waves enhanced and aligned horizontally (Fig. 54). Strong reflections correspond to the oceanic crust and décollement. Weaker reflections occur both above and below the décollement. The décollement reflection intersects the borehole at approximately the location of the deepest recording station (397 mbsf).

The stacked upgoing wavefield can be directly compared to the corresponding seismic line displayed in time (Fig. 55). Although the waveform of the VSP is different from that of the three-dimensional survey, the décollement reflection and the negative-polarity reflection just below the décollement match well. The oceanic crust reflection does not match as well, probably because of the difference in waveform between the two data sets. Additional source wavelet processing will be necessary.

Bottom-shot VSP

The bottom-shot VSP was recorded just above the seismic décollement in Hole 949C, at the bottom of the 13⅜-in. casing after cementing operations were completed. The shots were recorded on the ASI five-element, three-component borehole geophones. The spacing between three-component geophones was 15.24 m. The recording of shear waves requires good coupling of the casing to the surrounding formation. The location of the ASI within Hole 949C was limited to depths where the casing was cemented to the formation. Consequently, the recording site was above, rather than within, the décollement (which is the zone of greatest interest for seismic anisotropy investigations).

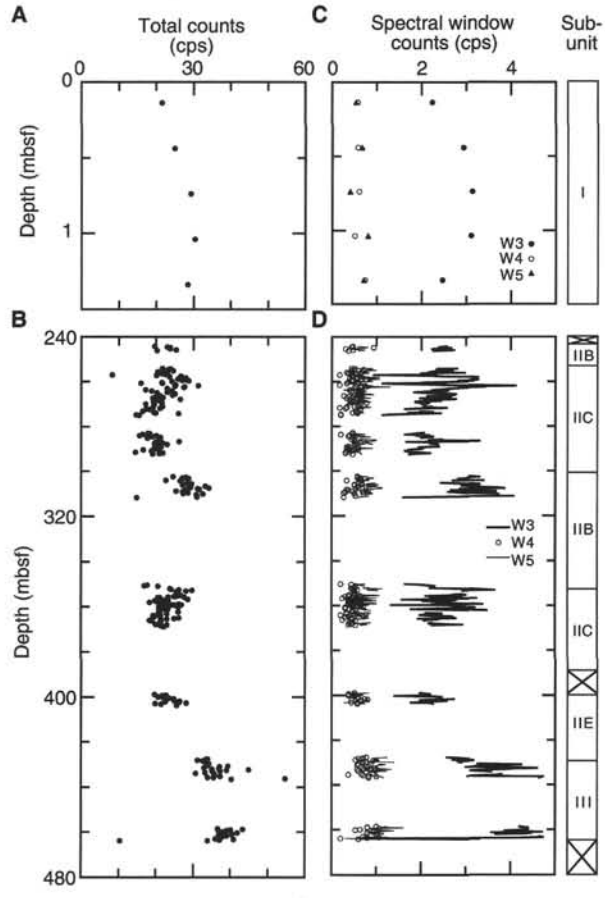

Figure 47. Natural gamma-ray data, Site 949. **A.** NGR total counts for mud-line Core 156-949A-1H. **B.** NGR total counts for Hole 949B. **C.** NGR spectral Windows 3, 4, and 5 counts for mud-line Core 156-949A-1H. **D.** NGR spectral Windows 3, 4, and 5 counts for Hole 949B.

Shot Positions

Twenty-one shots were launched from the drill ship while it was in "dynamic positioning mode," with the bottom of the drill string raised 20 m above the level of the reentry cone (Table 29). The range of the shots was 200 to 1000 m from the hole. The planned shot pattern (Fig. 56) was not the desired set of radial lines centered on the borehole (see "Explanatory Notes" chapter, this volume). The prevailing surface current was east to west, so the ship moved in eastward lines as we launched the shots to avoid overrunning them. We also tried to deposit each shot so that none was closer than 200 m to another, the top of the hole, or the acoustic location beacons (south of the hole). We avoided moving over seafloor elevations greater than 20 m above the top of the hole, so that the drill string would not drag on the seafloor.

Receiver Positions

The ASI occupied two depth positions with overlap of one shuttle position (Fig. 57). The shots were timed so that 10 would be recorded

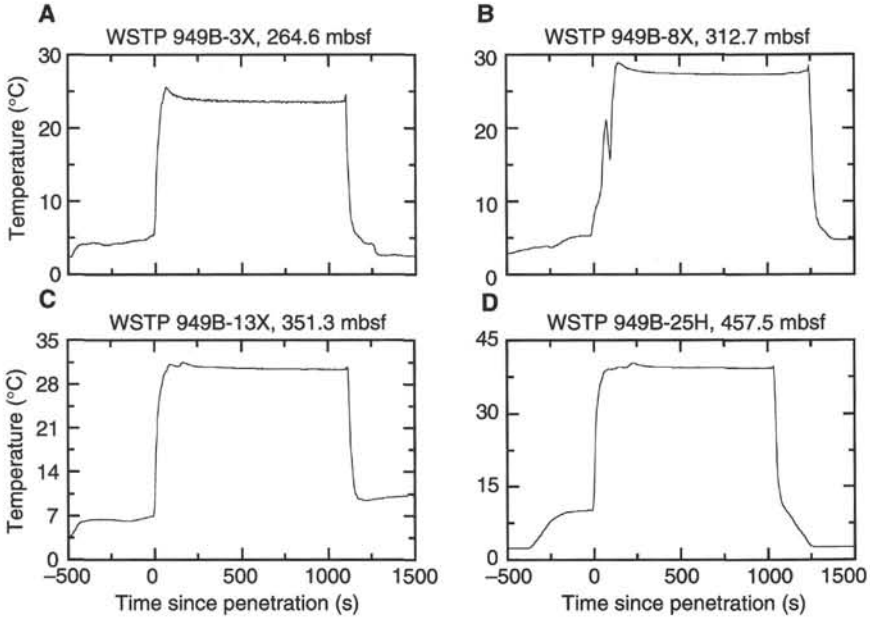

Figure 48. **A–D.** Temperature vs. time records for WSTP deployments in Hole 949B.

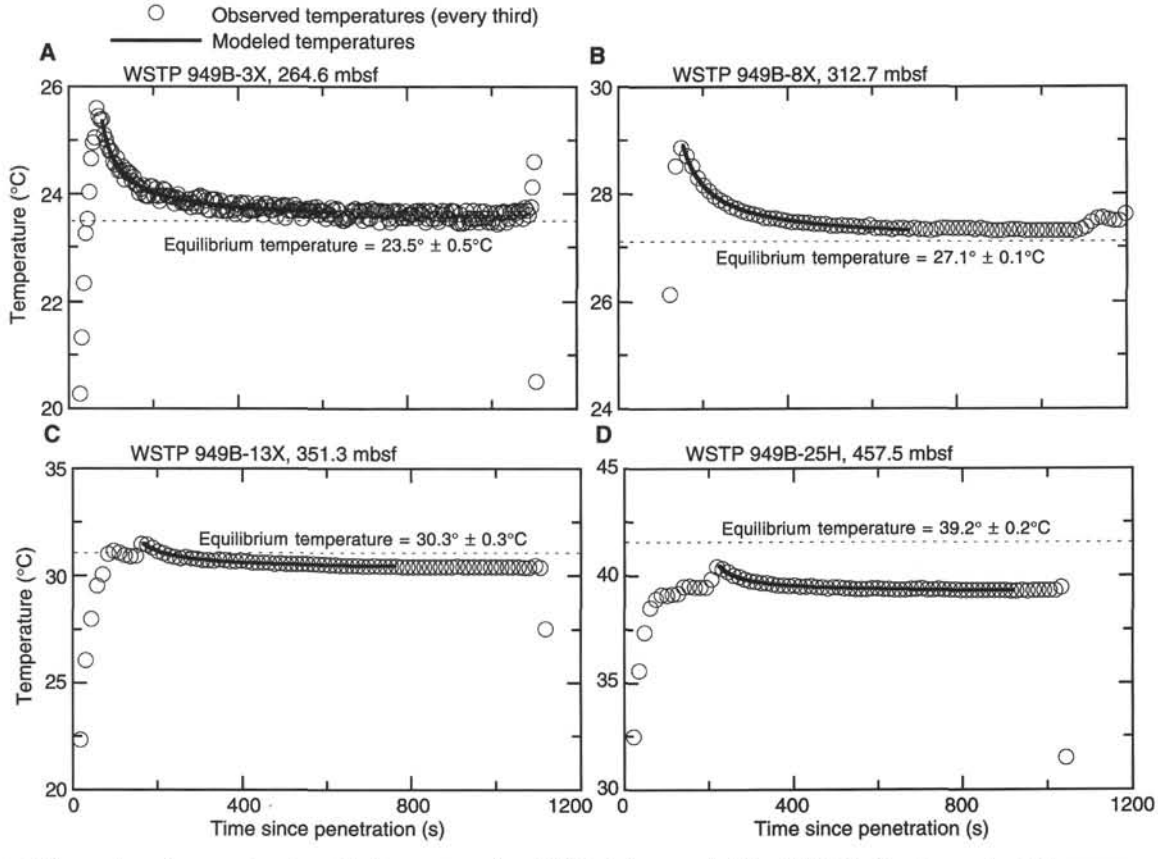

Figure 49. **A–D.** Comparison of measured with modeled temperatures from WSTP deployments in Hole 949B. In **B–D**, only one of each three measured temperature values is shown so that comparison with the model is easier to see.

while the ASI was in the lower position and 11 while the ASI was in the upper position. The range of incidence angles was 27° to 75°, assuming straight ray paths. The lowest geophone position was 397.2 mbsf.

At each of the two levels, we recorded a zero-offset shot from an air gun suspended from the ship to give vertical *P*-wave velocities and verify coupling of the casing to the formation. At the upper level, we also ran the internal "shaker" in each element of the ASI and compared the responses of the three components. These responses had to be similar for polarizations to be measured accurately.

We deployed two hydrophones, one 50 m below sea level from the starboard taut-wire boom (beside the moonpool) and one about 42 m

Table 29. Bottom-shot VSP: actual and desired shot deployment points.

Shot no. in order of deployment	Shot deployment goals		Actual shot deployment	
	North of Hole 949C (m)	East of Hole 949C (m)	North of Hole 949C (m)	East of Hole 949C (m)
1	192	240	206	218
2	172	–319	187	–311
3	231	–574	247	–582
4	270	–770	305	–747
5	457	–946	505	–1027
6	525	–681	533	–693
7	555	44	577	70
8	300	456	317	437
9	662	877	680	861
10	1084	24	1148	–12
11	574	–417	591	–402
12	555	–172	600	–180
13	437	240	451	227
14	231	701	238	695
15	192	936	210	912
16	849	740	875	747
17	927	495	973	445
18	1035	279	1055	299
19	1084	–230	1069	–275
20	976	–485	950	–487
21	878	–721	924	–690

below sea level from a davit at the extreme starboard corner of the fantail to record water reverberations from the shots. These records gave us time of shot, range, and azimuth. The latter hydrophone was connected to the MAXIS recording system and a chart recorder that ran continuously at 11 cm/s.

Operations

The experiment had three stages: launching the shots from the ship; returning to and reentering the hole to deploy the ASI; and recording the shots. These stages took 7, 4, and 4 hr, respectively. We saved time by lowering the ASI into the drill pipe to 250 m below the rig floor before beginning to launch the shots.

The ship moved from west to east in three lines to launch the shots, returning from east to west after each line. The prevailing current and the screws and thrusters all moved the shots astern from the launching point on the aft starboard corner of the fantail (just inboard of the starboard hydrophone-streamer winch). The shots had been made up the previous day and had been stored in a magazine near the launching point. The shot timers were pre-set to run for 24 hr and initiated at 10-min intervals 24 hr before the desired detonation time.

As the ship approached each launching position, the shot firers attached the detonator, paid the shot over the side of the ship on a 150-m cable, and then connected the numbered timer canister appropriate to that shot. The shots were launched at 10- to 25-min intervals.

For safety during shot launching, radio, radar, and some electrical equipment were shut down, including welding equipment and the rig motors. We kept watch for the forecast isolated thunderstorms, but the weather was fair apart from a brief shower and did not interrupt the operation.

After launching the shots, the ship returned to the hole and it was quickly reentered. The seafloor depth was verified as 5016 mbrf with the gamma-ray sensor at the top of the ASI; then the ASI was lowered to the bottom of the casing. The air guns were lowered from the aft port crane into position for the zero-offset VSP. We had time to record several air-gun shots for the zero-offset VSP before the first explosive shot was due.

The cement-bond log (see "Operations" section, this chapter) showed attenuated pipe ringing, indicating good coupling to the borehole wall between 417 and 359 mbsf and moderate coupling from 359 to 319 mbsf. We clamped the ASI bottom geophone shuttle at 397.2 mbsf (5413 mbrf). The other four shuttles were at 15.24-m intervals above this. We clamped the five geophone shuttles 1.7 m below the desired depth and dragged them up the casing to straighten the bridle between them. This ensured that the shuttles were vertical and at the correct spacing and improved their coupling. We recorded an air-gun shot to verify that all sensors were working and adequately coupled.

We recorded a 32-s window at a sampling rate of 2 ms, beginning 8 s before each shot was due. In previous experiments and test runs, the shot timers were accurate to ±4 s. Time was kept with a quartz wristwatch synchronized with the global positioning system time signal.

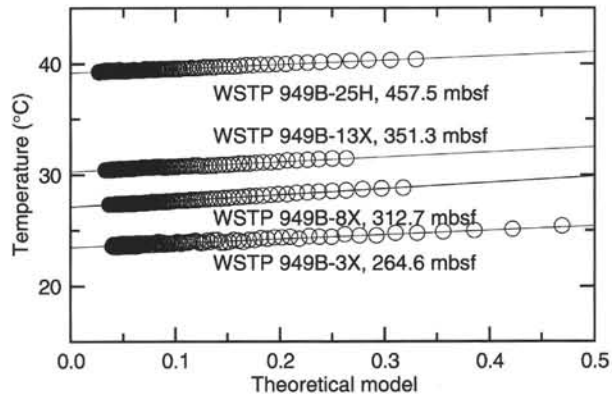

Figure 50. Temperatures vs. the theoretical model for all four WSTP deployments in Hole 949B.

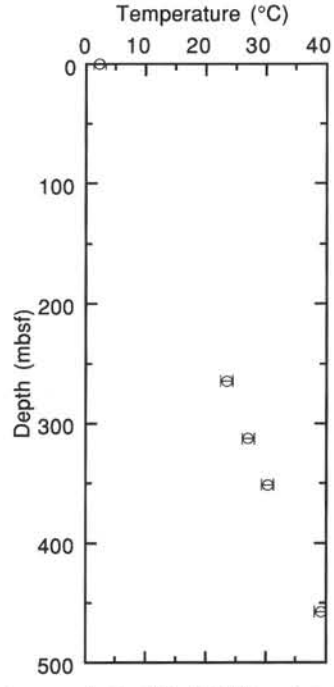

Figure 51. Temperatures vs. depth at Site 949. These data cluster tightly about a gradient of 80°C/km, but heat flow increases with depth.

Results

Of the 21 shots, 18 were recorded. Shots 1 and 7 misfired, and Shot 18 was not recorded because of a telemetry error from the ASI. Just before Shot 5, there was a temporary power loss to the wireline heave compensator; the shot appears in a quiet window between bursts of cable noise. Gains on the geophones were initially too high and were reduced to prevent clipping of the signal. The hydrophone recorded continuously on the chart recorder, which showed each shot as a single spike, verifying detonation. Signals observed on the chart recorder after Shots 5 and 9 could be the result of late detonation of Shots 1 and 7.

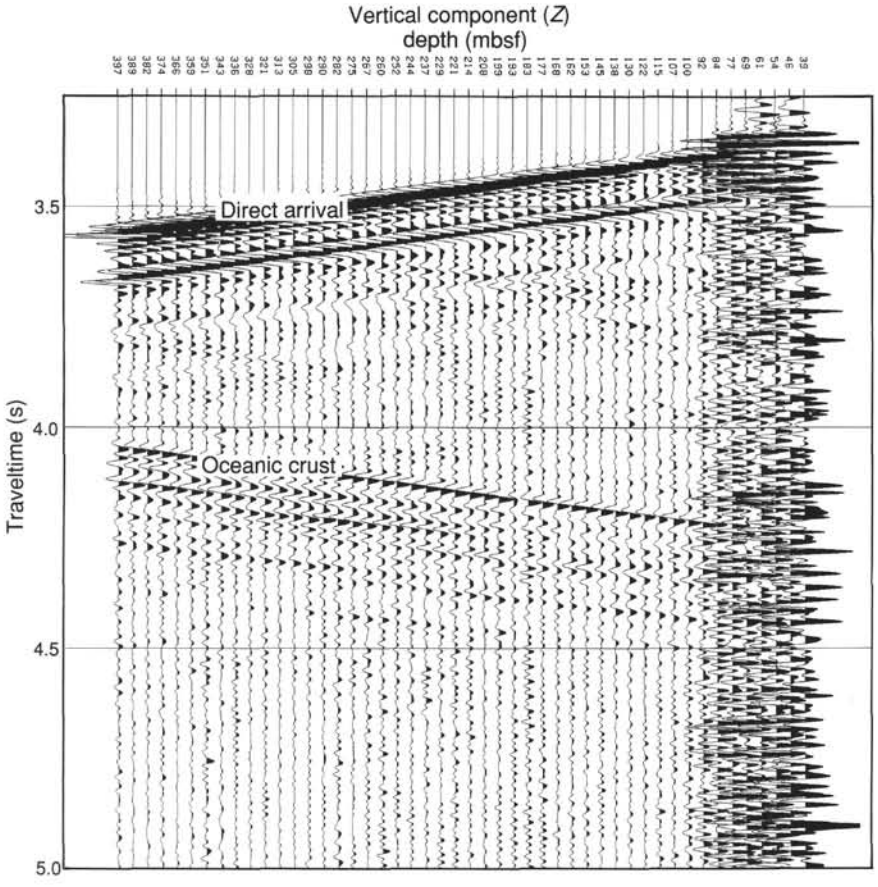

Figure 52. Stacked and bandpass-filtered (5–80 Hz) seismogram vs. receiver depth below seafloor for vertical component of VSP in Hole 949C.

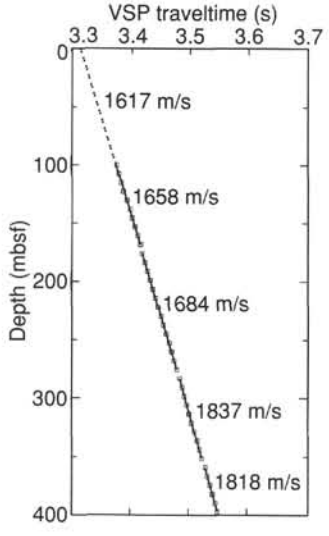

Figure 53. Traveltime vs. depth of first breaks selected from the vertical-component record for the upper part of the VSP. Lines show least-squares fit used to determine velocities.

Sample records from Shot 13 show the main arrivals on the ASI and the hydrophones (Fig. 58). The downgoing *P*-wave and slower downgoing and upgoing signals that may be shear or tube waves appear on *x*, *y*, and *z* components. The hydrophones show the water wave's arrival and a ghost reflection. Hydrophone 2 has reversed polarity with respect to Hydrophone 1.

The frequency band of the signals was higher than anticipated, 100 Hz up to the Nyquist, 250 Hz (Fig. 59). The sample interval of 2 ms was inadequate for capturing every detail of the waveform, and it is likely that the signal between 200 and 250 Hz has been contaminated with an aliased signal from 250 to 300 Hz. The ASI digitizer module applied an analog anti-alias filter with slope –36 dB/octave above 300 Hz, before digitizing the signal at a 0.5-ms sample interval. The MAXIS system then applied a 150-Hz anti-alias digital filter before resampling at 2 ms. The large amplitude at 250 Hz even after this filtering implies that the explosions had a very high-frequency-source signature.

PACKER EXPERIMENTS

The TAM straddle-packer was set in Hole 949C. The final configuration of casing and screen and the approximate location of packer seats are shown in Figure 60. Pressure records obtained from electronic gauges that hung below the go-devil during each experiment are shown in Figure 61. The following is a description of operations associated with these packer experiments, as well as preliminary interpretations. Considerable additional analysis will be required before more complete, and more quantitative, interpretations can be made.

Two days before the packer operations in Hole 949C, the rig plumbing was pressurized to 17.2 MPa and shut in. After we tightened several valves, the system was made pressure-tight. Packer work followed emplacement of a bridge plug intended to prevent flow of sediment up from the bottom of the open casing (see "Operations" section, this chapter). The pipe was tripped back to the rig floor and the packer attached. The sea state was calm throughout the experiment, but ship's heave occasionally exceeded 2 m, which affected packer operations negatively, as described below.

When the hole was located with the TV camera, no sediment was observed to exit the cone. Following reentry, the pipe was lowered to 392 mbsf (5408 mbrf), the depth of the first (lower) packer seat. This placed the packer in the middle of the first joint of casing above the screened zone (Fig. 60). One electronic and one mechanical gauge

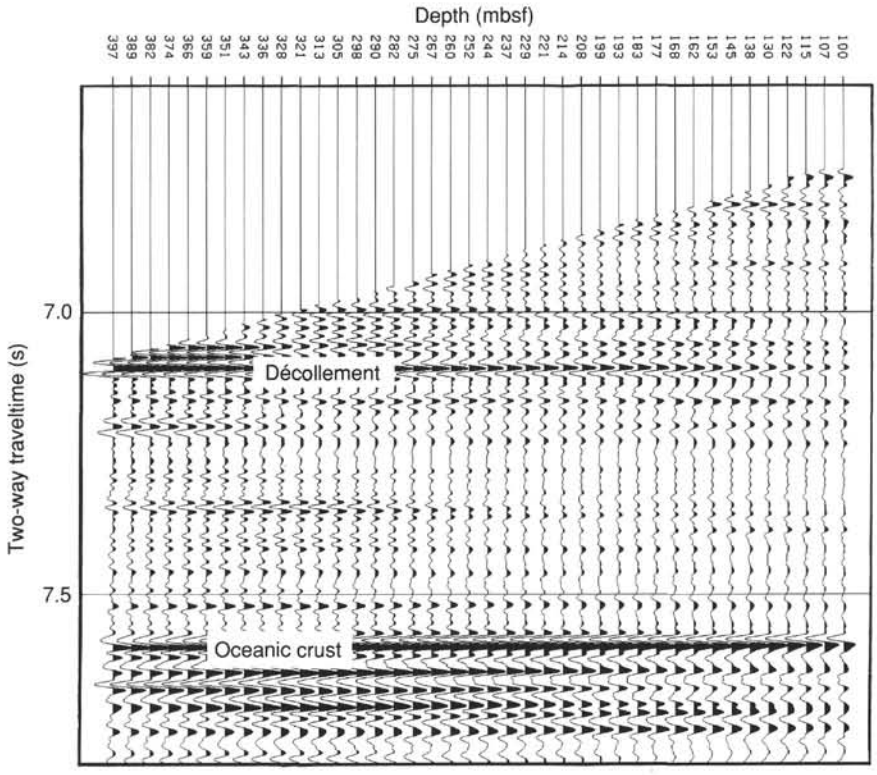

Figure 54. Upgoing wavefield of vertical component of VSP converted to two-way traveltime.

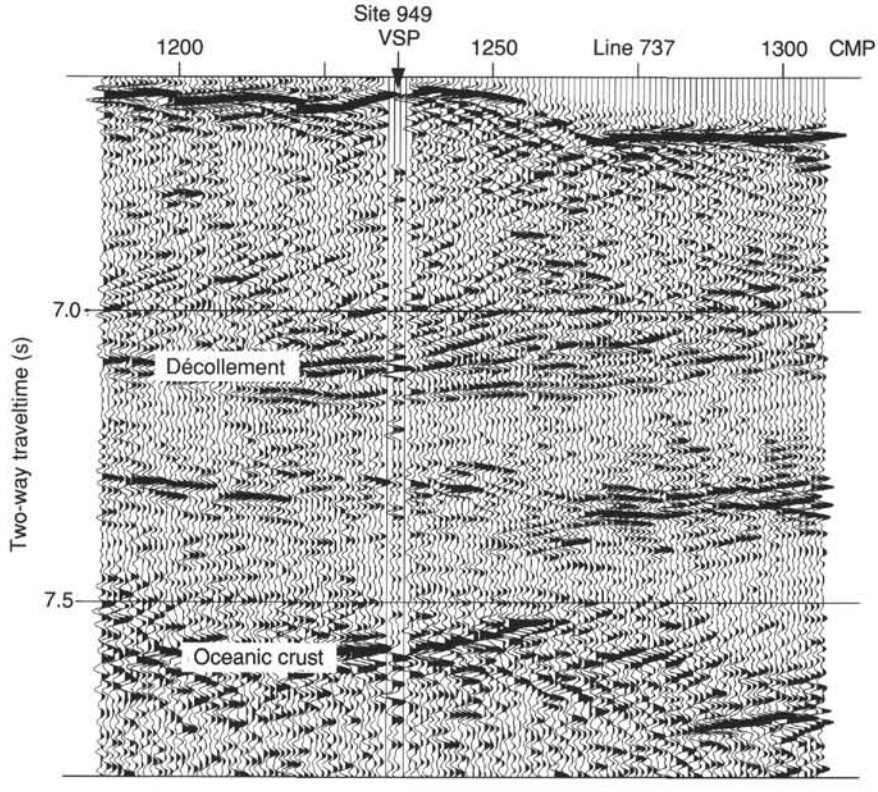

Figure 55. Stack of upgoing waves of vertical component inserted into seismic Line 737 at location of Site 949.

were dressed and attached to the bottom of the go-devil. A GRC gauge sampled with a 10.8-s data interval and a Kuster gauge produced a 12-hr analog record.

The go-devil was pumped down the pipe, landing 30 min after leaving the rig floor. We monitored hydrostatic pressure for 30 min, then inflated the packer element with 13.8 MPa and shut in this pressure at the rig floor. The pressure held for 10 min, with minor additional pumping. The inflation pressure was increased to 15.9 MPa, and the driller set down 9100 kg on the packer by releasing air from the heave compensator to shift the control sleeve and to lock the element while inflated. Internal pressure bled off quickly as the pressure was set, opening communication to the isolated zone.

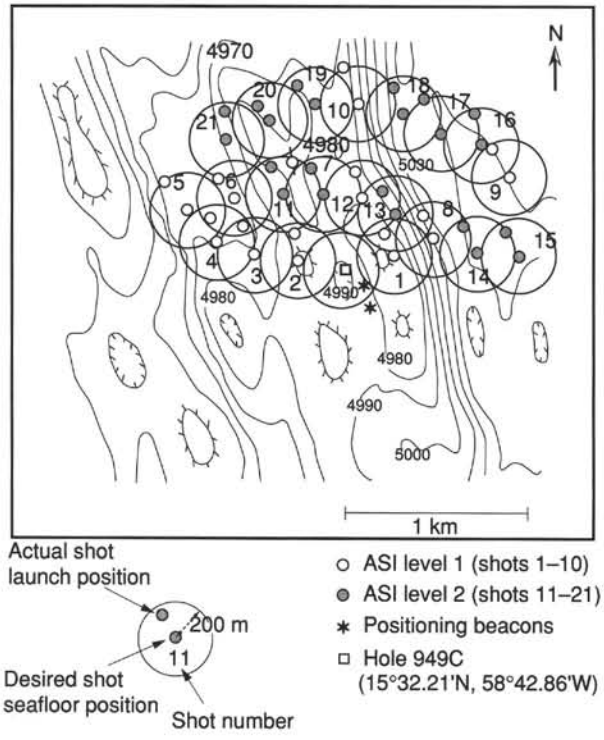

Figure 56. Map of area around Hole 949C showing actual and desired shot launching points and 200-m radii around each shot. Shot detonation positions will be determined later. Contours at 10-m intervals are from seafloor reflections recorded by Shipley et al. (1994).

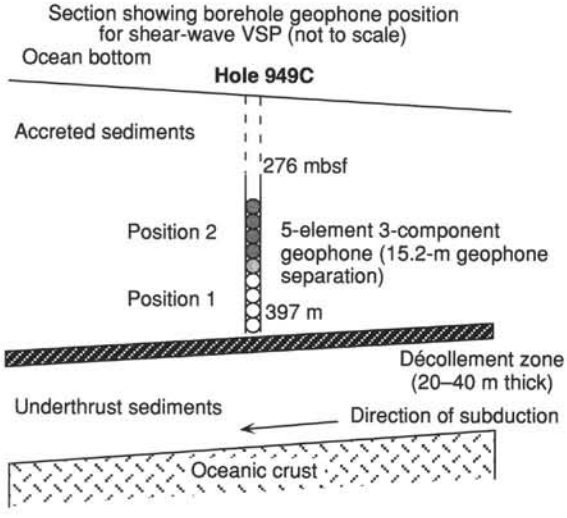

Figure 57. Schematic east–west section through Hole 949C, showing geophone positions for the bottom-shot VSP experiment.

Pressure in the isolated zone was shut in to monitor the decay following the setting of the element. We waited 30 min to record pressure in the isolated zone, then began a series of "negative" pulse and flow tests to expose the isolated formation to hydrostatic pressure and monitored recovery. We conducted two negative pulse tests by rapidly opening and closing the valve at the cement pump, which exposed the isolated zone to hydrostatic pressure. Following each pulse, we allowed 30 min for recovery. We then opened the valve at the cement pump and allowed the formation to flow back while we measured rate. Unfortunately, the formation produced little water;

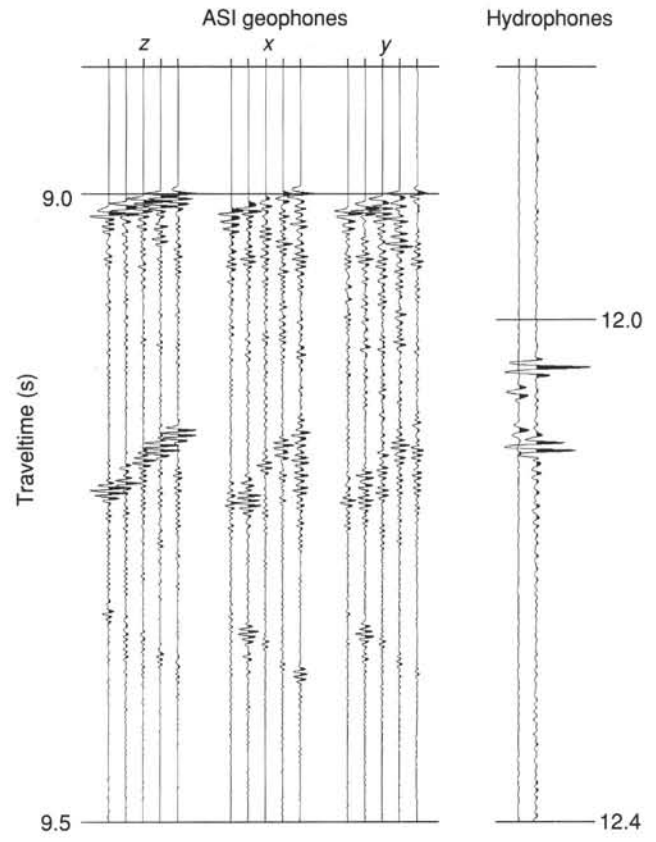

Figure 58. Seismic records from Shot 13, recorded on vertical (*V*) and horizontal (*X* and *Y*) components of the ASI geophones; and hydrophones (H) 1 (50 m deep, near moonpool) and 2 (67 m from 1, 40 m deep, starboard stern).

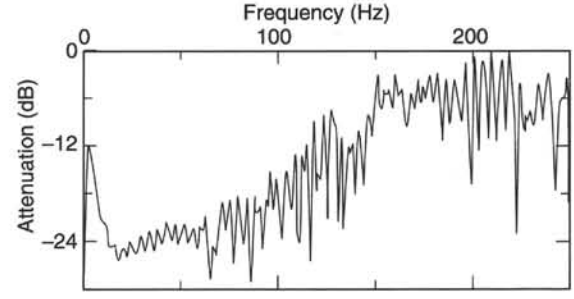

Figure 59. Amplitude spectrum of vertical component of ASI receiver 2 (second from bottom, 276 mbsf) for Shot 13. A 550-ms window covers main arrivals. Note that input record is raw (unintegrated) acceleration recorded by geophone accelerometer.

instead, the rig-floor standpipe emptied completely, allowing air to enter the system. We waited for 60 min, but pressure was not recovered. We could not continue the testing at this point, as our results would have been degraded seriously by the air in the pipe.

The only way to remove air from the system without deflating the packer and starting again was to pump through the standpipe while keeping a valve open at the highest point until all air was vented. The SEDCO core technician accomplished this by being lifted up in the derrick on a harness to vent the standpipe while fluid was pumped through the system at 10 to 13 L/s. When the air had vented and the valve was closed, pressure rose slightly in the shut-in pipe; so we waited another 30 min before continuing the pressure tests.

We attempted three positive slug tests by quickly pumping 120, 120, and 140 L of seawater into the formation, then shutting it in.

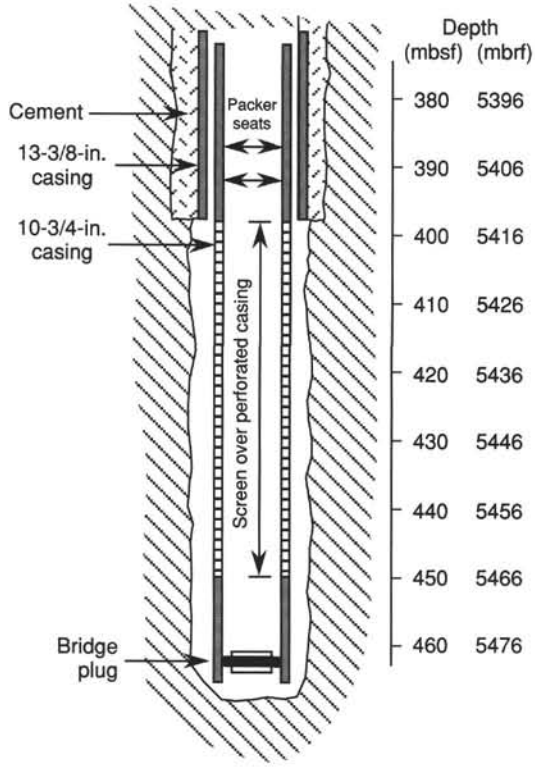

Figure 60. Configuration of the casing and open hole (approximate) during packer testing in Hole 949C. See the "Operations" section (this chapter) for a description of drilling and casing steps. The annulus between the 13⅜- and 10¾-in. casing strings may have been open up to the 10¾-in. casing hanger, where a rubber seal prevented communication with the overlying ocean, although it is also possible that the formation collapsed sufficiently tightly around the smaller casing so as to prevent communication with the casing annulus.

Finally, we attempted an injection test by pumping 2 L/s for 20 min. By the time we shut in the hole at the end of the injection test, the weight on the packer had risen to 13,600 kg (up from 9100 kg), indicating that the packer was being pushed from below. The system was shut in, but there was little decay. We retrieved the go-devil and gauges with the coring line, and good records were obtained.

While we were redressing the gauges and go-devil for a second series of tests, the depth of the hole was checked with a sinker bar attached to the coring line. The hole was found to contain 10 to 12 m of fill at the bottom, below the level of the screen. The pipe was washed to bottom and circulation maintained for 30 min. A dense plume of sediment-laden water was observed exiting the reentry cone during this time. Because time for packer work was limited, we then ended circulation and moved the packer to a new setting depth. We conducted the second tests with the packer at 387 mbsf (5403 mbrf), because this placed the packer element at the connection (a "tool joint") between two pieces of casing. We hoped that the irregular shape of the casing at this level would help to hold the packer in position during testing.

The second go-devil was pumped down the pipe and landed. When the go-devil landed, pressure rose sufficiently to partially inflate the packer element (perhaps 3–4 MPa), which began to grip the casing wall. Ship's heave had increased slightly by this time, and during an up-stroke, the packer was accidentally set with a low inflation pressure. Unsetting the packer then was a challenge, because when it had been set, communication was opened to the isolated zone. Elevated pressure in the isolated zone (either natural or induced) pushed up on the partially inflated element, so that when the driller tried to pull up on the packer to deflate it, the packer simply came up the hole. It was necessary to bleed off the excess pressure at the standpipe to deflate the packer. This sequence of events was repeated before the packer element finally was set with 15.8 MPa.

The pipe was shut in for 30 min, and then we attempted a single pulse test. The pipe was shut in for another 40 min. We then conducted an injection test at 3.2 L/s. After 18 min, the packer again began to rise up the hole, so we stopped pumping and shut in the hole for 60 min. The isolated interval held most of the excess pressure during this time. We then vented the pressure and pulled up on the packer, deflating the element and retrieving the go-devil. Once again, the gauges contained excellent records.

The pressure records from packer testing in Hole 949C are even more confusing at first glance than those from Hole 948D (see "Packer Experiment" section, "Site 948" chapter, this volume). In general, the formation at Site 949 seems to be less transmissive, although the injection test at the end of the second period of testing appears to indicate higher transmissivity than do the other tests, including the shut in and recovery immediately following injection. The negative pulse tests seem to have helped tighten up the formation or to have clogged the screen. A short-lived pressure pulse at the start of packer inflation during the first series of tests suggests a fluid pressure below the packer of about 1 MPa above hydrostatic pressure, but it is not clear whether this is a natural formation pressure.

SUMMARY AND CONCLUSIONS

Site 949 is located where the overlying prism is thinner, and the negative-polarity reflection is not as high amplitude as that at Site 947. The sedimentology deduced from the limited recovery is similar to that of Site 948. The poor recovery precludes any detailed comparison with other sites cored in this area during Leg 78A or 110. A stratigraphic inversion indicates a fault in the upper part of the cored section. Early Miocene radiolarians in a pale yellowish brown claystone occur at about 400 m. The underthrust brownish gray to greenish gray claystones with interbeds of siltstone turbidites and remobilized chalks occur near the bottom of the hole.

In the only two cores from the presumed décollement zone, structures are similar to those from Site 948, including inclined bedding, core-scale faults, mineralized veins, sediment-filled veins, brecciated zones and fracture networks, stratal disruptions, and scaly fabric. Scaly zones are narrow and the overall intensity of deformation is weaker than those at Site 948. Anisotropic magnetic susceptibility orientation fabrics exhibit a distinct difference in the orientation of principal strain between the prism and décollement zone.

Headspace gas analysis showed that methane concentrations were below 20 ppm by volume and did not show any trend with depth. The general chloride concentration-depth profiles indicate that the cored section has been diluted by freshwater. Three distinct zones of low chloride concentrations are located at about 270, 360, and 425 mbsf. Reversals in most concentration profiles from about 270 to 350 mbsf suggest vertical displacement of about 80 m. As little diffusive exchange was observed across the inferred thrust, its maximum age is about 35,000 yr.

Combined physical properties data for Holes 949B and 949C are sparse, and, thus, downhole profiles are incomplete. The physical property data will be of use to serve as a background for evaluating thermal and chemical information to be gained from the long-term measurements in the CORK hole. WSTP measurements reveal a near-linear thermal gradient of about 80°C/km with a bottom-hole temperature of 39°C at 458 m, suggesting that heat flow is not constant with depth.

A shear-wave VSP experiment used 21 explosive charges on the seafloor around Hole 949C. Eighteen shots were recorded to observe shear-wave velocities and polarizations, which should relate to deformation fabric alignment. A conventional air-gun VSP followed. Velocities decrease just above the décollement, as at Site 948.

A series of formation shut-in and flow tests using the packer measured hydrologic characteristics of the décollement. Preliminary

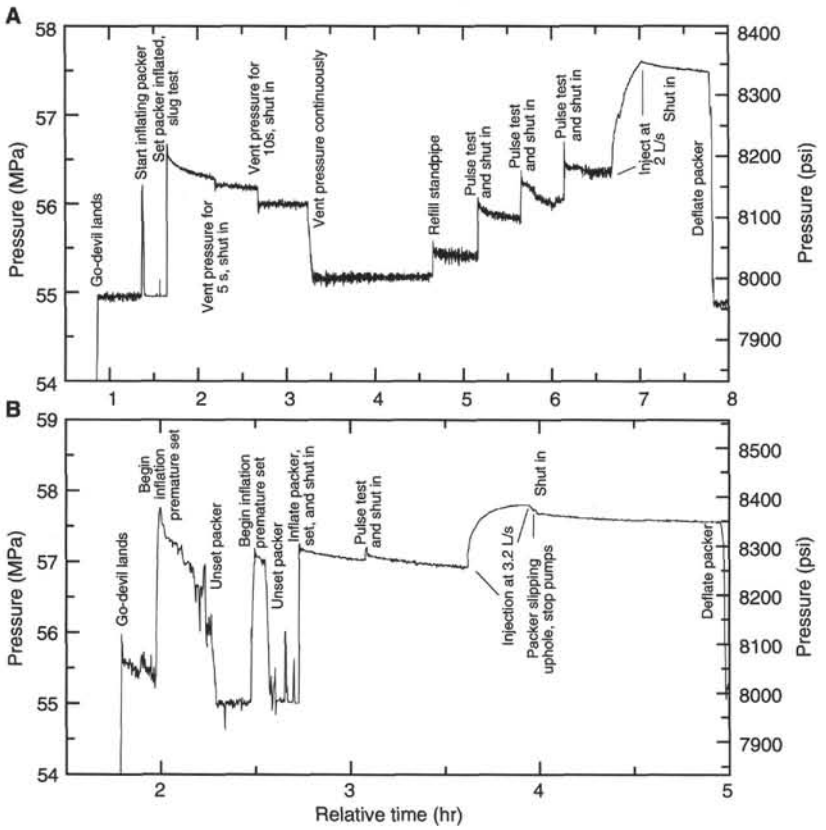

Figure 61. Annotated pressure vs. time records from electronic gauges hung below the go-devils during packer testing. Values are total pressures. **A.** First go-devil. **B.** Second go-devil.

analysis suggests modest overpressures, less than those at Site 948. This is consistent with the more subdued evidence for flow and casing filling at this site relative to Site 948.

For at least 2 yr, the CORK installation will provide temperature and pressure measurements, and the mechanical continuous fluid sampler will collect fluid.

Shipboard Conclusions

The décollement zone depth is not well defined, but it must be between 380 and 433 mbsf. Detailed lithostratigraphy and structural geology are not precisely known because of poor core recovery. Deformation structures are similar to those at Site 948, but are weaker in intensity, as are the geochemical indications of fluid flow. The less well-defined décollement and evidence of less intense strain are probably related to the location of the site only about 2 km from the thrust front. We did not have time to log this site, but the VSP provides direct correlation of the seismic data to the hole. Detailed velocity data also show a decrease in the 40-m interval above the décollement, suggesting density trends similar to those observed at the other sites. As at Site 948, we observed fluid flow out of the reentry cone and sediment filling the casing, which made operations challenging. The packer data are suggestive of overpressure within the décollement, but are lower than those at Site 948. Further analysis will be necessary to confirm these values and to estimate bulk permeabilities. The CORK measurements will provide other estimates of in situ conditions and will monitor for a longer period changes in fluid properties.

REFERENCES*

Cande, S.C., and Kent, D.V., 1992. A new geomagnetic polarity time scale for the Late Cretaceous and Cenozoic. *J. Geophys. Res.,* 97:13917–13951.

Ekdale, A.A., Bromley, R.G., and Pemberton, S.G. (Eds.), 1984. *Ichnology: The Use of Trace Fossils in Sedimentology and Stratigraphy.* SEPM Short Course, 15.

Gieskes, J.M., Blanc, G., Vrolijk, P., Elderfield, H., and Barnes, R., 1990. Interstitial water chemistry—major constituents. *In* Moore, J.C., Mascle, A., et al., *Proc. ODP, Sci. Results,* 110: College Station, TX (Ocean Drilling Program), 155–178.

Gieskes, J.M., Gamo, T., and Brumsack, H.J., 1991. Chemical methods for interstitial water analysis aboard *JOIDES Resolution. ODP Tech. Note,* 15.

Mascle, A., Moore, J.C., et al., 1988. *Proc. ODP, Init. Repts.,* 110: College Station, TX (Ocean Drilling Program).

Peters, K.E., 1986. Guidelines for evaluating petroleum source rock using programmed pyrolysis. *AAPG Bull.,* 70:318–329.

Shipboard Scientific Party, 1988. Site 676. *In* Mascle, A., Moore, J.C., et al., *Proc. ODP, Init. Repts.,* 110: College Station, TX (Ocean Drilling Program), 509–573.

Shipley, T.H., Moore, G.F., Bangs, N.L., Moore, J.C., and Stoffa, P.L., 1994. Seismically inferred dilatancy distribution, northern Barbados Ridge décollement: implications for fluid migration and fault strength. *Geology,* 22:411–414.

Tissot, B.P., and Welte, D.H., 1984. *Petroleum Formation and Occurrence* (2nd ed.): Heidelberg (Springer-Verlag).

Waples, D.W., 1985. *Geochemistry in Petroleum Exploration:* Boston (Int. Human Resour. Develop. Corp.).

* Abbreviations for names of organizations and publication titles in ODP reference lists follow the style given in *Chemical Abstracts Service Source Index* (published by American Chemical Society).

Ms 156IR-107

NOTE: Core description forms ("barrel sheets") and core photographs can be found in Section 3, beginning on page 261. Forms containing smear-slide data can be found in Section 4, on page 299. Cementation logs and GRAPE, index properties, magnetic susceptibility, natural gamma-ray, *P*-wave, and reflectance data for Site 949 are presented on CD-ROM (back pocket).